The People's Democratic Republic of Algeria

Ministry of Higher Education and Scientific Research

Amar Telidji University - Laghouat

Faculty of Sciences

Doctoral thesis

Specialty: Material Physics

Publicly presented on --/--/2021

by:

Ms AMEUR Anfal Saida

THEME

Study of some physical properties for new materials for nonlinear optics

Thesis committee:

Mr Khenchoul Salah	Class A assistant teacher	UAT Laghouat	President
Mr Bouhadda Youcef	Research director	CDER/URAER Ghardaïa	Examiner
Mr Benyelloul Kamel	Research director	CDER/URAER Ghardaïa	Examiner
Mr Bourourou Yahia	Class A assistant teacher	UAT Laghouat	Examiner
Mr Lagoun Brahim	Class A assistant teacher	UAT Laghouat	**Supervisor**
Mr Guibadj Abdenacer	Professor	UAT Laghouat	**Co-supervisor**

Acknowledgment

First of all, I thank the almighty ALLAH for his mercy and grace, which enabled me to complete this work.

The present work was carried out in the Laboratory Physics and Chemistry of Materials (LPCM) of the University of Laghouat.

This thesis could not have been written without the help of Allah and the support of many people who have contributed in many different ways.

I will start to thank MCA. **Lagoun Brahim**, Maître de conferences "A" and Co-supervisor; Professor **Guibadj Abdenacer** for their help, support, guidance and encouragement. Without their persistent help, the goal of this project would not have been realized.

My sincere gratefulness is dedicated to the thesis committee members, President **Khenchoul Salah,** the examiners: Research Director. **Bouhadda Youcef**, Research Director. **BenYelloul Kamel** and MCA. **Bourourou Yahia** for taking the time to assess this work and to attend the PhD defense.

DEDICATION

This work is dedicated to those who were beside me along the steps of the work;

my family, my father, Abderazek; my mother, Naima;

my brothers Labib, Nizar, and Iyad.

My sisters; Maissem, and Ritaj,

for their support and their patience with me all this time, you are my real blessing in life.

my mother, I will never forget your prayers every night and your patience and support that is indispensable to me. love you

my father, thank you for all the things you gave me throughout my life, thank you for faith in me even when I failed, and Today I hope you are proud of me. love you

thanks to my friends and colleagues who contributed achievement of this thesis.

Thank you all…

Ameur Anfal

SUMMARY

Figures list

Table list

Table. IV. B.11. EO tensor in (pm/V) for $CsIO_2F_2$. **162**

Nomenclatures

NLO	Nonlinear Optical.
SHG	Second Harmonic Generation.
NCS	Non-centrosymmetric
LDT	Laser damage threshold.
PO	Piezoelectric.
EO	Electro-optic.
$\Delta n(\omega)$	Birefringence.
Eg	Energy gap.
$\chi^{(2)}$	The second order susceptibility.
SOJT	Second-order Jahn-Teller.
SCALP	Stereochemical activity of lone pair electrons.
FBUs	Functional building units
DFT	Density Functional Theory.
U_{xc}	Exchange-correlation functional.
TB-mBJ	Becke-Johnson potential.
DFPT	Density-functional perturbation theory.
FP-LAPW	All-electron full-potential linear augmented plane wave.
LDA-PW	Local density Perdew–Wang92 functional approximation.
WC-GGA	Generalized gradient approximation by Wu and Cohen
PBE -GGA	Generalized gradient Approximation GGA developed by Perdew-Burker-Ernzerhof

PP-PW	Pseudo-potential plane wave
Exp.	Experimental
T-DOS	Total density of states.
P-DOS	Partial density of states.
VB	Valence band.
CB	Conduction band.
B	Bulk modulus
G	Shear modulus
E	Young's modulus.
ν	Poisson’s ratio.
Θ_D	Debye temperature.
A^U	Universal anisotropy factor.
A_B (%)	Percentage of bulk module anisotropy factors.
A_G (%)	Percentage of shear modulus anisotropy factors.

GENERAL INTRODUCTION

GENERAL INTRODUCTION

Nonlinear optical (NLO) materials development is crucial for the advancement of many modern technologies such as telecommunication, signal processing, data storage, super-resolution lithography …etc. [1-3]. NLO materials with well-defined designs on (sub) wavelength length scales, in particular, are considered important materials for the creation of the next generation of integrated photonic circuits, [4-8]. One of the most widely studied NLO phenomena is the second harmonic generation (SHG),[9] in which two photons of incident light combine and form a photon with twofold frequency and energy, which is one of the most extensively used second-order NLO phenomena. From a crystal structure standpoint, promising second-order NLO crystals should form in non-centrosymmetric (NCS) space groups. Unfortunately, NCS alone isn't enough to make an NLO material [10], A good NLO crystal should dictate the following requirements for second-harmonic-generation (SHG) applications: large NLO coefficient, a high value of laser damage threshold (LDT) that corresponds to band gap value, transparency in the required region (should run across the two atmospheric windows of 3–5 m and 8–12 m), moderate birefringence to allow phase matching, [11, 12].

Due to its multi-functional applications such as second-order nonlinear optics (NLO), piezoelectric (PO), as well as electro-optic (EO). NCS polar crystals are considered the major basis for modern fundamental material research [13-16].

According to their wavelength in the spectrum, these NLO materials are divided into four categories.: deep-ultraviolet (deep-UV, **λ< 0.2 μm**), ultraviolet (deep-UV, **0.2 μm <λ<0.4 μm**), visible-near infrared (vis−NIR, **0.4 μm <λ<3 μm**), mid-and far-infrared (MFIR, including **3 μm <λ<5 μm** and **8 μm <λ<13 μm**), [12, 17-19].

The KTP ($KTiOPO_4$) crystal has a broad transmission range, high-frequency for conversion efficiency, good phase-matchable wavelength, high laser damage threshold (LDT), and outstanding physical and chemical stability in the case of the Vis-NIR region.[20]. Chinese researchers have achieved significant advancements in the UV and deep-UV fields. The BBO [21], and LBO [22], also referred to as the "Chinese card" crystal, were created by Chen and his associates. To create all-solid-state lasers by optical parametric oscillation (OPO) or differential frequency generation (DFG), MFIR NLO materials are essential[23]. Numerous cutting-edge fields of research and technology, including infrared remote sensing[24], biological tissue imaging[25], and environmental monitoring [26], have significant uses for

tunable narrowband lasers employing NLO crystals. [27]. The three MFIR NLO crystals that are now commercially accessible have strong second-harmonic generation (SHG) coefficients: AgGaS2 (AGS), AgGaSe2 (AGSe), and ZnGeP2 (ZGP).[28]. These materials can't be used to generate MFIR lasers because of a few drawbacks. For instance, the AGS and AGSe laser damage threshold (LDT) values are inadequate (only about 25 MW/cm2 and 11 MW/cm2, respectively).[29] to support a powerful source of pumping. It is also not viable to use a Nd: YAG laser as the pumping source due to the significant two-photon absorption (TPA) in ZGP caused by its small bandgap (2.0 eV). Therefore, new MFIR NLO materials with good performance are urgently needed given the current rapid growth of mid-IR lasers.[30].

In contrast, metal iodates are superior candidates for NLO due to their improved relevant physical properties., [31]. They have a very wide transparency range stretching from the ultraviolet region to the beginning of the far-IR region, and they are thermally stable at least up to 400 C. They demonstrated good nonlinear optical coefficients and high optical damage thresholds in the Kurtz and Perry powder SHG experiments.[31]. The only extensively researched commercial iodate in this family is -$LiIO_3$[32]. However, it is only used to create piezoelectric transducers in commercially available devices. This is due to several factors, including impurities [24], inconsistent crystal formation[33], limited thermal stability, and local structural and phase transitions after laser irradiation [34].

The main difficulty right now is to create anionic groups with large electron cloud deformations, which will improve nonlinear polarizability and large NLO coefficients. By boosting their ionicity, on the other hand, to widen the optical energy gap, NLO materials with high LIDT values may be produced. For the same anionic group, these two characteristics, however, frequently work against one another since strong ionicity can hinder electron deformation and weak ionicity can result from significant electron cloud deformation. Developing NLO materials with high NLO coefficients and LIDT values is crucial to resolving this paradox. The following practical methods were suggested to achieve the final features; (i) Important prospects for polar crystals include compounds with $(n-1)d^{10}ns^0$ transition-metal cations (Ag^+, Cu^+, Zn^{2+}, Cd^{2+}, etc.), which have a polar displacement of the d^{10} cation center. (ii) Second-order Jahn-Teller (SOJT) effect occur on by lone-pair electrons may affect compounds containing ns2 main-group metal cations (Pb^{2+}, Sn^{2+}, Bi^{3+}, I^{+5}, Se^{4+}, Te^{4+}, etc.).[24, 35, 36]. (iii) Acentric building blocks like [PO_4], [CrO_4], and [IO_4] are used to create $[MO_4]^{-n}$ tetrahedrons. [35-37]. (iv) polar chalcogenide groups including ($[TeS_3]^{2-}$, $[AsS_3]^{3-}$, $[SbS_3]^{3-}$, etc). (V) There have been new developments in engineering, such as the IO_xF_{4-x} (x=1, 2, 3)

combination of fluoro-oxides and transition metal (TM) cations. [38-40]. When combining two or more NLO-active types to create functional crystals with potent NLO effects, which can then be further stacked in an additive model to produce structural building units,[39, 41].

First-principles calculations are a powerful and effective technique to study the crystal structure and properties linked to the electron configuration of material before its synthesis in recent years as a result of advancements in computational technology[42-47]. This thesis' goal is to examine these materials for a better understanding of the linear and non-linear optical characteristics, piezoelectricity, and electro-optical activity, spread over the non-centrosymmetric classes 2mm, I($\bar{4}$), and 3m, based on the qualities described above. In reality, there aren't many experimental or theoretical data points accessible for these qualities.

This thesis mostly relies on the following four chapters:

The first chapter is a bibliography that provides the NLO criteria and technique to generate high-performance NCS crystal structures and enumerates the various fundamental ideas connected to the phenomenon of linear and nonlinear. The promoters' NLO Compounds for the atmospheric transparent windows of the main types are also briefly discussed.

The second chapter will cover the fundamental ideas of the theoretical framework, density functional theory (DFT) and their formalization, density functional approximations that are employed, density functional perturbation theory (DFPT), and the contemporary theory of polarization.

The third chapter and **the fourth chapter** are devoted to the theoretical investigation of the linear and nonlinear optical (NLO) properties of; $RbLiCrO_4$, $AgBi(CrO_4)_2$ and $RbIO_2F_2$, $CsIO_2F_2$, respectively, our theoretical investigation is extended to the determination of information about the structural, electronic, elastic constant, piezoelectric, and electro-optic of these compounds.

Reference of general introduction

1. Garmire, E., *Nonlinear optics in daily life.* Optics express, 2013. **21**(25): p. 30532-30544.

2. Sereni, J.G.R., *Reference module in materials science and materials engineering.* 2016.

3. Dini, D., M.J. Calvete, and M. Hanack, *Nonlinear optical materials for the smart filtering of optical radiation.* Chemical Reviews, 2016. **116**(22): p. 13043-13233.

4. Xu, J., et al., *Organized chromophoric assemblies for nonlinear optical materials: towards (sub) wavelength scale architectures.* Small, 2015. **11**(9-10): p. 1113-1129.

5. Chervy, T., et al., *High-efficiency second-harmonic generation from hybrid light-matter states.* Nano letters, 2016. **16**(12): p. 7352-7356.

6. Xu, J., et al., *Controlling microsized polymorphic architectures with distinct linear and nonlinear optical properties.* Advanced Optical Materials, 2015. **3**(7): p. 948-956.

7. Guo, B., et al., *2D layered materials: synthesis, nonlinear optical properties, and device applications.* Laser & Photonics Reviews, 2019. **13**(12): p. 1800327.

8. Rosenne, S., et al., *Self-assembled organic nanocrystals with strong nonlinear optical response.* Nano letters, 2015. **15**(11): p. 7232-7237.

9. Franken, P., et al., *Generation of optical harmonics.* Physical review letters, 1961. **7**(4): p. 118.

10. Mao, F.F., et al., *Bi (IO3) F2: the first metal iodate fluoride with a very strong second harmonic generation effect.* Angewandte Chemie, 2017. **129**(8): p. 2183-2187.

11. Yao, W., et al., *Analysis of Deep-UV Nonlinear Optical Borates: Approaching the End.* Advanced Optical Materials, 2014. **2**(5): p. 411-417.

12. Tran, T.T., et al., *Deep ultraviolet nonlinear optical materials.* Chemistry of materials, 2016. **28**(15): p. 5238-5258.

13. Poplavko, Y., et al. *Microwave annealing of integrated ferroelectric films*. in *1994 24th European Microwave Conference*. 1994. IEEE.

14. Nikogosyan, D.N., *Periodically Poled Crystals and "Wafer" Materials.* Nonlinear Optical Crystals: A Complete Survey, 2005: p. 185-213.

15. Jones, D., S. Prasad, and J. Wallace. *Piezoelectric materials and their applications*. in *Key Engineering Materials*. 1996. Trans Tech Publ.

16. Nowacki, W., T. Matsumoto, and A. Edenharter, *Classification of crystalline substances by crystal systems, crystal classes, Bravais lattices and space groups.* Acta crystallographica, 1967. **22**(6): p. 935-940.

17. Shoji, I., et al., *Absolute measurement of second-order nonlinear-optical coefficients of CsLiB 6 O 10 for visible-to-ultraviolet second-harmonic wavelengths.* JOSA B, 2001. **18**(3): p. 302-307.

18. Chen, C., et al., *Deep-UV nonlinear optical crystal KBe2BO3F2—discovery, growth, optical properties and applications.* Applied Physics B, 2009. **97**(1): p. 9-25.

19. Guo, S.-P., Y. Chi, and G.-C. Guo, *Recent achievements on middle and far-infrared second-order nonlinear optical materials.* Coordination Chemistry Reviews, 2017. **335**: p. 44-57.

20. Bierlein, J.D. and H. Vanherzeele, *Potassium titanyl phosphate: properties and new applications.* JOSA B, 1989. **6**(4): p. 622-633.

21. Chen, C., et al., *A New-Type Ultraviolet SHG Crystal——β-BaB 2 O 4.* Science in China Series B-Chemistry, Biological, Agricultural, Medical & Earth Sciences, 1985. **28**(3): p. 235-243.

22. Chen, C., et al., *New nonlinear-optical crystal: LiB 3 O 5.* JOSA B, 1989. **6**(4): p. 616-621.

23. Petrov, V., *Frequency down-conversion of solid-state laser sources to the mid-infrared spectral range using non-oxide nonlinear crystals.* Progress in Quantum Electronics, 2015. **42**: p. 1-106.

24. Arriola, A., et al., *Mid-infrared astrophotonics: study of ultrafast laser induced index change in compatible materials.* Optical Materials Express, 2017. **7**(3): p. 698-711.

25. Zhao, Z., et al., *Mid-infrared supercontinuum covering 2.0–16 μm in a low-loss telluride single-mode fiber.* Laser & Photonics Reviews, 2017. **11**(2): p. 1700005.

26. Pestov, D., et al., *Single-shot detection of bacterial endospores via coherent Raman spectroscopy.* Proceedings of the National Academy of Sciences, 2008. **105**(2): p. 422-427.

27. Chung, I. and M.G. Kanatzidis, *Metal chalcogenides: a rich source of nonlinear optical materials.* Chemistry of materials, 2014. **26**(1): p. 849-869.

28. Ohmer, M.C. and R. Pandey, *Emergence of chalcopyrites as nonlinear optical materials.* Mrs Bulletin, 1998. **23**(7): p. 16-22.

29. Ruderman, W., et al., *Laser damage studies of silver gallium sulfide single crystals.* MRS Online Proceedings Library (OPL), 1997. **484**.

30. Schunemann, P.G. *Crystal growth and properties of nonlinear optical materials*. in *AIP Conference Proceedings*. 2007. American Institute of Physics.

31. Bentria, B., et al., *Crystal engineering strategy for quadratic nonlinear optics. Part II: Hg (IO3) 2.* Solid state sciences, 2003. **5**(2): p. 359-365.

32. Dmitriev, V.G., G.G. Gurzadyan, and D.N. Nikogosyan, *Nonlinear optical properties of crystals*, in *Handbook of Nonlinear Optical Crystals*1991, Springer. p. 53-127.

33. Anayan, É.S., et al., *Some features of lithium iodate used for intracavity second harmonic generation.* Soviet Journal of Quantum Electronics, 1984. **14**(8): p. 1115.

34. Atroshchenko, L. and N. Khodeeva, *Mechanical strengthening of lithium iodate monocrystals under laser irradiation.* Izvestiya Akademii Nauk SSSR, Neorganicheskie Materialy, 1990. **26**(7): p. 1526-1528.

35. Kang, L., et al., *Metal thiophosphates with good mid-infrared nonlinear optical performances: A first-principles prediction and analysis.* Journal of the American Chemical Society, 2015. **137**(40): p. 13049-13059.

36. Chemla, D., et al., *Silver thiogallate, a new material with potential for infrared devices.* Optics communications, 1971. **3**(1): p. 29-31.

37. Kang, L., et al., *First principles selection and design of mid-IR nonlinear optical halide crystals.* Journal of Materials Chemistry C, 2013. **1**(44): p. 7363-7370.

38. Hu, C., et al., *Advantageous units in antimony sulfides: exploration and design of infrared nonlinear optical materials.* ACS applied materials & interfaces, 2018. **10**(31): p. 26413-26421.

39. Zhang, J., et al., *Dielectric, piezoelectric and nonlinear optical properties of polar iodate BiO (IO3) from first-principles studies.* Journal of Solid State Chemistry, 2020. **281**: p. 121057.

40. Shi, G., et al., *Finding the next deep-ultraviolet nonlinear optical material: NH4B4O6F*. Journal of the American Chemical Society, 2017. **139**(31): p. 10645-10648.

41. Lagoun, B., B. Bentria, and I.K. Lefkaier, *Ab initio calculation of structural, electronic and optical properties of Hg (IO3) 2.* Physica B: Condensed Matter, 2014. **433**: p. 117-121.

42. Kolinko, M., I. Kityk, and A. Krochuk, *Band energy parameters and density functions of orthorhombic TlI.* Journal of Physics and Chemistry of Solids, 1992. **53**(10): p. 1315-1320.

43. Davydyuk, G., et al., *Photoelectrical properties and the electronic structure of Tl 1− x In 1− x Sn x Se 2 (x= 0, 0.1, 0.2, 0.25) single crystalline alloys.* Physical Chemistry Chemical Physics, 2013. **15**(18): p. 6965-6972.

44. Atuchin, V., et al., *Electronic structure of layered titanate Nd2Ti2O7.* Surface science, 2008. **602**(19): p. 3095-3099.

45. Khyzhun, O., et al., *Electronic properties of ZnWO4 based on ab initio FP-LAPW band-structure calculations and X-ray spectroscopy data.* Materials Chemistry and Physics, 2013. **140**(2-3): p. 588-595.

46. Atuchin, V., et al., *Low Thermal Gradient Czochralski growth of large CdWO4 crystals and electronic properties of (010) cleaved surface.* Journal of Solid State Chemistry, 2016. **236**: p. 24-31.

47. Nouneh, K., et al., *Band energy and thermoelectricity of filled skutterudites LaFe4Sb12 and CeFe4Sb12.* Journal of alloys and compounds, 2007. **437**(1-2): p. 39-46.

CHAPTER I

Basic concepts in linear and nonlinear optics, promoter classes

I.1. Introduction

The optical properties of the material can be described as the interaction of the electromagnetic wave with the matter, where the charged particles inside the medium interact with this electric field and create polarization. Under normal conditions, the response of a material induced by the electric field of this electromagnetic wave is linear. With the development of the laser in the 1960's, the optical increased response of the medium started to vary from this linear behavior. these phenomena correspond to Nonlinear optics (NLO) where the polarization induced inside material is not linear concerning the electric field owing to this material being made up of asymmetric molecules whose atoms have very different electron densities. In the nonlinear regime, the polarization can be extended in a Taylor series in terms of the total field. The induced polarization of the material is written as;

$$\vec{\mathbf{P}} = \boldsymbol{\varepsilon_0}[\underbrace{\tilde{\boldsymbol{\chi}}^{(1)}\vec{\mathbf{E}}}_{\textbf{Linear}} + \underbrace{\tilde{\boldsymbol{\chi}}^{(2)}.\vec{\mathbf{E}}.\vec{\mathbf{E}} + \tilde{\boldsymbol{\chi}}^{(3)}.\vec{\mathbf{E}}.\vec{\mathbf{E}}.\vec{\mathbf{E}}\ldots.,}_{\textbf{non linear}}] \quad \textbf{(I.1)}$$

$$\vec{\mathbf{P}} = \vec{\mathbf{P}}^{\mathbf{L}} + \vec{\mathbf{P}}^{\mathbf{NL}} \quad \textbf{(I.2)}$$

I.2. Linear Optics

Optical properties come among the important properties of a material, from the dielectric function we can characterize how a material responds to the incident electromagnetic wave of light. The transition from occupied to unoccupied states including single-particle excitations and plasmons is caused by the electric field the linear response of a material to electromagnetic radiation is described by the dielectric function **ε(ω),** [1];

$$\boldsymbol{\varepsilon(\omega)} = \boldsymbol{\varepsilon_1(\omega)} + \mathbf{i}\boldsymbol{\varepsilon_2(\omega)} \quad \textbf{(I.3)}$$

the $\boldsymbol{\varepsilon_1(\omega)}$; real part and $\boldsymbol{\varepsilon_2(\omega)}$;imaginary part of the dielectric function, which is closely related to the electronic structure. The $\boldsymbol{\varepsilon_2(\omega)}$ of the dielectric function can be expressed,[2, 3] :

$$\boldsymbol{\varepsilon_2(\omega)} = \frac{2\pi e^2}{\Omega\varepsilon_0}\sum_{\mathbf{k},\mathbf{v},\mathbf{c}} \boldsymbol{\delta}(\mathbf{E_k^c} - \mathbf{E_K^v} - \hbar\boldsymbol{\omega}) \mid < \boldsymbol{\Psi}_\mathbf{K}^\mathbf{C} \mid \mathbf{u}.\mathbf{r} \mid \boldsymbol{\Psi}_\mathbf{k}^\mathbf{v} \mid^2 \quad \textbf{(I.4)}$$

Here $\boldsymbol{\varepsilon_0}$ is the dielectric constant at vacuum, $\boldsymbol{\Omega}$ is the volume of the simulation cell, $\hbar\boldsymbol{\omega}$ is the incident photon energy, $\mathbf{u}$ is the polarization vector of the incident electric field, $\mathbf{u}.\mathbf{r}$ is the momentum operator, $\boldsymbol{\Psi}_\mathbf{K}^\mathbf{C}$ and $\boldsymbol{\Psi}_\mathbf{k}^\mathbf{v}$ are the wave functions of the conduction **(c)** and valence **(v)** bands at the k-point respectively.

The real part $\boldsymbol{\varepsilon_1(\omega)}$of the dielectric function can be derived from the imaginary part by the Kramers-Kronig relations, [4];

$$\boldsymbol{\varepsilon_1(\omega) = 1 + \frac{2}{\pi} P \int_0^{\infty} \frac{\varepsilon_2(\omega)\omega}{\omega^2 - \omega^2 + i\eta} d\omega} \qquad \textbf{(I.5)}$$

The principal value in this case is P. The imaginary portion of the dielectric function is connected to optical absorption and optical transition processes, whereas the real portion of the dielectric function is related to electronic polarization.

The additional optical properties, including ;absorption index **I(ω)**, refractive index **n(ω)**, loss-function **L(ω)** and reflectivity **R(ω)** are originate from $\boldsymbol{\varepsilon_1(\omega)}$and $\boldsymbol{\varepsilon_2(\omega)}$

I.2.1. The refractive index n(ω)

The refractive index **(n)** equals the difference between the speed of light in vacuum **(c)** and the speed of that same light in the medium **(v)**; $\mathbf{n = \frac{c}{v}}$. The refractive index transforms into a complicated function of the light wave frequency $\boldsymbol{\tilde{n}(\omega) = n(\omega) + iK(\omega)}$. The extinction coefficient is the term used to describe the relationship between the real portion $\boldsymbol{n(\omega)}$and the imaginary part $\boldsymbol{K(\omega)}$ of the complex refractive index $\boldsymbol{\tilde{n}(\omega)}$. The real and imaginary components of the dielectric function are directly proportional to the refractive index $\boldsymbol{n(\omega)}$, [5].

$$\boldsymbol{n(\omega) = \left[\frac{\varepsilon_1(\omega)}{2} + \frac{\sqrt{\varepsilon_1(\omega)^2 + \varepsilon_2(\omega)^2}}{2}\right]^{1/2}} \qquad \textbf{(I.6)}$$

The relationship between static refractive index and dielectric function is seen in equation **I.7.** In accordance with equation **I.7**, Analysis of the behavior of the static refractive index is done using the behavior of the dielectric function..[6]:

$$\boldsymbol{n(\omega) = \sqrt{\varepsilon(\omega)}} \qquad \textbf{(I.7)}$$

When a beam of nonpolarized light passes into crystal, the light is decomposed into 2 beams that refract at different angles. This phenomenon is called birefringence $\boldsymbol{\Delta n(\omega)}$, The ray for which Snell's law holds is called the ordinary or O-ray, and the other is called the extraordinary or E-ray (**Figure.I.1.).**

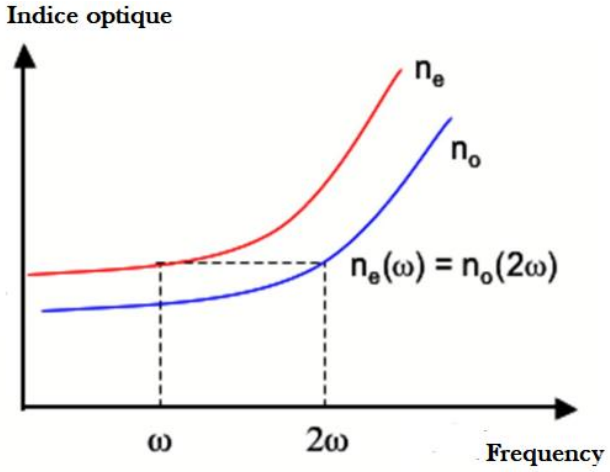

Figure. I. 1. Double refraction at the boundary of an anisotropic medium.

Birefringent materials reflect optically anisotropic (depending on the direction of light). This originates from their molecular and crystal structures. **Δn(ω)**, is a fundamental parameter for optical devices such as;phase-matching crystal, and wave plates, , …etc,.[7-14].

I.2.2. The absorption coefficient I(ω)

The absorption coefficient reflect the ability material to absorbs energy

$$\mathbf{I(\omega)} = \sqrt{\mathbf{2\omega}}\left(\sqrt{\boldsymbol{\varepsilon}_1^2(\omega) + \boldsymbol{\varepsilon}_2^2} - \boldsymbol{\varepsilon}_1(\omega)\right)^{1/2} \qquad \textbf{(I.8)}$$

An electron absorbs a photon (from the incident beam) in fundamental absorption **I(ω)**, moving from the valence to the conduction band. The energy of the photons must be more than or equal to the energy gap **(Eg)** of the material, [15].

I.2.3. Electron energy loss function L(ω)

Fast electrons cause core loss in the inner shell electrons or near-edge structure core level excitation. Plasmon excitations make up the majority of this in the case of interband transitions. The study of the phenomena connected to plasmon excitation has produced a broad field of research known as plasmonic. In materials having a modestly positive imaginary and negative real dielectric function, light induces the collective motion of electrons, which is known as a plasmon. Both the dimensions of the plasmonic material in relation to the excitatory radiation's wavelength and the characteristics of the excited electron density wave determine whether plasmons are propagating plasmons (or plasmon polaritons)

or confined surface plasmons. Peaks in the **L(ω)** curve correlate to properties of the plasma resonance [16], A plasma resonance can be produced even without a root in $\varepsilon_1(\omega)$, that is, if $\boldsymbol{\varepsilon_1(\omega) = 0}$. In contrast, not all roots $\boldsymbol{\varepsilon_1(\omega) = 0}$result in peaks in the electron energy-loss spectrum, [17].

the **L(ω)** function is calculated using the following relation, [18]:

$$\boldsymbol{L(\omega) = \frac{\varepsilon_2(\omega)}{\varepsilon_1(\omega^2)+\varepsilon_2(\omega^2)}} \qquad \textbf{(I.9)}$$

I.2.4. The reflectivity Rω

The reflectivity is the ratio of a wave's energy incident on a surface to its energy reflected from it.

$$\mathbf{R(\omega) = \left(\frac{\sqrt{\varepsilon(\omega)}-1}{\sqrt{\varepsilon(\omega)}+1}\right)^2} \qquad \textbf{(I.10)}$$

I.3 Nonlinear Optics

In 1961, Peter Franken et al. [19] discovered the second harmonic generation (SHG), which they used to detect the frequency doubling of a red laser passing through a nonlinear medium. This was the first nonlinear process they were able to achieve using a laser.

According to Equation **(I.1),** the second-order susceptibility $\boldsymbol{\chi^{(2)}}$ and third-order susceptibility $\boldsymbol{\chi^{(3)}}$, respectively, and a tensor are needed to generate an infinite Taylor series.

The second-order nonlinear optical susceptibility is linked to a variety of phenomena, including:

- ✓ **Second-harmonic generation (SHG);** involves the absorption of two identical photons and the production of polarization at a frequency twice as high.
- ✓ **Sum-frequency generation (SFG);** includes the destruction of two photons with different frequencies to create a single photon with the energy of the first two photons.
- ✓ **Difference frequency generation (DFG);** involves splitting an energetic photon into two photons with lesser energies.
- ✓ **The static Kerr effect** (was first noticed in 1875 by John Kerr and is also known as the quadratic electro-optic effect.[20].
- ✓ **The Pockels** Friedrich Carl Alwin Pockels discovered the effect in 1893[20], which will subsequently be referred to as the linear electro-optic effect in this thesis (LEO).

The refractive index of a material exposed to a static or low-frequency electric field changes in both of these processes.

We illustrate the physical phenomena regulated by the second-order nonlinear optical susceptibility component in Figure **I.2.**

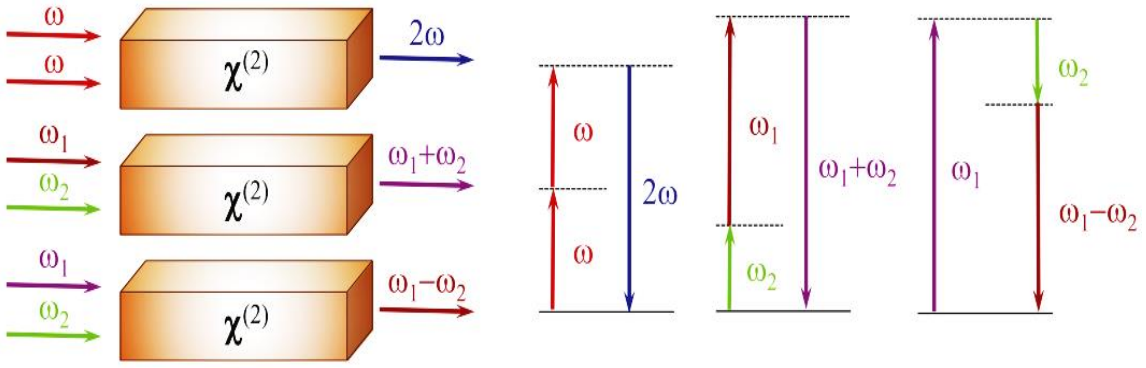

Figure. I. 2. Representation of second-order nonlinear optical processes. Schematic representation of the SHG, SFG, and DFG, arranged in ascending order of configuration. The SHG, SFG, and DFG are each represented by a graphic at a different energy level, [31].

One of the most popular nonlinear optical phenomena is second-harmonic generation (SHG). If there is an excited state with an energy that is twice as high as the entering photons, then there would be a real absorption of photons in this scenario. While many photons interact during a harmonic production, there is no actual absorption. This three-level concept is oversimplified when describing a genuine crystal because many-body effects manifest and more layers are involved. The material must fall into one of the 21 non-centrosymmetric (NCS) crystal classes to be used in SHG. Because NCS crystal classes lack an inversion center, the atoms' dipole moments might not cancel, giving rise to polar crystal classes. Because NCS crystal classes lack an inversion center, the atoms' dipole moments might not cancel, giving rise to polar crystal classes. Not all NCS crystal classes are polar, but all polar crystal classes are NCS. The even powered terms in the polarization power series fully disappear as a result of possessing inversion symmetry since the positive and negative polarizations with respect to time sum to zero.

$$\boldsymbol{P^{(2)}(t) = \chi^{(2)} E^{(2)}(t)} \qquad \textbf{(I.11)}$$

In a centrosymmetric medium, altering the sign of the applied electric field likewise requires altering the sign of the polarization.

$$-\boldsymbol{P}^{(2)}(\boldsymbol{t}) = \boldsymbol{\chi}^{(2)}[-\boldsymbol{E}(\boldsymbol{t})]^{2} \quad \textbf{(I.12)}$$

$$-\boldsymbol{P}^{(2)}(\boldsymbol{t}) = \boldsymbol{\chi}^{(2)}\boldsymbol{E}^{(2)}(\boldsymbol{t}) \quad \textbf{(I.13)}$$

$$\boldsymbol{\chi}^{(2)} = \mathbf{0} \quad \textbf{(I.14)}$$

Therefore, $\mathbf{P}^{(2)}(\mathbf{t}) = -\mathbf{P}^{(2)}(\mathbf{t})$, which can only be the case if $\boldsymbol{\chi}^{(2)}$is zero. Within materials with centrosymmetric crystal classes, NLO phenomena like SHG are not conceivable since the second-order linear susceptibility drops to zero.

The (NCS) crystals can only be utilized for the NLO, piezoelectric (PE), and electro-optic (EO) these features are all present at the same time in crystals .The proportion of acentric crystals, among all crystalline structures, makes up around 16%, but the proportion of crystals with desirable features is less than 2%, which limits the number of NCS crystals with a sufficient set of properties,[21, 22].

According to the Neumann principle, all crystal point symmetry components are included in the symmetry group of any physical characteristic [23-25]. Consequently, the relationship "structure-property" is the first crucial aspect of a triad (see figure **I.3**). The 32-point crystal symmetry defines the set of attributes, and there is a straightforward full one-to-one relationship between the crystallographic structure and a set of potential physical properties of crystals,[24, 26]. So, it is possible to create a full classification of the crystals on this basis, [24, 26].

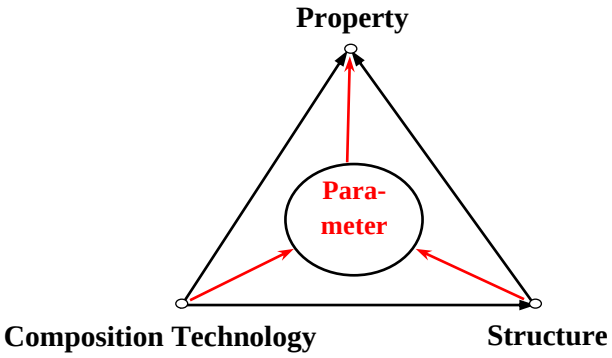

Figure. I. 3. Quaternion “composition-parameter-structure-property”, [37].

There are 21-point symmetry patterns among the acentric crystals, and only piezoelectric crystals are primarily exploited today in the development of optoelectronic devices, [27, 28]. According to **Table I.1**,these crystals feature 20-point symmetry patterns

[24-26, 29]. Additionally, they were separated into 6 affine groups (vertical column) based on a particular arrangement of their acentric features,[24, 26]. Four acentric qualities exist: enantiomorphism, piezoelectricity, polarity, and optical activity [24, 26, 30]. Ten polar (pyroelectric) and ten nonpolar (pure piezoelectric) shapes make up the collection of piezoelectric crystals.

Part of the polar crystals Enantiomorphism, polarity, and piezoelectricity in optical activity may include ferroelectrics. Electro-optical (EO) and nonlinear optical (NLO) characteristics are present in every piezoelectric crystal, [24, 25]. Piezoelectricity is the only acentric characteristic of crystals in the sixth affine group (NLO and EO). Piezoelectricity and polarity are two acentric features of the crystals in the first affine group. Three acentric characteristics piezoelectricity, polarity, and optical activity are present in the crystals of the second affine group. Piezoelectricity, optical activity, enantiomorphism, and polarity are all acentric qualities shared by the crystals in affine group three. Nonpolar crystals of the fourth affine group exhibit enantiomorphism, piezoelectricity, and optical activity as three acentric features. The fifth affine group of crystals exhibits the acentric properties of piezoelectricity and optical activity.

Piezoelectricity and optical activity are two acentric characteristics of the fifth affine group of crystals. As a result, each chosen affine group's crystal has a predetermined, straightforward set of acentric qualities. Moreover, the crystal system allows for the division of 20 piezoelectric crystals into three horizontal lines: higher (cubic), middle (hexagonal, tetragonal, and rhombohedral), and lower (orthorhombic, monoclinic, triclinic). Because of this, orthorhombic monoclinic and triclinic crystals have three light refraction indices, hexagonal tetragonal and rhombohedral crystals have two, and cubic crystals have one. The spaces groups of the NSC class are presented in **Table. I. 1.**

Table. I. 2. All piezoelectric crystals' relationships between their "structure-property".

	Para-elastic		**T**		**T_d**	**Cubic**
C_{6v}		**C_6**	**D_6**		**D_{3h}, C_{3h}**	**Hexagonal**
C_{4v}		**C_4**	**D_4**	**D_{2d}** **S_4**		**Tetragonal**
C_{3v}		**C_3**	**D_3**			**Rhombohedral**
Ferroelastic	**C_{2V}**		**D_2**			**Orthorhombic**
	Cs	**C_2**				**Monoclinic**
		C_1				**Triclinic**
I	**II**	**III**	**IV**	**V**	**VI**	
		Enantiomorphic				
	Optical active, OA					
Polar, ferroelectric Nonpolar, piezoelectric						
Nonlinear optical, Electro-optical, piezoelectric						

The symmetry requirements for second-order NLO behavior, or second-harmonic generation (SHG), are the same as those for piezoelectricity. [26].

Table. I. 3. the 32 groupings of crystallographic points. Point groups with only rotation axes are referred to as being enantiomorphic and are written in red, whereas polar point groups are **bolded**. Centrosymmetric point groups are written in blue. SHG is possible for all point groups that are not indicated in blue.

Crystal system	**32 Crystallographic Point Groups**						
Triclinic	**1**	**$\bar{1}$**					
Monoclinic	**2**	***m***	**2/m**				
orthorhombic	**222**	***mm2***	**mmm**				
Tetragonal	**4**	**$\bar{4}$**	**4/m**	**422**	***4mm***	**$\bar{4}$2m**	**4/mmm**
Trigonal	**3**	**$\bar{3}$**	**32**	***3m***	**$\bar{3}$m**		
Hexagonal	**6**	**$\bar{6}$**	**6/m**	**622**	***6mm***	**$\bar{6}$2m**	**6/mm**
Cubic	**23**	***m$\bar{3}$***	**432**	**$\bar{4}$3m**	**m$\bar{3}$*m***		

the lack of inversion symmetry is crucial for SHG the specific NCS point group .Therefore, it is no longer enough to describe $\boldsymbol{\chi^{(2)}}$as a scalar value. $\boldsymbol{\chi^{(2)}}$can now be written rather as a third-order tensor to encapsulate the symmetries of the crystal system along its three. crystallographic axes x, y, and z which are denoted as 1, 2, and 3 respectively as the subscripts for $\boldsymbol{\chi^{(2)}}$.

$$\begin{bmatrix} \mathbf{P_x^{\omega 1+\omega 2}} \\ \mathbf{P_y^{\omega 1+\omega 2}} \\ \mathbf{P_z^{\omega 1+\omega 2}} \end{bmatrix} = \boldsymbol{\varepsilon_0} \begin{bmatrix} \boldsymbol{\chi_{111}^{(2)}} & \boldsymbol{\chi_{122}^{(2)}} & \boldsymbol{\chi_{133}^{(2)}\chi_{123}^{(2)}} & \boldsymbol{\chi_{113}^{(2)}} & \boldsymbol{\chi_{112}^{(2)}} \\ \boldsymbol{\chi_{211}^{(2)}} & \boldsymbol{\chi_{222}^{(2)}} & \boldsymbol{\chi_{233}^{(2)}\chi_{223}^{(2)}} & \boldsymbol{\chi_{213}^{(2)}} & \boldsymbol{\chi_{212}^{(2)}} \\ \boldsymbol{\chi_{311}^{(2)}} & \boldsymbol{\chi_{322}^{(2)}} & \boldsymbol{\chi_{333}^{(2)}\chi_{323}^{(2)}} & \boldsymbol{\chi_{313}^{(2)}} & \boldsymbol{\chi_{312}^{(2)}} \end{bmatrix} \begin{bmatrix} \mathbf{E_x^{\omega 1}E_x^{\omega 2}} \\ \mathbf{E_y^{\omega 1}E_y^{\omega 2}} \\ \mathbf{E_z^{\omega 1}E_z^{\omega 2}} \\ \mathbf{E_y^{\omega 1}E_z^{\omega 2}+E_y^{\omega 2}E_z^{\omega 1}} \\ \mathbf{E_z^{\omega 1}E_x^{\omega 2}+E_z^{\omega 2}E_x^{\omega 1}} \\ \mathbf{E_x^{\omega 1}E_y^{\omega 2}+E_x^{\omega 2}E_y^{\omega 1}} \end{bmatrix} \quad \textbf{(I.15)}$$

P and **E** are now expressed in equation **I.15** in terms of their respective contributions to the applied optical field as well as their crystallographic orientations (x, y, and z). Indicate an optical frequency of $\boldsymbol{\omega_2}$ and a frequency of $\boldsymbol{\omega_1}$respectively.

The 18 tensor elements are represented with a shortened notation to simplify equation **I.15.** To indicate the location of the tensor element in the matrix, the last 2 digits are changed.

In In practical terms ,this means that the tensor elements crystallographic directions commute and are thus open to permutation. Several tensor elements are transformed into equivalent under Kleinman symmetry through these permutations of crystallographic directions. For example:

$$\boldsymbol{d_{12} \equiv d_{122} = d_{212} \equiv d_{26}} \quad \textbf{(I.16)}$$

It is changed to 1, 2, 3, 4, 5, and 6, accordingly, from 11, 22, 33, 23, 13, and 12. Second-order nonlinear optical susceptibility is denoted by a new variable, d, as per convention, where:

$$\mathbf{2d_{ijk} = \chi_{ijk}^{(2)}} \quad \textbf{(I.17)}$$

The resulting expression for second-order polarizability is given with the contracted notation when the **two** are factored out of the definition of **d**:

$$\begin{bmatrix} P_x^{\omega 1+\omega 2} \\ P_y^{\omega 1+\omega 2} \\ P_z^{\omega 1+\omega 2} \end{bmatrix} = 2\varepsilon_0 \begin{bmatrix} d_{11} & d_{12} & d_{13} & d_{14} & d_{15} & d_{16} \\ d_{21} & d_{22} & d_{23} & d_{24} & d_{25} & d_{26} \\ d_{31} & d_{32} & d_{33} & d_{34} & d_{35} & d_{36} \end{bmatrix} \begin{bmatrix} E_x^{\omega 1} E_x^{\omega 2} \\ E_y^{\omega 1} E_y^{\omega 2} \\ E_z^{\omega 1} E_z^{\omega 2} \\ E_y^{\omega 1} E_z^{\omega 2} + E_y^{\omega 2} E_z^{\omega 1} \\ E_z^{\omega 1} E_x^{\omega 2} + E_z^{\omega 2} E_x^{\omega 1} \\ E_x^{\omega 1} E_y^{\omega 2} + E_x^{\omega 2} E_y^{\omega 1} \end{bmatrix} \quad \textbf{(I.18)}$$

With the aid of Kleinman symmetry, which says that the components of nonlinear optical susceptibility tensors are frequency-independent, the formula for the second-order nonlinear optical susceptibility tensor in equation (**I.18**), may be made simpler.[31]. This presumption is accurate at low frequencies since the frequencies involved in SHG are substantially lower than the material's resonance frequency.

Due to these, the degeneracies under Kleinman symmetry result in the reduction of the d-unique tensor's elements from 18 to 10.

$$\begin{bmatrix} d_{11} & d_{12} & d_{14} & d_{14} & d_{31} & d_{21} \\ d_{21} & d_{22} & d_{32} & d_{32} & d_{14} & d_{12} \\ d_{31} & d_{32} & d_{23} & d_{23} & d_{13} & d_{14} \end{bmatrix} \quad \textbf{(I.19)}$$

Compounds with high d_{ij} values are the focus of research into NLO materials. High d_{ij} values indicate effective SHG, a high-quality crystal would be oriented along the crystallographic axis with the highest d_{ij} value.

I.3.1. Nonlinear Optics conditions

NLO effects are structurally restricted to compounds that have crystallized in NCS space groups; this restriction is a necessity rather than a sufficient requirement, thus not all NCS structures exhibit NLO effects.

Material must meet the following requirements in order to have practical applications: [32-34]:

1. For high power laser output, its transparency region 2 should cover the two atmospheric windows of 3–5 m and 8–12 m. A high laser damage threshold's dependence on a material's bandgap is inherent.
2. For high power laser output, a high laser damage threshold (LDT). LDT is intrinsically dependent on the bandgap of materials.[35].

3. Large second-order NLO coefficients. Higher conversion efficiencies are achievable in crystals with high NLO coefficients.
4. In frequency conversion procedures such optical parametric oscillation (OPO) and optical parametric amplification, the moderate birefringence n is required to achieve phase-matching (OPA).
5. For practical applications, good crystal growth habits and chemical stability are essential.

Exploring crystals with exceptional NLO features, particularly those with large NLO coefficients, high laser-induced damage thresholds (LIDTs), and phase match capability, is important in light of societal progress and the growing need for NLO crystals.[36].

Building units should be positioned to promote cooperative effects in their structures and have significant dipole moments for strong SHG intensity acentric constructions. The optical energy gap of a material can be controlled by doping or chemical substitution, and it has a significant impact on LDT readings. In order to increase nonlinear polarizability and high NLO coefficients, the research strategy for creating NLO materials is to build anionic groups with significant electron cloud deformations. On the other hand, by raising their ionicity to expand the optical energy gap, NLO materials with large LDT values might be produced. These two characteristics, frequently work against each other for the same anionic group since strong ionicity can hinder electron deformation and weak ionicity can result from significant electron cloud deformation. This contradiction must be resolved in order to create NLO materials with high LDT values and NLO coefficients.

It was suggested in 2001 to use the functional moiety theory to describe the physical behavior of structure-sensitive functional materials, [37]. The fundamental idea was that certain functional moieties might sense vibrations in the spatial arrangement of the atoms that made up those moieties. This sensitivity generated changes in different physical properties, such as the optical, electric, and magnetic ones. To better illustrate this principle, certain examples will be given. It is common knowledge that crystals without symmetric centers must exhibit SO NLO characteristics in their atomic configurations. Nevertheless, certain NCS-structured crystals are SHG-active whereas others are not. It could be helpful to study different functional moieties' influences on SO NLO characteristics to better understand this issue. On the other hand, this idea could be used to comprehend the connection between the crystal structures of NLO materials and their NLO characteristics. In order to study the

crystals' NLO properties and better comprehend the connection between the crystals' structures and NLO properties, theoretical calculations might also be used to determine electronic band structure, SO NLO coefficient, and birefringence. [38].

I.3.2. Strategies for designing NLO Compounds

Some feasible methods were suggested for obtaining high-performance NCS crystal structures, including

1) Transition metal d^0 cations, such as Ti^{4+}, Zr^{4+}, V^{5+}, Nb^{5+}, Cr^{6+}, and W^{6+}, with second-order Jahn-Teller (SOJT) distorted cations.
2) Cations such as Pb^{2+}, Sb^{3+}, I^{+5}, and Bi^{3+} exhibiting stereochemical activity of lone pair electrons (SCALP).
3) planar triangle made up of conjugated combinations of BO_3, CO_3, NO_3, and B_3O_6.
4) Polar displacement in d^{10} transition-metal cations such as Hg^{2+}, Zn^{2+}, and Cd^{2+}.
5) The $[MO_4]^{n-}$ tetrahedron is composed of acentric building blocks like $[PO_4]$, $[CrO_4]$, $[IO_4]$, $[Cr_2O_7]$, etc.[39].
6) Functional building units (FBUs) as MO_xF_{4-x} (x=1, 2, 3), [12, 40-49].
7) ns^2 main-group metal cations (Pb^{2+}, Sn^{2+}, Bi^{3+}, Se^{4+}, Te^{4+}, et al.) or (n-1) $d^{10}ns^0$ transition-metal cations (Ag^+, Cu^+, Zn^{2+}, Cd^{2+}, et al.) are significant prospects for polar crystals because the former polarizes the d^{10} cation center and the latter [46, 50, 51].

I.4 Promotors NLO Compounds

For all-solid-state lasers, which are widely used in scientific and industrial applications such as spectroscopy, free-space communication, generation of entangled photon pairs, and environmental monitoring, nonlinear optical (NLO) materials are essential tools for achieving frequency conversion [33, 38, 52, 53]. According to their working wavelength ranges, NLO crystals could be divided into four major categories, i.e., deep ultraviolet (DUV, $\lambda<0.2$ μm), ultraviolet (UV, $0.2\mu m<\lambda<0.4$ μm), visible/near-infrared (vis−NIR,0.4 μm$<\lambda<3\mu m$), and middle/far-infrared (MFIR, including $3<\lambda<5\mu m$ and $8<\lambda<13$ μm atmospheric transparent windows are the four main categories of NLO crystals based on their working wavelength ranges.

Numerous commercial NLO materials are already employed in the UV and vis-NIR ranges, such as KH_2PO_4 (KDP),[54] $LiNbO_3$ (LN),[55] $KTiOPO_4$ (KTP), [56] β-BaB_2O_4 (BBO),[57] LiB_3O_5 (LBO) , [58] CsB_3O_5 (CBO), [59] and $CsLiB_6O_{10}$ (CLBO), [60].

Table. I. 4. The NLO data of Borates, Niobates, Phosphates, chalcopyrite, Iodate.

Compounds	Space group	Band gap (eV)	Transparent region (μm)	SHG intensity	Δn	Refs
$KBe_2BO_3F_2$ (KBBF)	R32	6.19	0.155-3.6	d_{11} = 0.49	0.077	[61, 62]
LiNbO3 (LN)	R3c	3.1	0.33-5.5	d_{22}=2.10 d_{31}=-4.35 d_{33}=-27.2	0.080	[63]
BaB_2O_4 (BBO)	R3c	6.7	0.19–3.5	d_{22} = 1.6 d_{31}=0.07	0.113	[63]
LiB_3O_5 (LBO)	Pna21	8	0,16-2,6	d_{31}=-0.83 d_{33}=0.05 d_{32}=0.89	0.045	[63]
KH_2PO4 (KDP)	I$\bar{4}$2d	7,12	0,18-1,7	0.39	0,035	[64-66]
$KTiOPO_4$ (KTP)	Pna21	3.54	0,35-4,5	d_{31}=-1.4 d_{33}=10.7 d_{32}=2.56	0.090	[12, 67]
$AgGaSe_2$ (AGSe)	I$\bar{4}$2d	1.8	0.47 - 13.2	d_{36} = 33	0.032	[63, 68]
$AgGaS_2$ (AGS)	I$\bar{4}$2d	2.64	0.71 - 18.0	d_{36} = 13	0.053	[63, 68]
$ZnGeP_2$ (ZGP)	I$\bar{4}$2d	2.25	0.74-12	d_{36}=68.9	0.062	[68, 69]
α-$LiIO_3$	P63	3.93	0.3-6	d_{31}= 4.1	0.047	[70]

I.4.1. Borates (MB_xO_y)

numerous borate-based NLO materials have been continually developed, such as β-BaB_2O_4 (β-BBO),[71] LiB_3O_5, [58] $KBe_2BO_3F_2$(KBBF), [72]. Additionally, oxygen and boron atoms can coordinate three or four times, creating $(BO_3)^3$ planar triangles and $(BO_4)^5$ polyhedra. It is very helpful to the formation of huge macroscopic second-order susceptibility and birefringence that the $(BO_3)^3$ group has conjugated -orbital and highly anisotropic electron distribution[72]. The electronegativity of boron and oxygen atoms differ significantly, which is particularly advantageous for the transmission of short-wavelength light. In order to successfully widen the energy bandgap and shift the absorption edge toward the blue in borate crystals, dangling bonds on the oxygen anions in the B-O groups must be removed [73, 74]. Borate-based compounds come in a variety of structural forms due to the spatial combinations of the $(BO_3)^3$ and $(BO_4)^4$ groups.

Two significant NLO borates, β-BaB_2O_4 (BBO) [71, 75] and LiB_3O_5 (LBO) [58] In the visible and UV spectrums, demonstrate exceptional NLO performance. In spite of this, the comparatively small energy bandgap (Eg ~ 6.5 eV) in BBO as well as the low birefringence value. (Δn ~0.04) in LBO limited their applications in the DUV region. Another interesting NLO borate $KBe_2BO_3F_2$ (KBBF) [76-78] in Chen's team was found. This crystal has an enormous energy bandgap (Eg = 8.3 eV) and a moderately potent SHG effect. (~1.2 × KDP), [79]. This proves how advanced the crystals from the KBBF family that were used as the DUV NLO crystals were. However, because of the weak interaction between an alkali metal and fluorine cations, the KBBF family crystals' layering growth habit makes it extremely difficult to grow single crystals, which severely restricts their usefulness. Therefore, it is highly important to discover new borate-based crystals with good UV, especially DUV NLO capabilities .[80].

I.4.2. Niobates (MNbxOy)

$LiNbO_3$, which contains SOJT-active Nb^{5+} cations, has been regarded as one of the most commercial crystals for use in nonlinear optics because of its exceptional physical features, including significant NLO coefficients, mild birefringence, ability to match phases, and high crystal quality [81]. Despite the unique properties, $LiNbO_3$ very low damage threshold for photorefractive effects has limited the use of high power conditions and large device apertures The narrow optical transparency window (0.35–5 μm) of $LiNbO_3$ single

crystals also makes it impossible to manufacture NLO devices operating at wavelengths beyond 5 μm [82].

I.4.3. Phosphates

Potassium dihydrogen phosphate (KH_2PO_4, KDP) is a fantastic nonlinear optical (NLO) crystal with a high growth rate and optical homogeneity, which accounts for its widespread demand for applications in UV-tunable laser systems, frequency conversion, and optical data storage devices, laser-based imaging and remote sensing techniques, industrial photonics, and optoelectronics devices , [83]. The phosphate (PO_4) group is primarily responsible for the KDP crystal dominating second-order nonlinear optical (NLO) response, and the SHG efficiency coefficient (d_{36}) of the KDP crystal is estimated to be 0.39 pm/V, [66].

Potassium titanyl phosphate ($KTiOPO_4$, KTP) One of the most famous nonlinear optical crystals, [84]. Its nonlinear features are caused by its structure, which consists of chains of interconnected stiff PO_4 tetrahedra and TiO_6 octahedra with alternating long and short Ti–O links, [85]. High nonlinear coefficients, a broad range of angles and temperatures for phase matching, low absorption in the range of 0.35 μm to 4.5 μm, strong mechanical stability, and outstanding optical quality are KTP's advantages in the visible area. One of the few drawbacks of KTP is that it is vulnerable to photochromic degradation, also known as grey-tracking, which results in a gradual decline in light conversion efficiency, [86-88].

I.4.4. Chalcopyrite (ABX_2)

At now $AgGaS_2$ (AGS), $AgGaSe_2$ (AGSe), and $ZnGeP_2$ are the only mid-IR NLO crystals now available commercially (ZGP). They have high coefficients of second-harmonic generation (SHG), according to [102]. These materials can't be used to generate mid-IR lasers because of a few drawbacks, though. For instance, the AGS and AGSe laser damage threshold (LDT) values are too low [103] to support a high-power pumping source. Meanwhile, the strong absorption of two-photon in ZGP resulting from its small bandgap (2.25 eV) makes it difficult to use a Nd: YAG laser as the pumping source, [98]. Since mid-IR laser technology is now developing quickly, finding novel mid-IR NLO materials with good performance is urgently, [89].

I.4.5. Iodate

Due to their relation to structural variations and several significant uses in nonlinear optics, luminescence, photocatalysis, etc., iodates have drawn ongoing, intense research [90]. The iodates typically show strong second-order polarizability, significant optical anisotropy, and NCS crystallization due to the lone-pair electron cation **(I^{5+})** with stereochemical activity. Additionally, iodates are easily grown into large crystals under mild reaction conditions and have a broad range of visible wavelength regions (from UV/Vis to Mid-Infra). Metal iodates are also recognized to be prospective IR-NLO materials for their advantages of wide transparency which can be up to 12 μm, big SHG coefficients, high LDTs, and the gentle synthetic process, [38].

Metal iodates are also capable of taking on a range of unusual forms due to the presence of stereophonically active lone pair electrons that could function as a structure-directing agent. Asymmetric IO_3 or IO_4 groups additionally promote the growth of NCS structures with favorable NLO characteristics. Metal iodates have a far larger translucent range (up to 12 μm), reaching the middle infrared area, than the NLO crystals used in the UV regions, such as borates and phosphates. Additionally, the very highly asymmetric IO_3^- group exhibits an order of magnitude larger microscopic hyperpolarizability than that of PO_4^{-3} group. In the Vis , MIR, metal iodates are therefore potential second-order NLO materials.

Large NLO responsiveness, wide bandgap, high optical damage thresholds (LDT), and exceptional thermal stability are just a few of the outstanding characteristics of the commercial NLO crystal a-LiIO3 ,[91]. Although the IO_3 groups in a-$LiIO_3$ are perfectly parallelly aligned structurally and have the highest "addition" of the SHG effect, they have a number of drawbacks, including moisture sensitivity, poor stability, the existence of additional impurities, and ease of phase transition [107, 108]. Different NLO-active SBUs, however, may contribute to the anticipated variations in NLO performance from the perspective of function optimization (For exmple, a high LDT value results from a wide band gap, a wide transparency zone from the UV-Vis to the mid-infrared range, a big structure, thermal stability, etc..)[92], Due to their extensive transparency from the visible region to the beginning of the far-IR (12.5 m), metal iodates are excellent candidates for mid-IR NLO applications.[93] The additive polarization of the acentric structural units can be improved by using octahedrally-coordinated d^0-TM cations susceptible to SOJT distortions., [94] While replacing the more electronegative O_2^- with the more cationic F^- in TM cationic polyhedra can widen the band gap because of the more ionic M-F bonds.[95] Distorted M'On

(M' = Pb^{2+}, Te^{6+}, I^{5+}, W^{6+}, etc.) Because of their higher polarization and lower phonon frequencies, which increase the band gap and correspondingly the LDT, polyhedra made of heavy element cations in d0/d10 topologies are advantageous for light transmission. [96, 97]. The creation of an acentric structure may be aided by charge-balancing polarizable alkali/alkaline-earth cations with the proper ionic radii,[11]. These many functional SBUs may play specific roles for a range of NLO properties, and the combining and further alignment of these various NLO-active SBUs in one structure may result in a synergistic improvement in the qualities.

The structurally described fluoro-iodates of recent times include various F^-containing metal iodates, all of which have very basic structures with solitary [IO_2F2] anions (see figure **I.4**). Only isostructural compounds like K(IO_2F_2) (NCS, Pca21), [98] Rb(IO_2F_2) (NCS, Pca21), [99] Cs(IO_2F_2) (NCS), [100].

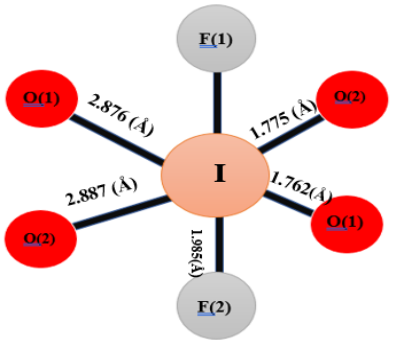

Figure. I. 4. Fluoro-iodates ion, $(IO_2F_2)^{2-}$

I.4.6. Chromate

Another alluring research candidate is the chromate ion. The chromate ions $(CrO_4)^{2-}$., $(Cr_2O_7)_2$, and so forth are examples of these ligands. The development of materials for quadratic nonlinear optics (NLO) is constrained by a number of stringent requirements, the first of which is that the crystal structure be acentric and have trigonal pyramidal and tetrahedral geometry (see figure **I.5**). As a result, materials with acentric crystal structures,

such as $RbLiCrO_4$, K Tb$(CrO_4)2$, and Ag Bi$(CrO_4)_2$, crystallize[100-102].

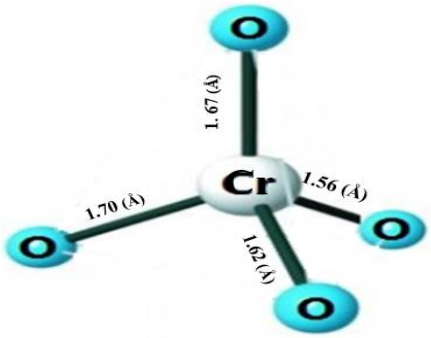

Figure. I. 5. Chromate ion, $(CrO_4)^{2-}$.

I.5. Conclusion

In nonlinear optics, one of the most widely used is Second-harmonic generation which involves the absorption of two photons of the same frequency and the creation of polarization at twice this frequency. This effect emerges only in asymmetric molecules whose atoms have very different electron densities. In this case, the true absorption of photons only occurs if there is an excited state at twice the energy of the incoming photons. accordingly, the nonlinear optics effects only occur in compounds crystallized in non-centrosymmetric space groups. But NSC is not a sufficient condition. For practical applications, a material must satisfy the following conditions; wide transparency region ,High LDT value, large nonlinear optical coefficients and moderate birefringence $\Delta n(\omega)$ .At now no one material has satisfied all these conditions simultaneously, the great challenge now is to find nonlinear optical material that has both strong nonlinear optical coefficients and large LIDT values. These two factors are usually contradictory for the same anionic group, as high electron cloud deformation could induce weak ionicity, and strong ionicity could make electron deformation difficult. Since the current situation requires parallelism between large distorted units and high ionicity in the same compound, the nonlinear optical materials based on metal flour-iodate and chrome metal are excellent candidates owing to the instinct of the asymmetric fluoro-iodate ion and chrome ion t a will investigated same of them in chapter III and IV.

Reference chapter I

1. Ambrosch-Draxl, C. and J.O. Sofo, Linear optical properties of solids within the full-potential linearized augmented planewave method. Computer physics communications, 2006. **175**(1): p. 1-14.

2. Zhang, X., et al., First-principles study of electronic and optical properties in wurtzite $Zn_{1-x}Cd_xO$. Journal of applied physics, 2008. **103**(6): p. 063721.

3. Gajdoš, M., et al., Linear optical properties in the projector-augmented wave methodology. Physical review B, 2006. **73**(4): p. 045112.

4. Kreibig, U., Kramers Kronig analysis of the optical properties of small silver particles. Zeitschrift fuer Physik, 1970. **234**(4): p. 307-318.

5. Saha, S., T. Sinha, and A. Mookerjee, Structural and optical properties of paraelectric $SrTiO_3$. Journal of Physics: Condensed Matter, 2000. **12**(14): p. 3325.

6. Kohn, W. and L.J. Sham, Self-consistent equations including exchange and correlation effects. Physical Review, 1965. **140**(4A): p. A1133.

7. Chen, X., et al., Designing an excellent deep-ultraviolet birefringent material for light polarization. Journal of the American Chemical Society, 2018. **140**(47): p. 16311-16319.

8. Zhang, M., et al., Rational design via synergistic combination leads to an outstanding deep-ultraviolet birefringent Li2Na2B2O5 material with an unvalued B2O5 functional gene. Journal of the American Chemical Society, 2019. **141**(7): p. 3258-3264.

9. Luo, M., et al., $M_2B_{10}O_{14}F_6$ (M= Ca, Sr): Two noncentrosymmetric alkaline earth fluorooxoborates as promising next-generation deep-ultraviolet nonlinear optical materials. Journal of the American Chemical Society, 2018. **140**(11): p. 3884-3887.

10. Guo, S.P., et al., Large Second Harmonic Generation (SHG) Effect and High Laser-Induced Damage Threshold (LIDT) Observed Coexisting in Gallium Selenide. Angewandte Chemie, 2019. **131**(24): p. 8171-8175.

11. Zou, G., et al., Rb3VO (O2) 2CO3: A Four-in-One Carbonatoperoxovanadate Exhibiting an Extremely Strong Second-Harmonic Generation Response. Angewandte Chemie International Edition, 2018. **57**(28): p. 8619-8622.

12. Atuchin, V., et al., Negative thermal expansion and electronic structure variation of chalcopyrite type $LiGaTe_2$. RSC advances, 2018. **8**(18): p. 9946-9955.

13. Atuchin, V., et al., Optical properties of LiGaS2: an ab initio study and spectroscopic ellipsometry measurement. Journal of Physics: Condensed Matter, 2009. **21**(45): p. 455502.

14. Dong, X., et al., CsSbF2SO4: an excellent ultraviolet nonlinear optical sulfate with a KTiOPO4 (KTP)-type structure. Angewandte Chemie, 2019. **131**(20): p. 6598-6604.

15. Omar, M.A., Elementary solid state physics: principles and applications1975: Pearson Education India.

16. Fox, M., Classical propagation. Optical properties of solids, 2001. **2**: p. 28-58.

17. Ravindran, P., et al., Optical properties of monoclinic SnI 2 from relativistic first-principles theory. Physical review B, 1997. **56**(11): p. 6851.

18. Wooten, F., Optical Properties of Solids (New York: Academic) p 60. 1972.

19. Franken, e.P., et al., Generation of optical harmonics. Physical review letters, 1961. **7**(4): p. 118.

20. Pestov, D., et al., Single-shot detection of bacterial endospores via coherent Raman spectroscopy. Proceedings of the National Academy of Sciences, 2008. **105**(2): p. 422-427.

21. Nowacki, W., T. Matsumoto, and A. Edenharter, Classification of crystalline substances by crystal systems, crystal classes, Bravais lattices and space groups. Acta crystallographica, 1967. **22**(6): p. 935-940.

22. Arkhipenko, D. and T. Moroz, Refinement of the space group of the mineral based on analysis of vibration spectra selection rules. Kristallografiya, 1996. **41**(6): p. 975-978.

23. Kidyarov, B., V. Atuchin, and N. Pervukhina, Crystal structure-property relationship as a factor in the refinement of structural physical data. Journal of structural chemistry, 2010. **51**(6): p. 1119-1125.

24. Kidyarov, B. and V. Atuchin, Universal crystal classification system "Point symmetry–Physical property". Ferroelectrics, 2007. **360**(1): p. 96-99.

25. Sirotin, I.U.r.I. and M.P. Shaskol′ska͡ia, Fundamentals of crystal physics1982: MIR publishers.

26. Halasyamani, P.S. and K.R. Poeppelmeier, Noncentrosymmetric oxides. Chemistry of materials, 1998. **10**(10): p. 2753-2769.

27. Rez, I. and Y.M. Poplavko, DIELECTRICS. Main properties and electronics applications. Edited in Russian, Moscow, 1989: p. 280.

28. Jones, D., S. Prasad, and J. Wallace, Piezoelectric materials and their applications. Key Engineering Materials, 1996. **122**: p. 71-144.

29. Strunz, H., Ferrokarpholith–Karpholith. Acta crystallographica, 1957. **10**(3): p. 238-238.

30. Urusov, V., Theoretical crystal chemistry. Moscow State University, Moscow, 1987.

31. Kleinman, D., Nonlinear dielectric polarization in optical media. Physical Review, 1962. **126**(6): p. 1977.

32. Kang, L., et al., Metal thiophosphates with good mid-infrared nonlinear optical performances: A first-principles prediction and analysis. Journal of the American Chemical Society, 2015. **137**(40): p. 13049-13059.

33. Tran, T.T., et al., Deep ultraviolet nonlinear optical materials. Chemistry of materials, 2016. **28**(15): p. 5238-5258.

34. Liang, F., et al., Analysis and prediction of mid-IR nonlinear optical metal sulfides with diamond-like structures. Coordination Chemistry Reviews, 2017. **333**: p. 57-70.

35. Lin, Z., et al., First-principles materials applications and design of nonlinear optical crystals. Journal of Physics D: Applied Physics, 2014. **47**(25): p. 253001.

36. Pan, Y., et al., Second-order nonlinear optical crystals with mixed anions. Coordination Chemistry Reviews, 2018. **374**: p. 464-496.

37. Guo, G., et al., Studies on the structure-sensitive functional materials. Progress in Chemistry, 2001. **13**(02): p. 151.

38. Guo, S.-P., Y. Chi, and G.-C. Guo, Recent achievements on middle and far-infrared second-order nonlinear optical materials. Coordination Chemistry Reviews, 2017. **335**: p. 44-57.

39. Norquist, A.J., et al., Polar Compounds Constructed with the [Cr2O7] 2-Anion. Inorganic Chemistry, 2001. **40**(9): p. 2015-2019.

40. Halasyamani, P.S., Asymmetric cation coordination in oxide materials: Influence of lone-pair cations on the intra-octahedral distortion in d0 transition metals. Chemistry of materials, 2004. **16**(19): p. 3586-3592.

41. Zhang, J., et al., Ferroelectric and nonlinear optical properties of the LiNbO3-type ZnGeO3 from first-principles study. Journal of alloys and compounds, 2012. **514**: p. 113-119.

42. Kim, J.-H. and P.S. Halasyamani, A rare multi-coordinate tellurite, NH4ATe4O9· 2H2O (ARb or Cs): The occurrence of TeO3, TeO4, and TeO5 Polyhedra in the same material. Journal of Solid State Chemistry, 2008. **181**(8): p. 2108-2112.

43. Hu, C., et al., Advantageous units in antimony sulfides: Exploration and design of infrared nonlinear optical materials. ACS applied materials & interfaces, 2018. **10**(31): p. 26413-26421.

44. Zhang, J., et al., Dielectric, piezoelectric and nonlinear optical properties of polar iodate BiO (IO3) from first-principles studies. Journal of Solid State Chemistry, 2020. **281**: p. 121057.

45. Shi, G., et al., Finding the next deep-ultraviolet nonlinear optical material: NH4B4O6F. Journal of the American Chemical Society, 2017. **139**(31): p. 10645-10648.

46. Inaguma, Y., M. Yoshida, and T. Katsumata, A polar oxide ZnSnO3 with a LiNbO3-type structure. Journal of the American Chemical Society, 2008. **130**(21): p. 6704-6705.

47. Yao, W., et al., Analysis of Deep-UV Nonlinear Optical Borates: Approaching the End. Advanced Optical Materials, 2014. **2**(5): p. 411-417.

48. Chang, H.-Y., et al., Alignment of lone pairs in a new polar material: synthesis, characterization, and functional properties of Li2Ti (IO3) 6. Journal of the American Chemical Society, 2009. **131**(7): p. 2426-2427.

49. Zhang, B., et al., Fluorooxoborates: beryllium-free deep-ultraviolet nonlinear optical materials without layered growth. Angewandte Chemie International Edition, 2017. **56**(14): p. 3916-3919.

50. Hu, C.-L. and J.-G. Mao, Recent advances on second-order NLO materials based on metal iodates. Coordination Chemistry Reviews, 2015. **288**: p. 1-17.

51. Cheng, W.-D., et al., Designing the syntheses and photophysical simulations of noncentrosymmetric compounds. Inorganic Chemistry Frontiers, 2015. **2**(2): p. 95-107.

52. Liu, X., et al., Nitrate nonlinear optical crystals: A survey on structure-performance relationships. Coordination Chemistry Reviews, 2019. **400**: p. 213045.

53. Wang, Y. and S. Pan, Recent development of metal borate halides: Crystal chemistry and application in second-order NLO materials. Coordination Chemistry Reviews, 2016. **323**: p. 15-35.

54. Smith, W.L., KDP and ADP transmission in the vacuum ultraviolet. Applied optics, 1977. **16**(7): p. 1798-1798.

55. Boyd, G., et al., LiNbO3: an efficient phase matchable nonlinear optical material. Applied Physics Letters, 1964. **5**(11): p. 234-236.

56. Stolzenberger, R.A., Nonlinear optical properties of flux growth KTiOPO 4. Applied optics, 1988. **27**(18): p. 3883-3886.

57. Chen, C., et al., New development of nonlinear optical crystals for the ultraviolet region with molecular engineering approach. Journal of applied physics, 1995. **77**(6): p. 2268-2272.

58. Chen, C., et al., New nonlinear-optical crystal: LiB 3 O 5. JOSA B, 1989. **6**(4): p. 616-621.

59. Wu, Y., et al., CsB3O5: A new nonlinear optical crystal. Applied Physics Letters, 1993. **62**(21): p. 2614-2615.

60. Sasaki, T., Y. Mori, and M. Yoshimura, Progress in the growth of a CsLiB6O10 crystal and its application to ultraviolet light generation. Optical Materials, 2003. **23**(1-2): p. 343-351.

61. Gui-Ling, W., et al., Determination of nonlinear optical coefficients of KBe2BO3F2 crystals. Chinese physics letters, 2003. **20**(2): p. 243.

62. Chen, C., Z. Lin, and Z.s. Wang, The development of new borate-based UV nonlinear optical crystals. Applied Physics B, 2005. **80**(1): p. 1-25.

63. Zhang, B., et al., First-principles high-throughput screening pipeline for nonlinear optical materials: Application to borates. Chemistry of materials, 2020. **32**(15): p. 6772-6779.

64. Lei, B.-H., et al., Second harmonic generation susceptibilities from symmetry adapted Wannier functions. Physical review letters, 2020. **125**(18): p. 187402.

65. Dmitriev, V.G., G.G. Gurzadyan, and D.N. Nikogosyan, Handbook of nonlinear optical crystals. Vol. 64. 2013: Springer.

66. Lin, Z., et al., Mechanism of linear and nonlinear optical effects of KDP and urea crystals. The Journal of chemical physics, 2003. **118**(5): p. 2349-2356.

67. Cheng, X., et al., The Large Second-Harmonic Generation of LiCs2PO4 is caused by the Metal-Cation-Centered Groups. Angewandte Chemie International Edition, 2018. **57**(15): p. 3933-3937.

68. Becker, P., Borate materials in nonlinear optics. Advanced Materials, 1998. **10**(13): p. 979-992.

69. Clerc, D. and H. Ledbetter, Mechanical hardness: A semiempirical theory based on screened electrostatics and elastic shear. Journal of Physics and Chemistry of Solids, 1998. **59**(6-7): p. 1071-1095.

70. Nikogosyan, D.N., Main Infrared Materials. Nonlinear Optical Crystals: A Complete Survey, 2005: p. 75-114.

71. Chen, C., et al., A New-Type Ultraviolet SHG Crystal——β-BaB 2 O 4. Science in China Series B-Chemistry, Biological, Agricultural, Medical & Earth Sciences, 1985. **28**(3): p. 235-243.

72. Soloveva, L. and V. Bakakin, CRYSTAL STRUCTURE OF POTASSIUM BORATOFLUOROBERYLLATE, KBE2 (BO3) F2. SOVIET PHYSICS CRYSTALLOGRAPHY, USSR, 1971. **15**(5): p. 802-&.

73. Jiang, X., et al., First-principles evaluation of the alkali and/or alkaline earth beryllium borates in deep ultraviolet nonlinear optical applications. Acs Photonics, 2015. **2**(8): p. 1183-1191.

74. Chen, C., et al., Nonlinear optical borate crystals: Principals and applications2012: John Wiley & Sons.

75. Eimerl, D., et al., Optical, mechanical, and thermal properties of barium borate. Journal of applied physics, 1987. **62**(5): p. 1968-1983.

76. Chen, C., et al., The vacuum ultraviolet phase-matching characteristics of nonlinear optical KBe2BO3F2 crystal. Applied Physics Letters, 1996. **68**(21): p. 2930-2932.

77. Mei, L., et al., Crystal structure of KBe2BO3F2. Zeitschrift für Kristallographie-Crystalline Materials, 1995. **210**(2): p. 93-95.

78. Chen, C., Recent advances in deep and vacuum-UV harmonic generation with KBBF crystal. Optical Materials, 2004. **26**(4): p. 425-429.

79. Kang, L., et al., Ab initio studies on the optical effects in the deep ultraviolet nonlinear optical crystals of the KBe2BO3F2 family. Journal of Physics: Condensed Matter, 2012. **24**(33): p. 335503.

80. Yang, Y., et al., Borate-based ultraviolet and deep-ultraviolet nonlinear optical crystals. Crystals, 2017. **7**(4): p. 95.

81. Lengyel, K., et al., Growth, defect structure, and THz application of stoichiometric lithium niobate. Applied Physics Reviews, 2015. **2**(4): p. 040601.

82. Weber, M., CRC handbook of optical materials. Vol. III, CRC Press, Boca Raton, FL, 2003.

83. Hussaini, S., et al., Growth and characterization of glycine doped KDP single crystal for optoelectronics applications. Optoelectron. Adv. Mater, 2007. **1**(12): p. 707-711.

84. Nikogosyan, D.N., Some Recent Applications. Nonlinear Optical Crystals: A Complete Survey, 2005: p. 399-412.

85. Sorokina, N. and V. Voronkova, Structure and properties of crystals in the potassium titanyl phosphate family: A review. Crystallography Reports, 2007. **52**(1): p. 80-93.

86. Rusov, V., et al., Using modulators based on KTP crystals in Nd: YAG lasers with high mean power. Journal of Optical Technology, 2009. **76**(6): p. 325-331.

87. Rusov, V., et al., Study of the electrical-conductivity kinetics of KTP crystals used in the modulators of solid-state lasers. Journal of Optical Technology, 2013. **80**(9): p. 532-536.

88. Rusov, V., et al., Electro-optical modulators based on KTP crystals for high-power lasers in the mid-IR region. Journal of Optical Technology, 2016. **83**(12): p. 716-721.

89. Lan, H., et al., Langasite family midinfrared nonlinear optical oxide materials: structure, property, and applications. International Journal of Optics, 2017. **2017**.

90. Petrov, V., Frequency down-conversion of solid-state laser sources to the mid-infrared spectral range using non-oxide nonlinear crystals. Progress in Quantum Electronics, 2015. **42**: p. 1-106.

91. Paufler, P., VG Dmitriev, GG Gurzadyan, DN Nikogosyan. Handbook of nonlinear optical crystals. Springer-Verlag Berlin 1991, 221 S., 32 Abb., Hardcover DM 98,–. ISBN 3-540-53547-0, 1994, Wiley Online Library.

92. Guo, S.P., Y. Chi, and H.G. Xue, SnI4·(S8) 2: A Novel Adduct-Type Infrared Second-Order Nonlinear Optical Crystal. Angewandte Chemie, 2018. **130**(36): p. 11714-11717.

93. Phanon, D. and I. Gautier-Luneau, Promising material for infrared nonlinear optics: NaI3O8 salt containing an octaoxotriiodate (V) anion formed from condensation of [IO3]− ions. Angewandte Chemie International Edition, 2007. **46**(44): p. 8488-8491.

94. Sun, C.-F., et al., Explorations of new second-order nonlinear optical materials in the potassium vanadyl iodate system. Journal of the American Chemical Society, 2011. **133**(14): p. 5561-5572.

95. Wu, C., et al., K5 (W3O9F4)(IO3): An efficient mid-infrared nonlinear optical compound with high laser damage threshold. Chemistry of materials, 2019. **31**(24): p. 10100-10108.

96. Lan, H., et al., Pushing nonlinear optical oxides into the mid-infrared spectral region beyond 10 μm: design, synthesis, and characterization of La3SnGa5O14. Journal of the American Chemical Society, 2018. **140**(13): p. 4684-4690.

97. Zhang, H., et al., Pb17O8Cl18: a promising IR nonlinear optical material with large laser damage threshold synthesized in an open system. Journal of the American Chemical Society, 2015. **137**(26): p. 8360-8363.

98. Helmholz, L. and M. Rogers, The crystal structure of potassium fluoroiodate, KIO2F2. Journal of the American Chemical Society, 1940. **62**(6): p. 1537-1542.

99. Wu, Q., et al., RbIO3 and RbIO2F2: Two promising nonlinear optical materials in mid-IR region and influence of partially replacing oxygen with fluorine for improving laser damage threshold. Chemistry of materials, 2016. **28**(5): p. 1413-1418.

100. Zhang, M., et al., Functional materials design via structural regulation originated from ions introduction: A study case in cesium iodate system. Chemistry of materials, 2018. **30**(3): p. 1136-1145.

101. Makarova, I., I. Verin, and K. Aleksandrov, Structure and twinning of RbLiCrO4 crystals. Acta Crystallographica Section B: Structural Science, 1993. **49**(1): p. 19-28.

102. Riou, A. and G. Roult, Etude par diffraction neutronique en temps de vol de la structure cristalline AgBi (CrO4) 2. Acta Crystallographica Section B: Structural Crystallography and Crystal Chemistry, 1979. **35**(11): p. 2494-2499.

CHAPTER II

Theoretical Framework, Concept, and Formalism

II.1. Introduction

In materials science, computational algorithms are asked for specific data that can be used to forecast a material's properties and its behavior under deformation or another physical (or chemical) processes. The necessary quantities are derived by ab initio methods from the estimated electronic structure.

II.2. Many-Body Problem

A solid is made up of a mixture of heavier, positively charged particles (nuclei) and lighter, negatively charged particles (electrons). We have an issue with N+ZN electromagnetically interacting particles if there are N nuclei. Due to the lightness of the particles, quantum mechanics is required to solve this many-body problem, which is a quantum many-body problem. Only the fundamental laws of quantum physics are used to describe how electrons interact. The time-independent Schrodinger equation can be solved to get the total amount of energy;

$$\hat{H}\left|\Psi_0\right> = E_0\left|\Psi_0\right> \qquad \textbf{(II.1)}$$

Unfortunately, for systems of interest in condensed matter physics or materials science, the Schrödinger equation, which is the primary instrument in quantum mechanics, cannot be precisely solved. To solve for models that are precise enough to provide a realistic description of the systems and processes under study, a sequence of approximations must be made.

The system's precise many-particle Hamiltonian is as follows:

$$\widehat{\boldsymbol{H}} = -\frac{\hbar^2}{2}\sum_i \frac{\nabla^2_{\vec{R}_i}}{M_i} - \frac{\hbar^2}{2}\sum_i \frac{\nabla^2_{\vec{r}_i}}{m_e} - \frac{1}{4\pi\varepsilon_0}\sum_{i,j}\frac{e^2 Z_i}{\left|\vec{R}_i - \vec{r}_j\right|} + \frac{1}{8\pi\varepsilon_0}\sum_{i\neq j}\frac{e^2}{\left|\vec{r}_i - \vec{r}_j\right|} + \frac{1}{8\pi\varepsilon_0}\sum_{i\neq j}\frac{e^2 Z_i Z_j}{\left|\vec{R}_i - \vec{R}_j\right|} \qquad \textbf{(II.2)}$$

The electrons are at $\vec{R}_i$ and have a mass of M_i. The kinetic energy operator T_N, for the nuclei is the first term, while T_e for the electrons is the second. The final three terms describe the Coulomb interaction between the nuclei U_{NN},electrons U_{ee}, and other nuclei U_{Ne},, respectively.[1, 2].

In 1928, BORN-OPPENHIEMER APPROXIMATION, based on the decoupling of the nuclear and electronic dynamics (The mass of the nucleus MI is considerably larger than the mass of an electron me, meaning that the motion of the electrons is much faster and can therefore be decoupled from the motion of the nuclei). This approximation leaves us with a group of negatively interacting NZ particles that are travelling in the nuclei's potential. The consequent division of the states into electronic and nuclear degrees of freedom is a very helpful simplification of the issue that enables one to treat the nuclei according to classical

principles. The electronic component of the system is still a quantum many-body problem; due to the interaction between the electrons, the system's electronic wave-function is dependent on their collective coordinates and cannot be dissociated into contributions from a single electron. Then, one can write the electronic Hamiltonian as;

$$\hat{H} = T_e + U_{ee} + U_{Ne} \quad \textbf{(II.3)}$$

In 1927, HARTREE, an approach for estimating the wave functions and energy of atoms and ions that is based on the idea that electrons are independent The Hartree function, which transforms the Z electron system into a collection of independent electrons by ignoring the interactions between electrons and spin states, is used to describe this phenomenon. [4]. A few years later, his students Fock and Slater each proposed a self-consistent function (SCF) with consideration of Pauli principles and a multi-electron wave function in the form of a determinant of one-particle orbitals (Slater-determinant) to overcome the complete loss of consideration of the anti-symmetry of the electron system [5].

$$\psi^{HF}(x_1, \dots x_N) = \frac{1}{\sqrt{N!}} \begin{vmatrix} \varphi_1(x_1) & \varphi_1(x_2) \dots \dots \dots & \varphi_1(x_N) \\ \varphi_2(x_1) & \varphi_2(x_3) \dots \dots \dots & \varphi_2(x_N) \\ \varphi_3(x_1) & \varphi_3(x_2) \dots \dots \dots & \varphi_3(x_N) \\ & . & \\ & . & \\ & . & \\ \varphi_N(x_1) & \varphi_N(x_2) \dots \dots \dots & \varphi_N(x_N) \end{vmatrix} \quad \textbf{(II.4)}$$

$1/\sqrt{N!}$ is the normalization constant.

The Hartree-Fock model's calculations are extremely difficult because there is no self-interaction, the effect of exchange V_x is introduced, and the correlation effect is not taken into consideration. The Hartree-Fock (HF) model, however, takes into account that the outcome is simply a rough estimate of the actual outcome , [6-8].

.

II.3. Density Functional Theory (DFT)

For the analysis of medium- and large-scale systems, DFT has emerged as the preferred technique. While formally precise, DFT is computationally very efficient thanks to the introduction of the electronic density as a fundamental variable in place of the many-body wave functions..

II.3.1. Hohenberg-Kohn theorems

The fundamental statement of DFT is that the problem of determining the ground-state energy of a many-particle system, which is characterized by a many-particle wave-function

Ψ_0, can be mapped on a physically equivalent problem of determining the ground-state electron densityρ_0 .It is crucial to take into account all the significant contributions to the kinetic and potential energies, while balancing with the calculation's efficiency. where $\hat{H}$ is the Hamiltonian of Born-Oppenheimer;

$$\hat{H} = \hat{T} + \hat{U} + \hat{V}_{ext} \quad \textbf{(II.5)}$$

The Hamiltonian is completely governed by the potential v_{ext} because $\hat{T}$ and$\hat{U}$ are the same for all physical systems.

$$\hat{v}_{ext} = \int drv_{ext}(r)\hat{\rho}(r) \quad \textbf{(II.6)}$$

which is an external potential for a single particle. This implies that every characteristic of the system, such as the density $\rho_0(r)$: and ground-state wave functions Ψ_0, is also governed by the external potential: The first Hohenberg-Kohn theorem states that the inverse is also true.

II.3.1.1 Theorem (Hohenberg and Kohn I, [9].)

With the exception of a constant, the ground-state density $\rho_0(r)$ of a system of interacting particles in an external potential$\hat{V}_{ext}(r)$defines this potential completely.

$$E_{v0}[\rho] = < \Psi_0[\rho] \left| \hat{T}[\rho] + \hat{U}[\rho] + \hat{V}_0[\rho] \right| \Psi_0[\rho] > \quad \textbf{(II.7)}$$

II.3.1.2 Theorem (Hohenberg and Kohn II, [9].)

For every external potential V_{ext}, a functional for the total energy E[ρ] of the electronic density ρ(r) may always be defined. The actual ground-state density $\rho_0(r)$ for a given $v_0(r)$: $E_{v0}[\rho] \geq E_{v0}[\rho_0]$, which minimizes this functional.

Their *first theorem* states that the external potential $v_{ext}(r)$ operating on the electron system is implicitly determined (to within a trivial constant) by the ground-state single-particle density ρ(r) .The Hamiltonian $\hat{H}$ is then finished by the external potential. All of the system's ground-state characteristics are implicitly determined once the Hamiltonian is understood. Given that the single-particle density depends only on three variables, this is a significant reduction of the many-electron problem. Therefore, the single-particle density may be thought of as having only one function, which includes all of the system's ground-state properties in general and the entire ground-state energy in particular. The ground-state electron density minimizes the total energy of the Z electron system, E[ρ], in accordance with the *second theorem*, which is expressed as a variational principle. As a result,

compared to the challenge of solving the 3N-dimensional Schrödinger equation, determining the ground-state electron density and total energy is incredibly straightforward. To determine the minimum of E[ρ], we simply vary the density ρ(r), a function with only three variables.

The Hohenberg and Kohn theorems only state that there are one-to-one mapping links between system attributes and electron density functional, but they don't specify what these relationships are. Only one year after the publication of Hohenberg and Kohn's significant study, Kohn and Sham published a paper[10], that transformed DFT into a useful tool and reduced the multi-electron problem to a problem of non-interaction electrons in an effective potential.

II.4 Kohn-Sham equations

Instead, Kohn and Sham (KS) proposed an additional system of free particles whose electrical density and other characteristics would be identical to those of the actual system.

II.4.1. Definition (Kohn and Sham)

Any systems of interacting particles in the external potential $\widehat{V_0}$ can be transferred to a system of hypothetical, non-interacting Kohn-Sham particles in the effective local potential $\widehat{V}_S$ S such that both have the same ground-state density ρ_0:

$$\widehat{H} = \widehat{T} + \widehat{U} + \widehat{V_0} \overset{\rho_0}{\leftrightarrow} \widehat{H_S} = \widehat{T_S} + \widehat{V_S} \quad \textbf{(II.8)}$$

According to[11, 12] the total energy of a system of electrons travelling in an external potential $v_{ext}(r)$;

$$E[\rho] = T_s[\rho] + \int \rho(r) v_{ext}(r) dr + J[\rho] + E_{xc}[\rho] \quad \textbf{(II.9)}$$

with exact equations for the Coulomb energy J[ρ];and non-interacting kinetic energy $T_s[\rho]$;

$$T_s[\rho] = \sum_i < \Psi_i \left| -\frac{1}{2}\nabla^2 \right| \Psi_i > \quad \text{(II.10)}$$

$$J[\rho] = \frac{1}{2}\iint \frac{\rho(r)\rho(r')}{|r-r'|} dr dr' \quad \textbf{(II.11)}$$

The exchange-correlation functional, which may be divided into its exchange and correlation parts ($E_{xc}[\rho] = E_x[\rho] + E_c[\rho]$) contains all the complexity that is currently present in many-body physics.

The Kohn-Sham equation's solutions are the orbitals that were used to generate the density, $\rho(r) = \sum \left| \Psi_i (r) \right|^2$.

$$\left(-\frac{1}{2}\nabla^2 + v_{ext}(r) + v_J(r) + v_{xc}(r)\right)\Psi_i(r) = \varepsilon_i\Psi_i(r) \quad \textbf{(II.12)}$$

where the Coulomb potential is $V_J(r) = \int \frac{\rho(r')}{|r-r'|}dr'$,and the exchange–correlation potential is given by the functional derivative of the exchange–correlation energy, $V_{xc}(r) = \frac{\delta E_{xc}[\rho]}{\delta\rho(r)}$, this is exact Kohn–Sham DFT, with the exact functional, the solution of the Kohn–Sham (equation **II.12**) to minimize the total energy (equation **II.9**) yields the exact energy and density of the Schrodinger equation.

For systems that are too complex or massive to be handled by trustworthy wave function approaches, Kohn-Sham density functional theory has been regarded as being particularly successful due to its high accuracy and low cost, [13]. For many electronic structure calculations in quantum chemistry, software packages based on density functional theory (DFT)[9] and the Kohn-Sham equation [10] for numerous quantum chemistry calculations of electronic structure [14] because it favors it above other alternative approaches by balancing the demands of accuracy and calculation speed. Although DFT is a theoretically sound theory, in order to characterize the exchange-correlation effects in practice as precisely as feasible, it is necessary to approximate the exchange-correlation (XC) energy, E_{xc}, as a function of density.

Density functional approximations must be used because the precise form of $E_{xc}[\rho]$ is uncertain (DFA). DFAs provide an approximate density, E_{XC}^{DFA} and eigenvalues with the help of their approximate energy expression, E_{XC}^{DFA}, and approximate Kohn-Sham potential, $\{\varepsilon_i^{DFA}\}$.

II.5. Density Functional Approximations

For any practical Kohn-Sham calculation, the exchange-correlation energy Exc is the quantity for which an approximative functional must be chosen. The local density approximation (LDA), which solely considers the density at a specific position to calculate the energy density at that point, was the first approximation to the XC energy. Since LDA is determined using the uniform gas's known energy density, this is true for a uniform gas exactly. The LDA approximation[15, 16] which serves as the foundation for the creation of the majority of other kinds of approximations, takes the following form:

$$E_{xc}[\rho] = \int \varepsilon_{xc}[\rho(r)]dr^3 \quad \textbf{(II.13)}$$

The natural successor to LDA is a semi-local (or gradient-corrected) approximation that adds information about the derivative of the density at that point, the gradient of the electron

density is used to better describe atoms and molecules. Where $\boldsymbol{\varepsilon_{xc}}$the exchange-correlation energy per unit volume, which is a function of the electron density [$\varepsilon_{xc} = -\frac{3}{4}(\frac{3}{\pi})^{\frac{1}{3}}\rho^{\frac{4}{3}}$], When using GGA, the exchange-correlation energy is

$$E_{xc}[\rho] = \int \varepsilon_{xc}^{GGA}\ [\rho(r), \nabla\rho(r)]d^3r \qquad \textbf{(II.14)}$$

For ease of use, we only provide the exchange portion E_x of the functionals we tested, which is the majority of the exchange-correlation energy. We then formulate the GGA exchange-energy functional as follows:

$$E_X^{GGA}[\rho] = -C_X \int \rho^{4/3}(r)F(s(r))d^3r \qquad \textbf{(II.15)}$$

where $C_X = (3/4)(3/\pi)^{1/3}$and F(s) is the enhancement factor with $s = |\nabla\rho|/(2\rho K_F)$ and $K_F = (3\pi^2\rho)^{1/3}$.In this notation the LDA approximation corresponds to $F^{LDA}(s) = 1$.

There are a number of approxapproximationsimation for E xc is flexible to employ, such as Perdew- Burke- Ernzerhof (PBE 96), [17], Wu-Cohen 2006 (WC),[18] of GGA form, where the enhancement factor in the PBE and WC are as follows;

$$F^{PBE}(S) = 1 + k - \frac{k}{1+\frac{\mu}{k}S^2} \qquad \textbf{(II.16)}$$

$$F^{WC}(S) = 1 + k - \frac{k}{1+\frac{x(S)}{k}} \qquad \textbf{(II.17)}$$

Where k=0.804 [19] , μ=0.21951, and $x(s) = \frac{10}{81}S^2 + \left(\mu - \frac{10}{81}\right)S^2e^{-S^2} + Ln(1 + CS^4)(c = 0.0079325)$.

In terms of solids, Wu and Cohen [18] have demonstrated that their WC functional outperforms LDA and PBE96 in terms of solid geometrical characteristics and bulk modulus. For solids having 3D transition elements, PBE is thought to be the most effective strategy [19]. However, for some classes of solids, such as the 5d transition metals, LDA is still among the best methods[19]. In Refs , [19, 20]. For excited-state qualities, this is frequently not the case.

The prediction of excited-state features is one of DFT's biggest weaknesses, though. For instance, the KS band gap of semiconductors and insulators is frequently grossly overestimated, and occasionally even a metallic state is obtained instead of an insulating state. The energy difference between the conduction band minimum (CBM) and the valence band maximum (VBM), as determined by a multiplicative (i.e., common for all orbitals) potential, is what we refer to as the KS band gap ,[21]. The experimental band gap, which is determined by subtracting the ionization potential from the electron affinity I-A, should not be compared to the KS band gap in theory.

In fact, the derivative discontinuity**Δxc**,[22, 23] which can be as large as the KS band gap itself, is one way that the precise KS band gap differs from the experimental one (see, e.g., Ref. [24]). According to some evidence, the KS band gap computed using LDA and GGA may not differ significantly from the actual KS gap,[24] but these approximations have a self-interaction inaccuracy, which is a problem, [25] and do not display a derivative discontinuity (Δxc = 0), which is crucial when comparing the KS band gap with the experimental band gap, [22, 23]. This is because the exact exchange functional is subjected to the optimum effective potential (OEP) approach, which results in KS band gaps that are reasonably near to the experimental values, [26, 27] To obtain KS band gaps in good agreement with experiment. However, this method requires a lot of computer power and is probably in some ways "empirical" due to the missing xc. There are several approaches to getting an estimate of the experimental band gap; one of them involves utilizing a nonmultiplicative potential and a procedure that is outside the KS framework. Despite the fact that the local-density approximation (LDA), [15] or the generalized gradient approximation (GGA) [17] are generally wise options, but they fall short when considering strongly linked electron systems like those seen in transition-metal combinations.

Recently, Tran and Blaha [28] developed a new semilocal potential that combines the modified Becke-Johnson potential[29] and LDA, giving it the same precision as the more costly hybrid functionals and GW techniques while being computationally as affordable as LDA or GGA. By doing so, it can determine precise band gaps. The TB-mBJ potential is expressed as follows [30] ;

$$\upsilon_{x,\sigma}^{TB-mBJ}(r) = c\upsilon_{x,\sigma}^{BR}(r) + (3c-2)\frac{1}{\pi}\sqrt{\frac{5}{6}}\sqrt{\frac{t_\sigma(r)}{\rho_\sigma(r)}} \qquad \textbf{(II.18)}$$

Where $\rho_\sigma(r) = \sum_{i=1}^{N_\sigma} |\Psi_{i,\sigma}|^2$ denotes the electron density and $t_\sigma = \frac{1}{2}\sum_{i=1}^{N_\sigma} \nabla\Psi_{i,\sigma}^*(r)\nabla\Psi_{i,\sigma}$ is the kinetic-energy density.

$$\upsilon_{x,\sigma}^{BR}(r) = -\frac{1}{b_\sigma(r)}(1 - e^{-x_\sigma(r)} - \frac{1}{2}x_\sigma(r)e^{-x_\sigma(r)}) \qquad \textbf{(II.19)}$$

Using a nonlinear with and while, the becke roussel potential[31] , which was established to simulate the coulomb potential induced by the exchange hole, is calculated. $\boldsymbol{x_\sigma}$ is calculated using a nonlinear with ρ_σ , $\nabla\rho_\sigma$, $\nabla^2\rho_\sigma$, and t_σ , while $b_\sigma$is determined using $b_\sigma = \left[\frac{x_\sigma^3 e^{-x_\sigma}}{8\pi\,\rho_\sigma}\right]^{1/3}$.

The value of parameter **c** in equation **II.18** is calculated using

$$c = \alpha + \beta\left(\frac{1}{v_{cell}}\int_{cell}\frac{|\nabla\rho(r')|}{\rho(r')}d^3r'\right)^{1/2} \qquad \textbf{(II.20)}$$

where V_{cell} is the unit cell volume and $\alpha = -0.012$ and $\beta = 1.023\ \text{bohr}^{1/2}$ are parameters determined according to a fit to experimental values [30].

The XC potential for equation (II.12) is obtained as the functional derivative of the XC-energy functional E_{xc} with respect to the electron density $\rho_\sigma(v_{xc,\sigma} = \delta E_{xc}/\delta\rho_\sigma)$. This is a quick and trustworthy explanation for ground-state features that can aid in the interpretation of experimental data and also has a amount of predictive power. Tran and Blaha[30] have shown that, for the majority of cases, the TB-mBJ potential yields band gaps that are in good agreement with experiment, leading to typical errors of lower than 10%. They have used the TB-mBJ potential for several solids, including strongly correlated 3d transition metal oxides, wide band gap insulators, and small band gap semiconductors. The BJ exchange potential has been implemented [32] self consistently into the WIEN2K code[33] this uses the local orbitals approach and the FP-LAPW wave to solve the KS equations for periodic systems. It would be interesting to know which aspect of the modified Becke-Johnson potential, as compared to other exchange-correlation functionals, is responsible for the calculations' best agreement with the experimental spectra. The Becke-Johnson potential includes a term with the kinetic-energy density [second term in equation] in addition to a term that models the Coulomb potential of the exchange hole equation **II.19** The TB-mBJ exchange potential has the advantage that, as a multiplicative potential, it has the ability to predict band gaps of semiconductors and insulators with greater accuracy than any other multiplicative potential and to do so at a computational cost comparable to a standard GGA calculation, [32]. Additionally, a parameter that modifies the weighting between these two elements is included in the modified Becke-Johnson potential (equation **II.19**) [30]. During the calculation, its value is derived from each material's electron density.

Using the equation, the band gap typically increases monotonically with respect to equation. **II.20** produces satisfactory results for a wide range of systems, including transition metal oxides, wide gap insulators, and tiny band gap semiconductors.[34], Setting c = 1 restores the original Becke-Johnson potential. It is noteworthy that a functional derivative of an exchange functional cannot be used to produce the TB-mBJ potential. (there is no E_x such that $v_{x,\sigma}^{TB-mBJ} = \delta E_x/\delta\rho_\sigma$, [30, 35]. Consequently, this potential should not be used for force calculations, energy comparisons, or geometry optimization, [32].

II.6. Numerical details

For Kohn-Sham equations to be solved, the basis function set must be chosen carefully. On pseudo-potentials and a plane-wave basis set with explicitly periodic boundary conditions, the majority of density functional theory computations on materials are conducted.

Equation **II.9** solution depends on the basis set used to expand the KS orbitals, which are defined by $\boldsymbol{u_{n,K}}$.in equation **II.22** .

II.6.1. Bloch's theorem

It is crucial to take into account the periodicity of the system in order to eliminate a sizable number of electrons (proportional to the Avogadro number) in electronic structure calculations for solids. This suggests that the substance being studied is crystalline. In such scenario, periodic boundary conditions are accounted for by utilizing the crystal's translational symmetry, and only the atoms contained within the crystallographic unit cell are explicitly taken into account. Such a strategy is founded on Bloch theorem, which stipulates that for potential with the lattice periodicity;

$$v_s(r) = v_s(r + R) \quad \textbf{(II.21)}$$

where R is a lattice vector

The eigenstates of the single-particle Hamiltonian can be defined by;

$$\Psi_{n,K} = e^{iK.r}u_{n,K}(r) \quad \textbf{(II.22)}$$

where $u_{n,K}$is a periodic function in the unit cell, i.e., $u_{n,K}(r) = u_{n,K}(r + R)$. Bloch states of equation **II.21** are defined by two indices n and k which represent the band index and the crystal momentum, respectively.

Without any loss of information, the dependency of the Bloch states with respect to k can be restricted to the first Brillouin zone (FBZ) of the reciprocal space. The Bloch theorem allows us to integrate the expression of the energy over the (FBZ), that is, from the starting problem of solving the KS equations for an infinite number of electrons, n in equation **II.9**, to the calculation for a finite number of bands at an unlimited number of k-points.

$$E_{KS}[\rho] = \frac{1}{V_{FBZ}} \int_{FBZ} dK E_K[\rho_K] \quad \textbf{(II.23)}$$

II.6.2. Plane waves and pseudo-potentials

Plane-waves (PWs) have a number of benefits, including the following:**(i)** their mathematical formulation is quite straightforward, **(ii)** Since there is no overlap between them, they are mutually orthogonal. **(iii)** The absence of Pulay factors in the calculation of energy derivatives is a particularly significant benefit of PWs that are unaffected by atomic

locations. As a result, when a PW basis set is utilized, the HF equations for forces and force constants are valid without any modifications. **(iv)** The kinetic-energy cutoff and the fast Fourier transform (FFT) technique make it possible to swiftly go from reciprocal to real space, making it very easy to check for convergence by simply expanding the size of the basis set.The KS orbitals are expressed as, using the plane-wave basis set.

$$\Psi_{n,K}(r) = \sum_G C_{n,k}(G) e^{i(K+G)r} \quad \textbf{(II.24)}$$

where the set of coefficients $\{C_{n,K}\}$ is obtained by diagonalizing the equation **II.9** matrix form for each k-point, and the sum is carried out over all feasible reciprocal lattice vectors G. The total over G is constrained to a set of reciprocal lattice vectors contained in a sphere of radius $|k + G|$, which is typically defined by the kinetic energy cutoff, in order to restrict the expansion in equation II.24.

$$\frac{\hbar |K+G|^2}{2m} \leq E_{cut} \quad \textbf{(II.25)}$$

As a result, adjusting the calculation's convergence is as simple as raising the energy cutoff.

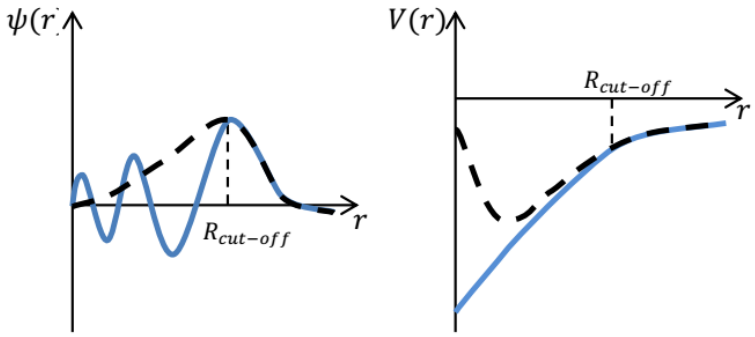

Figure. II. 1. Schematic illustration of pseudo-potential. Comparison of a wave function in the coulomb potential of the nucleus blue to one in the pseudo potential black shows that, up to a specific cutoff radius Rcut, the real and the pseudo wave functions and potentials are identical.

The major challenges arises from the valence electrons' incredibly fast oscillations close to the atom cores, which makes numerically representing this portion of the wave functions highly expensive. It is permissible to think of core electrons as observers of the interactions of atoms in molecules or solids because it has been established that the electrons that are primarily involved in chemical bonding are those that are occupying the valence states. Together with PPs, PWs are employed. A PP is a fake electron-ion interaction potential, acting solely on valence electrons, that simulates the interaction with the inner electrons,

which are thought to be frozen in the core, as well as the effective repulsion exerted by the latter on the former due to their mutual orthogonality.

For systems with up to hundreds of atoms in the unit cell, the KS equations can be solved quickly and effectively by using PWs and separable PPs, FFT, and iterative diagonalization or reduction techniques. Because core valence electron oscillations no longer exist, there is less of a demand for plane waves with high kinetic energy, which lowers the value of E cut as defined in equation **II.25**. The pseudo-wave functions fluctuate smoothly in the core region, as seen in figure **III.1**. The disadvantage of this strategy is that the majority of pseudo-potentials are non-local, allowing various states to experience various potentials.

Local pseudo-potentials, in contrast, behave uniformly over all wave-functions, which reduces their accuracy and discourages their use. Recasting the angular-momentum dependent portion of PPs into a sum across a few projectors is highly practical from a computational perspective (Kleinman and Bylander 1982). The introduction of this non-local component into the potential results in the velocity operator no longer being the same as the momentum operator $\hat{p}$, this is known as the separable form of PP's. Certainly, we have;

$$\hat{v} = i\left[\hat{H}, r\right] = \hat{p} + i[\hat{V}_{nl}, \hat{r}] \qquad \textbf{(II.26)}$$

where $\hat{V}_{nl}$ denotes the pseudo-non-local potential's contribution. The optical response must take this nonlocal contribution into account.

II.6.3. Full-potential augmented plane-wave (FP-APW)

The augmented plane wave (APW) method [36, 37] reliable computations of the electrical and magnetic characteristics of polyatomic systems using density-functional theory, and in particular its linearized form, the LAPW approach (DFT),[10, 38]. The program package WIEN, a piece of code created by Blaha, Schwarz, and others, is one successful use of the full-potential LAPW (FP-LAPW) technique.[39] . It has been effectively used to solve a variety of issues, including those involving electric field gradients. [40] additionally, systems like high-temperature superconductors [41], anti-ferromagnetic oxides, transition metal surfaces, minerals, and even molecules, [42]. The application of atomic forces made it possible to minimize the overall energy of a system by relaxing the atomic coordinates for complicated systems, and even molecular dynamics became practical.

The augmented plane-wave (APW) approach divides space into non-overlapping muffin-tin (MT) spheres centered at the atomic sites and an interstitial region (IR). The MT spheres are commonly chosen so that they approximately (to account for structural

relaxations) fill the maximum amount of space while not overlapping. The potential inside the muffin tins is roughly spherically symmetric, and the interstitial potential is frequently kept constant. Shape-approximations are a general term for the probable limitations. The basic set for the IR consists of plane waves $\mathbf{exp^{(ik.r)}}$.This enables a precise description of both the smoother portion of these values in between the atoms and the quickly varying (oscillating) wave-functions, potential, and electron density close to the nuclei. Some significant benefits of the plane-wave basis set include:

(i) Due to their simplicity, plane-wave based algorithms are easy to implement and have the advantages of being orthogonal and diagonal in momentum space. **(ii)** The praise is due to Slater. [43] Realizing that the plane wave expansion would converge very slowly, large wave vectors (K_{max}) would be required to accurately represent the wave-functions, making the setup and diagonalization of the Hamiltonian matrix in terms of plane waves difficult, if not impossible. This is because electron wave-functions near the nucleus are changing rapidly due to the singularity of the crystal potential at the nucleus and the plane wave expansion would converge very slowly.

later proposed replacing the Bessel functions $j_l(Kr)$ in the Rayleigh decomposition of the planewave inside the sphere with radial functions $u_l(K,r)$, which match the Bessel functions in value at the sphere radius Rmt and whose product with the spherical harmonics $Y_L(\hat{r})$ are the solutions in a spherical potential. Slater noted that plane-waves solve the Schroedinger The term "augmentation" is used to describe this process. Consequently, the single wave-functions are written as trial functions, $\Psi_{K,v}(r)$

$$\Psi_{K,v}(r) = \sum_{|G+K| \le K_{max}} c_{K,v}^{G} \varphi G(K,r) \qquad \textbf{(II.27)}$$

In terms of the APW basis functions;

$$\varphi G(K,r) = \begin{cases} e^{i(K+G)r} & \text{interstitial region} \\ \sum_{lm} a_L^{\mu G}(K) u_l(r^{\mu} \,|E) Y_L(\hat{r}^{\mu}) & \text{muffin} - \text{tin } \mu \end{cases} \qquad \textbf{(II.28)}$$

The position r inside the spheres μ located at τ^{μ} (see Figure.II.2.) is given with respect to the center of each sphere. L abbreviates the quantum numbers l and m and u_l is the regular solution of the radial Schr*ö*dinger equation;

$$\left\{-\frac{\hbar^2}{2m}\frac{\partial^2}{\partial r^2}+\frac{\hbar^2}{2m}\frac{l(l+1)}{r^2} + V(r) - E\right\} r u_l(r) = 0 \qquad \textbf{(II.26)}$$

to the energy parameter E_l. Here, $V(r)$ is the spherical component of the potential $V(r)$. The coefficients $V(r)$;

$$a_L^{\mu G}(K) = a_L^{\mu}(K+G) = 4\pi \exp(ik\tau^{\mu})\, i^l Y_L^*(\hat{K}) \frac{j_l(KR^u)}{u_l(R^u)}, \quad k = K+G \qquad \textbf{(II.27)}$$

are established by the necessity that, for the kinetic energy to be precisely characterized, the wave-functions be continuous at the boundary of the muffin-tin spheres. The wave-function in the interstitial region is solely determined by the variational coefficients c^G.

The Hamiltonian may be formulated in terms of this basis if E were maintained constant and only used as a parameter during the basis' creation. This would result in a typical secular equation for the band energies, where a set of band energies E_v is computed for a particular k-point in the Brillouin zone (BZ). Unfortunately, it turns out that if E is kept constant, the APW basis does not provide enough variational freedom. Only when the energies are set to the correct band energies $E_{K,v}$. can an accurate description be obtained (K,v). In this scenario, the Hamiltonian matrix H is dependent on $E_{K,v}$,, $H(E_{K,v})$, and cannot be found by a straightforward diagonalization.

The secular equation's solution becomes a nonlinear issue, which is computationally considerably more difficult than a secular problem because it depends on the band energies in this case. Instead of diagonalizing a matrix to discover all the bands at a particular k, one approach to solve this problem is to fix the energy E and scan over k to find a solution, i.e., find one band at a time.

As a result, in Slater's formulation of the approach, E is introduced as a second non-linear variational parameter, changing the shape of the functions u l until the best shape is discovered for the desired band energies $E_{K,v}$ .The APW approach has a number of additional drawbacks. The asymptote problem, or the decoupling of the radial function and the plane wave when $u_l(R)$ in equation II.27 reaches zero at the MT boundary, is the first and most visible.[43]. Andersen created linearized techniques in the middle of the 1970s to get around problems with the APW method caused by the Hamiltonian's energy dependence. [44]and Koelling and Arbman , [45]. Based on an idea proposed by Marcus [46], The energy derivatives of the basic functions u l in the muffin tins were added, however both $\dot{u}_l$and u_l are now evaluated at a fixed energy E_l. The Taylor series thus takes the place of the radial basis function's initial energy dependence:

$$u_l(E) = u_l(E_l) + (E - E_l)\dot{u}_l(E_l) + \cdots \qquad \textbf{(II.29)}$$

following the linear term, ended. This causes a quadratic inaccuracy in the eigenvalue E_l divergence from the energy parameter E, which only affects the wave-functions up to the fourth order.[45]. With this addition, the basic functions' explicit form is now:

$$\varphi G(K,r) = \begin{cases} e^{(i(K+G)r)} & \text{interstitial region} \\ \sum_{l,m}(a_L^{\mu,G}(K)u_l^{\mu}(r) + b_{lm}^{\mu,G}(K)\dot{u}_l^{\mu}(r))Y_{lm}(\hat{r}^{\mu}) & \text{muffin} - \text{tin } \mu \end{cases} \quad \textbf{(II.30)}$$

The energies E_l are situated in the center of gravity of the l like bands in order to reduce the linearization mistakes. It should be noted that the choice of the energy parameter affects the wave function's nodal structure in a specific way. A basis function that uses the l=1 energy parameter to describe a wave function that resembles a 2s in a particular muffin tin will not be appropriate to describe a 3s or a 1s state. Naturally, the size of the muffin-tin radius, R, also affects how flexible the fundamental function is; by selecting a lower R, two branches may occasionally be pushed to "collapse" into one, [47]. On the other hand, less flexibility makes it possible to calculate core- and valence states separately. Thus, in a normal computation, only high-lying valence states (such as 3s, 3p, and 3d) are estimated, whereas extremely localized states (such as 1s, 2s, and 2p) are disregarded. The l=0 portion of the muffin-tin potential is then used to address these states in a distinct calculation that is atomic in nature.Since the a and b coefficients in equation II.30 should ensure continuity across the muffintin boundary, the plane-wave cutoff, $G_{max}$and the l cutoff, l_{max}, are normally chosen to match: A planewave with wavevector G_{max} (given in inverse atomic units) has $G_{max} = \pi$ nodes per atomic unit. A spherical harmonic with $l = l_{max}$ has $2l_{max}$nodes along a great circle on the muffin-tin sphere, i.e., there are $l_{max}/(\pi R)$nodes per atomic unit.

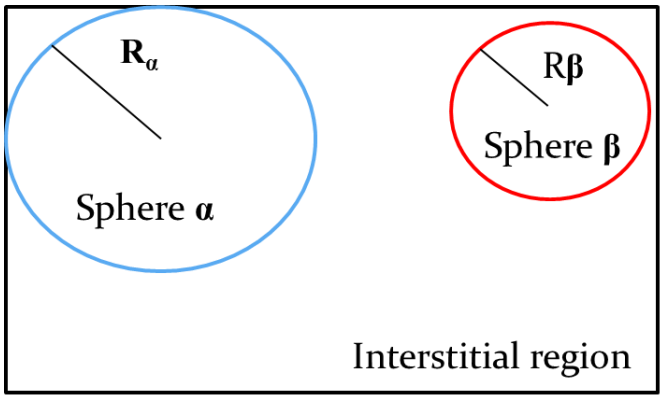

Figure. II. 2. Distribution of the unit cell, an interstitial region and spherical regions: α and β spheres of muffin-tin radii R_α and R_β, respectively, [47].

II.7 Density functional Perturbation Theory (DFPT)

II.7.1. Introduction

The methods of density-functional theory (DFT) [47] and density-functional perturbation theory (DFPT) [48] been demonstrated to successfully describe the dielectric, piezoelectric, and nonlinear optical properties of a variety of materials with weak electronic correlations,[49, 50].

Finite differences allow for the direct computation of many parameters of interest, such as elastic constants from the stress resulting from a small applied strain or dynamical effective charges from polarizations. [51] resulting from little displacements of the substrate. The usage of DFPT methods, on the other hand, is growing in popularity since they may be used to immediately compute such response properties without the need for numerous ground-state calculations, delivering the needed response qualities in a more automated, systematic, and reliable way. As a result, more advanced DFPT capabilities have recently been added to various computer code packages that are often utilized by the community of computational electronic structures. The open-source ABINIT computer package, which has the ability to handle strain disturbances, is the example of this advancement that has gone the furthest. [52] atomic displacement and electric-field perturbations, which were previously implemented, have lately been added.

The possibility of treating three different types of perturbations in insulating crystals, including periodicity-preserving atomic displacements (also known as zone-center phonons), homogeneous electric fields, and homogeneous strains, in a systematic manner is made possible by this research. Particularly in polar materials employed in contemporary ferroelectric, piezoelectric, and dielectric applications, these three degrees of freedom are frequently strongly correlated.

II.7.2. Formalism

II.7.2.1 Elementary response tensors

Take into account a crystal of insulation that contains N atoms per unit cell. The reference state we select has the following properties: the atomic coordinates are $R_m^{(0)}$, the lattice vectors are a_1, a_2, and a_3, the cell volume is Ω_0, etc. Here, m is a composite label (atom and displacement direction) spanning 1,..., 3N. We assume that this structure is the equilibrium one in a vanishing macroscopic electric field.

We look at three different types of perturbations that can be given to such a crystal:

(i) μ_m= displacements of the atoms away from their equilibrium positions $R_m^{(0)}$

(ii) η_j = strain in Voigt notation (j=1,..…6)

(iii) ε_α= homogeneous electric fields where α = {x, y, z} are Cartesian directions.

We exclusively consider atomic displacements that maintain the periodicity of the primitive cell, i.e., degrees of freedom that correspond to zone-center phonon modes. Additionally, we will limit ourselves to only zero-temperature attributes (the entropy will never enter, and the distinction between thermodynamic functions written in terms of temperature vs. in terms of entropy will never arise).

The corresponding responses that are conjugate to these three perturbations are (i) forces F_m, (ii) st σ_j, and (iii) polarizations P_α. From these, one can construct the response functions of primary interest: three diagonal-block tensors and the three off-diagonal-block tensors;

diagonal-block tensors	off-diagonal-block tensors
$K_{mn} = dF_m/d\mu_n$ (force-constant matrix)	$Z_{m\alpha} = dP_\alpha/d\mu_m$ (Born effective charge)
$\chi_{\alpha\beta} = dP_\alpha/d\varepsilon_\beta$ (dielectric susceptibility)	$\Lambda_{mj} = dF_m/d\eta j$ (internal strain)
$C_{jk} = d\sigma_j/d\eta_k$ (elastic constants)	$e_{\alpha j} = dP_\alpha/d\eta_j$ (piezoelectric response)

However, to define these quantities carefully, it is important to clarify the constraints or boundary conditions that apply to each definition.

The DFPT is systematically defining all response properties as appropriate second derivatives of the energy E per unit volume with respect to the perturbations. To be more precise, in the presence of strains we define E as the energy per unreformed unit cell volume Ω_0, while in the presence of electric fields E is modified to become an electric enthalpy [53] by adding a term proportional to -P.ε, where P is the electric polarization, [51]. (While a direct treatment of finite E-fields is now possible,[54, 55] only infinitesimal E-fields need to be considered here.) In general, E as;

$$E(\mu, \varepsilon, \eta) = \frac{1}{\Omega_0}[E_{cell}^{(0)} - \Omega\varepsilon.P] \quad \textbf{(II.31)}$$

where $E_{cell}^{(0)}$ is the usual zero-field Kohn-Sham energy per cell of the occupied Bloch functions and Ω is the deformed cell volume.

Accordingly, we write $E = E(\mu, \varepsilon, \eta)$ as a function of arguments μ_m, ε_α, and η_j, as

$$E = E_0 + A_m\mu_m + A_\alpha\varepsilon_\alpha + A_j\eta_j + \frac{1}{2}B_{mn}\mu_m\mu_n + \frac{1}{2}B_{\alpha\beta}\varepsilon_\alpha\varepsilon_\beta + \frac{1}{2}B_{jk}\eta_j\eta_k + B_{m\alpha}\mu_m\varepsilon_\alpha + B_{mj}\mu_m\eta_j + B_{\alpha j}\varepsilon_\alpha\eta_j + \text{terms of third and higher order} \quad \textbf{(II.32)}$$

The first-order coefficients A_m, A_α, and A_j encode are the forces ($F_m = -\Omega_0 A_m$), polarizations ($P_\alpha = -A_\alpha$), and stresses ($\sigma_j = A_j$), respectively. (Here, we assume the atomic coordinates and strains are fully relaxed in the reference system, so that $A_m = A_j = 0$) .

The diagonal-block second-order coefficients B_{mn}, $B_{\alpha\beta}$ and B_{jk} and off-diagonal second-order coefficients $B_{m\alpha}$, B_{mj}, and $B_{\alpha j}$ correspond to the force constant, elastic-constant, and susceptibility tensors, and the Born-charge, internal-displacement, and piezoelectric tensors, respectively, hence the elementary second-derivative response-function tensors are defined as follows;

The force-constant matrix; $K_{mn} = \Omega_0 \frac{\partial^2 E}{\partial\mu_m\,\partial\mu_n}$ **(II.33)**

The frozen-ion dielectric susceptibility; $\bar{\chi}_{\alpha\beta} = -\frac{\partial^2 E}{\partial\varepsilon_\alpha\,\partial\varepsilon_\beta}\Big|_{\mu,\eta}$ **(II.34)**

The frozen-ion elastic tensor; $\bar{C}_{jk} = \frac{\partial^2 E}{\partial\eta_j\,\partial\eta_k}\Big|_{\mu,\eta}$ **(II.35)**

are the elementary diagonal-block tensors, while the off-diagonal blocks are;

The Born dynamical effective charge tensor; $Z_{m\alpha} = -\Omega_0 \frac{\partial^2 E}{\partial\mu_m\,\partial\mu_\alpha}\Big|_{\eta}$ **(II.36)**

The force-response internal-strain tensor; $\Lambda_{mj} = -\Omega_0 \frac{\partial^2 E}{\partial\mu_m\partial\mu_j}$ **(II.37)**

The frozen-ion piezoelectric tensor; $\bar{e}_{\alpha j} = -\frac{\partial^2 E}{\partial\varepsilon_\alpha\partial\eta_j}\Big|_{\mu}$ **(II.38)**

The bar on quantities $\bar{\chi}_{\alpha\beta}$, $\bar{C}_{jk}$, and $\bar{e}_{\alpha j}$ indicates a frozen-ion quantity, i.e., the fact that atomic coordinates are not allowed to relax as the electric field or homogeneous strain is applied. Note that the clamped-ion elastic tensor $\bar{C}_{jk}$ and piezoelectric tensor $\bar{e}_{\alpha j}$ are generally not physically relevant quantities, except in cases of high symmetry where atomic displacements do not occur to first order in strain. The clamped-ion susceptibility tensor $\bar{\chi}_{\alpha\beta}$ is the purely electronic one that is measured in response to optical fields at frequencies well above the phonon-frequency range. The force-response internal-strain tensor Λ_{mj} should be distinguished from the displacement-response internal strain tensor $\Gamma_{nj} = \Lambda_{mj}(K^{-1})_{mn}$ that illustrates the first order displacements yielding from a first-order strain. The piezoelectric tensor $e_{\alpha j}$ describes the change of polarization arising from a strain, or stress arising from a change of E field.

We shall refer to the quantities defined in the equations. (II.33-II.38) as the "elementary" or "bare" response tensors. These are the quantities that will be calculated once and for all using the DFPT capabilities of a code package such as ABINIT.

II.7.2.2 Relaxed-ion tensors

Generally, the physical static response properties of interest must take into account the relaxations of the ionic coordinates. This becomes especially important for non-centrosymmetric polar systems, such as ferroelectric ones, where these various effects become coupled. Instead of "clamped-ion" quantities $\bar{\chi}$, $\bar{C}$ and $\bar{e}$ defined at fixed μ, we can define the corresponding "relaxed-ion" or "dressed" response tensors C, χ, and e as follows

$$\tilde{E}(\eta, \varepsilon) = \min_{\mu} E(\mu, \varepsilon, \eta) \quad \textbf{(II.39)}$$

Referring back to equation II.32, setting $\partial E/\partial u_n = 0$, $\partial E/\partial E_\alpha = 0$, and $\partial E/\partial \eta_j = 0$, and assuming that the reference configuration is one in which the forces Am vanish, we find

$$0 = B_{nm}\mu_m + B_{n\alpha}\varepsilon_\alpha + B_{nj}\eta_j \quad \textbf{(II.39)}$$

from which it follows that

$$\mu_m = -(B^{-1})_{mn}[B_{nj}\eta_j + B_{n\alpha}\varepsilon_\alpha] \quad \textbf{(II.41)}$$

Defining

$$\chi_{\alpha\beta} = -\frac{\partial^2 \tilde{E}}{\partial \varepsilon_\alpha \partial \varepsilon_\beta}\Big|_\eta \quad \textbf{(II.42)}$$

$$C_{jk} = \frac{\partial^2 \tilde{E}}{\partial \eta_j \partial \eta_k}\Big|_\varepsilon \quad \textbf{(II.43)}$$

$$e_{\alpha j} = -\frac{\partial^2 \tilde{E}}{\partial \varepsilon_\alpha \partial \eta_j} \quad \textbf{(II.44)}$$

and using equations. **(II.33-II.38)**, we find that the physical relaxed-ion dielectric, elastic, and piezoelectric tensors become;

$$\chi_{\alpha\beta} = \bar{\chi}_{\alpha\beta} + \Omega_0^{-1} Z_{m\alpha}(K^{-1})_{mn} Z_{n\beta} \quad \textbf{(II.45)}$$

$$C_{jk} = \bar{C}_{jk} - \Omega_0^{-1} \Lambda_{mj}(K^{-1})_{mn} \Lambda_{nk} \quad \textbf{(II.46)}$$

$$e_{\alpha j} = \bar{e}_{j\alpha} + \Omega_0^{-1} Z_{m\alpha}(K^{-1})_{mn} \Lambda_{nj} \quad \textbf{(II.47)}$$

the equations. **(II.45- II.47)** cannot be naively evaluated as written because the force-constant matrix K is singular, due to the fact that K has three vanishing eigenvalues associated with translational symmetry.

II.7.2.2.1 Pseudo-inverse of the force-constant matrix

The force-constant matrix K should have three vanishing eigenvalues as a result of translational symmetry. Moreover, in soft-mode systems, other eigenvalues may be close to

zero. Thus, for the many operations that use K^{-1}, there is a danger of numerical instabilities arising from attempting to invert a singular, or nearly singular, matrix. For this reason, the implemented a careful procedure for obtaining the \pseudo-inverse" of K, is K^{-1}, it's meant the pseudo-inverse. Briefly, we begin by identifying the three-dimensional space of acoustic modes (i.e., uniform translations), and project the matrix K onto the complementary subspace of dimension $3N-3$. We then invert in this subspace, reporting a warning message if any eigenvalues are very small, and then transform back to the full space. Thus, by construction, the resulting pseudo-inverse is zero in the subspace of translational modes, and is the inverse of the original matrix in the complementary subspace. As a result, any time K^{-1}, is multiplied by another tensor, a pre-projection onto the complementary subspace of dimension $3N-3$ is effectively carried out. In other words, \the acoustic sum rule is effectively enforced" in any operation involving K^{-1}.

II.7.3. Other derived tensor quantities

In the above, we showed how to obtain the static dielectric susceptibility tensor $\chi_{\alpha\beta}$, the elastic tensor C_{jk}, and the piezoelectric tensor $e_{\alpha j}$. These quantities are defined under conditions of controlled strain and electric field. From these three ingredients, it is straight forward to form many other useful tensor quantities describing physical properties defined under other constraints or boundary conditions.

II.7.3.1 Dielectric tensors

The susceptibility tensor $\chi_{\alpha\beta}$ is defined at fixed strain; the corresponding dielectric tensor is;

$$\varepsilon_{\alpha\beta}^{(\eta)} = \varepsilon_0(\delta_{\alpha\beta} + \chi_{\alpha\beta}) \qquad \textbf{(II.48)}$$

where ε_0 is the susceptibility of free space (SI units are used throughout) and the superscript (η) indicates that the derivative is taken at fixed strain. Often one is interested instead in the free -stress dielectric tensor

$$\varepsilon_{\alpha\beta}^{(\sigma)} = \varepsilon_0(\delta_{\alpha\beta} + \chi_{\alpha\beta}^{\sigma}) \qquad \textbf{(II.49)}$$

which incorporates the free-stress susceptibility χ^{σ}. An expression for the latter is easily derived from the elastic enthalpy;

$$\hat{H}(\sigma,\varepsilon) = \min_{\eta}[\breve{E}(\eta,\varepsilon) - \eta_j\sigma_j] \qquad \textbf{(II.50)}$$

Following a line of reasoning similar to that leading from equation **II.38** to equation (**II.44-II.46**) and setting $\sigma_j = 0$, one obtains;

$$\chi^{\sigma}_{\alpha\beta} = \chi_{\alpha\beta} + e_{\alpha j}(c^{-1})_{jk}e_{\beta} \quad \textbf{(II.51)}$$

Typically, a dielectric measurement will access the true static susceptibility χ^{σ}as long as the frequency is much less than that of sample resonances (elongational, bending, or torsional modes), and $\chi^{(\eta)}$at frequencies much higher than sample resonances (but much less than phonon frequencies).

we note that it is convenient to define inverse dielectric tensors for later use.

$$\beta^{(\eta)} = (\varepsilon^{(\eta)})^{-1} \quad \textbf{(II.52)}$$

$$\beta^{(\sigma)} = (\varepsilon^{(\sigma)})^{-1} \quad \textbf{(II.53)}$$

II.7.3.2 Elastic and compliance tensors

When a crystal is subjected to an external loading (with the stress state described by a stress tensorσ_{ij}), its shape and dimensions change. The change of a crystal geometry is describe by the strain tensor ε_{kl}. Relation between these 2 tensors (within the linear elastic limit) can be explained by the generalized form of Hooke's law

$$\sigma_{ij} = C_{ijkl}\varepsilon_{kl} \quad \textbf{(II.54)}$$

The C_{ijkl} is characterizes the stiffness of the crystal. For this reason, C_{ijkl} is often called elastic stiffness constants. the term ''elastic modulus'' is sometimes used for an (in a sense) inverse quantity S_{ijkl} that expresses elastic compliance of the crystal.

$$C^{(\varepsilon)}_{jk} = \frac{\partial \sigma_j}{\partial \eta_k}\Big|_{\varepsilon} \quad \textbf{(II.55)}$$

For some purposes, we may be interested instead in the elastic constant tensor at fixed displacement field D:

$$\boldsymbol{C^{(D)}_{jk}} = \frac{\partial \sigma_j}{\partial \eta_k}\Big|_{D} \quad \textbf{(II.56)}$$

The inverse of the elastic constant tensor is the compliance tensor. It can be defined either at fixed E or D:

$$S^{(\varepsilon)}_{jk} = \frac{\partial \eta_j}{\partial \sigma_k}\Big|_{\varepsilon} \quad \textbf{(II.57)}$$

$$S^{(D)}_{jk} = \frac{\partial \eta_j}{\partial \sigma_k}\Big|_{D} \quad \textbf{(II.58)}$$

It is also straightforward to obtain the corresponding elastic compliance tensors either under zero E-field boundary conditions

$$S^{(\varepsilon)} = (C^{(\varepsilon)})^{-1} \quad \textbf{(II.59)}$$

$$S^{(D)} = (C^{(D)})^{-1} \quad \textbf{(II.60)}$$

II.7.3.2.1 Mechanical Properties

The elastic constants are the ratio of stress to the strain of material. These are essential for describing the mechanical properties, type of bond, presence of different forces, and mechanical stability of the compounds, [56, 57]. They are also useful in predicting the aging behavior of the materials, [58]. Therefore, they have a great role in determining the strength of the crystals. They are also associated with thermodynamic behavior such as thermal expansion, specific heat, melting point, and Debye temperature.

- ✓ For orthorhombic type crystals there are 9 independent elastic constants (**C_{11}, C_{12}, C_{13}, C_{22}, C_{23}, C_{33}, C_{44}, C_{55} and C_{66}**) ,[59];

$$\boldsymbol{C}_{\text{orthorombic}} = \begin{pmatrix} \boldsymbol{C_{11}} & \boldsymbol{C_{12}} & \boldsymbol{C_{13}} & \mathbf{0} & \mathbf{0} & \mathbf{0} \\ \mathbf{0} & \boldsymbol{C_{22}} & \boldsymbol{C_{23}} & \mathbf{0} & \mathbf{0} & \mathbf{0} \\ \mathbf{0} & \mathbf{0} & \boldsymbol{C_{33}} & \mathbf{0} & \mathbf{0} & \mathbf{0} \\ \mathbf{0} & \mathbf{0} & \mathbf{0} & \boldsymbol{C_{44}} & \mathbf{0} & \mathbf{0} \\ \mathbf{0} & \mathbf{0} & \mathbf{0} & \mathbf{0} & \boldsymbol{C_{55}} & \mathbf{0} \\ \mathbf{0} & \mathbf{0} & \mathbf{0} & \mathbf{0} & \mathbf{0} & \boldsymbol{C_{66}} \end{pmatrix} \quad \textbf{(II.61)}$$

The mechanical stability criteria can be represented in a uniform manner for orthorhombic structure **$C_{ii}>0$ (i=1-6), $C_{11}+C_{22}+C_{33}+2(C_{12}+C_{13}+C_{23})>0$, $C_{11}+C_{22}-2C_{12}>0$, $C_{11}+C_{33}-2C_{13}>0$, $C_{22}+C_{33}-2C_{23}>0$** **(II.62)**

- ✓ For trigonal type crystals, there are 6 independent elastic constants **(C_{11}, C_{12}, C_{13}, C_{14}, C_{33}, C_{44})**

$$\mathbf{C}_{\text{trigonal}} = \begin{pmatrix} \mathbf{C_{11}} & \mathbf{C_{12}} & \mathbf{C_{13}} & \mathbf{C_{14}} & \mathbf{0} & \mathbf{0} \\ \mathbf{0} & \mathbf{C_{11}} & \mathbf{C_{13}} & \mathbf{-C_{14}} & \mathbf{0} & \mathbf{0} \\ \mathbf{0} & \mathbf{0} & \mathbf{C_{33}} & \mathbf{0} & \mathbf{0} & \mathbf{0} \\ \mathbf{0} & \mathbf{0} & \mathbf{0} & \mathbf{C_{44}} & \mathbf{0} & \mathbf{0} \\ \mathbf{0} & \mathbf{0} & \mathbf{0} & \mathbf{0} & \mathbf{C_{44}} & \mathbf{C_{14}} \\ \mathbf{0} & \mathbf{0} & \mathbf{0} & \mathbf{0} & \mathbf{0} & \mathbf{C_{66}} \end{pmatrix} \quad \textbf{(II.63)}$$

$C_{66} = (C_{11} - C_{12})/2$.

The mechanical stability criteria can be represented in a uniform manner for trigonal structure; $\mathbf{C_{44} \geq 0}$; $\mathbf{C_{11} > |C_{12}|}$; $\mathbf{C_{14}^2 < \frac{1}{2} C_{44}C_{66}}$; $\mathbf{C_{13}^2 < \frac{1}{2} \cdot C_{33} \cdot (C_{11}+C_{12})}$ **(II.64)**

- ✓ For Tetragonal (II) type crystals, there are 7 independent elastic constants **(C_{11}, C_{12}, C_{13}, C_{16}, C_{33}, C_{44}, and C_{66}.)**

$$C_{\text{Tetragonal}} = \begin{pmatrix} C_{11} & C_{12} & C_{13} & 0 & 0 & C_{16} \\ 0 & C_{11} & C_{13} & 0 & 0 & -C_{16} \\ 0 & 0 & C_{33} & 0 & 0 & 0 \\ 0 & 0 & 0 & C_{44} & 0 & 0 \\ 0 & 0 & 0 & 0 & C_{44} & 0 \\ 0 & 0 & 0 & 0 & 0 & C_{66} \end{pmatrix} \quad \textbf{(II.65)}$$

For tetragonal structures, the mechanical stability criterion can be represented uniformly;

$$C_{44} > 0 \; ; \; C_{11} > |C_{12}| \; ; \; 2 \cdot C_{16}^2 < C_{66} \cdot (C_{11} - C_{12}) \; ; \; 2 \cdot C_{13}^2 < C_{33} \cdot (C_{11} + C_{12}) \quad \textbf{(II.66)}$$

The bulk (B) and shear (G) modulus are calculated from the Voigt-Reuss-Hill (V-R-H) approximations. The Voigt (V) approximation represented the strain in the structure as upper limit for the parameters that are expressed the elastic coefficients C_{ij}. Unlike the Reuss (R) approximation, that assumed, the parameters in lower limit through the elastic compliance tensor S_{ij}.

$$B_H = \frac{1}{2}(B_V + B_R) \quad \textbf{(II.67)}$$

$$G_H = \frac{1}{2}(G_V + G_R) \quad \textbf{(II.68)}$$

In orthorhombic structure Voigt approximation, the bulk **(B_V)** and shear moduli **(G_V)** were estimated as:

$$B_V=((C_{11}+C_{22}+C_{33}) +2(C_{12}+C_{13}+C_{23}))/9. \quad \textbf{(II.69)}$$

$$G_V=((C_{11}+C_{22}+C_{33}) +2(C_{12}+C_{13}+C_{23}+ 3 (C_{44}+C_{55}+C_{66}))/15. \quad \textbf{(II.70)}$$

$$1/B_R=(S_{11}+S_{22}+S_{33}) +2(S_{12}+S_{13}+S_{23}). \quad \text{(II.71)}$$

$$15/G_R=4(S_{11}+S_{22}+S_{33})-4(S_{12}+S_{13}) +(S_{44}+S_{55}+S_{66}). \quad \textbf{(II.72)}$$

In trigonal structure Voigt approximation, the bulk (B_V) and shear moduli (G_V) were estimated as:

$$B_V = \frac{1}{9}[C_{11} + C_{22} + C_{33} + 2(C_{12} + C_{23} + C_{13})] \quad \textbf{(II.73)}$$

$$G_{V=} \frac{1}{15}[C_{11} + C_{22} + C_{33} - C_{12} - C_{23} - C_{13} + 3(C_{44} + C_{55} + C_{66})] \quad \textbf{(II.74)}$$

$$\frac{1}{B_R} = [S_{11} + S_{22} + S_{33} + 2(S_{12} + S_{23} + S_{13})] \quad \textbf{(II.75)}$$

$$\frac{1}{G_R} = 15[4(S_{11} + S_{22} + S_{33} - S_{12} - S_{23} + S_{13}) + 3(S_{44} + S_{55} + S_{66})] \quad \textbf{(II.76)}$$

In tetragonal structure Voigt approximation, the bulk (B_V) and shear moduli (G_V) were estimated as:

$$B_V = \frac{[2.(C_{11}+C_{12})+4.C_{13}+C_{33}]}{9} \quad \textbf{(II.78)}$$

$$G_V = \frac{M+3C_{11}-3C_{12}+6(2C_{44}+C_{66})}{30} \quad \textbf{(II.79)}$$

$$B_R = \frac{C^2}{M} \text{ , } M = C_{11} + C_{12} + 2C_{33} - 4C_{13} \text{ , } C^2 = (C_{11} + C_{12})C_{33} - 2C_{13}^2 \quad \textbf{(II.80)}$$

$$G_R = 15\left[\left(\frac{18.B_V}{C^2}\right) + \left(\frac{6}{C_{11}-C_{12}} + \frac{6}{C_{44}} + \frac{3(C_{11}-C_{12})^2+12.C_{16}^2}{(C_{11}-C_{12}).d^2}\right)\right]^{-1}, C^2 = (C_{11} + C_{12})C_{66} - 2C_{16}^2$$

(II.81)

Due to the special importance of the Young, Shear, and Bulk moduli, Pugh's ratio, Anisotropy, and Poisson's ratio for high-tech applications, which are computed from elastic constants. The ratio of stress to strain that determines the stiffness of materials is called young's modulus, the greater its value stiffer will be the material, and vice versa. It measures the ability of a material to withstand changes in length under a given amount of stress. It is given by the equation [60]:

$$E = \frac{9.B.G}{3.B+G} \quad \textbf{(II.82)}$$

The Poisson ratio determines the nature of the bond. Its values for covalent, ,ionic and metallic bonds in a crystal are 0.1,, 0.25 and 0 respectively , [61]. Poisson's ratio may also be used for determining the central forces in solids, also indicate the compressibility of materials. The Poisson's ratio ν is calculated from the following relation [60]:

$$\nu = \frac{3.B-2.G}{2(3.B+G)} \quad \textbf{(II.83)}$$

For central forces in crystals, the limits of Poisson's ratio are 0.5 to0.25 , [58]. The value of calculated Poisson's ratio under consideration remains between these two limits which reveal the predominance of the central inter-atomic forces. In addition, it can also reflect the ductile and brittle property by (ductile> 0.26= ν >brittle).

Bulk modulus B is one of the most important parameters of the engineering materials, [62]it gives information about the nature of the bond and cohesive and binding energies of the material,[63]. Shear modulus G is another important mechanical property that determines the resistance toward reversible deformations resulting from shear stress. The harder a substance is, the higher the shear modulus value becomes. It describes the hardness of material better than that by bulk modulus. The criterion for brittleness or ductility of a material is the value of the Pugh's ratio, B/G.The lesser and higher values of the B/G ratio than 1.75 reflect the brittle and ductile natures of the material, respectively, [64].

II.7.3.2.2 The Debye temperature

The Θ_D is known as an fundamental parameter related to many physical properties as melting temperature and specific heat, [65]. The Debye temperature can be estimated from the average sound velocity (v_m) by the following equation [66].

$$\Theta_D = \frac{h}{K_B}\left[\frac{3n}{4\pi}\left(\frac{N_A\rho}{M}\right)\right]^{1/3} v_m \quad \textbf{(II.84)}$$

where h is Planck's constant, k is Boltzmann's constant, N_A is Avogadro's number, n is the number of atoms per formula unit, M is the molecular mass per formula unit, $\rho = m/V$ is the density, and v_m is given [67] as

$$\mathbf{v_m} = \left[\frac{1}{3}\left(\frac{2}{v_t^3} + \frac{1}{v_l^3}\right)\right]^{-1/3} \quad \textbf{(II.85)}$$

where $\mathbf{v_l}$ and $\mathbf{v_t}$, are the longitudinal and transverse elastic wave velocity, respectively, which are obtained from Navier's equation

$$\mathbf{v_t} = \left(\frac{G}{\rho}\right)^{1/2} \quad \text{and} \quad \mathbf{v_l} = \left(\frac{3B+4G}{3\rho}\right)^{1/2} \quad \textbf{(II.86)}$$

II.7.3.2.3 Elastic anisotropy

Another interesting physical parameter related to the elastic properties of solids is elastic anisotropy. It is the measure of the intensity of a property in different directions. In different crystallographic planes, shear anisotropy gives a measure of the level of anisotropy in atomic bonding in different planes. Additionally, it provides information on stiffness. mechanical robustness and hardness ductility, binding, and brittleness between nearby atomic planes

The elastic anisotropy of a crystal is characterized by the universal anisotropic index A^U and by the indexes describing the behavior in shear and compression (A_G and A_B). The universal elastic anisotropy index A^U and indexes A_G and $A_B$for a crystal with any symmetry may be proposed as follows [130, 131]:

$$A^U = 5\frac{G_V}{G_R} + \frac{B_V}{B_R} - 6 \quad \textbf{(II.87)}$$

$$A_B = \frac{B_V - B_R}{B_V + B_R} \times 100\% \quad \textbf{(II.88)}$$

$$A_G = \frac{G_V - G_R}{G_V + G_R} \times 100\% \quad \textbf{(II.89)}$$

A^U is single crystal elastic anisotropy[68]. Universal index is equal to zero for isotropic materials. The deviation of $A^U$from zero defines the extent of elastic anisotropy.

$A_B = A_G = 0$ represents the elastic isotropy, and $A_B = A_G = 1$ means the maximum elastic anisotropy, [69].

The shear anisotropic factors provide measures of the degrees of anisotropy in atomic bonding in different crystallographic planes. Therefore, the determination of the elastic anisotropy of material is crucial to understanding its behaviors and finding means for improving its hardness and durability.

Plotting mechanical moduli in two- and three-dimensional space as a function of direction is the most effective technique to demonstrate the anisotropy of mechanical moduli.

The directional dependence of young modulus E or bulk modulus B from the elastic constants or compliance constants:

- ✓ For the orthorhombic crystal system [70]

$$\frac{1}{E}=S_{11}(l_1^4+l_2^4)+(2S_{13}+S_{44})(l_1^2l_3^2+l_2^2l_3^2)+S_{33}l_3^4+(2S_{12}+S_{66})l_1^2l_2^2+l_3^2(1-l_3^2)(2s_{13}+s_{44})+[2l_1l_2(l_1^2-l_2^2)s_{16}] \quad \textbf{(II.90)}$$

$$\frac{1}{B}=(S_{11}+S_{12}+S_{13})l_1^2+(S_{12}+S_{22}+S_{33})l_2^2+(S_{13}+S_{23}+S_{33})l_3^2 \quad \textbf{(II.91)}$$

- ✓ For trigonal crystal system [70]

$$\frac{1}{E}=S_{11}(l_1^4+l_2^4)+(2S_{13}+S_{44})(l_1^2l_3^2+l_2^2l_3^2)+S_{33}l_3^4+(2S_{12}+S_{66})l_1^2l_2^2+l_3^2(1-l_3^2)(2s_{13}+s_{44})+[2l_1l_2(l_1^2-l_2^2)s_{16}] \quad \textbf{(II.92)}$$

$$\beta=\frac{1}{B}=(S_{11}+S_{12}+S_{13})-(S_{11}+S_{12}-S_{13})-S_{13})\,l_3^2 \quad \textbf{(II.93)}$$

- ✓ For tetragonal crystal system [70]

$$\frac{1}{E}=S_{11}(l_1^4+l_2^4)+(2S_{13}+S_{44})(l_1^2l_3^2+l_2^2l_3^2)+S_{33}l_3^4+(2S_{12}+S_{66})l_1^2l_2^2+l_3^2(1-l_3^2)(2s_{13}+s_{44})+[2l_1l_2(l_1^2-l_2^2)s_{16}] \quad \textbf{(II.94)}$$

$$\beta=\frac{1}{B}=(S_{11}+S_{12}+S_{13})-(S_{11}+S_{12}-S_{13})-S_{13})\,l_3^2 \quad \textbf{(II.95)}$$

II.7.3.3 Piezoelectric tensors

The piezoelectric property is the derivative of the polarization versus the homogeneous strain, and therefore it is a mixed second-order derivative of the total energy versus electric field and strain. When stress is applied to a piezoelectric crystal, its interior will produce a polarization phenomenon where opposing positive and negative charges appear on its two opposite surfaces. This phenomenon is called the positive piezoelectric effect. Unlike, also deform when the electric field is applied in the polarization direction of the crystal.

This phenomenon is called the reverse piezoelectric effect.

$$\delta\eta_j = d_{j\alpha}\delta\varepsilon_\alpha$$
$$\delta D_\alpha = d_{j\alpha}\delta\sigma_j$$
$$\delta\sigma_j = -e_{j\alpha}\delta\varepsilon_\alpha$$
$$\delta D_\alpha = e_{j\alpha}\delta\eta_j \qquad \textbf{(II.96)}$$

The first of the four equations above is to describe the "converse" piezoelectric effect, while the second one describes the "direct" piezoelectric effect, and the third and the fourth describe the "inverse" piezoelectric effect. Thus, one sometimes refers to d as the coefficient of the "direct piezoelectric effect" while e (denoted as c almost as often as e these notations are equivalent) is the coefficient of the "inverse piezoelectric effect." Restating, the piezoelectric coefficients may be defined via;

$$e_{j\alpha} = \frac{\partial D_a}{\partial \eta_j}\Big|_\varepsilon = \frac{\partial P_\alpha}{\partial \eta_j}\Big|_\varepsilon \quad \text{or} \quad e_{j\alpha} = -\frac{\partial \sigma_j}{\partial \varepsilon_\alpha}\Big|_\varepsilon \qquad \textbf{(II.97)}$$

and

$$dj_\alpha = \frac{\partial \eta_j}{\partial \varepsilon_\alpha}\Big|_\sigma \quad \text{or} \quad dj_\alpha = \frac{\partial D_\alpha}{\partial \sigma_j}\Big|_\varepsilon = \frac{\partial P_\alpha}{\partial \sigma_j}\Big|_\varepsilon \qquad \textbf{(II.98)}$$

The e and d tensors are related by;

$$ej_\alpha = C_{jk}^{(\varepsilon)} d_{k\alpha} \quad \text{or, equivalently} \quad d_{j\alpha} = S_{jk}^{(\varepsilon)} e_{k\alpha} \qquad \textbf{(II.99)}$$

We calculate the piezoelectric characteristics using homogenous stresses and electric fields as perturbations. [70]

$$d_{\text{orthorombic}} = \begin{pmatrix} 0 & 0 & 0 & 0 & d_{15} & -2d_{22} \\ -2d_{22} & d_{22} & 0 & d_{15} & 0 & 0 \\ d_{31} & d_{31} & d_{33} & 0 & 0 & 0 \end{pmatrix} \qquad \textbf{(II.100)}$$

$$d_{\text{trigonal}} = \begin{pmatrix} -d_{12} & d_{12} & 0 & 0 & d_{15} & 0 \\ 0 & 0 & 0 & d_{15} & 0 & d_{12} \\ d_{15} & d_{15} & d_{33} & 0 & 0 & 0 \end{pmatrix} \qquad \textbf{(II.101)}$$

$$d_{\text{tetragonal}} = \begin{pmatrix} 0 & 0 & 0 & d_{14} & d_{15} & 0 \\ 0 & \overline{0} & 0 & \overline{d_{15}} & d_{14} & 0 \\ d_{31} & \overline{d_{31}} & 0 & 0 & 0 & d_{36} \end{pmatrix} \qquad \textbf{(II.102)}$$

II.7.3.1 Non-linear optical property

II.7.3.1.1 Introduction

The knowledge of the first-order derivatives of the wave functions is enough to calculate the second-order derivatives of the total energy, this is a special case of a very general theorem, known as the “2n+1 “theorem, which states that the knowledge of the

derivatives of the wave-functions up to order n allows the calculation of the derivatives of the energy up to order 2n + 1. In this context, the third-order derivatives of the total energy can be obtained from the first-order derivatives of the wave-functions. This opens the possibility to study phenomena that depends upon third-order anharmonic terms in the energy expansion such as phonon line widths, Raman scattering cross-sections, or nonlinear optical responses with a computational effort of the same order as for harmonic properties (because the time-consuming step is the calculation of the first-order derivatives of the wave-functions).

II.7.3.1.2 "2n+1 "theorem

The calculations of nonlinear optical properties are based on the 2n+1 theorem , [71]. The ground state and the first-order perturbed densities can be used to calculate the mixed third-rank derivatives of the energy by applying three Hermitian perturbations ($\boldsymbol{\lambda_1}$, $\boldsymbol{\lambda_2}$, and $\boldsymbol{\lambda_3}$).

$$E^{\lambda_1\lambda_2\lambda_3} = \frac{1}{6}\frac{\partial^3 E}{\partial\lambda_1\,\partial\lambda_2\,\partial\lambda_3}\Big|_{\lambda_1=0,\lambda_2=0,\lambda_3=0} \qquad \textbf{(II.103)}$$

can be computed from the ground-state and first-order wave-functions

$$E^{\lambda_1\lambda_2\lambda_3} = \frac{1}{6}(\tilde{E}^{\lambda_1\lambda_2\lambda_3} + \tilde{E}^{\lambda_1\lambda_2\lambda_3} + \tilde{E}^{\lambda_2\lambda_1\lambda_3} + \tilde{E}^{\lambda_2\lambda_3\lambda_1} + \tilde{E}^{\lambda_3\lambda_2\lambda_1} + \tilde{E}^{\lambda_3\lambda_1\lambda_2}) \qquad \textbf{(II.104)}$$

With the general expression of the third-order energy derivatives as;

$$\tilde{\mathbf{E}}^{\lambda_1\lambda_2\lambda_3} = \sum_{\alpha}\Big[< \Psi_\alpha^{\lambda_1} \Big|(\mathbf{T}+\mathbf{v_{ext}})^{\lambda_2\lambda_3}\Big|\Psi_\alpha^{(0)}> + < \Psi_\alpha^{\lambda_1}\Big|(\mathbf{T}+\mathbf{v_{ext}}+\mathbf{v_{Hxc}})^{\lambda_2}\Big|\Psi_\alpha^{\lambda_3}> + <$$

$$\Psi_\alpha^{(0)}\Big|(\mathbf{T}+\mathbf{v_{ext}})^{\lambda_1\lambda_2\lambda_3}\Big|\Psi_\alpha^{(0)}> + < \Psi_\alpha^{(0)}\Big|(\mathbf{T}+\mathbf{v_{ext}})^{\lambda_1\lambda_2}\Big|\Psi_\alpha^{\lambda_3}>] - \sum_{\alpha,\beta}\Lambda_{\beta,\alpha}^{\lambda_2} <$$

$$\Psi_\alpha^{\lambda_1}\Big|\Psi_\beta^{\lambda_3}> + \frac{1}{6}\int \mathbf{dr\,dr'dr''}\,\frac{\boldsymbol{\delta^3 E_{Hxc}[n^{(0)}]}}{\boldsymbol{\delta n(r)\delta n(r')\delta n(r'')}}\mathbf{n^{\lambda_1}(r)n^{\lambda_2}(r')n^{\lambda_3}(r'')} +$$

$$\frac{1}{2}\int \mathbf{dr\,dr'}\,\frac{\mathbf{d}}{\mathbf{d\lambda_2}}\frac{\boldsymbol{\delta^2 E_{Hxc}[n^{(0)}]}}{\boldsymbol{\delta n(r)\delta n(r')}}\Big|_{\boldsymbol{\lambda=0}}\mathbf{n^{\lambda_{(1)}n^{\lambda_{(3)}}}(r')}\Big] + \frac{1}{2}\int \mathbf{dr}\,\frac{\mathbf{d^2}}{\mathbf{d\lambda_1 d\lambda_3}}\frac{\boldsymbol{\delta E_{Hxc}[n^{(0)}]}}{\boldsymbol{\delta n(r)}}\Big|_{\boldsymbol{\lambda=0}}\mathbf{n^{\lambda_2}(r)} +$$

$$\frac{\mathbf{1}}{\mathbf{6}}\frac{\mathbf{d^3 E_{Hxc}[n^{(0)}]}}{\mathbf{d\lambda_1 d\lambda_2 d\lambda_3}}\Big|_{\boldsymbol{\lambda=0}} \qquad \textbf{(II.105)}$$

T is the kinetic energy and E_{Hxc}(resp.v_{Hxc}) is the sum of the Hartree and exchange correlation energy (resp. potential).The first-order potential $v_{Hxc}^{\lambda_2}$can be computed as a second-order functional derivative of E_{Hxc} [72]

$$v_{Hxc}^{\lambda_2} = \int \frac{\delta^2 E_{Hxc}[n^{(0)}]}{\delta n(r)\delta n(r')} n^{\lambda_2}(r')dr' + \frac{d}{d\lambda_2}\frac{\delta E_{Hxc}[n^{(0)}]}{\delta n(r)}\Big|_{\lambda=0} \qquad \textbf{(II.106)}$$

Within the parallel gauge, the first-order Lagrange multipliers are given by

$$\Lambda_{\beta\alpha}^{\lambda_2} = < \psi_\beta^{(0)}\Big|(T+v_{ext}+v_{Hxc})^{\lambda_2}\Big|\psi_\alpha^{(0)}> \qquad \textbf{(II.07)}$$

As a consequence of the "2n + 1" theorem, the evaluation of the equation. **II.105** requires no higher-order derivative of the wave functions than the first one. These first-order wave functions are nowadays available in several first-principles codes. They can be computed from the linear response by minimizing a stationary expression of the second-order energy, [48].

II.7.3.1.3 Non-linear optical susceptibilities

In an insulator the polarization can be expressed as a Taylor expansion of the macroscopic electric field

$$P_i = P_i^s + \sum_{J=1}^{3} \chi_{ij}^{(1)} \varepsilon_j + \sum_{j,l=1}^{3} \chi_{ijk}^{(2)} \varepsilon_j \varepsilon_k + \cdots \quad \textbf{(II.108)}$$

where P_i^s is the zero-field (spontaneous) polarization, $\chi_{ij}^{(1)}$ the linear dielectric susceptibility (second rank tensor) and $\chi_{ijK}^{(2)}$the second-order non-linear optical susceptibility (third rank tensor). In the litterature on non-linear optics, was often finds another definition of the nonlinear optical susceptibility: instead of $\chi_{ijK}^{(2)}$, it is more convenient to rely on the d tensor defined as

$$d_{ijk} = \frac{1}{2}\chi_{ijk}^{(2)} \quad \textbf{(II.109)}$$

In general, the polarization depends on valence electrons as well as ions. we deal only with the electronic contribution(ionic cores as clamped to their equilibrium positions).

$$\chi_{ijk}^{(2)}(-\omega_\beta-\omega_\gamma;\omega_\beta,\omega_\gamma) = \chi_{ijk}^{(2)}(-\omega_\beta-\omega_\gamma;\omega_\beta,\omega_\gamma) + \eta_{ijk}^{2}(-\omega_\beta-\omega_\gamma;\omega_\beta,\omega_\gamma) + \frac{i\sigma_{ijk}^{2}(-\omega_\beta-\omega_\gamma;\omega_\beta,\omega_\gamma)}{\omega_\beta+\omega_\gamma} \quad \textbf{(II.110)}$$

The first term in equation **II.110** describes the contributions of the interband transitions to second-order susceptibility. The second term represents the contribution from the modulation of the linear susceptibility by the intraband motion of the electrons. Finally, the third term describes the portion of the susceptibility resulting from the modification of interband motion by the polarization energy associated with the interband motion, [73].

The negative value of d_{ijk} coefficient means that the induced second-order susceptibility is in the opposite direction from the external electric field. We should note that the NLO coefficients are difficult to measure accurately and those values reported by various authors are often in substantial disagreement , [74].Experimentally, The electronic contribution to the linear and nonlinear susceptibilities is measured for electric fields at frequencies high enough to exclude ionic relaxation but low enough to prevent electronic excitations. In $\chi_{ijk}^{(2)}$, this

constraint implies that both the frequency of E, and it's second harmonic, are lower than the fundamental absorption gap.

The NLO susceptibility tensor $d_{ijk}$is a third-rank tensor having the units of m/V (or cm/statvolt). d_{ijk} can be contracted to a 3x6 matrix, d_{il} using simplified subscript indices since j and k can be exchanged based upon intrinsic permutation symmetry arguments. We simplify the notation by introducing a contracted matrix d_{il} according to the prescription

$$jK \rightarrow 11 \;\; 22 \;\; 33 \;\; 23.32 \;\; 31.13 \;\; 21.12$$

$$l \rightarrow \;\; 1 \quad 2 \quad 3 \quad 4 \quad 5 \quad 6$$

The nonlinear susceptibility tensor can be represented as the 3×6 matrix

$$d_{il} = \begin{pmatrix} d_{11} & d_{12} & d_{13} & d_{14} & d_{15} & d_{16} \\ d_{21} & d_{22} & d_{23} & d_{24} & d_{25} & d_{26} \\ d_{31} & d_{32} & d_{33} & d_{34} & d_{35} & d_{36} \end{pmatrix} \qquad \textbf{(II.111)}$$

The form of tensor d_{il} has to be consistent with the symmetry of the crystal. Thus, not even harmonics can be produced by materials with a center of symmetry or an inversion center. When an NLO material is chosen for an application, the NLO coefficient and the transparency range are among the most important properties. In general, a large NLO coefficient is a desired characteristic of a device crystal. According to the requirements of crystal symmetry, the number of independent components can be further reduced. d_{il} tensor for some ferroelectric crystals is shown in the sequel (in Voigt notation)

Point group 2mm

$$d_{\text{orthorombic}} = \begin{pmatrix} 0 & 0 & 0 & 0 & d_{33} & 0 \\ 0 & 0 & 0 & d_{32} & 0 & 0 \\ d_{31} & d_{32} & d_{33} & 0 & 0 & 0 \end{pmatrix} \qquad \textbf{(II.112)}$$

Point group 3m

$$d_{\text{trigonal}} = \begin{pmatrix} -d_{12} & d_{12} & 0 & 0 & d_{31} & 0 \\ 0 & 0 & 0 & d_{31} & 0 & d_{12} \\ d_{31} & d_{31} & d_{33} & 0 & 0 & 0 \end{pmatrix} \qquad \textbf{(II.113)}$$

Point group 4mm

$$d_{\text{tetragonal}} = \begin{pmatrix} 0 & 0 & 0 & d_{14} & d_{15} & 0 \\ 0 & 0 & 0 & \overline{d_{15}} & d_{14} & 0 \\ d_{31} & \overline{d_{31}} & 0 & 0 & 0 & d_{36} \end{pmatrix} \qquad \textbf{(II.114)}$$

II.7.3.1.4 Electrooptic tensor

The principal electro-optic (also known as Pockels) effect occurs in NCS compounds when the change in refractive index is linearly proportional to the electric field.The variations of refractive index (n) induced by a low-frequency electric field are as follows:

$$\Delta(\varepsilon^{-1})_{ij} = \sum_{\gamma=1}^{3} r_{ijk}\varepsilon_{\gamma k} \quad \textbf{(II.115)}$$

where $(\varepsilon^{-1})_{ij}$ is the inverse of the electronic dielectric tensor and r_{ijk} the EO tensor. Within the Born and Oppenheimer approximation, the EO tensor can be determine as the sum of 3 contributions: a bare electronic part r_{ijk}^{el}, an ionic contribution r_{ijk}^{ionic} and a piezoelectric contribution r_{ijk}^{piezo}.The electronic part is due to an interaction of ε_k with the valence electrons when considering the ions artificially as clamped at their equilibrium positions. It can be computed from the non-linear optical coefficients. As can be seen from equation **II.108**, $\chi_{ijk}^{(2)}$, defines the second-order change of the induced polarization with respect to E_k. Taking the derivative of equation **II.108**, we also see that $\chi_{ijk}^{(2)}$, defines the first-order change of the linear dielectric susceptibility, which is equal to $\frac{1}{4\pi}\Delta\varepsilon_{il}$. Since the EO tensor depends on $\Delta(\varepsilon^{-1})_{il}$ rather than $\Delta\varepsilon_{il}$, we have to transform $\Delta\varepsilon_{il}$, by the inverse of the zero-field electronic dielectric tensor , [75].

$$\Delta(\varepsilon^{-1})_{il} = -\sum_{m,n=1}^{3} \varepsilon_{im}^{-1}\Delta(\varepsilon)_{mn}\varepsilon_{nl}^{-1} \quad \textbf{(II.116)}$$

Using equation **II.116** we obtain the following expression for the electronic **EO** tensor

$$r_{ijk}^{el} = -8\pi\sum_{l,l'=1}^{3}(\varepsilon^{-1})_{il}\chi_{ll'k}^{(2)}(\varepsilon^{-1})_{l'j} \quad \textbf{(II.117)}$$

Equation**II.117** principal axes of the crystal under investigation [71]

$$r_{ijk}^{el} = \frac{-8\pi}{n_i^2 n_j^2}\chi_{ijk}^{(2)} \quad \textbf{(II.118)}$$

where the n_i coefficients are the principal refractive indices.

How ionic contributions came into being the EO tensor result of the atomic positions relaxing as a result to the applied electric field $E_\gamma$and the variations of ε_{ij} induced by these displacements. It is possible to calculate the ionic EO tensor as the sum of the transverse optic phonon modes at $q = 0$;

$$r_{ijk}^{ion} = -\frac{4\pi}{\Omega n_i^2 n_j^2}\sum_m \frac{\alpha_{ij}^m p_{m,k}}{\omega_m^2} \quad \textbf{(II.119)}$$

$$\alpha_{ij}^m = \sqrt{\Omega}\sum_{k,\beta}\frac{\partial\chi_{ij}^{(1)}}{\partial\tau_{k\beta}}u_m(k\beta) \quad \textbf{(II.120)}$$

$$p_{m,k} = \sum_{k,\beta} Z_{k,k\beta}^{*} u_m(k\beta) \quad \textbf{(II.121)}$$

where α^m is the Raman susceptibility of mode m, and $p_{m,k}$ the mode polarity that is directly linked to the mode's oscillator strength;

$$S_{m,\alpha\beta}=p_{m,\alpha}\cdot p_{m,\beta} \quad \textbf{(II.122)}$$

For simplicity, we have expressed equation **II.119** in the principal axes while a more general the expression can be derived from equation **II.116**.

Finally, the piezoelectric contribution is due to a relaxation of the unit cell shape due to the converse piezoelectric effect [71], it can be computed from the elasto-optic coefficients p_{ijuv} and the piezoelectric strain coefficients d_{kuv}

$$r_{ijk}^{piezo} = \sum_{u,v=1}^{3} p_{ijuv} d_{kuv} \quad \textbf{(II.123)}$$

In the discussion of the EO effect, we have to specify whether we are dealing with strain free (clamped) or stress-free (unclamped) mechanical boundary conditions. The clamped EO tensor r_{ijk}^{η} takes into account the electronic and ionic contributions but neglects any modification of the unit cell shape due to the converse piezoelectric effect [71, 76]

$$r_{ij\gamma}^{\eta} = r_{ij\gamma}^{el} + r_{ij\gamma}^{ion} \quad \textbf{(II.124)}$$

Experimentally, it can be measured for frequencies of E_k high enough to eliminate the relaxations of the crystal lattice but low enough to avoid excitations of optical phonon modes (usually above ~ 100 MHz). To investigate the unclamped EO tensor r_{ijk}^{σ} , we have to add the piezoelectric contribution to r_{ijk};

$$r_{ijk}^{\sigma} = r_{ijk}^{\eta} + r_{ijk}^{piezo} \quad \textbf{(II.125)}$$

Experimentally, r_{ijk}^{σ}can be measured for frequencies of E_k below the (geometry dependent) mechanical body resonances of the sample [77](usually below ~ 1 MHz). The experimentally determined NLO and linear EO coefficients can be either negative or positive. The sign of these parameters will be often difficult to measure experimentally. Besides, d_{il} and EO tensors are expressed in the standard crystallographic coordinate system in which the z direction represents the optical axis of the crystal. The negative value of d_{il} coefficient means that the induced second-order susceptibility is in the opposite direction with the external electric field. We should note that the NLO coefficients are difficult to measure accurately and those values reported by various authors are often in substantial disagreement, [74].

The linear EO effect is described by a third rank tensor, commonly represented as a 6 × 3 matrix. Since ε_{il} is real and symmetric, its inverse η_{ij} must also be real and symmetric, and consequently r_{ijk} must be symmetric in its first two indices.

This relationship can be written explicitly as;

$$r_{il}=\begin{pmatrix} r_{11} & r_{12} & r_{13} \\ r_{21} & r_{22} & r_{23} \\ r_{31} & r_{32} & r_{33} \\ r_{41} & r_{42} & r_{43} \\ r_{51} & r_{52} & r_{53} \\ r_{61} & r_{62} & r_{63} \end{pmatrix} \quad \textbf{(II.126)}$$

The simplified linear EO coefficient tensors of some of the point groups;

Point group 31m;

$$r_{il}=\begin{pmatrix} r_{11} & 0 & r_{13} \\ -r_{11} & 0 & r_{13} \\ 0 & 0 & r_{33} \\ 0 & r_{51} & 0 \\ r_{51} & 0 & 0 \\ 0 & -r_{11} & 0 \end{pmatrix} \quad \textbf{(II.127)}$$

Point group mm2;

$$r_{il}=\begin{pmatrix} 0 & 0 & r_{13} \\ 0 & 0 & r_{23} \\ 0 & 0 & r_{33} \\ 0 & r_{42} & 0 \\ r_{51} & 0 & 0 \\ 0 & 0 & 0 \end{pmatrix} \quad \textbf{(II.128)}$$

Point group $\bar{4}$;

$$r_{il}=\begin{pmatrix} r_{11} & 0 & r_{13} \\ -r_{11} & 0 & r_{13} \\ 0 & 0 & r_{33} \\ 0 & r_{51} & 0 \\ r_{51} & 0 & 0 \\ 0 & -r_{11} & 0 \end{pmatrix} \quad \textbf{(II.129)}$$

II.8 The modern theory of polarization

II.8.1. Introduction

For many years an unsolved problem in solid state physics was the correct definition of polarization in periodic systems. This definition is intrinsically related to the one the dipole operator, that is a problematic object for extended systems. In order to understand the problem, let's start the discussion from the polarization in isolated systems. In a system with open boundary conditions, the dipole operator is well defined and therefore one can write down the polarization as:

$$P = \frac{e<\vec{r}>}{V} = \frac{e}{V}\int \vec{r}n(r)dr \quad \textbf{(II.130)}$$

where $n(r)$ is the electronic density.

The simplest idea for the definition of the polarization in periodic systems would be to generalize the previous formula. The integral in equation **II.130** can be redefined in different possible ways in periodic systems. In an insulator the contributions from the dipoles inside the material cancel each other and only the surfaces contribute to the total polarization;

$$\Delta P = \frac{(\Delta\sigma L^2)L}{L^3} \qquad \textbf{(II.131)}$$

where $\Delta\sigma$ is related to the charges accumulated on the surfaces. This definition equation II.131 [77]is not suitable for numerical calculations because it requires the simulation of the entire sample and moreover the above defined polarization is not a bulk property but it depends from the surfaces.

The second possibility is to define the polarization as $P = < \vec{r} >_{cell}/V_{cell}$ .But this definition is completely arbitrary. In fact, different choices of the unit cell give completely different polarizations for the same material. A last possibility exists, the use of the dipole matrix elements in terms of Bloch orbitals, but also in this case there is problem since the dipole operator is unbounded in periodic systems. Finally, let mention that also the well know Clausius-Mossotti formula for the polarizability cannot be used in real solids because wave-functions are not localized objects.

The main reason makes polarization definition so difficult in solids; the dipole operator is ill defined in periodic systems, because $\vec{r}$ is not periodic while wave-functions are.

Until the early nineties, the formulation of a quantum-mechanical theoretical framework for the study of the physics of electric polarization in solids had remained a challenging problem, [78].This picture changed in 1993 when King-Smith and Vanderbilt (KS-V) [51] proposed a formulation (the modern theory of polarization - MTP), the problem of a correct definition of polarization solved, which resolved the conceptual difficulties associated with the definition of this quantity for continuous, periodic, charge distributions.

In their seminal paper, they shown that bulk polarization can be expressed as a closed integral on the wave-function phase in the Brillouin zone, a particular case of the Berry's phase. Their formulation solved all problems with the previous attempts to define the polarization. In fact, the King-Smith and Vanderbilt (KSV) polarization is a bulk quantity, its time derivative gives the current and its derivatives respect to the external field reproduce the polarizabilities at all orders.

In their work, the electric polarization of an insulating crystal is related to a Berry phase[79] computed from the valence wave-functions.Besides settling, the important conceptual question related to the definition of polarization as a bulk quantity, the KS-V

theory provided an entirely new framework for the computation of the polarization of a crystal maintained at vanishing homogeneous electric field. Since its formulation, the theory has been examined in greater detail by KS-V [51] and by Resta [78], and extended to many-body systems by Ortiz and Martin , [80]. The relation between polarization and the phases of the wave-functions has also led to a reexamination of the role this quantity plays in (DFT)[9] formulation of the ground-state properties of extended systems.[72, 81-83].Of no less importance is the conceptual relationship between the spontaneous polarization and the centers of charge of the Wannier functions (WF) of the occupied bands, which was also discussed by KS-V [51] and previously by Zak. [84] This connection was later generalized by Nunes and Vanderbilt [85] (NV) to deal with insulators placed in non-zero external homogeneous electric fields: they introduced field-dependent "polarized" WF's and a method for their computation.

Within DFT the NV method has recently been applied to the computation of the polarized WF's and the dielectric constant. The latter quantity is related to the change of polarization due to a change of homogeneous electric field, in the linear regime, or equivalently, to the second-derivative of the total energy with respect to the homogeneous electric field. Specific treatments have been developed (noticeably within DFT) for the study of the response of crystals to "external" perturbations, like phonons, stresses or homogeneous electric fields. After the MTP was developed, Dal Corso and Mauri [86], building on the NV work, gave a very succinct equation for the second-order susceptibility, which was later effectively used to compute this quantity for a number of systems, [87] using the variation-perturbation theory. The MTP method is used to directly implement the theory in reciprocal space using the Berry phase associated with the occupied bands of the perturbed crystal. Before its relationship with the electronic polarization was confirmed by ksv, the existence of a band structure berry phase had previously been discussed by zak and colleagues.

II.8.2. Berry's phase polarization

In the MTP [51, 77, 78] The self-consistent kohn-Sham potential is defined as the change in electric polarization per unit volume caused by an adiabatic change in the crystalline potential in the setting of DFT.

$$\Delta P = \int_{\lambda 1}^{\lambda 2} \frac{\partial P}{\partial \lambda} d\lambda = P(\lambda_2) - P(\lambda_1) \qquad \textbf{(II.132)}$$

with $P(\lambda)$ given in terms of a Berry phase associated with the occupied bands of the system

$$P(\lambda) = -\frac{2ie}{(2\pi)^3} \sum_n \underline{\int}_{BZ} dk < u_{nK}^{\lambda} \left| \nabla_K \right| u_{nK}^{\lambda} > \qquad \textbf{(II.133)}$$

where $-e$ is the electron charge, λ is a parameter representing the adiabatic change in the potential, and the factor of 2 in the numerator accounts for spin (we will consider only spin-unpolarized systems).

The gauge relation between periodic functions $u_{nK} + G(r) = e^{-iG.r}u_{nK}(r)$is established by requiring that the Bloch eigenstates be periodic in reciprocal space, i.e., $\Psi_{nK} = \Psi_{nK} + G$, where G is a reciprocal-lattice vector. With this choice of gauge, the polarization changes given by equation **II.132** are defined to within a factor of $(2e/\Omega)R$, where R is a lattice vector, [51] equation. **II.133** was derived under the restriction that the macroscopic electric field inside the crystal vanishes. Moreover, it also requires that the set of wave-functions be differentiable with respect to **k**.

The actual evaluation of the polarization in equation **II.134** is carried out on a discrete mesh of points in reciprocal space. Because this expression depends on the phase relationships of wave-functions at different k-points, the following discretized version was proposed by KS-V:

$$P_{\|}(\lambda) = \frac{e}{4\pi^3}\underline{\int} dK \perp \sum_{j=1}^{N_k} Im\{lndet\left[< u_{nKj}^{(\lambda)} \left| u_{mKj+1}^{(\lambda)} > \right.\right]\} \qquad \textbf{(II.134)}$$

where $P_{\|}$ is the component of the polarization along the direction of a short reciprocal lattice vector, $G_{\|}$, and N_K is the number of k-points sampling the Brillouin zone along that direction for each value of $K_{\perp}$, with $K_j = K_{\perp} + jG_{\|}/N_K$.

From a calculational point of view, this discretized expression ensures that the final result is unaffected by random numerical phases which may be introduced in the wave functions at different k-points, when these are independently determined by the diagonalization routine.However, Resta has taken the view that the discretized expression is to be regarded as more fundamental than the continuous form, [87].For the formulation of the electric-field response that we develop in the present work, discretization is crucial in order to define a numerically stable minimization procedure. It is possible to convert the berry phase expression into a real space integral involving the occupied bands' wannier functions, which results in a physically transparent expression for the polarization in terms of the wannier functions' centers of charge.

$$P(\lambda) = -\frac{2e}{\Omega}\sum_n \underline{\int} \left| r\omega_n^{(\lambda)} \right|^2 dr \qquad \textbf{(II.135)}$$

where Ω is the unit-cell volume.

In principle, the above expressions are valid only at vanishing electric field. However, it was soon realized that equation. **II.135** could be extended to the non-zero field problem, by

introducing the so-called polarized Wannier functions. Polarization effects were then related to the field-induced shifts in the Wannier-function centers of charge. The equation. **II.134** is applied to the non-zero-field problem, thus defining a field-dependent Berry phase containing the polarization effects. This allows us to work out a perturbative approach for the finite-field problem.

King-Smith and Vanderbilt demonstrated the validity of equation **II.135** by means of Wannier functions. They supposed that is possible to map Bloch orbitals in maximal localized Wannier functions then wrote the polarization in terms of the last ones, and finally show that this is equivalent to the equation **II.134** Another proof was proposed some years later by R. Resta that generalized the previous formula to the many-body case and show that it reproduces the integral of the total current.

II.9.Conclusion

In this chapter, we present the basic principles of Theoretical Framework, Density functional theory (DFT) and their Formalism, Density Functional Approximations which is used, Density functional Perturbation Theory (DFPT), and the modern theory of polarization, were presented in this chapter. A good choice of basis function set is crucial for solving KohnSham equations. Our calculations performed on solids are based on both Plane waves and pseudo-potentials(PP-PW) implemented in the ABINIT package and Full-potential augmented plane-wave (FP-APW) implemented in the Wien2k package; Moreover, the elastic properties and non-linear (NLO) properties, within the framework of the modern theory of polarization and density functional perturbation theory (DFPT), making use of the 2n+1 theorem, are calculated and stored in the derivative database (DDB), and analyzed by the ANADDB package within the ABINIT Package (chapter III and IV)

Reference chapter II

1. Thomas, L.H. The calculation of atomic fields. in Mathematical proceedings of the Cambridge philosophical society. 1927. Cambridge University Press.
2. Fermi, E., Eine statistische Methode zur Bestimmung einiger Eigenschaften des Atoms und ihre Anwendung auf die Theorie des periodischen Systems der Elemente. Zeitschrift für Physik, 1928. **48**(1): p. 73-79.
3. Thomas, L.t. and K. Umeda, Atomic scattering factors calculated from the TFD atomic model. The Journal of chemical physics, 1957. **26**(2): p. 293-303.
4. Hartree, D. The wave mechanics of an atom with a non-coulomb central field. part iii. term values and intensities in series in optical spectra. in Mathematical Proceedings of the Cambridge Philosophical Society. 1928. Cambridge University Press.
5. Slater, J.C., A simplification of the Hartree-Fock method. Physical Review, 1951. **81**(3): p. 385.
6. Lozovoi, A.Y., A. Alavi, and M.W. Finnis, Surface stoichiometry and the initial oxidation of NiAl (110). Physical review letters, 2000. **85**(3): p. 610.
7. Kerkar, M., et al., An unusual adsorption site for methoxy on Al (111) surfaces. Journal of Physics: Condensed Matter, 1992. **4**(22): p. 5043.
8. Hanbicki, A., et al., Hydrogen-induced structural changes on NiAl (110). Surface science, 1996. **365**(1): p. L639-L646.
9. Hohenberg, P. and W. Kohn, Inhomogeneous electron gas. Physical Review, 1964. **136**(3B): p. B864.
10. Kohn, W. and L.J. Sham, Self-consistent equations including exchange and correlation effects. Physical Review, 1965. **140**(4A): p. A1133.
11. Honenberg, P. and W. Kohn, Inhomogeneous electron gas. RESONANCE-JOURNAL OF SCIENCE EDUCATION, 2017. **22**(8): p. 810-811.
12. Sham, L.J. and W. Kohn, One-particle properties of an inhomogeneous interacting electron gas. Physical Review, 1966. **145**(2): p. 561.
13. Kohn, W., A.D. Becke, and R.G. Parr, Density functional theory of electronic structure. The Journal of Physical Chemistry, 1996. **100**(31): p. 12974-12980.
14. Trickey, S.B., Short Course on Density Functional Theory and Applications X. References and Omitted Topics. Phys. Rev. A, 2006. **73**(012513): p. 1-12.
15. Perdew, J.P. and Y. Wang, Erratum: Accurate and simple analytic representation of the electron-gas correlation energy [Phys. Rev. B 45, 13244 (1992)]. Physical review B, 2018. **98**(7): p. 079904.

16. Dirac, P.A. Note on exchange phenomena in the Thomas atom. in Mathematical proceedings of the Cambridge philosophical society. 1930. Cambridge University Press.
17. Perdew, J.P., K. Burke, and M. Ernzerhof, Generalized gradient approximation made simple. Physical review letters, 1996. **77**(18): p. 3865.
18. Wu, Z. and R.E. Cohen, More accurate generalized gradient approximation for solids. Physical review B, 2006. **73**(23): p. 235116.
19. Haas, P., et al., Insight into the performance of GGA functionals for solid-state calculations. Physical review B, 2009. **80**(19): p. 195109.
20. Csonka, G.I., et al., Assessing the performance of recent density functionals for bulk solids. Physical review B, 2009. **79**(15): p. 155107.
21. Kümmel, S. and L. Kronik, Orbital-dependent density functionals: Theory and applications. Reviews of Modern Physics, 2008. **80**(1): p. 3.
22. Perdew, J.P., et al., Density-functional theory for fractional particle number: derivative discontinuities of the energy. Physical review letters, 1982. **49**(23): p. 1691.
23. Sham, L.J. and M. Schlüter, Density-functional theory of the energy gap. Physical review letters, 1983. **51**(20): p. 1888.
24. Grüning, M., A. Marini, and A. Rubio, Density functionals from many-body perturbation theory: The band gap for semiconductors and insulators. The Journal of chemical physics, 2006. **124**(15): p. 154108.
25. Perdew, J., E. McMullen, and A. Zunger, Density-functional theory of the correlation energy in atoms and ions: a simple analytic model and a challenge. Physical Review A, 1981. **23**(6): p. 2785.
26. Städele, M., et al., Exact exchange Kohn-Sham formalism applied to semiconductors. Physical review B, 1999. **59**(15): p. 10031.
27. Engel, E., Relevance of core-valence interaction for electronic structure calculations with exact exchange. Physical review B, 2009. **80**(16): p. 161205.
28. Ruderman, W., et al., Laser damage studies of silver gallium sulfide single crystals. MRS Online Proceedings Library (OPL), 1997. **484**.
29. Becke, A.D. and E.R. Johnson, A simple effective potential for exchange. The Journal of chemical physics, 2006. **124**(22): p. 221101.
30. Tran, F. and P. Blaha, Accurate band gaps of semiconductors and insulators with a semilocal exchange-correlation potential. Physical review letters, 2009. **102**(22): p. 226401.

31. Becke, A.D. and M.R. Roussel, Exchange holes in inhomogeneous systems: A coordinate-space model. Physical Review A, 1989. **39**(8): p. 3761.
32. Tran, F., P. Blaha, and K. Schwarz, Band gap calculations with Becke–Johnson exchange potential. Journal of Physics: Condensed Matter, 2007. **19**(19): p. 196208.
33. Blaha, P., et al., wien2k. An augmented plane wave+ local orbitals program for calculating crystal properties, 2001. **60**.
34. Laskowski, R. and P. Blaha, Understanding the L 2, 3 x-ray absorption spectra of early 3 d transition elements. Physical review B, 2010. **82**(20): p. 205104.
35. Gaiduk, A.P. and V.N. Staroverov, How to tell when a model Kohn–Sham potential is not a functional derivative. The Journal of chemical physics, 2009. **131**(4): p. 044107.
36. Slater, J., Suggestions from Solid-State Theory Regarding Molecular Calculations. The Journal of chemical physics, 1965. **43**(10): p. S228-S228.
37. Wimmer, E., et al., Full-potential self-consistent linearized-augmented-plane-wave method for calculating the electronic structure of molecules and surfaces: O 2 molecule. Physical review B, 1981. **24**(2): p. 864.
38. Hohenberg, P. and W. Kohn, Density functional theory (DFT). Phys. Rev, 1964. **136**: p. B864.
39. Blaha, P., et al., Full-potential, linearized augmented plane wave programs for crystalline systems. Computer physics communications, 1990. **59**(2): p. 399-415.
40. Blaha, P., K. Schwarz, and P. Herzig, First-principles calculation of the electric field gradient of Li 3 N. Physical review letters, 1985. **54**(11): p. 1192.
41. Schwarz, K., C. Ambrosch-Draxl, and P. Blaha, Charge distribution and electric-field gradients in YBa 2 Cu 3 O 7− x. Physical review B, 1990. **42**(4): p. 2051.
42. Kohler, B., et al., Force calculation and atomic-structure optimization for the full-potential linearized augmented plane-wave code WIEN. Computer physics communications, 1996. **94**(1): p. 31-48.
43. Slater, J.C., Wave functions in a periodic potential. Physical Review, 1937. **51**(10): p. 846.
44. Andersen, O.K., Linear methods in band theory. Physical review B, 1975. **12**(8): p. 3060.
45. Koelling, D. and G. Arbman, Use of energy derivative of the radial solution in an augmented plane wave method: application to copper. Journal of Physics F: Metal Physics, 1975. **5**(11): p. 2041.

46. Marcus, P.M., Variational methods in the computation of energy bands. International Journal of Quantum Chemistry, 1967. **1**(S1): p. 567-588.
47. Soler, J.M. and A.R. Williams, Simple formula for the atomic forces in the augmented-plane-wave method. Physical review B, 1989. **40**(3): p. 1560.
48. Gonze, X. and C. Lee, Dynamical matrices, Born effective charges, dielectric permittivity tensors, and interatomic force constants from density-functional perturbation theory. Physical review B, 1997. **55**(16): p. 10355.
49. Baroni, S. and A. Quattropani, Nuovo Cimento D 5, 89 (1985); S. Baroni, P. Giannozzi, and A. Testa. Phys. Rev. Lett, 1987. **58**: p. 1861.
50. de Gironcoli, S., S. Baroni, and R. Resta, Piezoelectric properties of III-V semiconductors from first-principles linear-response theory. Physical review letters, 1989. **62**(24): p. 2853.
51. King-Smith, R. and D. Vanderbilt, Theory of polarization of crystalline solids. Physical review B, 1993. **47**(3): p. 1651.
52. Vanderbilt, D. Polarization, electric fields and dielectric response in insulators. in Conference on Computational Physics, Rutgers University. 2005.
53. Nunes, R. and X. Gonze, Berry-phase treatment of the homogeneous electric field perturbation in insulators. Physical review B, 2001. **63**(15): p. 155107.
54. Souza, I., J. Íniguez, and D. Vanderbilt, First-principles approach to insulators in finite electric fields. Physical review letters, 2002. **89**(11): p. 117602.
55. Umari, P. and A. Pasquarello, Ab initio molecular dynamics in a finite homogeneous electric field. Physical review letters, 2002. **89**(15): p. 157602.
56. Lingam, C.B., et al., Structural, electronic, bonding, and elastic properties of NH3BH3: a density functional study. Journal of computational chemistry, 2011. **32**(8): p. 1734-1742.
57. Saidi, F., et al., Structural and mechanical properties of Laves phases YCu2 and YZn2: First principles calculation analyzed with data mining approach. Computational Materials Science, 2014. **89**: p. 176-181.
58. Ravindran, P., et al., Density functional theory for calculation of elastic properties of orthorhombic crystals: Application to TiSi 2. Journal of applied physics, 1998. **84**(9): p. 4891-4904.
59. Musgrave, M., Crystal Acoustics: Introduction to the Study of Elastic Waves and Wibrations in Crystals1970: Holden-Day.

60. Koc, H., et al., Elastic, electronic, and optical properties of Sb2S3 and Sb2Se3 compounds: ab initio calculation. arXiv preprint arXiv:1205.3344, 2012.
61. Murugan, A., et al., Structural, electronic, mechanical and magnetic properties of rare earth nitrides REN (RE= Pm, Eu and Yb). Journal of Magnetism and Magnetic Materials, 2015. **385**: p. 441-450.
62. Verma, A., Bulk modulus and hardness of chalcopyrite structured solids. Materials Chemistry and Physics, 2013. **139**(1): p. 256-261.
63. Chen, K., L. Zhao, and J.S. Tse, Ab initio study of elastic properties of Ir and Ir 3 X compounds. Journal of applied physics, 2003. **93**(5): p. 2414-2417.
64. Pugh, S., XCII. Relations between the elastic moduli and the plastic properties of polycrystalline pure metals. The London, Edinburgh, and Dublin Philosophical Magazine and Journal of Science, 1954. **45**(367): p. 823-843.
65. Deligoz, E., et al., The first principles study on PtC compound. Materials Chemistry and Physics, 2008. **111**(1): p. 29-33.
66. Liu, L., et al., First-principles investigations on structure stability, elastic properties, anisotropy and Debye temperature of tetragonal LiFeAs and NaFeAs under pressure. Journal of Physics and Chemistry of Solids, 2017. **104**: p. 243-251.
67. Chen, C., et al., First-principles study of deformation-induced phase transformations in Ti–Al intermetallics. Journal of Materials Research, 2009. **24**(5): p. 1662-1666.
68. Ranganathan, S.I. and M. Ostoja-Starzewski, Universal elastic anisotropy index. Physical review letters, 2008. **101**(5): p. 055504.
69. Ozisik, H., K. Colakoglu, and E. Deligoz, First-principles study of structural and mechanical properties of AgB2 and AuB2 compounds under pressure. Computational Materials Science, 2012. **51**(1): p. 83-90.
70. Cabuk, S., The nonlinear optical susceptibility and electro-optic tensor of ferroelectrics: first-principle study. Central European Journal of Physics, 2012. **10**(1): p. 239-252.
71. Veithen, M., X. Gonze, and P. Ghosez, Nonlinear optical susceptibilities, Raman efficiencies, and electro-optic tensors from first-principles density functional perturbation theory. Physical review B, 2005. **71**(12): p. 125107.
72. Gonze, X., Perturbation expansion of variational principles at arbitrary order. Physical Review A, 1995. **52**(2): p. 1086.
73. Sipe, J. and E. Ghahramani, Nonlinear optical response of semiconductors in the independent-particle approximation. Physical review B, 1993. **48**(16): p. 11705.

74. Cabuk, S., Ab initio study of the linear and nonlinear optical responses in BiAlO3. Philosophical Magazine, 2016. **96**(2): p. 190-207.
75. Sanchez, F., Optique non-linéaire: cours et problèmes résolus1999: Ellipses.
76. Wemple, S. and M. DiDomenico, Applied Solid State Science. III, Academic Press, New York, 1972.
77. Vanderbilt, D. and R. King-Smith, Electric polarization as a bulk quantity and its relation to surface charge. Physical review B, 1993. **48**(7): p. 4442.
78. Resta, R., Macroscopic polarization in crystalline dielectrics: the geometric phase approach. Reviews of Modern Physics, 1994. **66**(3): p. 899.
79. Berry, M.V., Quantal phase factors accompanying adiabatic changes. Proceedings of the Royal Society of London. A. Mathematical and Physical Sciences, 1984. **392**(1802): p. 45-57.
80. Ortiz, G. and R.M. Martin, Macroscopic polarization as a geometric quantum phase: Many-body formulation. Physical review B, 1994. **49**(20): p. 14202.
81. Gonze, X., P. Ghosez, and R. Godby, Density-functional theory of polar insulators. Physical review letters, 1997. **78**(2): p. 294.
82. Resta, R., Density-polarization-functional theory and long-range correlation in dielectrics. Physical review letters, 1996. **77**(11): p. 2265.
83. Martin, R.M. and G. Ortiz, Functional theory of extended Coulomb systems. Physical review B, 1997. **56**(3): p. 1124.
84. Michel, L. and J. Zak, Physical equivalence of energy bands in solids. EPL (Europhysics Letters), 1992. **18**(3): p. 239.
85. Nunes, R. and D. Vanderbilt, Real-space approach to calculation of electric polarization and dielectric constants. Physical review letters, 1994. **73**(5): p. 712.
86. Dal Corso, A. and F. Mauri, Wannier and Bloch orbital computation of the nonlinear susceptibility. Physical review B, 1994. **50**(8): p. 5756.
87. Dal Corso, A., F. Mauri, and A. Rubio, Density-functional theory of the nonlinear optical susceptibility: Application to cubic semiconductors. Physical review B, 1996. **53**(23): p. 15638.

Results and discussions

In this part, we interpret and analyze the results of two compounds $RbLiCrO_4$ and $AgBi(CrO_4)_2$, each compound will be in a part independent.

Part A

Compound $RbLiCrO_4$

III. A. 1. Introduction

In recent years, due to the improvement of computational technologies, it has been proven that the first-principles calculation is a strong and useful tool to predict the crystal structure and properties related to the electron configuration of material before its synthesis.

The acentric oxide building blocks like (AX_4 = BeP_4, SO_4, CrO_4, PO_4)$^-$ have been contributing to the most widely used second-order SO NLO materials in inorganic crystals such as BaB_2O_4 (BBO), LiB_3O_5 (LBO), KH_2PO_4 (KDP), $KTiOPO_4$ (KTP), $LiNbO_3$ (LN), $ZnGeP_2$ and $AgGaSe_2$, [1-8]. The KTP crystal has a very high-frequency conversion efficiency, wide transmission range, high laser damage threshold (LDT), and excellent physical and chemical stability [9], but it suffered from susceptibility to photochromic damage, that is, grey-tracking, that causes the slow deterioration of light conversion efficiency, [10-12].

Promising SO NLO materials should have a non-centrosymmetric (NCS) space group, large NLO coefficients (strong second harmonic generation (SHG) intensity) large laser-induced damage thresholds (LIDTs), and high thermal stability. the current situations consider strong SHG response and high LDT value are the most important factors. Several aspects should be considered to obtain NCS structures. These criteria were summarized in several articles, [13-16].

The coordination of acentric ligands to cations favors the formation of NCS structures, among these ligands, we can mention the chromate ion $(CrO_4)^{2-}$, having a trigonal pyramidal and tetrahedral geometry which leads to materials crystallizing with acentric structures such as $RbLiCrO_4$, K $Tb(CrO4)_2$ and Ag $Bi(CrO_4)_2$, [17, 18].

In this part, we perform first-principles DFT calculations to investigate the electronic ground state properties of the polar chromate $RbLiCrO_4$, the framework of these structures are built up of 6 membered rings of vertex-connected CrO_4 and LiO_4 tetrahedra changing their orientations during phase transitions [19], due to the space group of $RbLiCrO_4$ is (P31c) belongs to the polar point group 3m [20], we calculate the nonlinear optical coefficients, electro-optic, and piezoelectric tensors according on the density functional perturbation theory (DFPT), [21, 22].

III.A.2 Calculation Method

Our calculations are based on the framework of density functional theory (DFT). We used two methods, the first is the all-electron full-potential linear augmented plane wave (FP-LAPW) in a computer code WIEN2k [23], having diverse approximations used as an exchange-correlation functional (U_{xc}). The geometrical structures are optimized within the generalized gradient approximation by Wu and Cohen (WC-GGA), [24]. The resulting relaxed geometrical structures are used to calculate the ground-state properties utilizing the recently modified Becke-Johnson potential (TB-mBJ) [25], which efficiently optimizes the other corresponding potentials, especially for the electronic, band structures calculations, and linear optical parameters. In the irreducible wedge of the corresponding first Brillouin zone, 162 k-points are considered which to the grids of 12 12 10. we selected the muffin-tin radii (RMTs) to be 1.8 a.u. for Rb, 1.5 a.u. for Li, 1.5 a.u. for the Cr, and 1.4 a.u. for O. We further expanded the corresponding potential plus the charge density in corresponding muffin-tin spheres (MT). we put cut-off parameters $K_{max}= 7/R_{mt}$ and l_{max} =6. The $RbLiCrO_4$ is with the electronic configurations as Rb ($4s^2$ $4p^6$ $5s^1$), Li ($1s^2 2s^1$), Cr ($4s^1$ $3d^5$) and O ($2s^2$ $2p^2$).

Second, we adopt norm-conserving pseudopotentials based on the local density approximation (LDA) as exchange-correlation potentials, we mainly used the ABINIT package. The calculations of the piezoelectric property are based on linear response functions, while the computations of nonlinear optical properties are based on nonlinear response functions. Most properties of solids depend much more on the valence electrons than on the core electrons. The wave functions are expanded up to a kinetic energy cutoff of 50 Hartree. Integrals over the Brillouin zone (BZ) are approximated by sums on a 10 10 6 Monkhorst–Pack mesh of special k-points, [26]. The second-order nonlinear optical susceptibilities and electro-optic coefficients are obtained within a nonlinear response formalism taking advantage of the $2n + 1$ theorem, [27, 28].

III.A.3. Ground state properties

III.A.3.1. Structural properties

$RbLiCrO_4$ material crystallize in an NSC trigonal symmetry space group, i.e. (P31c). The illustrated figure.III. A.1 give the crystal structure of the $RbLiCrO_4$ crystal.

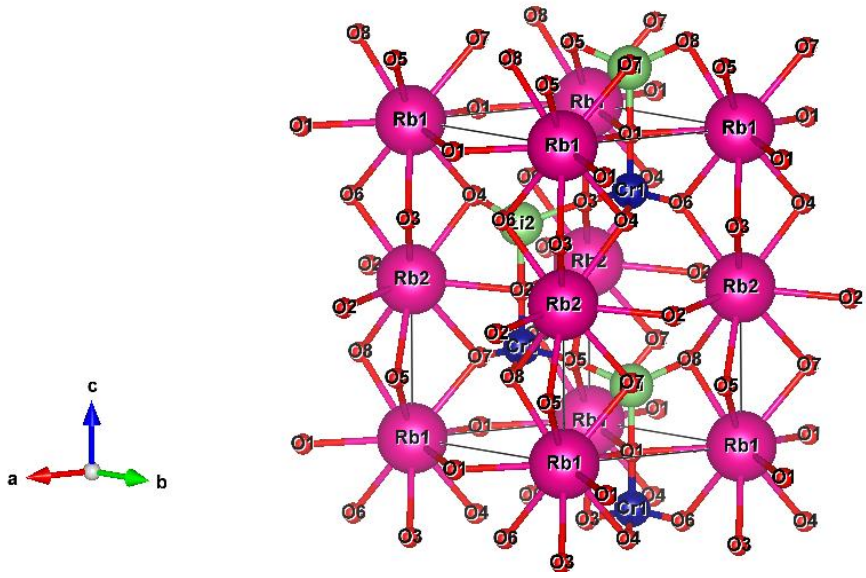

Figure. III.A. 1. Conventional Cell of $RbLiCrO_4$.

A great deal of computational effort is required to determine both the lattice parameters and the inner coordinates of all the atoms by ab initio calculations based on the DFT. In this present work, we have calculated the stable atomic structure concerning the inner coordinates of all the atoms in the unit cell, as well as the lattice parameters, atomic positions, and bond lengths.

Structural optimization for the P31c space group(a=b≠c) was performed in two steps. Firstly, the fully relaxed crystal structure was obtained to determine the unstrained structure with assumed lattice symmetry. Secondly, relaxation of atomic positions was carried by fixing the lattice parameters to experimentally obtained values by using the minimized forces which act on atoms.

In FP-LAPW, employing the (WC-GGA) approximation, we optimized the atomic positions using the minimized forces which act on atoms, we examined the energy-volume curve near the equilibrium volume, where we optimized the lattice constant ratio (a_0/c_0, V) and the atomic positions for several volumes.

In PP-PW, the structural properties were generated using LDA-PW approximation. Table.III.A.1 and table. III.A.2 displays the optimized crystal structural data and atomic positions; we analyzed the bond length in the table.III.A.3 for both methods, as compared to experimental.

Table. III.A. 1. Calculated and experimental lattice parameters of $RbLiCrO_4$

Parameter	Exp(Å) [29]	GGA-WC	ΔX /X	LDA-PW	ΔX /X
a(Å)	5.40212	5.40359	0.05%	5.05843	6.38 %
C(Å)	9.17530	9.25831	0.9%	8.77112	4 .4%

Table. III.A. 2. Calculated and experimental atomic positions of $RbLiCrO_4$.

Atoms	Exp. [29]	GGA-WC	LDA-PW
Rb	(0;0 ;0)	(0;0 ;0)	(0;0 ;0)
Li	(0.33333; 0.66667; 0.18240)	(0.33333; 0.66667; 0.18543)	(0.333; 0.6666; 0.190513)
Cr	(0.33333; 0.66667; 0.79510)	(0.33333; 0.66667; 0.79810)	(0.3333; 0.66667; 0.7939010)
O(1)	(0.33333; 0.66667; 0.97310)	(0.33333 ;0.66667; 0.97810)	(0.3333; 0.6666; 0.98393)
O(2)	(0.34900;0.38640; 0.73870)	(0.34900; 0.39648; 0.73865)	(0.3106; 0.3420283; 0 .73554)

Table. III.A. 3. Calculated and experimental bond length of $RbLiCrO_4$.

Binding length (Å)	Exp[29]	WC-GGA	ΔX /X	LDA-PW	ΔX /X
Cr-O (1)	1.633	1.647	0.8 %	1.608	1.53%
Cr-O (2)	1.642	1.643	0.06%	1.574	4.14%
Cr-Li	3.286	3.585	9.09%	3.397	3.37%
Li-O (1)	1.92	1,937	0.88%	1.7586	8.85%
Li-O (2)	1.946	1.947	0.05%	1.75061	10.07%
Rb-O (1)	3.128	3.129	0.03%	3.397	8.5%
Rb-O (1)	2.962	2.976	0.47%	2.885	2.59%

Our optimized structure parameters result as listed in the table. III.A.1, the optimized lattice parameters in the case of FP-LAPW yield a very good agreement compared to the experimental lattice parameters with an overestimate than the corresponding experimentally calculated results, which confirms the general (GGA) behavior which often overestimates the lattice parameters of solid materials. For PP-PW, our lattice parameters are lesser than the corresponding experimentally calculated results, which confirms the general (LDA) behavior that often underestimates the lattice parameters.

The results are listed in table III.A. 3, the agreement between the theoretical and experimental bond lengths was rather good, although small deviations existed because of the different lattice parameters and their coordinates.

This reliability and significant consistency in-between our computed structural parameters with corresponding experimental data verify the accuracy of our employed computational approach and provide a validation of the reliability of the calculated results for the electronic and optical properties.

III.A.3.2. Electronic structure

The chemical bond is one of among important factors that determine the geometrical structure of a solid and its focused study is necessary for understanding the electronic structure and its properties.

The electronic structure is comprised of the band structure, total and partial electronic state density, and charge-density distribution.

III.A.3.2.1 Band structure

The line of high symmetry points of P31c (N°159) in the Brillouin zone is illustrated in figure. III. A.2.

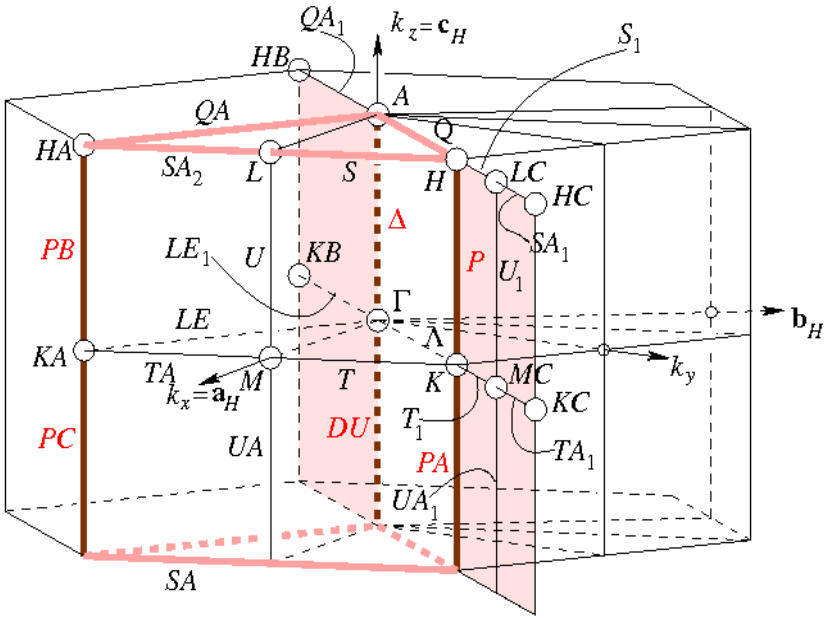

Figure. III.A. 2. The line of high symmetry points of P31c (159) in the Brillouin zone.

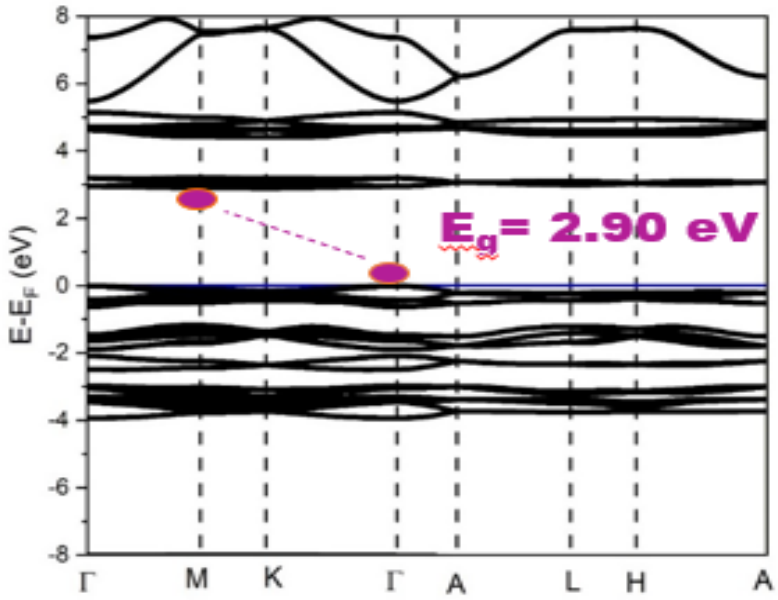

Figure. III.A. 3. Calculated band structure by (WC-GGA) for $RbLiCrO_4$.

Our calculated electronic band structure of $RbLiCrO_4$ is illustrated in the figure.A.III.3 by (WC-GGA) approximation, which is along the selected previous path. By the analyzed band structure of $RbLiCrO_4$ from the valence-band (which is at the top i.e., the maximum of HOVB which is the (highest occupied valence-bands) and the corresponding conduction-band bottom i.e., the minimum of LUCB which is the (lowest un-occupied conduction-bands, $RbLiCrO_4$ has an indirect band gap between the point Γ for the top of valance band and point M of the bottom for the conduction band with the energy value of 2.90 eV.

By using TB-mBJ potential our computed band gap value is opening than the WC-GGA approximation by 0.7 eV value with display indirect electronic transition from HOVB by the point Γ to the LUCB point M with the energy value of 3.60 eV is shown in the Figure.III. A.4. Because there is no experimental data available for the electronic structure of our study compound, from the successful of TB-mBJ potential we adopt it to investigate the others properties.

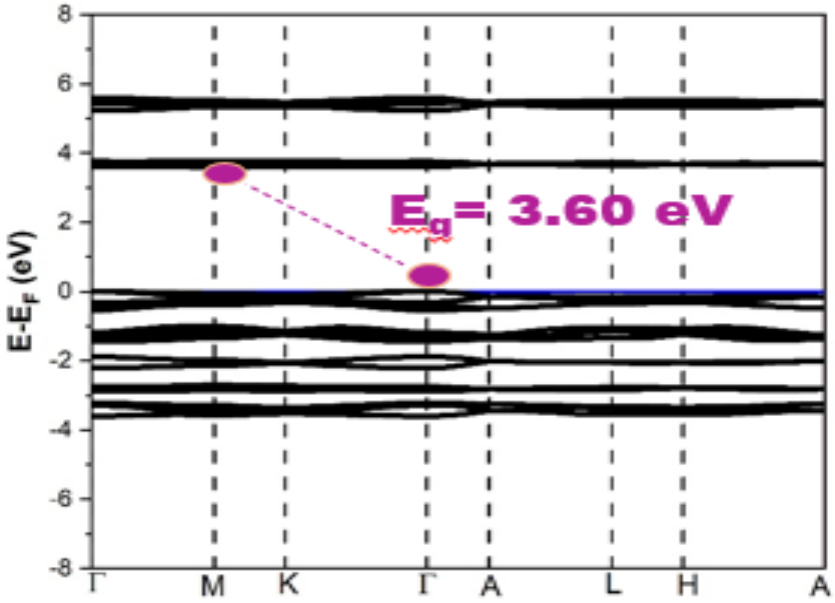

Figure. III.A. 4. Calculated band structure by (TB-mBJ) for $RbLiCrO_4$.

III.A.3.2.2 Density of states

For explain the contributions of various electronic states in the valence/conduction and to determine the characters' band of $RbLiCrO_4$ with further details, we calculated the total density of states i.e. (T-DOS), and the partial density of states which is (P-DOS), as presented in the figure.III. A.5. The non-centrosymmetric sublattices states occupying near the Fermi level have important contributions to SHG response. Where the major electronic states near the Fermi level are mainly consist from d state of the Chrome atom and p state of the Oxygen atom, with very little contributions of p states Rubidium and Lithium atoms. We can consider his small contributions as negligible state, so, we can say that the Chrome- Oxygen unit is the main source of second-harmonic generation response in $RbLiCrO_4$.

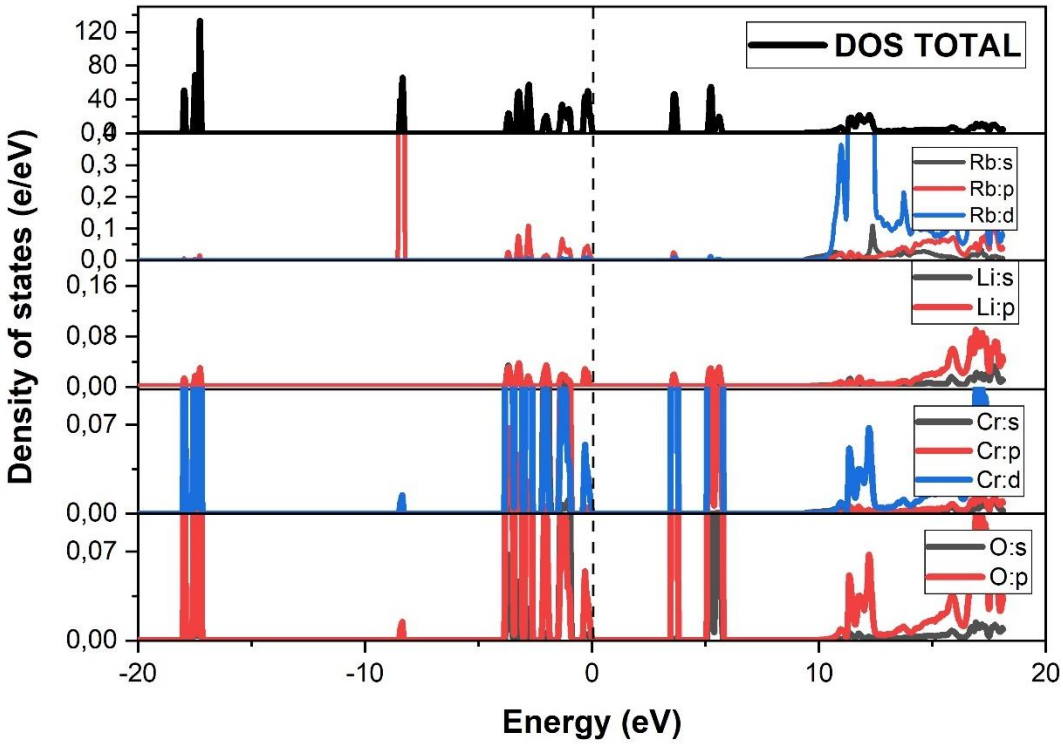

Figure. III.A. 5. Calculated total and partial DOS for $RbLiCrO_4$.

III.A.3.2.3. Charge-Density Distribution

For the calculated stable configuration, the valence charge distribution was calculated to clarify the character of the bond among atoms of $RbLiCrO_4$.

Figure.III.A.6 shows the distribution of the valence charge in the unit cell. The distribution is spherical around the Chrome or the Oxygen atoms, this situation can be described by the covalent character, the distributions is not spherical around the Lithium atom and the ligand (CrO_4), can be described by double characters band, while the charge distributions between the Rubidium atom and the ligand (CrO_4) indicating the character ionic between them.

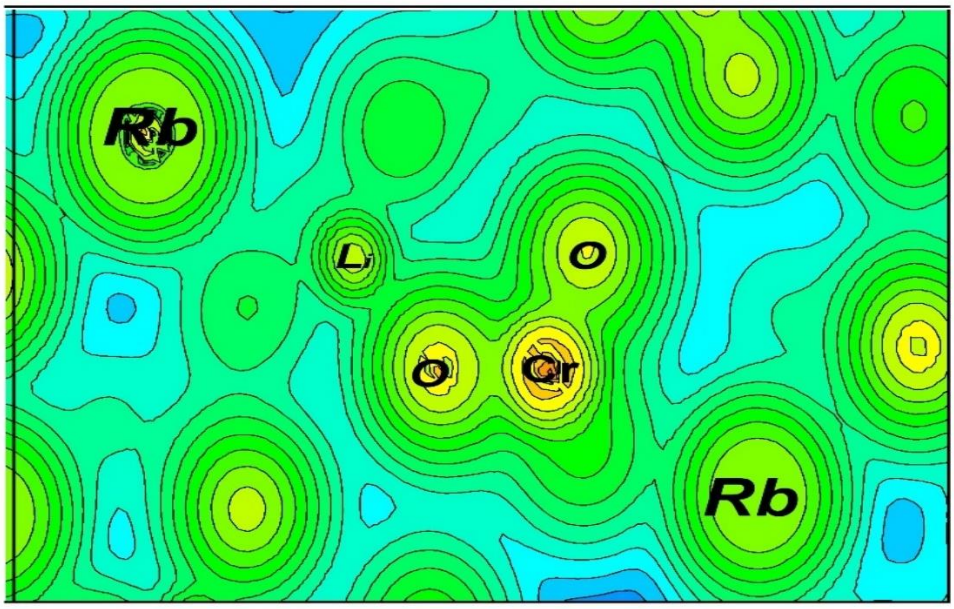

Figure. III.A. 6. Calculated density of charge in a plane containing Rb, Cr and O atoms.

III.A.3.3. Optical properties

The optical properties can provide more detailed information about the electronic structure of the materials. It is well-known that the optical properties are very sensitive to the energy band gap. Therefore, the accuracy of our results will be sensitive to the selection of the exchange-correlation functional and it can play a major role in the accuracy of our results, based on previous experiences with using TB-mBJ potential, we have used TB-mBJ potential to calculate the electronic band structures and hence the optical properties $RbLiCrO_4$[30, 31].

In this part, we investigated the optical response of $RbLiCrO_4$ in the energy range 0– 40 eV. A linear response of a material to electromagnetic radiation is described by calculating the real $\varepsilon_1(\omega)$ and imaginary $\varepsilon_2(\omega)$ parts of complex dielectric function $\varepsilon(\omega)$, (see chapter I). In the trigonal crystal structure, the optical spectra are anisotropic along the crystallographic a, and c axes are plotted in figure. III.A.7. So, according to the symmetry of the crystal, the dielectric tensor has only one dependent component ($\varepsilon_{xx}=\varepsilon_{yy}\neq\varepsilon_{zz}$).

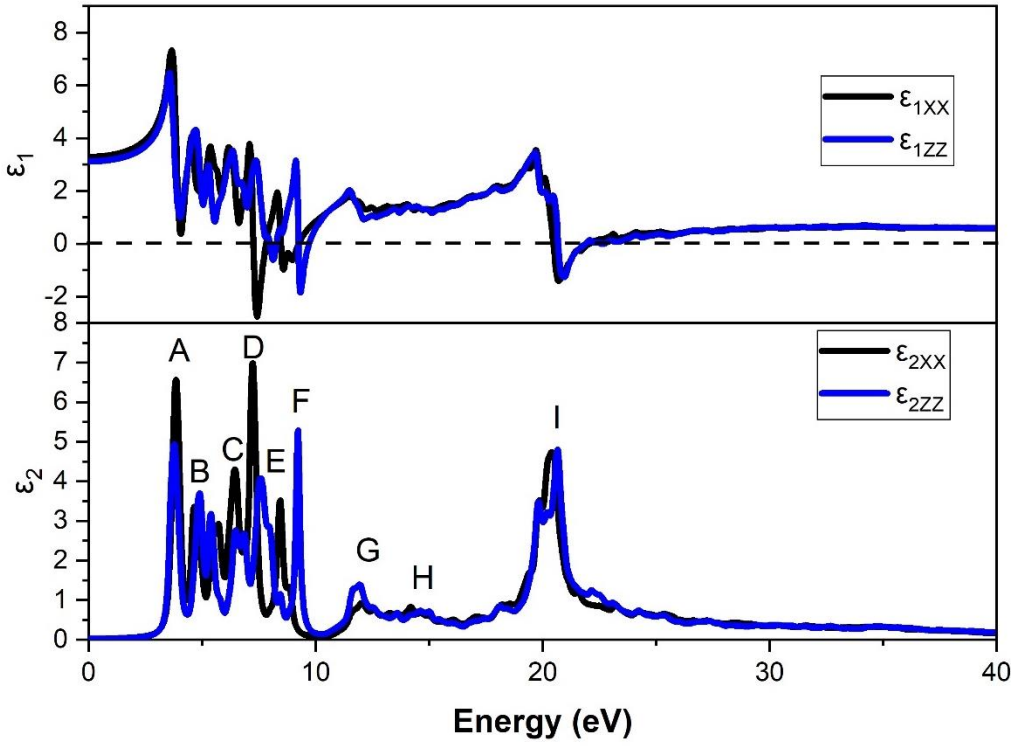

Figure. III.A. 7. Calculated imaginary $\varepsilon_2(\omega)$ and real $\varepsilon_1(\omega)$ parts of the dielectric function for $RbLiCrO_4$.

The $\varepsilon_2(\omega)$ in figure.III.A.7, is a display of the main 9 peaks (A, B, C, D, E, F, G, H, I) which are related to the interband transitions from the valence to the conduction band states, based on the TDOS (Figure .III.A.5) we can determine these transitions, which are given in the table. III. A.4, these transitions are including; plasmons and single-particle excitations, which are caused by the electric field of a photon which contributes to the second-order NLO properties.

Table. III.A. 4. Peak positions of the $\varepsilon_2(\omega)$ spectrum together with the dominant inter-band transition contributions to every peak for $RbLiCrO_4$.

Dominant inter-band transition contributions			
Peak position	**Energy(eV)**	**Valence band (VBs)**	**Conduction band (CBs)**
A	**3.86**	**d-Cr**	**p-O**
B	**4.77**	**d-Cr**	**p-O**

C	**6.39**	**s, p-Li, p-Cr, s-O**	**d-Cr, p-O**
D	**6.88**	**s, p-Li, p-Cr, s-O**	**d-Cr, p-O**
E	**8.42**	**p-Li, s, d-Cr,**	**d-Cr, p-O**
F	**9.23**	**s-Rb, S, p-Li**	**d-Cr, p-O**
G	**11.86**	**s-Rb, S, p-Li**	**d-Cr, p-O**
H	**14.39**	**s-Rb, S, p-Li**	**d-Cr, p-O**
I	**20.33**	**s, p-Li**	**s-Rb**

The real part $\varepsilon_1(\omega)$ provides information on the behavior of electromagnetic waves in the material according to crystallographic directions (figures.III.A.7.) which reflects the behavior isotropic in plus haut energy. when $\varepsilon_1(\omega)$ values become negative in some regions [7.15 to 9.78] eV and [20.31 to 22.44] eV this means that there is a total reflection of the incident electromagnetic waves. Those points that correspond to plasmon frequencies and the negative regions of $\varepsilon_1(\omega)$ be examined in figure.III.A.7. The $\varepsilon_{1xx}(\omega)$ and $\varepsilon_{1zz}(\omega)$ take zero values at the following photon energies (7.04;7.75;8.56;9.07;20.49;22.11)eV and (7.85;8.26;9.37;9.78;20.72;21.83) eV, respectively. The static dielectric constants, $\varepsilon_1(0)$, were calculated as 3.30 toward a and 2.95 toward c directions.

The other optical properties such as absorption coefficients I (ω), refractive index n (ω), energy loss function L (ω), and reflectivity R (ω) are plotted in the figure.III.A.8.

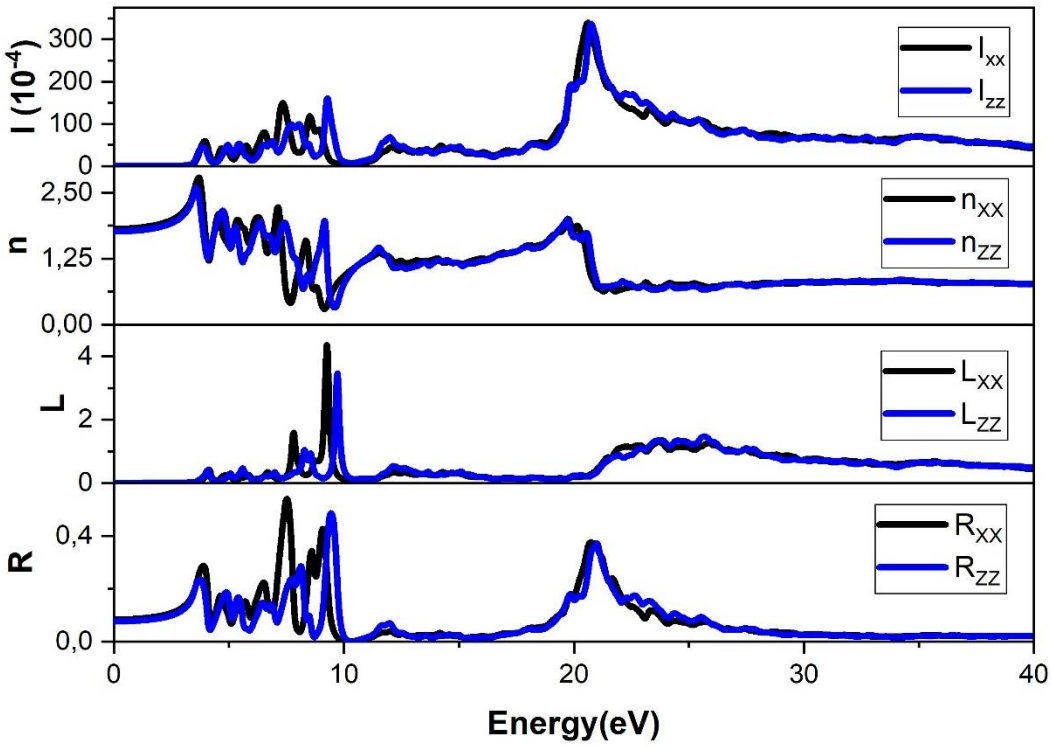

Figure. III.A. 8. Calculated optical properties: absorption coefficient I(ω) (10^{-4}/cm), reflectivity R(ω), electron energy loss function L(ω) and refractive index n(ω) as function of energy of the incident photon for $RbLiCrO_4$.

The absorption coefficient I(ω) show an gap at 3.61 eV, which is reflected in the transparency of our compound along with the Infrared (IR), Visible (Vis), and ultraviolet (UV). A substantially increased absorption occurs in VUV, UV-C region, while a steeper increase emerges in the EUV region.

It is known that the refractive index n(ω) can be obtained theoretically from the dielectric function (see chapter I). Furthermore, our calculated frequency dependent, refractive index n(ω) is in figure.III. A.8. The corresponding static values of the refractive index, n(ω) for $RbLiCrO_4$ that were observed are $n_{xx}(0) = 1{,}81176$ and $n_{zz}(0) = 1{,}71433$ respectively. For frequency doubling and generation of sum and difference frequencies, it is required that the incoming and generated lights are in a defined phase relation along the path of interaction. It is well known to phase matching. Birefringent phase matching Δn(ω) is a technique for achieving phase matching of a nonlinear process by exploiting the birefringence of a nonlinear crystal. Therefore, the birefringence properties of $LiRbCrO_4$ as nonlinear crystal ($n_e(n_{xx}(0)) > n_o(n_{zz}(0))$) make this compound potential candidate for these applications, [32] . The

calculated wavelength Birefringent index for $LiRbCrO_4$ crystals is shown in figure.III.A.9. As a phase matching crystal in order 0.047.

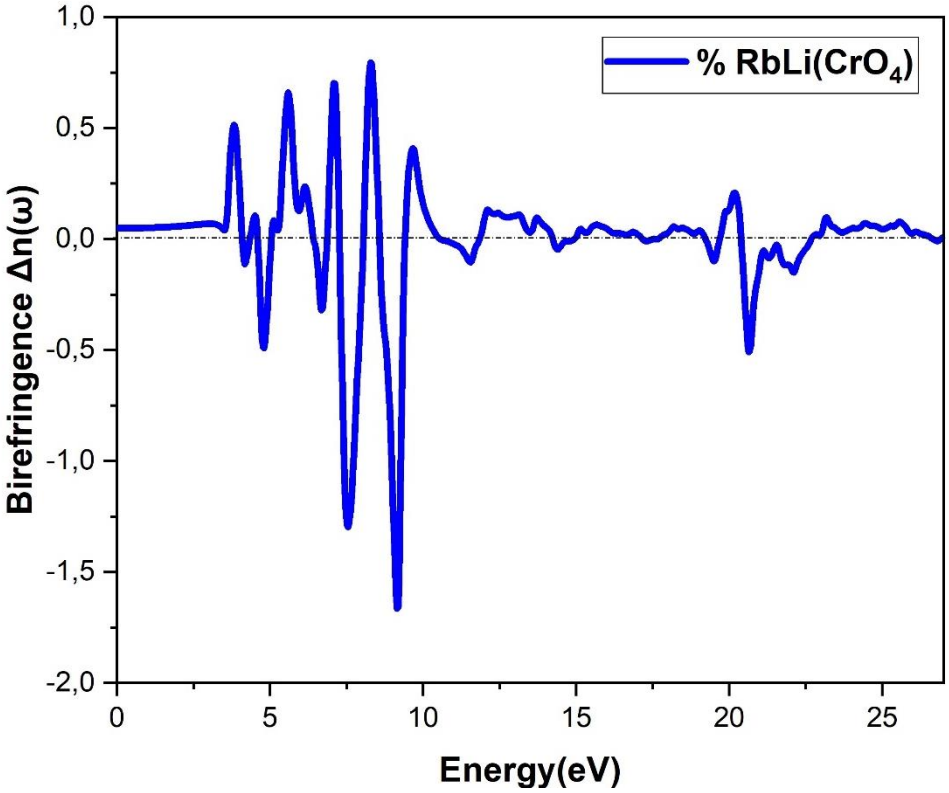

Figure.III.A. 9. Birefringence of $LiRbCrO_4$.

When the refractive index $n(\omega)$ of a material depends on the wavelength of light or photon frequency (photon energy), this dependence is called the dispersion (dn/dE) of the material. There are two types of dispersion: normal and anomalous. The region in which the frequencies range lies below resonance frequency ω_0 is called the normal dispersion region. In this region n increases with increasing frequency (increasing photon energy), dn/dE is positive. The anomalous dispersion region is that of the frequencies range lies that above ω_0. In this region n decreases with increasing frequency (increasing photon energy), dn/dE is negative[33, 34] which is clear from the figure.III.A.8, that the refractive index $n(\omega)$ increases with increasing photon energy at the range of photon energies lower than 3.64 eV (the energy gap of the material is 3.60 eV). This means that the $RbLiCrO_4$ has normal dispersion at this range of photon energies. The reverse behavior of $n(\omega)$ at the range of photon energies above 3.64 eV indicates the effect of fundamental absorption edge and the anomalous dispersion, [34]. These parameters are used to determine the propagation of light through the optical medium. In telecommunications, for example, the dispersion and its parameters are used to describe the processes which cause that the signal carried by the electromagnetic wave and propagating in an optical fiber to be degraded as a result of the dispersion phenomena. This degradation occurs

because the different components of radiation having different frequencies propagate with different velocities.

The essential optical parameter energy loss function i.e., L(ω), which tells and describe the energy lost by fast moving electrons, traversing in a material. From the shown figure. III. A.8, it is clear that $L_{xx}(\omega)$ and $L_{zz}(\omega)$are demonstrate one maximum peak which is at 9.27 eV, and 9.68 eV, respectively. These values are of L(ω) is related to plasma frequency $\hbar\omega_p$ and the phenomena is known to be plasma resonance, [35]. Beyond these observed high values the energy loss function, L(ω) declines rapidly, which is a correlation with maximum peak occurred in our reflectivity spectra and to the crossing zero of refractive index static value, and correspond to edges in the reflection spectrum R (ω) which presented in figure. III.A.8.

III.A.3.4. Mechanical and piezoelectric properties

To investigate the structural stability of $RbLiCrO_4$, we calculate the elastic constants by processing homogeneous strains as perturbations based on DFPT.

Elastic anisotropy of crystal results in different features of bonding in different directions.

The prediction of six non-zero elastic constants of this compound are C_{11}, C_{12}, C_{13}, C_{14}, C_{33}, and C_{44}. Additionally, it should be pointed out that $C_{66}= (C_{11}- C_{12})/2$, of the trigonal system (space group P31c), are presented in table. III.A. 5. There is no experimental or theoretical data on the elastic properties of $RbLiCrO_4$ for comparison.

In table.III.A.5, the point group of $RbLiCrO_4$ belongs to the triangle crystal. As mentioned in chapter II, the triangle crystal needs to satisfy the Born mechanical stability criterion. The results are presented in the table.A.III.5 reveals that the elastic constants of the $RbLiCrO_4$ satisfy the constraints of the Born stability condition. Therefore, the structure of $RbLiCrO_4$ is stable.

Table. III.A. 5. The calculated elastic constants C_{ij} (in GPa) for $RbLiCrO_4$.

Elastic Constants	C_{11}	C_{12}	C_{13}	C_{14}	C_{33}	C_{44}
$RbLiCrO_4$	**242.90876**	**83.11265**	**60.53233**	**23.08618**	**270.22082**	**58.72605**

We can estimate the elastic anisotropy using simple ratios of the elastic constants. As there is a difference between C_{11} and C_{33}, $RbLiCrO_4$ will show anisotropy in its elastic properties, while the comparative values of C_{12} and C_{13} indicate the ductile nature of $RbLiCrO_4$.

Voigt -Reuss -Hill presented the well-known way to quantify mechanical behavior of crystals,

based on the predicted C_{ij}'s Calculated elastic modulus are listed in the table. III.A. 6; Bulk modulus B(GPa), Shear modulus G(GPa), Young's modulus E(GPa), Poisson's ratio **ν** are computed as to equations in chapter II.

Table. III. A. 6. Bulk modulus B (GPa), shear modulus G (GPa), Young's modulus E (GPa), Poisson's ratio ν and B/G ratios for $RbLiCrO_4$.

Modulus	B_V	B_R	B	G_V	G_R	G	E	ν	B /G
$RbLiCrO_4$	**129.38**	**129.37**	**129.37**	**72.797**	**61.314**	**67.055**	**171.53**	**0.28**	**1.92**

The $RbLiCrO_4$ has a comparatively low shear modulus, which is indicative of its low coefficient of friction and good machinability. The ratio of the bulk modulus B to shear elastic constant C_{44} is used to measure the plasticity, [36] . The values of ($C_{11} – C_{12}$) and young's modulus E can also estimate the plasticity of materials [37]. $RbLiCrO_4$ has better plasticity due to its smaller values of ($C_{11} – C_{12}$) and E. The Pugh's criterion B /G and the Frantsevich rule ν which are justified the ductile nature of $RbLiCrO_4$.

III.3.4.1. Debye temperature

The Θ_D calculated from elastic constants using the Voigt -Reuss -Hill approximation method is calculated from the single-crystal elastic constants, which is proportioned to the studied v_m (the average sound velocity), v_l (the longitudinal sound velocity), and v_t (transverse elastic wave velocity) are given in chapter II.

Table. III. A. 7. Transverse (v_t in m/s), Longitudinal (v_l in m/s), mean sound velocity (v_m in m/s) and Debye temperature (Θ_D in K) for $RbLiCrO_4$.

	v_t	v_l	v_m	Θ_D
$RbLiCrO_4$	**5203.66**	**2647.7**	**2967.1**	**444.8**

From table.A.III.7. $RbLiCrO_4$ has the Debye temperature (444.8K).

III.A.3.4.2. Anisotropic factors

There are a variety of methods to characterize the anisotropy of a crystal structure, for instance, the universal elastic anisotropy index A^U, the percent bulk and shear modulus factors (A_B and A_G). (See chapter II). These all factors are listed in table. III. A.8.

Table. III. A. 8. Universal anisotropy factor (A^U), percentage of bulk module (A_B) and shear modulus (A_G) anisotropy factors for $RbLiCrO_4$.

Anisotropy	A^U	A_B (%)	A_G (%)
$RbLiCrO_4$	**0.93**	**0**	**0.08**

From table.A.III.8. A^U is 0.93, this value deviates from 0, indicating the relatively elastic anisotropy characteristic of $RbLiCrO_4$.In addition, the percent of A_B factor is 0, meaning that compressibility is isotropic unlike the percent of A_G factor is 0.08 which reflect the small anisotropic of resistance from shear stress.

For better visualization of the anisotropy of young module E and bulk module B, the anisotropy of the two molds in 2D and 3D was plotted by the relationships as mentioned in chapter II.

We have studied the bulk module for all directions, the 2D and 3D representation of shear modulus in the xy, xz, and yz planes for $RbLiCrO_4$ is shown in the figure. III.A.10. From figure. III.A. 10, the 2D and 3D directional dependence are exhibit a spherical shape and circular shape, respectively, which reflects an isotropic material.

The 2D and 3D directional dependences of the young module at different planes for $RbLiCrO_4$ are plotted in figure. III. A.11. From figure. III.A. 11 we can see that the 2D and 3D figures of the young module for $RbLiCrO_4$ have more deviation in circular shape and sphere shape, which indicates that the young module shows strong anisotropic for different planes.

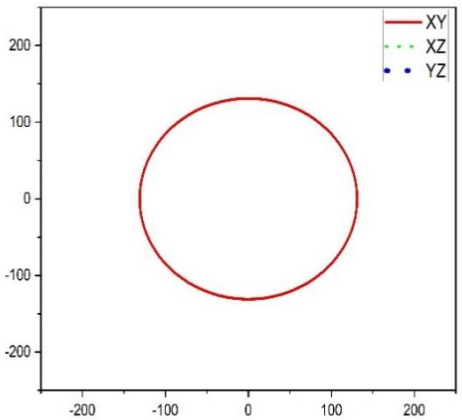

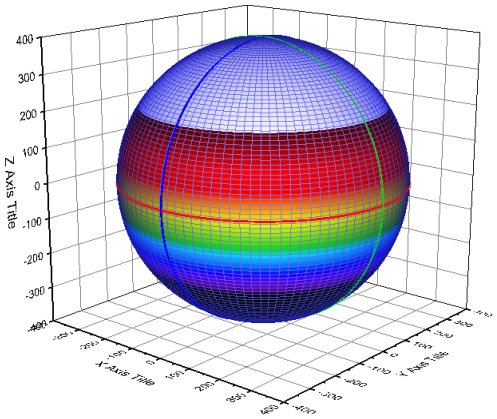

Figure. III.A. 10. The 2D projection of bulk moduli and your 3D projection of $RbLiCrO_4$.

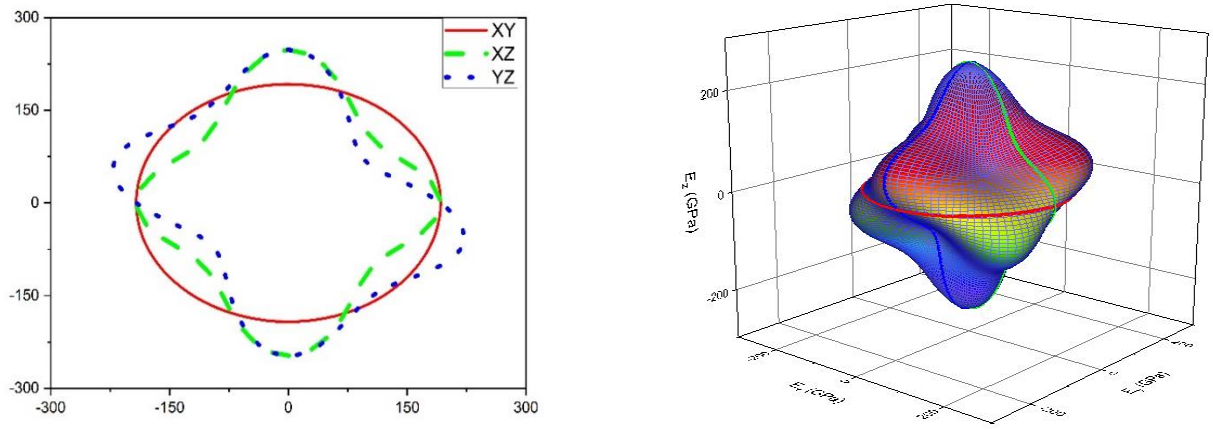

Figure. III.A. 11. The 2D projection of Young and your 3D projection of $RbLiCrO_4$.

III.A.3.4.3. Piezoelectric property

To investigate the piezoelectric properties of $RbLiCrO_4$, we calculate the piezoelectric constants by treating homogeneous strains as perturbations based on DFPT. Our compound under 31m group point to the triangle crystal. According to Voigt notations (see chapter II), The obtained piezoelectric tensor of $RbLiCrO_4$ has four independent elements; d_{15}, d_{22}, d_{31}, d_{33} are resumed in the table .A.III.9.

Table. A. III. 9. Relaxed ion piezoelectric tensor d_{ij} in (pC/N) for $RbLiCrO_4$

	d_{15}	**d_{22}**	**d_{31}**	**d_{33}**
$LiRbCrO_4$	**22.24**	**0.014**	**-1.68**	**3.20**

From table A.III.9, we see that; $RbLiCrO_4$ shows the value of the largest component d_{15} among the others, which is about nine times larger than that of a-quartz d_{11}(-2.3 pC/N). The large value of d_{15} means that; the polarization along the direction (001) is easily affected by external stress. The large piezoelectric constants reveal that $RbLiCrO_4$ is a promising candidate piezoelectric material.

III.A.3.5. Nonlinear optical properties

III.A.3.5.1. nonlinear optical susceptibilities

The $RbLiCrO_4$ belongs to the 31m point group, therefore it has second-order susceptibility $\chi^{(2)}$ is double the SHG coefficient d_{ij}. First of all, we note that the equations for SHG consist of a number of resonant terms. In this sense the imaginary part, $\mathrm{Im}X_{ijk}^{(2)}(-2\omega,\omega,\omega)$ (equation II.110) resembles $\varepsilon_2(\omega)$ and provides a link to the band structure. The difference, however, is that whereas in $\varepsilon_2(\omega)$only the absolute value of the matrix elements squared enters, the matrix elements entering the various terms in $\mathrm{Im}X_{ijk}^{(2)}(\omega)$ are more varied. they are in general complex and can have any sign. Thus, $\mathrm{Im}X_{ijk}^{(2)}(\omega)$ can be both positive and negative. Secondly, both resonances appear when 2ω equals an interband energy and when ω equals an interband energy. Third, we note that the 2ω resonances occur at half the frequency corresponding to the interband transition. Thus, the incoming light need not be as high in the ultraviolet (UV) to detect this higher lying interband transition.

This is important for wide band gap material like $RbLiCrO_4$ compound where laser light sources reaching the higher interband transitions are not available. Nevertheless, one still need to be able to detect the corresponding 2ω signal in the UV. That is attributed to the fact that the second harmonic response $\mathrm{Im}X_{ijk}^{(2)}(\omega)$ contains the 2ω resonance along with the usual ω resonance. The structure in $\mathrm{Im}X_{ijk}^{(2)}(\omega)$ can be understood from the structures in $\varepsilon_2(\omega)$ .Unfortunately, the intrinsic richness of the $\mathrm{Im}X_{ijk}^{(2)}(\omega)$ spectra remains largely to be explored experimentally.

By using electric fields and atomic displacements as perturbations based on DFPT. According to the Kleiman symmetry relation[38, 39], there is only four independent SHG coefficients are given in table.III.A.10. The calculated results show that the three independent elements of the NLO tensor of this compound are d_{31}, d_{22}, and d_{33} (Voigt notations). If we compared our result for referential available results materials NLO such as KDP (d_{33}=0.39 pm/V) and KTP (d_{3l} = 6.5 d_{32} =5.0, d_{33}= 13.7, d_{24}= 7.6, d_{15}= 6.1) we can present $RbLiCrO_4$ as larger than KDP and lesser than KTP component in nonlinear optical magnitude.

Table. A. III. 10. Static nonlinear optical coefficients dij (pm /V) for $RbLiCrO_4$.

	d_{31}	d_{22}	d_{33}
$RbLiCrO_4$	**-1.621**	**2.272**	**4.51**

The real response for each material corresponds to their d_{eff}, which depends on the anisotropy, optical axis, crystal orientation, phase matching types ...etc. For this crystal class (31m), the d_{eff} is directly related to d_{31} and d_{22}, for all different possible phase matching types. the d_{eff} possible values, depending on crystal rotation and phase matching type by the following relations;

$$\mathbf{d_{eff} = d_{31}\sin\theta - d_{15}\cos\theta\sin 3\phi}$$

$$\mathbf{d_{eff} = d_{22}\cos^2\theta\cos 3\phi - d_{15}\cos\theta\sin 3\phi}$$

The direction of the wave vector is specified by spherical coordinates ($\boldsymbol{\theta}$, $\boldsymbol{\phi}$) referenced to the crystalline axes; $\boldsymbol{\rho}$is the birefringent walk-off angle.

III.A.3.5.2 Electro-optic tensor

As we obtained the second-order nonlinear optical susceptibility, all the elements that are needed to calculate the EO tensor, which describes the dependence of the optical dielectric tensor on the static (or low-frequency) electric field, are available. With the same procedure as second-order nonlinear optical susceptibility (see chapter II).For ease of comparison, the EO coefficients of $RbLiCrO_4$, total and electronic contribution is also listed in the table. A .III.11. Our obtained EO coefficients are r_{11}, r_{13}, r_{33}, and r_{51}.

The large NLO susceptibilities and EO coefficients reveal that the $RbLiCrO_4$ is a high-performance nonlinear optical crystal. Moreover, the electronic contributions are found to be small.

Table .A. III. 11. linear electro-optic (EO) r_{ij} (Pm / V) for $RbLiCrO_4$.

	r_{11}	r_{13}	r_{51}	r_{33}
Electronic contribution	**1.106**	**0.789**	**0.789**	**-1.995**
Total contribution	**-3.70**	**-0.886**	**-0.886**	**-2.170**

III.A.4. Conclusion

In summary, we perform first-principles DFT calculations to investigate systematically the lattice dynamics, electronic structure, dielectric, linear optical, and piezoelectric properties of the polar chromate $RbLiCrO_4$ owing the space group of $RbLiCrO_4$ (P31c) belongs to the polar point group 3m. The theoretical results of lattice dynamics, atomic position, and binding length by both methods FP-LAPW and PP-PW are compared to the available experimental data and a good agreement is found.

In the FP-LAPW method the electronic properties were investigated by TB-mBJ potential which was that improve them significantly for the opening of the band gap than the GGA-WC approximation (2.9 eV). It's exhibited an electronic indirect band gap (3.6eV). The calculations of the dielectric spectra ε(ω) in the energy range 0–40 eV. Therefore, from calculated absorption spectra I(ω) the large band gap 3.61 eV, is reflected in the transparency of Rb Li CrO4 along with the Infrared (IR), Visible (Vis), and ultraviolet (UV). The birefringence of RbLi(CrO4) (Δn=0.047). The loos spectra L(ω) have a few main peaks, which are related to excitation (VBs to BCs). The energy of the maximum of L(ω) (9.47 eV) is related to the energy of volume plasmon $\hbar\omega_p$.

In the PP-PW method, the computed elastic constant indicates that the compound is mechanically stable according to the elastic stability criteria. We have calculated the bulk moduli, shear moduli, Young moduli, Poisson ratio, Debye temperature, and anisotropy value from the obtained elastic constants according to the Voight-Reuss-Hill approximation. Our compound possesses ductile nature with respect to the B/G criterion and Poisson's ratio. Additionally, the calculated young have suggested that this compound is a potential hard material and has strong bonds. The obtained Debye temperature value for $RbLiCrO_4$ indicates, relatively, thermal conductivity and confirms the strength of chemical bonding in the crystal structure. Furthermore, the elastic anisotropy has been visualized in detail by plotting the directional 2D and 3D dependences of bulk and Young's moduli.

A large SHG coefficients d_{31}= -1.621 pm/V, d_{22}=2.272 pm/V, and d_{33}=4.51 pm/V than KDP (0.39 pm/V) [84] and KTP (d_{3l} = 6.5, d_{32} =5.0, d_{33}= 13.7, d_{24}= 7.6, d_{15}= 6.1) and high electro-optic coefficients which has a great potential as a candidate material for the (IR), (Vis), and (UV) regions.

One the other hand, Rb Li CrO_4 exhibit higher piezoelectric coefficients d_{15}, d_{22}, d_{31}, d_{33} are 22.24 pC/N,0.014pC/N, -1.68pC/N,3.20 pC/N which in comparison with quartz (d_{14} = 0.727 pC/N, d_{11} = 2.310 pC/N) promising candidate for piezoelectric applications.

Part B

Compound $AgBi(CrO_4)_2$

III.B.1. Introduction

The Non-centrosymmetric (NCS) polar crystals display the main part of natural minerals and are considered the main basis for Modern fundamental material science owing to their multi-functionally applications such as second-order nonlinear optics (NLO) piezoelectric (PO), electro-optic(EO) and optoelectronics, [40-47]. However, these crystals' high performance (NLO) in the mid-infrared region has of great attention due to their application in field remote sensing, telecommunication, laser guidance, and medical diagnostics, [48-52].

A good mid-IR NLO crystal must dictate the following requirements for second-harmonic-generation (SHG) applications; large NLO coefficient, the high value of laser damage threshold (LDT) that correspond to band gap value, transparency in the requited region, moderate birefringence to allow phase matching, thermal and mechanical stability. To obtain the last features, firstly must provide inherently NSC molecules, so some feasible strategies were proposed including; (i) Compounds containing (n-1)$d^{10}ns^{0}$ transition-metal cations are important candidates for polar crystals(Ag^{+}, Cu^{+}, Zn^{2+}, Cd^{2+}, et al) has a polar displacement of d^{10} cation center (ii) Compounds containing ns2 main-group metal cations (Pb^{2+}, Sn^{2+}, Bi^{3+}, I^{+5}, Se^{4+}, Te^{4+}, et al) could be subjected to the second-order Jahn-Teller (SOJT) effect caused by lone-pair electrons [14, 53, 54]. (iii) (iii) The $[MO4]^{-n}$tetrahedron is acentric building block such as [PO4],[CrO4],[IO4]… [55-57]. (iv) polar chalcogenide groups ($[TeS3]^{2-}$, $[AsS3]^{3-}$, $[SbS3]^{3-}$, etc), [58].To achieve functional crystals with strong NLO effects can combine two or more types of NLO-active and be further stacked in an additive model to afford structural building units, [59-61].

These mid-IR NLO crystals can be classified into three categories according to their compositions: (1) IR NLO chalcogenide, such as $AgGaS_2$ [62] $AgGaSe_2$ [63],ZGP [6] etc; possess very large SHG responses but relatively low LDTs. (2) IR NLO oxides including KTiOPO4,[2] LiNbO3 [2] etc; normally possess large LDTs and NLO responses but narrow IR transparency (usually < 6 μm). (3) IR NLO iodates comprising XIO_3 (X = Li,[64] Rb,[64, 65] Cs [66]), NaI_3O_8,[67] etc, iodates usually have wide transparent range (0.4–12 μm) in the IR region. Despite metal oxide NLO crystals have been developed for ultraviolet, visible and near-infrared regions ,but rarely to found excellent mid-IR NLO crystals. [61]

Double bismuth-argent chromate Ag Bi $(CrO_4)_2$ crystalize in the tetragonal space group of $I\bar{4}$ belonging to the polar point group $\bar{4}$, he exhibits two types of polyhedra $[AgO_8]$ and $[BiO_8]$, each one consisting from dodecahedron $[AgO_8]$ shares four others with four different

dodecahedra [BiO_8] and vice versa; each of the vertices of the dodecahedron [AgO_8] or [BiO_8] is in common with a chromate tetrahedron [CrO_4]. On the other hand, each oxygenate belonging to a chromate group is also bonded to a silver atom and a bismuth atom, [18].

This part is devoted to the theoretical investigation of the linear and nonlinear optical (NLO) properties, The experimental data show that this compound is not only promising in the field of nonlinear optical (NLO) through building structural but also as a potential candidate for electrochemical with carried at the empirical level , [68]. Our theoretical investigation is extended to the determination of information about the electronic, linear optical, elastic, piezoelectric, electro-optic coefficient, and nonlinear optical (NLO) properties of Ag Bi $(CrO_4)_2$ by using a first-principles calculation based on the density functional theory (DFT) that nowadays has become a powerful tool for predicting accurately the properties of materials.

III.B.2. Calculation Method

In this work, we adapt our calculation within the framework of density functional theory (DFT) by using different methods. At first, we have used the full-potential linearized augmented plane wave method (FP-LAPW) [69] implemented in WIEN2K code[70] , because this method treated very accurately the core of the electron, [71]. The generalized gradient approximation (GGA) by Wu and Cohen (GGA-WC) [24] is adopted for the electron exchange and correlation (U_{XC})for calculation of lattice dynamical . In order to obtain more accurately the band gap (Eg) , we adopting the Tran and Blaha modified Becke-Johnson potential (TB-mBJ) [72-74] into properties like electronic and linear optical .The last proprieties of Ag Bi$(CrO_4)_2$ were studied with use the values of R_{mt} were taken as 2, 2,1.6 and 1.4 Ag, Bi, Cr and O respectively. The valence electrons in electronic configuration are as follows; Ag: $5s^1\ 4d^{10}$, Bi: $6s^2\ 6p^3$, Cr $4s^1\ 3d^5$, and O :$2s^2\ 2p^4$. The plane wave cut-off for the basis function was set to R_{Kmax} 7.0 and for the irreducible Brillouin Zone (BZ) the integration was use on the grid of 379 (12 12 27) k points.

The calculations of elastic and piezoelectric (PO) properties are based on linear response functions, while the second-order nonlinear optical (NLO) and electro-optic (EO) tensor are based on nonlinear response. The linear and nonlinear response are calculated within the framework of modern theory of polarization and DFPT. We use the local density Perdew–Wang92 functional approximation (LDA-PW) [75, 76] as the exchange correlation potential implemented on ABINIT code. A 6 × 6 × 6 Monkhorst-Pack k-point mesh is used with a plane wave cut-off of 30 hartrees. The elastic constants we can obtained from the second derivatives of the total energy versus strain , while the other quantities mentioned above are related to

spontaneous polarization which it calculated by using a Berry-phase approach, [77]. The nonlinear optical and electro-optic (EO) tensors, are calculated based on (2n+1) theorem [78] which is present the computation of third-order energy by Taylor expansion can be obtained the electric polarization [78] for calculated the derivatives of the total energy versus to electric fields and strains with is the piezoelectric tensor [78] which are implemented systematically in ABINIT code.

III.B.3. Ground state properties

III.B.3.1 Structural properties

Structural properties are the first fundamental step to predicting other properties of the studied material. Therefore, their good determination led to afford accurate information's. so After the fixing of computation parameters, considering the experimental lattice as starting point, we have determined the cell parameters after relaxation of the atomic positions to minimize the Hellmann-Feynman forces exerted on each atom, [79]. The lattice parameters and atomic positions calculated are listed in the table. III.B. 1 and 2, respectively where they are compared to the experimental data. The Ag Bi $(CrO_4)_2$ compound investigated has a tetragonal structure of space group $I\bar{4}$ (No. 82), the crystal structure is shown in figure. III. B.1.

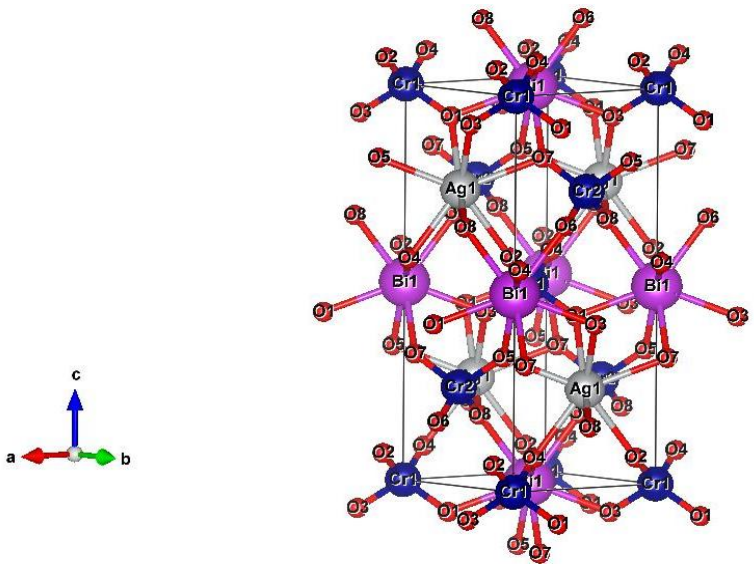

Figure. III.B. 12. Conventional cell of Ag Bi $(CrO_4)_2$.

In the FP-LAPW method, we needed optimization many cycles (volume and c/a) to reach the optimal structure by using GGA-WC approximation, we can observe that their GGA-WC is overestimate the lattice parameters with is agree with the trend of the GGA for the

structural parameters,[80]. In the PP-PW method by using LDA-PW approximation after we have optimized and relaxation of the atoms to annul Hellmann-Feynman forces in the structure as a prerequisite, our results exhibit an underestimate of the lattice parameters is close to experimental data which is an agreement of trend general of LDA-PW approximation, [79]. In general, our results show a very good arrangement with experimental data.

Table. III.B. 12. Calculated and experimental lattice parameters of $AgBi(CrO_4)_2$.

Parameter	Exp [18]	GGA-WC	ΔX /X	LDA-PW	ΔX /X
a (Å)	**5.0978**	**5.0987**	**0.01%**	**5.0067**	**1.79%**
c (Å)	**11.6514**	**11.6554**	**0.03%**	**11.2586**	**3.37%**

Table. III.B. 13. Calculated and experimental atomic positions of $AgBi(CrO_4)_2$.

atoms	Exp [18]	GGA-WC	LDA-PW
Ag	**(0; 0.5; 0.75)**	**(0; 0.5; 0.75)**	**(0; 0.5; 0.75)**
Bi	**(0.5; 0.5 ;0)**	**(0.5; 0.5; 0)**	**(0,5; 0,5; 0)**
Cr (1)	**(0; 0; 0)**	**(0; 0; 0)**	**(0; 0; 0)**
Cr (2)	**(0.5; 0; 0.75)**	**(0.5; 0; 0.75)**	**(0.5; 0; 0.75)**
O (1)	**(0.86939;0.24338;0.92352)**	**(0.86949; 0.24438.92362)**	**(0.93573; 0.32803; 0.84295)**
O (2)	**(0.24338;0.13061;0.07648)**	**(0.23061;0.15662;0.09235)**	**(0.22131; 0.8290070.84295)**
O (3)	**(0.13061;0.75662;0.92352)**	**(0.13062;0.75672;0.92452)**	**(0.17099;0.64268;0.841475)**

O (4)	**(0.75662;0.86939;0.07648)**	**(0.75662;0.86929;0.07658)**	**(0.79984;0.92074; 0.06676)**
O (5)	**(0.37694;0.24126;0.82938)**	**(0.37695;0.24426;0.82968)**	**(0.35731; 0.28039 ;0.84295)**
O (6)	**(0.24126;0.62306;0.17062)**	**(0.24326;0.62326;0.17162)**	**(0.20015;0.58838;0.13235)**
O (7)	**(0.62306;0.75874;0.82938)**	**(0.62336;0.75974;0.82968)**	**(0.79984; 0.72074;0.86764)**
O (8)	**(0.75874;0.37694;0.17062)**	**(0.75974;0.37994;0.17362)**	**(0.73251; 0.41161; 0.16764)**

As well as bond length Which is show excellent agreement between the experimentally [18] data and results of our calculation for $AgBi(CrO_4)_2$ compound are summered in the table.III.B.4.This level of agreement is important to validate our comparisons between resultants structures and experimental structures.

Table. III.B. 14. Calculated and experimental bond length of $AgBi(CrO_4)_2$.

Bond length (Å)	Exp [18]	GGA-PBE	ΔX /X	LDA-PW	ΔX /X
Cr (1)-O	**1,686**	**1.663**	**1.36 %**	**1.819**	**7.88 %**
Cr (2)-O	**1,647**	**1.661**	**0.85 %**	**1.816**	**10.26 %**
Ag-O	**2,526**	**2.49**	**1.42 %**	**2.485**	**1.62%**
Bi-O	**2,467**	**2.45**	**0.68 %**	**2.49**	**0.93 %**

III.B.3.2. Electronic structure

III.B.3.2.1. Band structure

The chemical bond is one of among important factors that determine the geometrical structure of a solid and its focused study is necessary for understanding the electronic structure and its properties.

The line of high symmetry points of $I\bar{4}$ (82) in the Brillouin zone is illustrated in figure. III.B.2.

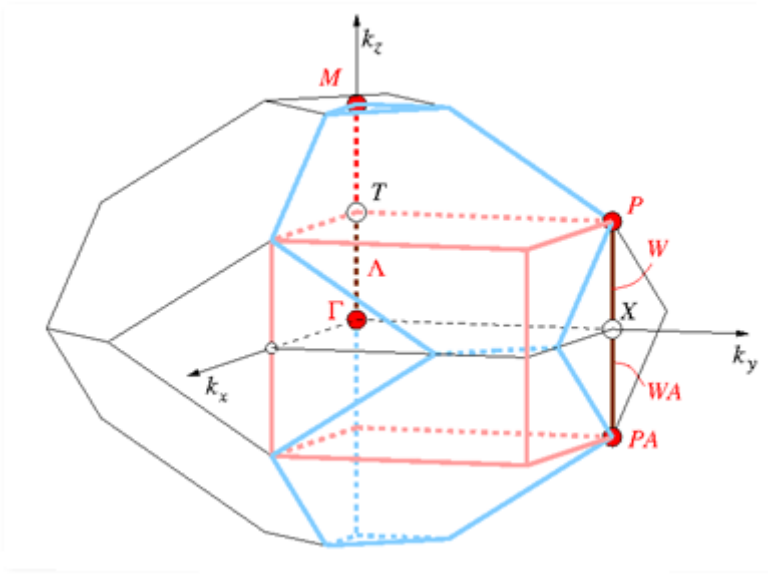

Figure. III.B. 2. The line of high symmetry points of $I\bar{4}$ (82) in the Brillouin zone.

In this section, we provide a study of the electronic structure by the computed electronic energy band dispersion along the selected high-symmetry lines within the BZ using the GGA-WC and TB-mBJ are depicted in figure. III. B.3 and 4, respectively. The GGA-WC show no band gap, while TB-mBJ show the AgBi $(CrO_4)_2$ has an indirect band gap semiconductor, where the valence band maximum is located at the Γ point while the conduction band minimum is located at the N point which ranges from 1.38 eV.

The experimental band gap for $AgBi(CrO_4)_2$ is not yet available, we adopt the TB-mBJ potential to investigate the other properties .

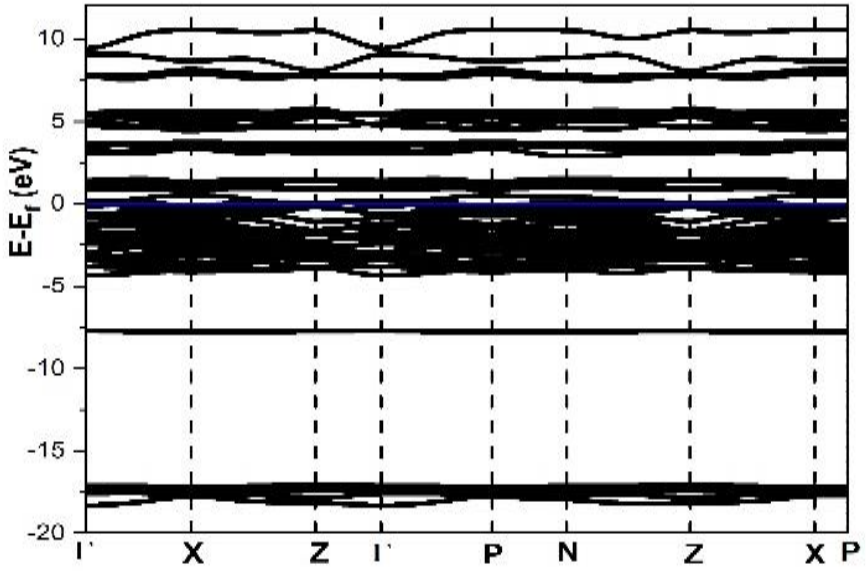

Figure. III.B.3. Calculated band structure of $AgBi(CrO_4)_2$ using WC-GGA.

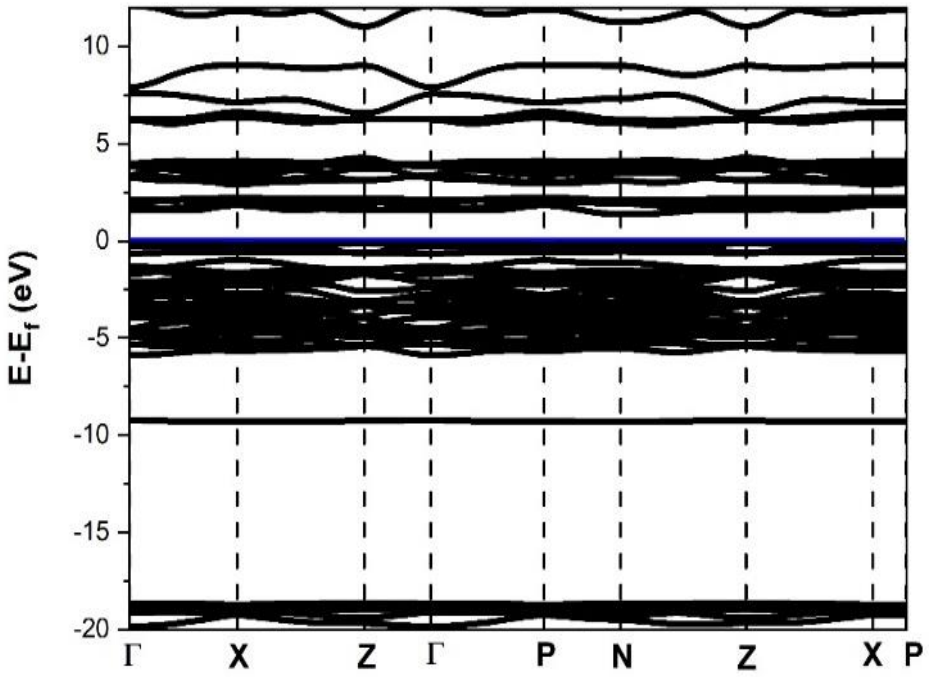

Figure. III.B. 4. Calculated band structure for $AgBi(CrO_4)_2$ using TB-mBJ.

III.B.3.2.2. Density of states

Figure. III.B.5. shows the total and partial density of states (DOSs) of Ag Bi $(CrO_4)_2$. The valence band (B_V) can be divided into two energies range from [-5.83; -0.94] eV and [-0.75;0] eV, the former consists of the Ag-d state with contributions from the O-p, Cr-d states, and the Bi-s, p states, the latter consists Ag-d, Cr-d, O-p, there are hybridizations between Cr-d and O-p, Bi-p and Ag-d with O-p state. Above the Fermi level conduction band (B_C), the total DOS mainly arises from Ag -s,d, Cr-d, Bi – p, and O-p states.

The charge distribution of Ag-O and Cr-O bonds indicates that the empty ($3d^0$) orbital in Cr more easily forms a covalent bond with O atoms than the fully occupied ($4d^{10}$) orbital in Ag. This hybridization results in a lowering of symmetry about Cr atom (SOJT effects) [81-87] with hence plays an important role in a variety of important properties such as; the piezoelectric and nonlinear optical properties of Ag $Bi(CrO_2)_4$. While at the bottom of the (B_V) as the filled Ag ($4d^{10}$) orbital interact with the O 2p orbital and appear at higher energy in (B_C) the unfilled Ag $5s^1$ state, that means the lowest energy excitation from the (B_V) to the (B_C) is occurring from Ag ($4d^{10}$) – O 2p orbitals to the unfilled Ag 5s orbitals so this charge transfer play a key role in reducing the bandgap. On another side, the hybridization between the dominated O-2p states with minor Bi-6s states upper valence band, is responsible for the asymmetric local environment of electron distribution around the Bi atoms due to the presence of a stereo-chemically active electron lone pair. [88].

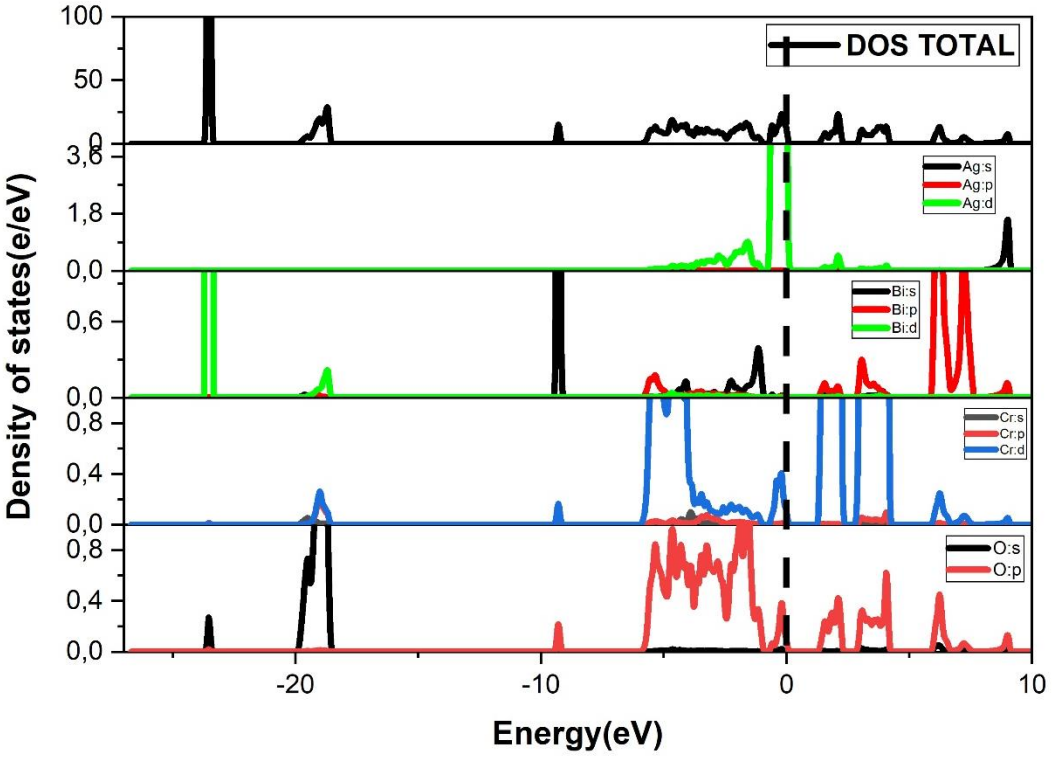

Figure. III.B. 5. Calculated partial and total DOS for Ag $Bi(CrO_4)_2$.

III.B.3.2.3. Charge-Density Distribution

Obviously in the figure. III.B.6. The density of charge indicates that; the chemical bonding of the Cr-O confirms the covalent trend and both Ag-O, Bi-O bonds have double character the former is a more ionic trend and the latter is more covalent.

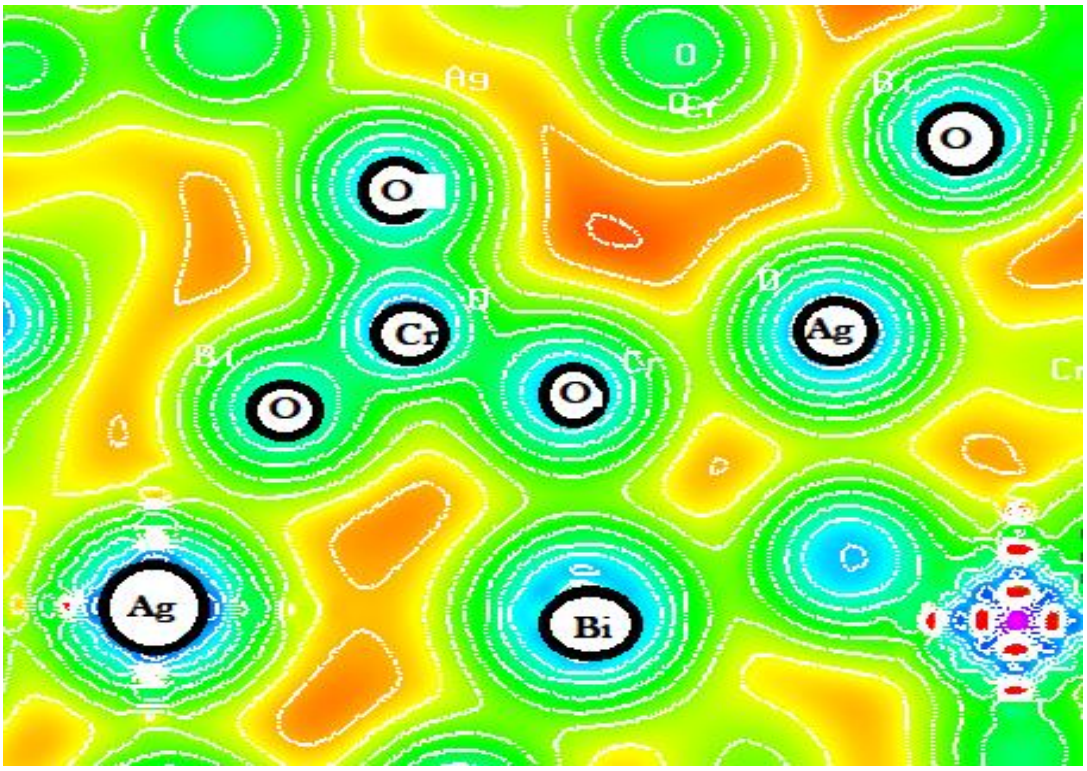

Figure. III.B. 6. Calculated density of charge in a plane containing Ag, Cr and O atoms.

III.B.3.3. Optical properties

The response of materials to electromagnetic radiation is described by the optical constants, the linear response was determined for $AgBi(CrO_4)_2$ in our work by the conventional optical effects such as; refractive index n(ω), absorption coefficient I(ω), loss function L(ω) and reflectivity R(ω)are displayed in figure. III.B. 8. These last optical constants can be extracted from the complex dielectric functions $\varepsilon(\omega) = \varepsilon_1(\omega) + i\varepsilon_2(\omega)$, which is mainly characterized by the imaginary part $\varepsilon_2(\omega)$ which adopt the electronic properties and the real part $\varepsilon_1(\omega)$ which adopt on the electronic polarizability with are displayed in figure. III. B.7.

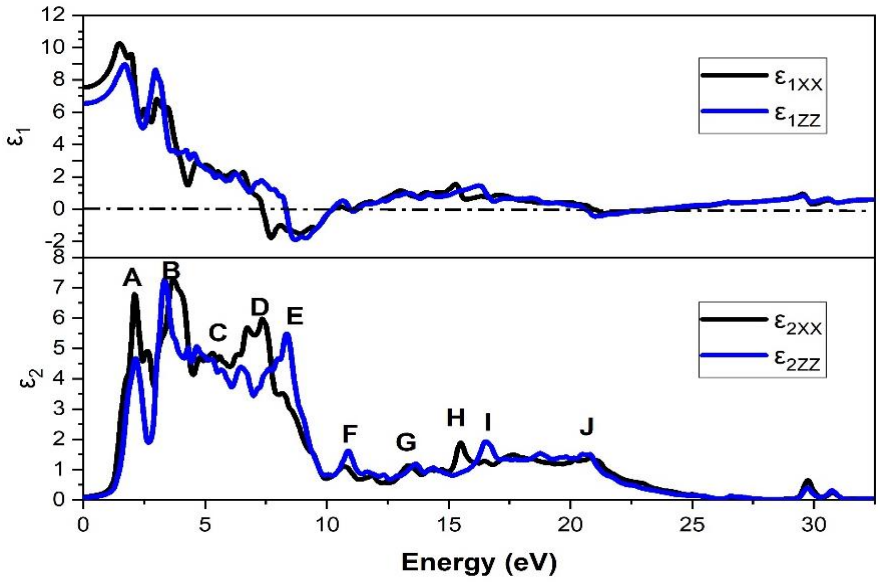

Figure. III.B. 7. Calculated imaginary $\varepsilon_2(\omega)$ and real $\varepsilon_1(\omega)$ parts of the dielectric function for Ag Bi $(CrO_4)_2$.

The formula expression for the $\varepsilon_2(\omega)$ can be found in chapter I. It's calculated by a direct evaluation of the transition matrix elements between the valence and conduction bands. In general, second-order NLO properties are determined by the optical excitations from all occupied states of the VBs to all unoccupied states of the CBs via the intermediate states. We can identify these excitations by comparing the PDOS plots (figure. III.B.5) [89]. Based on the TDOS (figure. III.B.5), we can note the positions of the main 9 peaks A, B, C, d, E, F, J, H, I transition that contribute dominantly to the optical structures are given in the table. III.B.15.

Table. III.B. 15. Peak positions of the $\varepsilon_2(\omega)$ spectrum together with the dominant inter-band transition contributions to every peak for $AgBi(CrO_4)_2$.

Dominant inter-band transition contributions			
Peak position	**Energy(eV)**	**Valence band (VBs)**	**Conduction band (CBs)**
A	**2.5**	**d-Ag, d-Cr, p-O**	**p-Bi**
B	**3.4**	**d-Ag, s-Bi, p-O**	**p-Bi, d-Cr**
C	**5.6**	**s-Bi, p-O**	**d-Ag, p-Bi, d-Cr**

D	**7.28**	**s-Bi, p-O**	**d-Ag, p-Bi, d-Cr**
E	**8.18**	**p-Bi, p-O**	**d-Ag, d-Cr**
F	**10.68**	**s-Bi, d-Cr, p-O**	**d-Ag, p-Bi**
G	**13.4**	**s-Bi**	**p-Bi, d-Cr, p-O**
H	**15.2**	**s-Bi, d-Cr, p-O**	**s-Ag, p-Bi**
I	**16.3**	**s-Bi, d-Cr, p-O**	**s-Ag, p-Bi**
J	**20.6**	**d-Bi, s-O**	**d-Ag, d-Cr, p-O**

The curve $\varepsilon_1(\omega)$ is calculated from the imaginary part by a transformation of The Kramers-Kronig (KK) relations (the equations given in chapter I).In $AgBi(CrO_4)_2$ the $\varepsilon_1(\omega)$ decreases from 7.5 for ε_{1xx} and 6.52 for ε_{1zz} to across zero, There are two intervals of negative value, the first in [7.34 eV to 10.22 eV] range and the second in [20.54 eV to 22.56 eV] with exhibit an anisotropic quite obvious owing of this anisotropy, the found the $\varepsilon_{1xx}(\omega)$ change sign at 7.34 eV which is different from that for $\varepsilon_{1zz}(\omega)$ at 8,33 eV for the first region and $\varepsilon_{1zz}(\omega)$ at 20.54 eV and $\varepsilon_{1xx}(\omega)$ at 21.12 eV for the second region. This negative sign difference causes to extended frequency window of the Plasmonic field, in this range the intrinsic plasmonic excitations can boost nonlinear optical effects owing to the coupling of light to plasmons with electromagnetic waves leading to the strong local electromagnetic field, this field has a strong sensitivity to refractive index change with hence to influence significantly the optical processes and nonlinear response enhancing [90]. After the second region negative our compound settle down almost close to 0 as an isotope characteristic compound.

The other optical properties such as absorption coefficients I (ω), refractive index n (ω), energy loss function L (ω), and reflectivity R (ω) are plotted in figure. III.B.8.

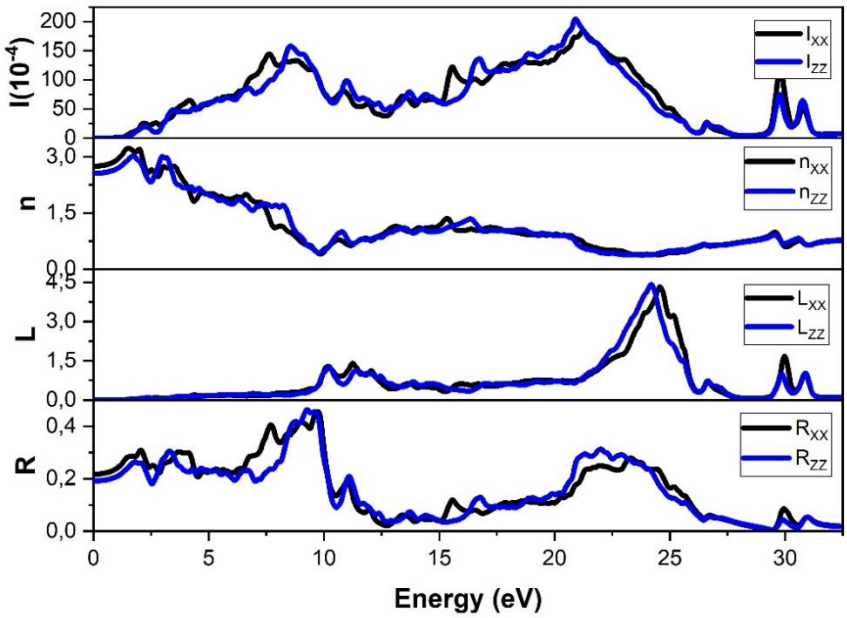

Figure. III.B.8. Calculated optical properties: absorption coefficient I(ω) (10^{-4}/cm), reflectivity R(ω), electron energy loss function L(ω) and refractive index n(ω) as function of energy of the incident photon for Ag Bi $(CrO_4)_2$.

we present the refractive indices n(ω) to assess the optoelectronic of Ag Bi $(CrO_4)_2$ the distinct refractive index become promising in the near UV region. Mean zero-limit of n(ω) is related with static limit of $\varepsilon_1(\omega)$ by the relation $n(\omega) = \sqrt{\varepsilon_1(\omega)}$. The birefringence Δn (ω) is one of the catalysts whether an NLO material has the value of the study because of its strong correlation with phase-matchability, a phenomenon underling for effective NLO[91] , so we present the Δn (ω) in figure.III.B.9. It is noteworthy that Ag Bi $(CrO_4)_2$ has reasonably high birefringence positive $(n_{xx}-n_{zz})$~0.18 (Δn greatly surpasses 0.08) [52, 92, 93] that changes alternately between positive to negative values along the range study suggesting its versatility character behaviors witch make a potential candidate for these applications, [32].

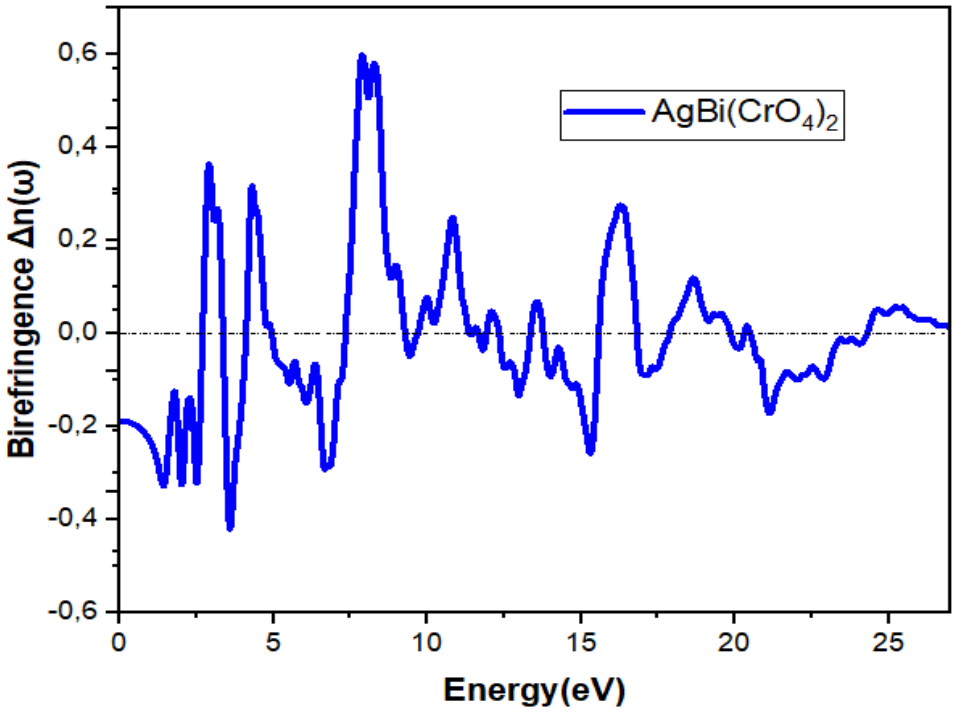

Figure. III.B.9. Birefringence of $AgBi(CrO_4)_2$.

The absorption coefficient I(ω) show an optic gap at 1.5 eV, hence is reflected in the transparency of our compound along the mid-infrared region,. A substantially increased absorption first occurs in VUV, UV-C region, while a steeper increase emerges in the EUV region.

The loss function is an important factor to measure the energy loss of an electron of fast velocity traversing a material. This curve is usually associated with a peak at an energy which gives the bulk plasma frequency, ω_p, A sharp maximum of the L(ω) spectrum located at approximately 24 eV that is consistent with the onset of $\varepsilon_2 < 1$ and $\varepsilon_1 = 0$, in this point Ag Bi $(CrO_4)_2$ becomes transparent with corresponding to edges in the reflection spectrum R (ω).

III.3.4. Mechanical and piezoelectric properties

To study the structural stability should be investigated of the elastic constants C_{ij} of solids to understand many of their fundamental physical properties, owing gives important information predictions about the mechanical stability, strength, stiffness, hardness, and ductile or brittleness behavior of materials, [94]. In addition, there are another physical parameter related to the elastic properties of solids is the elastic anisotropy, the good proper description of it gives insight into understanding the anisotropic behavior of different bonding natures in different planes crystallographic, [95].

The predicted elastic constants of tetragonal $I\bar{4}$ AgBi $(CrO_4)_2$ are shown in table.III. B. 6. For the mechanically stable crystal, the elastic constants should be satisfying the conditions indicated in chapter II. The C_{ij} calculated are satisfy mechanical stability criteria suggesting that the examined system is mechanically stable.

Table. III.B. 16. The calculated elastic constants C_{ij} (in GPa) for $AgBi(CrO_4)_2$.

Elastic Constants	C_{11}	C_{12}	C_{13}	C_{16}	C_{33}	C_{44}	C_{66}
Ag Bi $(CrO_4)_2$	**218.56**	**123.99**	**112.53**	**-16.36**	**243.39**	**60.71**	**76.15**

The elastic constants C_{11} and C_{33} are mainly related to the resistances to linear compression in <100> and<001> directions, respectively, and the other elastic constants namely C_{12}, C_{13}, C_{44}, and C_{66} are closely associated with are related to the elasticity in shape. According to table. III.B. 6, $C_{33} > C_{11}$, which indicates that the atomic bonding strength along the <001> direction between the nearest neighbors is stronger than that along the <100> direction. This means that the compressibility along the x-axis should be more easily than along the z-axes, [95] .On the other hand, we can be explained their elastic anisotropic by the ratios of C_{11}/C_{33} [96], the higher (lower) value of the ratio than 1.0 indicates the more compressible z (x) axis than the x (z) axis. It can be seen that for our compound lower is 0.8 than 1.0, with mean the <100> direction is more compressible than the <001> direction.
In addition, C_{66} is greater than C_{44} implies that the <1 0 0> (0 1 0) shear is harder than the <1 0 0> (0 0 1) shear [97].

Based on the predicted C_{ij}'s, the elastic modulus (bulk modulus B, shear modulus G, Young's modulus E, and Poison's coefficient **ν**) is shown in table. III. B.7. can be calculated according to the Voigt-Reuss-Hill method, which was mentioned in chapter II.

Table. III.B. 17. Bulk moduli B (GPa), shear moduliG (GPa), Young moduli E (GPa), Poisson ratio ν and G/B ratios for Ag Bi $(CrO_4)_2$.

Modulus	B_V	B_R	B	G_V	G_R	G	E	ν	G /B
Ag Bi $(CrO_4)_2$.	**153.19**	**153.08**	**153.13**	**61.613**	**58.269**	**59.941**	**159.07**	**0.32**	**0.39**

The large value of Bulk modulus B is closely related to the bond strength among atoms in the crystal, which presents the ability of material volume to resist elastic deformation.

According to Pugh criteria, the G/B ratio of 0.57 separates ductile and brittle materials (ductile< 0.57<brittle). In addition, Poisson ratio can also reflect the ductile property by (ductile> 0.26= **ν** >brittle). In our case, the value of the G/B is smaller than 0.57 and higher than 0.26 which indicates the character ductile. However, the bond strength among atoms resulting in the higher value B will lead to weaker ductility in the crystal. Is known that if the value of E increases, the material is stiff [98], In this context, the $AgBi(CrO_4)_2$ is implying its high hardness and strong bonding.

III.B.3.4.1. Debye temperature

Many physical properties of a solid such as; thermal conductivity and melting temperature-related by the fundamental parameter Debye temperature with is related by the mean velocity (v_m), the longitudinal (v_l), and transverse (v_t) elastic wave velocity.

Table. III.B. 18. Transverse (v_t in m/s), Longitudinal (v_l in m/s), mean sound velocity (v_m in m/s) and Debye temperature (Θ_D in K) for $AgBi(CrO_4)_2$.

	v_t	v_l	v_m	Θ_D
$AgBi(CrO_4)_2$	**3657,85**	**1861,17**	**2085,68**	**347,498**

From table. III. B.8. $AgBi(CrO_4)_2$ has the Debye temperature (347.49 K). This value implies, relatively, better thermal conductivity and strength of chemical bonding, the strong chemical bonding leads to higher melting temperature and higher hardness. It can be also noted that the transverse sound velocities are faster than longitudinal and mean sound velocities.

III.B.3.4.2. Anisotropic factors

The universal elastic anisotropy index A^U, the percent elastic anisotropy in shear (A_G), and compression (A_B) to estimate the anisotropic characteristic by the relations given in chapter II.

Table. III.B. 19. Universal anisotropy factor (A^U), percentage of bulk module (A_B) and shear modulus (A_G) anisotropy factors for $AgBi(CrO_4)_2$.

Anisotropy	**A^U**	**A_B (%)**	**A_G (%)**
Ag Bi $(CrO_4)_2$	**0.28**	**0.035**	**0.027**

For isotropic materials must be $A^U = 0$ and $A_B=A_G=0$. The further the values deviate from zero, the larger the anisotropy of the material. The predicted values are tabulated in the table.III. B. 9.

A^U is 0.28, this value deviates slightly from 0, indicating the relatively small elastic anisotropy characteristic of Ag Bi $(CrO_4)_2$, In addition, the calculated A_B (0.035) is relatively high than A_G (0.027), meaning that compressibility anisotropy is larger than shear anisotropy. Most crystals exhibit elastic anisotropy of varying degrees in different planes and directions. The three-dimensional surface and the plane projections (XY), (XZ), and (YZ) are given in Figure. III.B.10. and III.B.11, are showing the variation anisotropy of the Young and bulk modulus of the directional dependences with can be defined as given in chapter II.

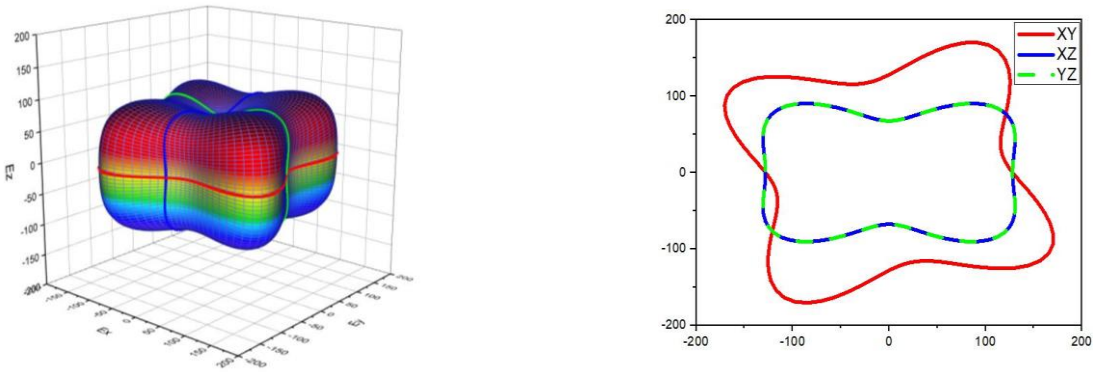

Figure. III.B. 130. The 2D and 3D projections of Young moduli of AgBi $(CrO_4)_2$.

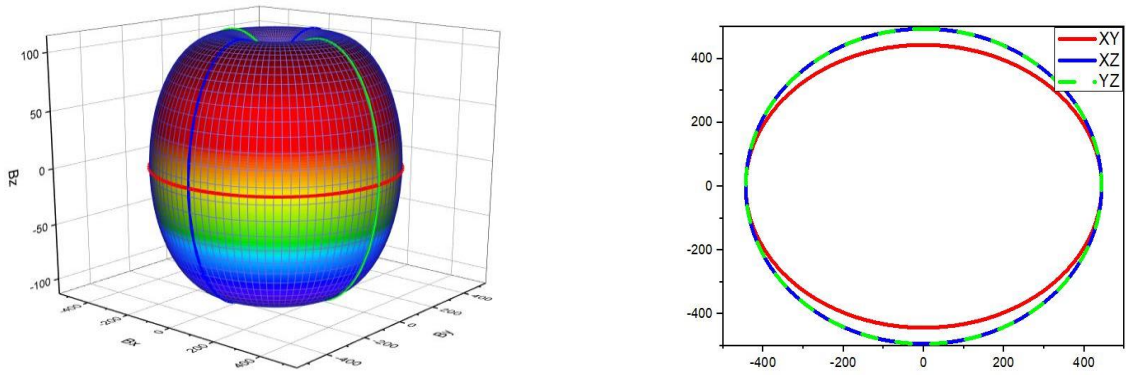

Figure. III.B.11. The 2D and 3D projections of bulk moduli of AgBi $(CrO_4)_2$.

For an isotropic system, 3D directional dependence should be a spherical shape, while the deviation degree from spherical shape give rise to the content of anisotropy.

The variation of Young's modulus shows great anisotropy in all planes and directions showing that possesses a maximum of young modulus for XY plane and a minimum for XZ

and YZ planes. Additionally, the variation of bulk modulus with B_{max} for XZ and YZ planes and B_{min} for XY plane.

III.B.7.4.3. Piezoelectric property

Piezoelectric property is the ability of acentric materials to create an electric potential in response to applied mechanical stress. Then, piezoelectricity is associated with the lattice deformations and depends on the polarization in crystals for more detail, [77]. We have four independent piezoelectric constants, in Voigt, notations are presented in the table. III.B.10. which in comparison with quartz (d_{14} = 0.727 pC/N, d_{11} = 2.310 pC/N) suggests that promising candidate for piezoelectric applications.

Table. III.B. 20. Relaxed ion piezoelectric tensor d_{ij} in (pC/N) for $AgBi(CrO_4)_2$.

	d_{14}	d_{15}	d_{31}	d_{36}
Ag Bi $(CrO_4)_2$	**1.76**	**-4.72**	**-10.47**	**-10.92**

III.B.3.5 Nonlinear optical properties

III.B.3.5.1. nonlinear optical susceptibilities

The SHG phenomenon of a polar material is identified from how the electrons of the medium respond to the oscillating electric field E of light. The polarization is linearly dependent on the applied field. Which can be described by the electric polarization P by Taylor expansion as;

$$\mathbf{P_i^{(2)}(\omega) = \varepsilon_0 \chi_{ijk}^{(2)}(\omega) E_j(\omega_1) E_k(\omega_2)}$$

$P^{(2)}$ is second-order polarizations, ε_0 denoting the electric permittivity of the vacuum and using the Einstein summation convention,ω is the frequency of the response signal while ω_1 and $\omega_2$are those of the pump lights with $\omega = \omega_1 + \omega_2$and the nonlinear electric susceptibility tensor (SHG coefficient tensor) $\chi^2$is a third-rank tensor which presented as the second-order functional derivatives of P with respect to E. The analysis symmetries of material NLO to find nonzero SHG coefficients χ_{ijk}^2 is necessary to understand why an NLO material has an SHG response, and understand its relation to the electronic structure of the material. The space group of material is dictated by the crystal symmetry and other symmetries governing the

susceptibility tensors , [99]. The second-order electronic susceptibility χ^2_{ijk} has 27 components, χ^2_{ijk} by the application of symmetries the SHG tensor in Voigt notation for space group of $I\bar{4}$ leads to only two nonequivalent components d_{14},d_{15} [38] were presented in the table.III.B.11**,**if we compared our result for referential available results materials NLO such as KDP(0.39 pm/V) [100] and KTP (d_{3l} = 6.5 d_{32} =5.0,d_{33}= 13.7, d_{24}= 7.6 ,d_{15}= 6.1). we can present the Ag Bi $(CrO_4)_2$ as promising in nonlinear optical.

Table. III.B. 21.Static nonlinear optical coefficients d_{ij} (Pm / V) for Ag Bi $(CrO_4)_2$.

	d_{14}	**d_{15}**
Ag Bi $(CrO_4)_2$	**8.5**	**16.71**

The real response for each material corresponds to their d_{eff}, which depends on the anisotropy, optical axis, crystal orientation, phase matching types ...etc. For this crystal class ($\bar{4}$), the d_{eff} is directly related to d_{14} and d_{15}, for all different possible phase matching types. the d_{eff} possible values, depending on crystal rotation and phase matching type by the following relations;

$$\mathbf{d_{eff} = (d_{14}sin2\phi + d_{15}sin2\phi)sin\theta}$$
$$\mathbf{d_{eff} = (d_{15}sin2\phi + d_{14}sin2\phi)sin\theta}$$

The direction of the wave vector is specified by spherical coordinates ($\boldsymbol{\theta}$, $\boldsymbol{\phi}$) referenced to the crystalline axes; $\boldsymbol{\rho}$is the birefringent walk-off angle.

III.B.3.5.2. Electro-optic tensor

Another nonlinear optical property is the electro-optic effect which reflects the change in refractive index caused by a static electric field. This modified refractive index leads to changes in phase, amplitude, or path of light traveling through a medium and is exploited in various technological applications , [101]. It contains three contributions, a purely electronic one, an ionic contribution, and a piezoelectric contribution. For details, we refer the reader to Veithen et al , [102]. The obtained EO tensor (Voigt notations) of the $AgBi(CrO_4)_2$ has four independent elements[103] are present in table.B.III.12. We adopt here the EO tensor from total and electronic contribution that is directly related to the nonlinear optic tensor [102].

Table. III.B. 22.linear electro-optic (EO) r_{ij} (Pm / V) for $AgBi(CrO_4)_2$

	r_{13}	r_{41}	r_{51}	r_{63}
Electronic contribution	**-0.83**	**-0.51**	**-0.99**	**-0.42**
Total contribution	**1.01**	**-2.08**	**-3.07**	**-0.38**

III.B.4. Conclusion

In summary, we perform first-principles DFT calculations to investigate systematically the lattice dynamics, electronic structure, dielectric, linear optical, and piezoelectric properties of the polar double bismuth-argent chromate $AgBi(CrO_4)_2$ belongs to the polar point group $\bar{4}$. The theoretical results of lattice dynamics, atomic position, and binding length by both methods FP-LAPW and PP-PW are compared to the available experimental data and a good agreement is found.

In the FP-LAPW method the electronic properties were investigated by TB-mBJ potential which were improved significantly for the opening of the band gap than the GGA-WC approximation. It's exhibited an electronic indirect band gap (1.38eV). The calculations of the dielectric spectra ε(ω) in the energy range 0–40 eV, Therefore, the large birefringence of $AgBi(CrO_4)_2$ (Δn=0.18) makes this compound a potential candidate for these applications. The calculated wavelength dispersions of the absorption index reflect the optical band (1.5eV) which is transparency along the mid-infrared region. The loos spectra L(ω) have a few main peaks, which are related to excitation (VBs to BCs). The energy of the maximum of L(ω) (24 eV) is related to the energy of volume plasmon ($\hbar\omega_p$).

In the PP-PW method, the computed elastic constant indicates that; $AgBi(CrO_4)_2$ is mechanically stable according to the elastic stability criteria. We have calculated the bulk moduli, shear moduli, young moduli, Poisson ratio, Debye temperature, and anisotropy value from the obtained elastic constants according to the Voigte-Reuss-Hill approximation. Ag $Bi(CrO_4)_2$ possess ductile nature with respect to the B/G criterion and Poisson's ratio. Additionally, the calculated young have suggested that this compound is a potential hard material and has strong bonds. The obtained Debye temperature value for $AgBi(CrO_4)_2$ indicate, relatively, thermal conductivity and confirm the strength of chemical bonding in the crystal structure. Furthermore, the elastic anisotropy has been visualized in detail by plotting the directional 2D and 3D dependences of compressibility and Young's modulus.

a large SHG coefficients d_{14}= 8.55 pm/V and d_{15}=16.71 pm/V than KDP (0.39 pm/V and high electro-optic coefficients which has a great potential as a candidate material for the mid-IR region.

One the other hand, $AgBi(CrO_4)_2$ exhibit higher piezoelectric coefficients d_{14}, d_{15}, d_{31}, d_{36} are 1.76 pC/N, -4.72 pC/N, -10.47 pC/N, -10.92 pC/N which in comparison with quartz (d_{14} = 0.727 pC/N, d_{11} = 2.310 pC/N) promising candidate for piezoelectric applications.

Reference chapter III

1. Wickleder, M.S., Inorganic lanthanide compounds with complex anions. Chemical Reviews, 2002. **102**(6): p. 2011-2088.

2. Becker, P., Borate materials in nonlinear optics. Advanced Materials, 1998. **10**(13): p. 979-992.

3. Chen, C., et al., Design and synthesis of an ultraviolet-transparent nonlinear optical crystal Sr2Be2B2O7. nature, 1995. **373**(6512): p. 322-324.

4. Chen, C., et al., A New-Type Ultraviolet SHG Crystal——β-BaB 2 O 4. Science in China Series B-Chemistry, Biological, Agricultural, Medical & Earth Sciences, 1985. **28**(3): p. 235-243.

5. Dmitriev, V.G., G.G. Gurzadyan, and D.N. Nikogosyan, Nonlinear optical properties of crystals, in Handbook of Nonlinear Optical Crystals1991, Springer. p. 53-127.

6. Boyd, G., E. Buehler, and F. Storz, Linear and nonlinear optical properties of ZnGeP2 and CdSe. Applied Physics Letters, 1971. **18**(7): p. 301-304.

7. Liao, J.-H., et al., α-and β-A2Hg3M2S8 (A= K, Rb; M= Ge, Sn): Polar quaternary chalcogenides with strong nonlinear optical response. Journal of the American Chemical Society, 2003. **125**(31): p. 9484-9493.

8. Zhang, Q., et al., Chalcogenide chemistry in ionic liquids: nonlinear optical wave-mixing properties of the double-cubane compound [Sb7S8Br2](AlCl4) 3. Journal of the American Chemical Society, 2009. **131**(29): p. 9896-9897.

9. Bierlein, J.D. and H. Vanherzeele, Potassium titanyl phosphate: properties and new applications. JOSA B, 1989. **6**(4): p. 622-633.

10. Rusov, V., et al., Using modulators based on KTP crystals in Nd: YAG lasers with high mean power. Journal of Optical Technology, 2009. **76**(6): p. 325-331.

11. Rusov, V., et al., Study of the electrical-conductivity kinetics of KTP crystals used in the modulators of solid-state lasers. Journal of Optical Technology, 2013. **80**(9): p. 532-536.

12. Rusov, V., et al., Electro-optical modulators based on KTP crystals for high-power lasers in the mid-IR region. Journal of Optical Technology, 2016. **83**(12): p. 716-721.

13. Guo, S.-P., et al., A Series of New Infrared NLO Semiconductors, ZnY6Si2S14, Al x Dy3 (Si y Al1− y) S7, and Al0. 33Sm3SiS7. Inorganic Chemistry, 2009. **48**(15): p. 7059-7065.

14. Hu, C.-L. and J.-G. Mao, Recent advances on second-order NLO materials based on metal iodates. Coordination Chemistry Reviews, 2015. **288**: p. 1-17.

15. Wang, Y. and S. Pan, Recent development of metal borate halides: Crystal chemistry and application in second-order NLO materials. Coordination Chemistry Reviews, 2016. **323**: p. 15-35.

16. Chung, I. and M.G. Kanatzidis, Metal chalcogenides: a rich source of nonlinear optical materials. Chemistry of materials, 2014. **26**(1): p. 849-869.

17. Bueno, I., et al., Crystal growth and crystal structure of KTb (CrO4) 2. Journal of Solid State Chemistry, 1990. **85**(1): p. 83-87.

18. Riou, A. and G. Roult, Etude par diffraction neutronique en temps de vol de la structure cristalline AgBi (CrO4) 2. Acta Crystallographica Section B: Structural Crystallography and Crystal Chemistry, 1979. **35**(11): p. 2494-2499.

19. Makarova, I., I. Verin, and K. Aleksandrov, X-ray diffraction study of RbLiCrO4. Ferroelectrics, 1991. **124**(1): p. 91-96.

20. Makarova, I., Atomic structure and twinning of RbLiCrO4 crystals. Butlletí de les Societats Catalanes de Física, Química, Matemàtiques i Tecnologia, 1992: p. 127-136.

21. Gonze, X., Perturbation expansion of variational principles at arbitrary order. Physical Review A, 1995. **52**(2): p. 1086.

22. Gonze, X. and J.-P. Vigneron, Density-functional approach to nonlinear-response coefficients of solids. Physical review B, 1989. **39**(18): p. 13120.

23. Beister, H., et al., Structural phase transitions and optical absorption of LiInSe 2 under pressure. Physical review B, 1991. **43**(12): p. 9635.

24. Wu, Z. and R.E. Cohen, More accurate generalized gradient approximation for solids. Physical review B, 2006. **73**(23): p. 235116.

25. Lai, W.-H., et al., Second Harmonic Generation Response Optimized at Various Optical Wavelength Ranges through a Series of Cubic Chalcogenides Ba6Ag2. 67+ 4δSn4. 33− δS16–x Se x. Chemistry of materials, 2015. **27**(4): p. 1316-1326.

26. Monkhorst, H.J. and J.D. Pack, Special points for Brillouin-zone integrations. Physical review B, 1976. **13**(12): p. 5188.

27. Veithen, M., X. Gonze, and P. Ghosez, First-principles study of the electro-optic effect in ferroelectric oxides. Physical review letters, 2004. **93**(18): p. 187401.

28. Gonze, X., et al., P. h. Ghosez, M. Veithen, J. Y. Raty, V. Olevano, F. Bruneval, L. Reining, R. Godby, G. Onida, DR Hamann and DC Allan, Z. Kristallogr, 2005. **220**: p. 558.

29. Makarova, I., I. Verin, and K. Aleksandrov, Structure and twinning of RbLiCrO4 crystals. Acta Crystallographica Section B: Structural Science, 1993. **49**(1): p. 19-28.

30. Koller, D., F. Tran, and P. Blaha, Merits and limits of the modified Becke-Johnson exchange potential. Physical review B, 2011. **83**(19): p. 195134.

31. Huang, H., et al., Bi 2 O 2 (OH)(NO 3) as a desirable [Bi 2 O 2] 2+ layered photocatalyst: strong intrinsic polarity, rational band structure and {001} active facets co-beneficial for robust photooxidation capability. Journal of Materials Chemistry A, 2015. **3**(48): p. 24547-24556.

32. Zernike, F. and J.E. Midwinter, Applied nonlinear optics2006: Courier Corporation.

33. Wooten, F., Optical Properties of Solids, ed, 1972, Elsevier.

34. Jenkins, F.A. and H.E. White, Fundamentals of optics. Indian Journal of Physics, 1957. **25**: p. 265-266.

35. Penn, D.R., Wave-number-dependent dielectric function of semiconductors. Physical Review, 1962. **128**(5): p. 2093.

36. Vitos, L., P.A. Korzhavyi, and B. Johansson, Stainless steel optimization from quantum mechanical calculations. Nature materials, 2003. **2**(1): p. 25-28.

37. Mattesini, M., R. Ahuja, and B. Johansson, Cubic Hf 3 N 4 and Zr 3 N 4: A class of hard materials. Physical review B, 2003. **68**(18): p. 184108.

38. Kleinman, D., Nonlinear dielectric polarization in optical media. Physical Review, 1962. **126**(6): p. 1977.

39. Bäuerle, D., et al., Phase-matched second harmonic generation in urea. Physica Status Solidi Applied Research, 1977. **42**(2): p. K119-K121.

40. Rez, I. and Y. Poplavko, Dielectrics. Main properties and applications; Radio and Svyaz '. 1989.

41. Kaminskii, A.A., et al., New crystalline lasers for the 1-μm wavelength range. Quantum Electronics, 1996. **26**(1): p. 1.

42. Nikogosyan, D.N., Periodically Poled Crystals and "Wafer" Materials. Nonlinear Optical Crystals: A Complete Survey, 2005: p. 185-213.

43. Arkhipenko, D. and T. Moroz, On the possible refinement of a space group of a mineral by analyzing the selection rules for vibrational spectra. Crystallography Reports, 1996. **41**(6): p. 925-928.

44. Jones, D., S. Prasad, and J. Wallace, Piezoelectric materials and their applications. Key Engineering Materials, 1996. **122**: p. 71-144.

45. Brenier, A., The self-doubling and summing lasers: overview and modeling. Journal of luminescence, 2000. **91**(3-4): p. 121-132.

46. Nowacki, W., T. Matsumoto, and A. Edenharter, Classification of crystalline substances by crystal systems, crystal classes, Bravais lattices and space groups. Acta crystallographica, 1967. **22**(6): p. 935-940.

47. Strunz, H., Ferrokarpholith–Karpholith. Acta crystallographica, 1957. **10**(3): p. 238-238.

48. Cotter, D., et al., Nonlinear optics for high-speed digital information processing. science, 1999. **286**(5444): p. 1523-1528.

49. Chung, I., et al., Strongly Nonlinear Optical Chalcogenide Thin Films of APSe6 (A= K, Rb) from Spin-Coating. Angewandte Chemie, 2011. **123**(46): p. 11059-11062.

50. Burland, D.M., R.D. Miller, and C.A. Walsh, Second-order nonlinearity in poled-polymer systems. Chemical Reviews, 1994. **94**(1): p. 31-75.

51. Liu, H., et al., ABi2 (IO3) 2F5 (A= K, Rb, and Cs): A Combination of Halide and Oxide Anionic Units To Create a Large Second-Harmonic Generation Response with a Wide Bandgap. Angewandte Chemie, 2017. **129**(32): p. 9620-9624.

52. Chen, C., et al., Deep-UV nonlinear optical crystal KBe 2 BO 3 F 2—discovery, growth, optical properties and applications. Applied Physics B, 2009. **97**(1): p. 9-25.

53. Inaguma, Y., M. Yoshida, and T. Katsumata, A polar oxide ZnSnO3 with a LiNbO3-type structure. Journal of the American Chemical Society, 2008. **130**(21): p. 6704-6705.

54. Cheng, W.-D., et al., Designing the syntheses and photophysical simulations of noncentrosymmetric compounds. Inorganic Chemistry Frontiers, 2015. **2**(2): p. 95-107.

55. Phillips, M., et al., Electronic effects of substitution chemistry in the KTiOPO4 structure field: structure and optical properties of potassium vanadyl phosphate. Inorganic Chemistry, 1990. **29**(11): p. 2158-2163.

56. Munowitz, M., R. Jarman, and J. Harrison, Theoretical study of the nonlinear optical properties of potassium titanyl phosphate (KTiOPO4): cooperative effects in extended--Ti--O--Ti--O--chains. Chemistry of materials, 1993. **5**(5): p. 661-671.

57. Hagerman, M.E. and K.R. Poeppelmeier, Review of the structure and processing-defect-property relationships of potassium titanyl phosphate: A strategy for novel thin-film photonic devices. Chemistry of materials, 1995. **7**(4): p. 602-621.

58. Bera, T.K., et al., Soluble semiconductors AAsSe2 (A= Li, Na) with a direct-band-gap and strong second harmonic generation: a combined experimental and theoretical study. Journal of the American Chemical Society, 2010. **132**(10): p. 3484-3495.

59. Zhang, J., et al., Dielectric, piezoelectric and nonlinear optical properties of polar iodate BiO (IO3) from first-principles studies. Journal of Solid State Chemistry, 2020. **281**: p. 121057.

60. Lagoun, B., B. Bentria, and I.K. Lefkaier, Ab initio calculation of structural, electronic and optical properties of Hg (IO3) 2. Physica B: Condensed Matter, 2014. **433**: p. 117-121.

61. Wu, C., et al., K5 (W3O9F4)(IO3): An efficient mid-infrared nonlinear optical compound with high laser damage threshold. Chemistry of materials, 2019. **31**(24): p. 10100-10108.

62. Tell, B. and H. Kasper, Optical and electrical properties of agga s 2 and agga se 2. Physical review B, 1971. **4**(12): p. 4455.

63. Simon, U., et al., Design considerations of an infrared spectrometer based on difference–frequency generation in AgGaSe 2. Applied optics, 1993. **32**(33): p. 6650-6655.

64. Guo, S.-P., Y. Chi, and G.-C. Guo, Recent achievements on middle and far-infrared second-order nonlinear optical materials. Coordination Chemistry Reviews, 2017. **335**: p. 44-57.

65. Wu, Q., et al., RbIO3 and RbIO2F2: Two promising nonlinear optical materials in mid-IR region and influence of partially replacing oxygen with fluorine for improving laser damage threshold. Chemistry of materials, 2016. **28**(5): p. 1413-1418.

66. Zhang, M., et al., Functional materials design via structural regulation originated from ions introduction: A study case in cesium iodate system. Chemistry of materials, 2018. **30**(3): p. 1136-1145.

67. Phanon, D. and I. Gautier-Luneau, Promising material for infrared nonlinear optics: NaI3O8 salt containing an octaoxotriiodate (V) anion formed from condensation of [IO3]− ions. Angewandte Chemie International Edition, 2007. **46**(44): p. 8488-8491.

68. Messina, R., et al., Electrochemical behaviour of new cathodic materials usable in lithium batteries: AgBi (CrO4) 2 and Bi2O (CrO4) 2. Journal of Power Sources, 1982. **8**(2): p. 277-288.

69. Schwarz, K. and P. Blaha, Solid state calculations using WIEN2k. Computational Materials Science, 2003. **28**(2): p. 259-273.

70. Bentria, B., et al., Crystal engineering strategy for quadratic nonlinear optics. Part II: Hg (IO3) 2. Solid state sciences, 2003. **5**(2): p. 359-365.

71. Singh, D.J. and L. Nordstrom, Planewaves, Pseudopotentials, and the LAPW method2006: Springer Science & Business Media.

72. Tran, F. and P. Blaha, Accurate band gaps of semiconductors and insulators with a semilocal exchange-correlation potential. Physical review letters, 2009. **102**(22): p. 226401.

73. Fan, S., X. Huang, and G. Gao, Density functional theory study on electronic structures and magnetism for nitrogen-doped ZnS. Journal of Superconductivity and Novel Magnetism, 2018. **31**(5): p. 1443-1448.

74. Fan, S., L. Yang, and G. Gao, The electronic structures and properties for carbon doped aluminum phosphide. Physics Letters A, 2019. **383**(25): p. 3138-3142.

75. Ceperley, D.M. and B.J. Alder, Ground state of the electron gas by a stochastic method. Physical review letters, 1980. **45**(7): p. 566.

76. Perdew, J.P. and Y. Wang, Pair-distribution function and its coupling-constant average for the spin-polarized electron gas. Physical review B, 1992. **46**(20): p. 12947.

77. Vanderbilt, D., Berry-phase theory of proper piezoelectric response. Journal of Physics and Chemistry of Solids, 2000. **61**(2): p. 147-151.

78. Perdew, J.P., K. Burke, and M. Ernzerhof, Generalized gradient approximation made simple. Physical review letters, 1996. **77**(18): p. 3865.

79. Asada, T. and K. Terakura, Generalized-gradient-approximation study of the magnetic and cohesive properties of bcc, fcc, and hcp Mn. Physical review B, 1993. **47**(23): p. 15992.

80. Kidyarov, B.I., Comparative interrelationship of the structural, nonlinear-optical and other acentric properties for oxide, borate and carbonate crystals. Crystals, 2017. **7**(4): p. 109.

81. Pilcova, R., et al., Leptin levels in obese children: effects of gender, weight reduction, and androgens. Physiological research, 2003. **52**(1): p. 53-60.

82. Rao, P.P. and M. Reddy, Synthesis and characterisation of (BiRE) 2O3 (RE: Y, Ce) pigments. Dyes and pigments, 2004. **63**(2): p. 169-174.

83. Imanaka, N., T. Masui, and M. Itaya, Synthesis of an environmentally friendly and nontoxic new pigment based on rare earth phosphate. Chemistry letters, 2003. **32**(4): p. 400-401.

84. Fujishima, A. and K. Honda, Electrochemical photolysis of water at a semiconductor electrode. nature, 1972. **238**(5358): p. 37-38.

85. Eng, H.W., et al., Investigations of the electronic structure of d0 transition metal oxides belonging to the perovskite family. Journal of Solid State Chemistry, 2003. **175**(1): p. 94-109.

86. Tandon, S. and J. Gupta, Diffuse reflectance spectrum of chromic oxide. physica status solidi (a), 1970. **3**(1): p. 229-234.

87. Tauc, J., Absorption edge and internal electric fields in amorphous semiconductors. Materials Research Bulletin, 1970. **5**(8): p. 721-729.

88. Walsh, A., et al., Stereochemistry of post-transition metal oxides: revision of the classical lone pair model. Chemical Society Reviews, 2011. **40**(9): p. 4455-4463.

89. Lei, B.-H., et al., Second harmonic generation susceptibilities from symmetry adapted Wannier functions. Physical review letters, 2020. **125**(18): p. 187402.

90. Kauranen, M. and A.V. Zayats, Nonlinear plasmonics. Nature photonics, 2012. **6**(11): p. 737-748.

91. Bian, Q., et al., First principle assisted prediction of the birefringence values of functional inorganic borate materials. The Journal of Physical Chemistry C, 2014. **118**(44): p. 25651-25657.

92. Chen, C., et al., Second-harmonic generation from a KBe 2 BO 3 F 2 crystal in the deep ultraviolet. Optics letters, 2002. **27**(8): p. 637-639.

93. Wu, B., et al., Linear and nonlinear optical properties of the KBe2BO3F2 (KBBF) crystal. Optical Materials, 1996. **5**(1-2): p. 105-109.

94. Ateser, E., et al., The structural and mechanical properties of CdN compound: A first principles study. Computational Materials Science, 2011. **50**(11): p. 3208-3212.

95. Guechi, N., et al., Structural, elastic, electronic and optical properties of the newly synthesized monoclinic Zintl phase BaIn2P2. Solid state sciences, 2014. **29**: p. 12-23.

96. Duan, Y.-H., et al., Structural and anisotropic elastic properties of Zintl M2Pb (M= Ca, Sr and Ba) compounds as a function of pressure. Journal of alloys and compounds, 2014. **614**: p. 334-344.

97. Zeng, M.-X., et al., Elastic and electronic properties of tI26-type Mg12RE (RE= Ce, Pr and Nd) phases. Modelling and Simulation in Materials Science and Engineering, 2012. **20**(3): p. 035018.

98. Rajagopalan, M., S.P. Kumar, and R. Anuthama, FP-LAPW study of the elastic properties of Al2X (X= Sc, Y, La, Lu). Physica B: Condensed Matter, 2010. **405**(7): p. 1817-1820.

99. Cheng, X., et al., The Large Second-Harmonic Generation of LiCs2PO4 is caused by the Metal-Cation-Centered Groups. Angewandte Chemie International Edition, 2018. **57**(15): p. 3933-3937.

100. Dmitriev, V.G., G.G. Gurzadyan, and D.N. Nikogosyan, Handbook of nonlinear optical crystals. Vol. 64. 2013: Springer.

101. Lines, M.E. and A.M. Glass, Principles and applications of ferroelectrics and related materials2001: Oxford university press.

102. Veithen, M., X. Gonze, and P. Ghosez, Nonlinear optical susceptibilities, Raman efficiencies, and electro-optic tensors from first-principles density functional perturbation theory. Physical review B, 2005. **71**(12): p. 125107.

103. Kleinman, D., Theory of second harmonic generation of light. Physical Review, 1962. **128**(4): p. 1761.

CHAPTER IV

In this part, we focused on the theoretical investigation of the properties of fluoro-iodate.

$RbIO_2F_2$, $CsIO_2F_2$, each compound will be in a part independent.

Part A

compound $RbIO_2F_2$

IV.A.1. Introduction

In recent years, Infrared nonlinear optical (IR-NLO) materials with a height *Laser damage threshold (LDT)* had great attention in materials science due to their significant military and civilian applications, for example; the ferroelectricity, piezoelectricity, and second-order nonlinear optical (NLO) properties,[1-3]. The development of IR-NLO materials is still limited, [4, 5]. Currently, commercial IR-NLO materials are only available for; $AgGaS_2$ (AGS)[6] , $AgGaSe_2$ [7] , and $ZnGeP_2$ [8] ; the two former are suffered lower (LDTs), while the ZnGeP2 have strong two-photon absorption within their working wavelength range. As a result, their applications cannot be fully satisfied.

Metal iodates are one of the important types of inorganic functional materials for various fields of study like nonlinear optical (NLO), ferroelectric, and piezoelectric properties [9-11] unit with the lone electron pair of I^{+5} ion, They have been able to produce materials with outstanding second harmonic generation (SHG) capabilities, including a wide transparency range from visible to the beginning of the far-IR region, as well as moderate birefringence to fulfill phase matching behaviors, [12, 13] . In this family, $LiIO_3$ is the only compound, used in commercial devices, and its fabrication is limited to piezoelectric transducers [14, 15], owing to many reasons; lowly of the damage threshold laser (LDT), low thermal stability[16], little reproducibility of growth of the crystal [17], and presence of impurities [18]. Therefore, new engineering strategies have been developed, such as; the combination with functional building units IO_xF_{4-x} (x=1, 2, 3) in fluoro-oxoidates and transition metal (TM) cations [19-22], which greatly enrich the researches of iodates, with excellent NOL properties, such as $Bi(IO_3)F_2$[23], $RbIO_2F_2$[24], $CsIO_2F_2$[25], $Ce(IO_3)_2F_2.H_2O$[26], $Bi_3OF_3(IO_3)_4$[27], $CsBi_2(IO_3)_2F_5$ and $KBi_2(IO_3)_2F_5$[28], where the introduction of electronegative fluorine is an effective strategy in metal iodates to obtain high LDT.

Rb (IO_3) is transparent from (0.3−13) μm, thus confirming its wider optical transmission range to extend its applications in the entire ultraviolet, visible and NIR regions. The optical band gap is found to be 4 eV from the Tauc's plot. As an inorganic material, the developed crystal has moderate SHG efficiency (20 times KDP), good thermal stability of 550 °C, and high LDT of 125 MW/cm^2 (20 times $AgGaS_2$)[24].

In 2016, Qi Wu et al[24] synthesized a new polar iodate $Rb(IO_2F_2$), by replacing oxygen with fluorine atoms in the $Rb(IO_3)$ compound. They found that it crystallizes in the acentric space group $Pca2_1$ with a thermal stability at up to 400 °C, a wide transparency range

(2.5−12.34) μm and a highest LDT value of 156 MW/cm^2 (33 times $AgGaS_2$), [7] . It has a band gaps of 4.2 eV, exhibiting a good SHG effect (4 times KDP[29]).). Its SHG coefficients (d_{ij}) have been determined by the ab initio calculations, using plane-wave pseudo-potential, as implemented in CASTEP code, [24].

In this part , we are interested in the fluoridate $RbIO_2F_2$ because it satisfies the basic requirements for NLO application , [24]. To determine its performance in various properties such us lattice dynamics, electronic structure and optical properties, we have performed first-principles calculations DFT with the Full Potential Linearized Augmented Planes Waves (FP-LAPW) method. The space group of ($Pca2_1$), for the compound $RbIO_2F_2$, belongs to the point group mm2 as multifunctional non-Centrosymmetric space group (NCS**)**. Using the pseudo-potential plane waves (PP-PW) method, based on the density functional perturbation theory (DFPT), we carried out the calculations of the mechanical properties, nonlinear optical coefficients, electro-optic tensors and piezoelectric.

IV.B.2. Computational details

In this study, we have used the ab-initio calculations, based on the density functional theory (DFT), [30, 31]. The ion-electron interactions characterizes the separation of valence and core states by the FP-LAPW method [32] implemented in the WIEN2K Package, [33]. To treat the exchange and correlation potential (U_{XC}) we used the Generalized Gradient Approximation GGA developed by Perdew-Burker-Ernzerhof (GGA-PBE)[34] to calculate the structural properties (lattice parameters: a, b and c and atomic positions). We used Tran and Blaha modified Becke-Johnson (TB-mBJ) [35] potential to investigate the electronic and linear optical properties .The muffin-tin radii values R_{mt} were fixed to 1.8, 1.4, 1.75 and 1.4 Bohr for Rb, F, I and O atoms, respectively, and their valence states are taken respectively $4s^2 4p^6 5s^1$, $2s^2 2p^5$, $4d^{10} 5s^2 5p^2$and $2s^2 2p^4$. We used full relativistic effects for core states to treat their fully relativistically effects. The number of the plane wave functions for parameter Rmt x Kmax =7. For The special K-point of irreducible Brillion zone (IBZ), we have used (10×12×10) grid to calculate the structural properties. In order to obtain a good convergence of the electronic and linear optical properties, (12×14 ×12) grid has been used. Moreover, the elastic properties and non-linear (NLO) properties, within the framework of modern theory of polarization and density functional perturbation theory (DFPT), making use of the 2n + 1 theorem, are calculated and stored in the derivative database (DDB), and analyzed by the ANADDB package within in ABINIT Package [36]. The self-consistent norm-conserving pseudo potentials, used in our

computations, generated by the Troullier-Martins scheme [37], are used to perform this study. The exchange-correlation terms were treated with the LDA parameterized by Perdew–Wang 92 (LDA-PW), [38, 39] . A convergence study was made 30 Hartree for cutoff energy and a 6×6×6 mesh grid. The ground state structure was fully optimized by minimizing the total energy and Hellmann–Feynman forces.

IV .B.3. Ground state properties

IV .B.3.1 Structural properties

$RbIO_2F_2$ crystallizes in the NCS orthorhombic with space group $Pca2_1$ (Figure. IV.A.1) After optimizing the structural parameters (b_0/a_0, c_0/a_0, V), the atomic positions are relaxed to reduce the Hellmann-Feynman forces and energy. The calculated parameters, atomic positions and binding length of $RbIO_2F_2$ are listed in table. IV.A.1 ,2 and 3 ,respectively, with the available experimental lattice parameters, [24]. From these results, we observe that the GGA-PBE overestimate the lattice parameters while LDA-PW underestimate it. These results are in agreement with the general trend of both methods in structural parameters [40]. The results are listed in table IV.A.1 ,2 and 3, the agreement between the theoretical and experimental atomic positions and bond lengths have good accord.

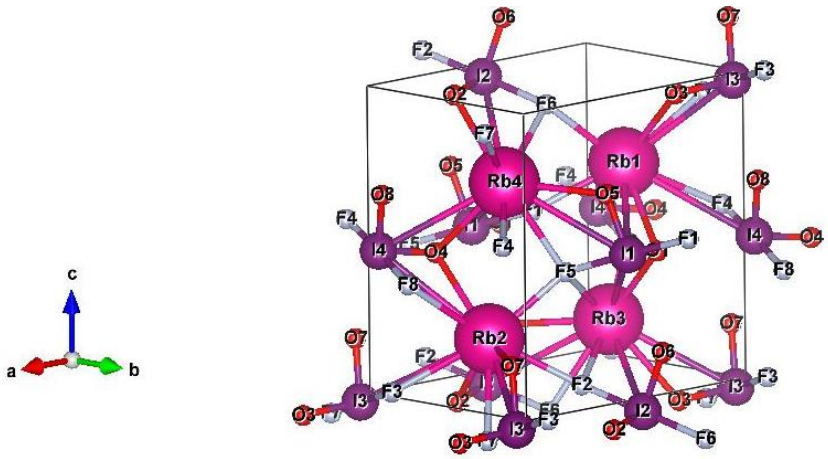

Figure. IV.A. 1. Conventional cell of $RbIO_2F_2$

Table. IV.A. 1. Calculated and experimental lattice parameters of $RbIO_2F_2$

Parameters	Exp [24]	GGA-PBE	ΔX /X	LDA-PW	ΔX /X
***a* (Å)**	**8.567**	**8.679**	**1.3%**	**7.793**	**9.03%**
***b* (Å)**	**6.151**	**6.231**	**1.3%**	**5.825**	**5.29%**
***c* (Å)**	**8.652**	**8.765**	**1.3%**	**7.856**	**9.2%**

Table. IV.A. 2. Calculated and experimental atomic positions of $RbIO_2F_2$.

Atomes	Exp[24]	GGA-PBE	LDA-PW
F(1)	(0.4269; 0.2415; 0.5338)	(0.42662 ;0.24345 ;0.53416)	(0.42502;0.24670 ;0.54455)
F(2)	(0.5731;0.7585 ;0)	(0.57338 ; 0.75655 ;0.03416)	(0.57497;0.75329 ;0.04455)
I	(0.49321;0.94720 ;0.46628)	(0.49250 ; 0.94659 ;0.46671)	(0.50056;0.93782 ;0.46133)
O(1)	(0.2974; 0.8583; 0.4418)	(0.29607 ; 0.85829 ;0.44171)	(0.28440;0.84098 ;0.43910)
O(2)	(0.7026 ; 0.1417 ; 0.908)	(0.70393 ; 0.1417 ; 0.94171)	(0.70260; 0.14170;0.9418)
Rb	(0.21229;0.53082 ;0.68916)	(0.21205 ; 0.53071 ;0.68873)	(0.20217;0.53876 ;0.67831)

Table. IV.A. 3. Calculated and experimental bond length of $RbIO_2F_2$.

Bond length (Å)	Exp [24]	GGA-PBE	ΔX /X	LDA-PW	ΔX /X
F(1)-I	1.985	2.024	1.96%	1.835	7.55%
F(2)-I	2.017	2.054	1.83%	1. 903	5.65%
I-O(1)	1.764	1.799	1.98%	1.758	0.34%
I-O(2)	1.777	1.804	1.51%	1.718	3.32%

IV. A.3.2. Electronic structure

It's very useful to understand the electronic properties (band structures, state densities and charge density) of solids, owing to the fact that most of the physical properties of solids are related to them.

IV.A.3.2.1 Band structure

The line of high symmetry points of $Pca2_1$ (29) in the Brillouin zone is illustrated in Figure. IV.A.2

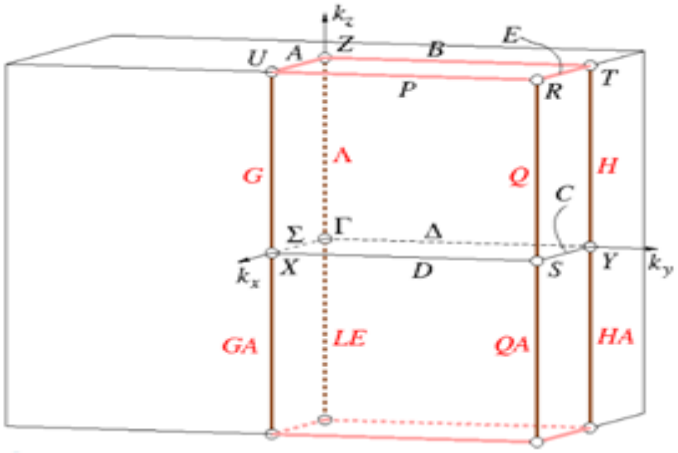

Figure. IV.A. 2. The line of high symmetry points of $Pca2_1$ (N°29) in the Brillouin zone.

The band structure of $RbIO_2F_2$ is calculated using the TB-mBJ potential along the high symmetry directions in the Brillouin Zone (BZ). The calculated energy band structure is represented in figure. IV.A. 3. There is an indirect band gap between the point X for the top of valance band (V_B) and point Y of the bottom for the conduction band (C_B) with the energy value of 4.17 eV. Our result is in a good agreement with the experimental result, which is 4.2 eV with an error of 0.47%. While in the other calculation, using the LDA approximation, as implemented in the CASTEP code, is yield a difference of 1.9 % [24] . Therefore, in our study, the TB-mBJ potential shows its ability to accurately treat the E_g quantifying, confirming its efficiency as in many theoretical studies , [41].

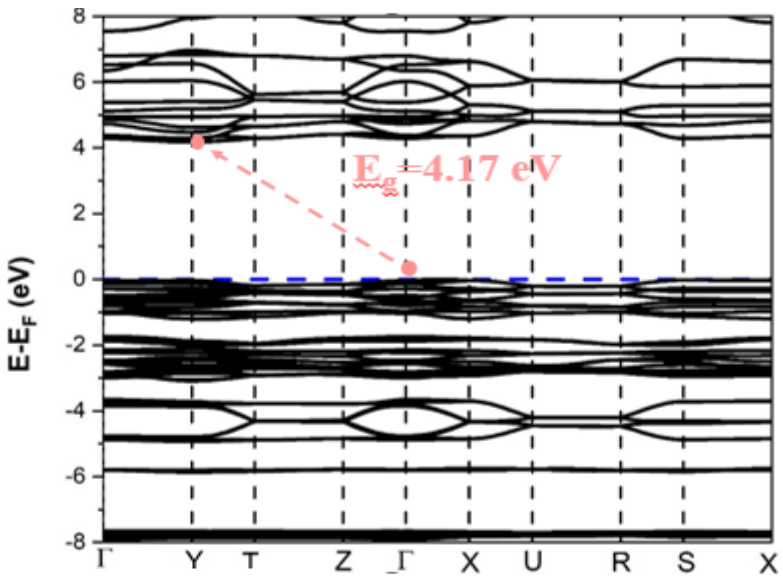

Figure. IV.A. 3. Calculated band structure by (TB-mBJ) for $RbIO_2F_2$.

IV.A.3.2.2. Density of states

The total and partial densities of states (TDOS and PDOS) for $RbIO_2F_2$, in the region of [-25 to 18] eV, are shown in figure.IV.4. In this figure, the zero scale of energy reveals the Fermi energy. Under the Fermi level, there is the valence band (V_B) state while the conduction band (C_B) state is located above it. The PDOS show that the Rb atom is positioned by $4s^2$ and $4p^6$ orbitals in the (V_B) at [-23.6, -23.5] eV and [-8.8, -7.5] eV, respectively, exhibiting localized non-bonding orbitals. The V_B along [-22.02, -9. 95] eV is known by four energy bands; the first one [-22.16,-21.29] eV is mainly formed by the $2s^2$ orbital of F atom and particularly by the $5s^2$orbital of I atom , the second energy band [-18.8,-18.04] eV is dominated by the $2s^2$,$5s^2$,$2s^2$ orbitals for F, I and O atoms, respectively, the third one [-17,-16.24] eV is mainly formed by the $2s^2$orbital of O atom and particularly by $5p^2$ orbital of I atom , and the last one [-11.3,-9.88] eV is formed by the $5s^2$ orbital of I atom and a small contribution of both $2s^2$ and $2p^5$ orbitals of O and F atoms . These bands, mentioned above (V_B), arise from the short I-O and I-F links. The energy ranges near the Fermi level can be divided into three different energy bands around [-5.9, -5.4] eV, [-5, -3.5] eV, [-3.1, -1.5] eV, and [-1.3, 0] eV.

[-5.9, -5.4] eV exhibits a localization of the $2p^5$, $4p^6$, $5p^2$ orbitals of F, Rb and I atoms, respectively. [-5, -3.5] eV shows a hybridization of the $2p^5$, $2p^4$, and $5p^2$ orbitals of F, O, I atoms, respectively. [-3. 1, -1.5] eV is dominated by $2p^5$, $2p^4$, $4p^6$ orbitals of F, O, Rb atoms, respectively, with small contributions of a mix $5s^2$ and $5p^2$ orbitals of I atom. [-1.3, 0] eV is mainly formed by $2p^4$ orbital of O atom and by the contributions of $2p^5$, $5p^2$ orbitals of F and I atoms. Usually non-centrosymmetric sublattices with the states occupying near the Fermi level have important contributions to SHG response [42], denoting that the I-O-F units are the key index for determining the nonlinear properties in the $RbIO_2F_2$ compound. The CB is mainly formed by the $2p^5$ and $5p^2$ orbitals of F and I atoms, respectively.

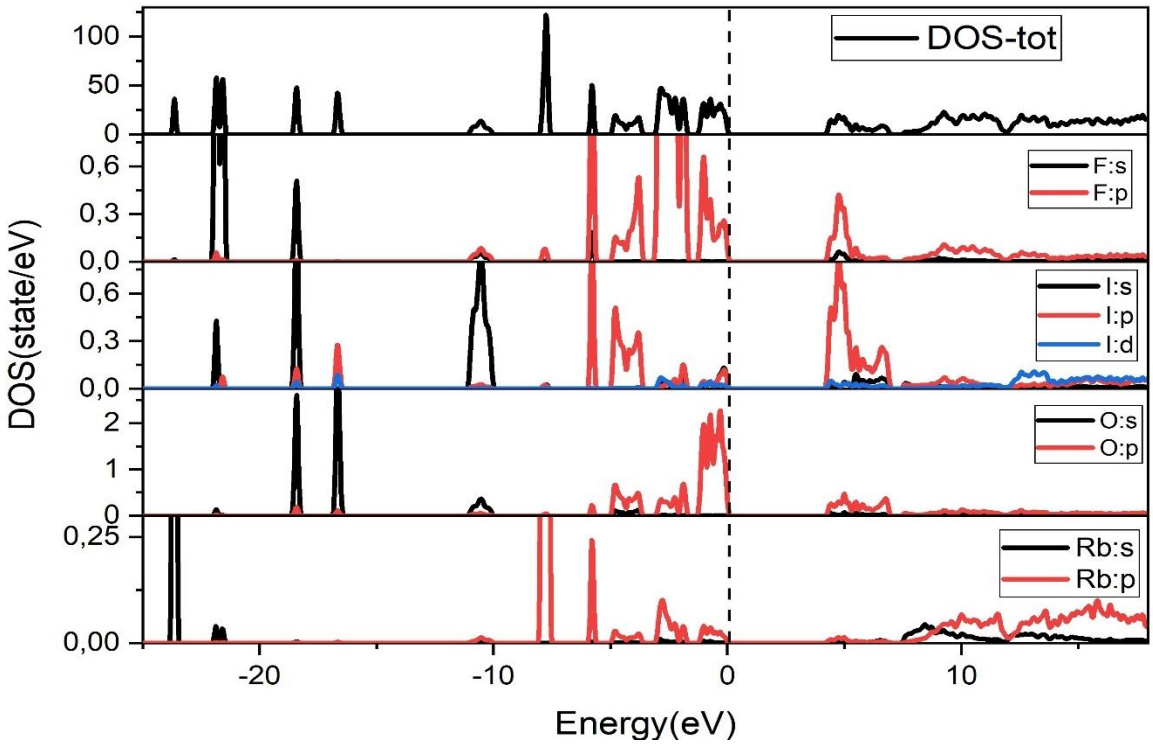

Figure. IV.A. 4. Calculated partial and total DOS for $RbIO_2F_2$.

IV.A.3.2.3. Charge-Density Distribution

The total charge density is a powerful tool to characterize the nature of the chemical bonds in $RbIO_2F_2$, through the shapes of the planar charge density around the atoms figure. IV.A.5, illustrates the planes, containing Rb, I and O atoms for $RbIO_2F_2$. We find out that I-O and I-F are the covalent bond. The quasi-spherical charge distributions around the site of Rb-O bond indicate the pronounced covalent bond character. Therefore, Rb-F is ionic bond. These results are confirmed from the reported DOS.

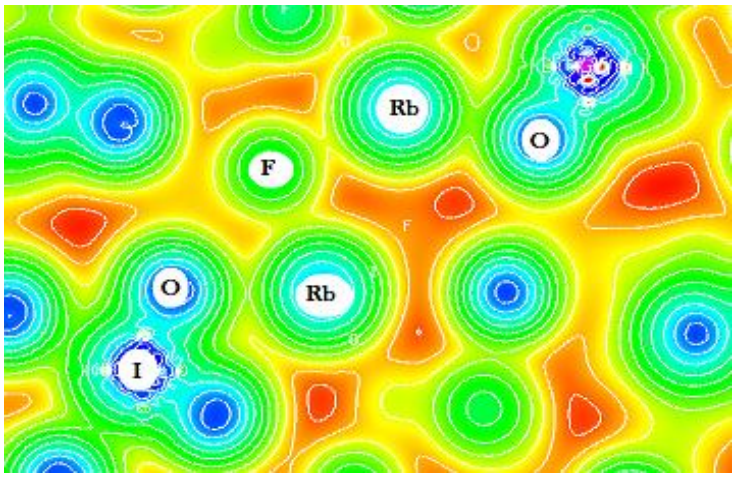

Figure. IV.A. 5.Calculated density of charge in a plane containing Rb, O and I atoms.

IV.A.3.3. Optical properties

The dielectric function and its evolution are the most important properties to reveal the optical responses and guide the design of related devices. The dielectric function $\varepsilon(\omega) = \varepsilon_1(\omega) + i\varepsilon_2(\omega)$, consists of two contributions: The imaginary part $\varepsilon_2(\omega)$ of the interband contribution and real part $\varepsilon_1(\omega)$. It can be calculated via the Kramers-Kronig relation, which is typically treated in plasmatic transition. This process is defined as the interaction of photons from an electromagnetic wave with electrons in a crystal, expressed by the equations are given in chapter II. we have systematically investigated the dielectric constant of $RbIO_2F_2$ over an ultra-broad spectral range (0–40 eV) as shown in figure.IV.A.6. $\varepsilon_2(\omega)$ is determined by the electronic inter-band transitions, which are related to the valence and conduction band states involved in the optical transition. Our curve, in figure.IV.A.6, reflects the presence of 12 main peaks positioned at different energies which are given in table. IV.A.4

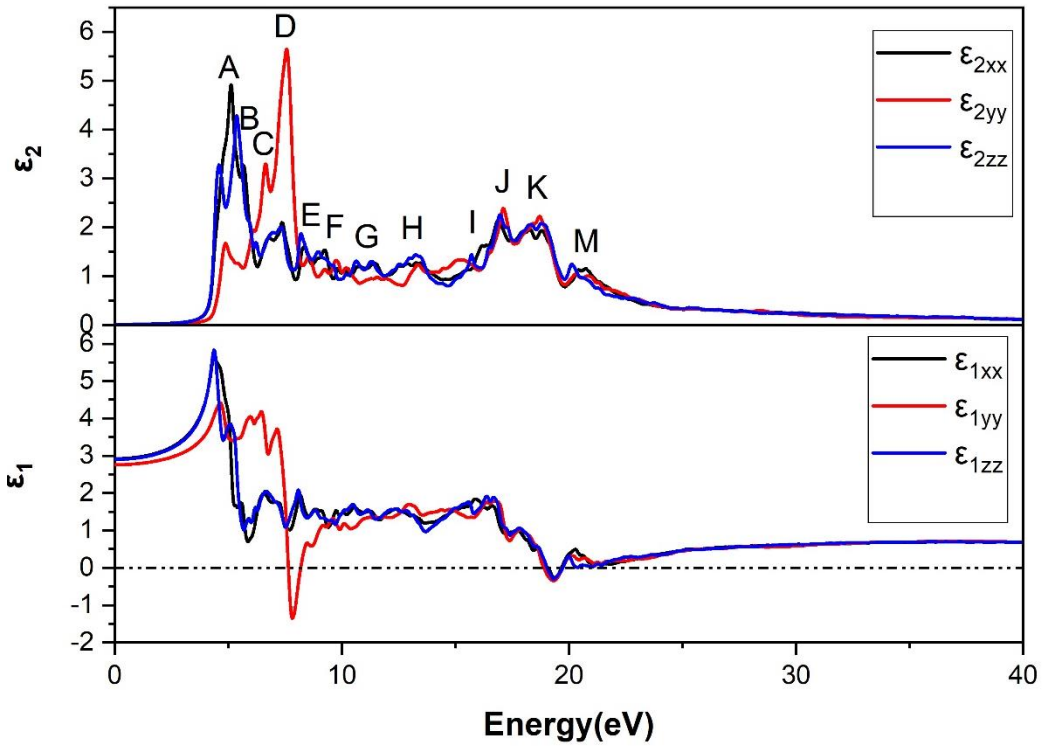

Figure. IV.A. 6. Calculated imaginary $\varepsilon_2(\omega)$ and real $\varepsilon_1(\omega)$ parts of the dielectric function for $RbIO_2F_2$.

Table. IV.A. 4. Peak positions of the $\varepsilon_2(\omega)$ spectrum together with the dominant inter-band transition contributions to every peak for $RbIO_2F_2$.

Dominant inter-band transition contributions			
Peak position	**Energy(eV)**	**Valence band (VBs)**	**Conduction band (CBs)**
A	**[4.51;4.82;4.51]**	**p-F, p-O**	**s-I**
B	**[5.68;6.1;5.38]**	**p-F, p-O, p-Rb**	**s-I**
C	**[7.3;6.65;6.21]**	**p-F, d-I, p-O, p-Rb**	**p-I**
D	**[8.24;7.56;8.44]**	**p-F, d-I, p-O, p-Rb**	**p-I**
E	**[9.26;8.47;9.7]**	**p-F, d-I, p-O, p-Rb**	**p-I**
F	**[10.61;9.6;10.26]**	**p-F, p-O**	**p-I**
G	**[11.4;11.81;11.68]**	**p-F, d-I, p-Rb**	**p-O**
H	**[13.45;13.3;13.4]**	**p-Rb**	**p-I**
I	**[16;15.25;15]**	**s-I**	**s-F, p-I, p-O**
J	**[16.89;17.11;17]**	**p-Rb, p-F**	**p-F**
K	**[18.81;18.7;18]**	**p-Rb**	**p-F**
L	**[20.74;20.32;20.33]**	**s-F, s-I, s-O**	**p-F, p-I, s-p -Rb**

It should be emphasized that any peak of $\varepsilon_2(\omega)$ can result from several direct and indirect inter-band transitions with the same energy. The limit static ε_1 (0) of dielectric constant is very important to assess anisotropy and birefringence. figure.IV.A.6, illustrates the polarization of $RbIO_2F_2$, showing an intrinsic anisotropy, and identical performance of the (100) and (001) planes, unlike the (010) plane.

The epsilon-across-zero points, in the real part of dielectric function, are related to the surface plasmon modes in $RbIO_2F_2$, and raised by hybridization of photons and Plasmon of metal. Plasmon-Polariton waves are electromagnetic waves that involve a quasi-particle. (SPP)[43], which propagates at the junction of a conductor and a dielectric [44]. Typically, the negative sign of ε_1 is used to represent this [45]. Hence, $RbIO_2F_2$ shows two across- zero; the first at [7.5,8.2] eV by (010) direction, and the second at [18.7,19.08] eV by all directions of the system. This strong anisotropy leads to an extended frequency window VUV, UV-C and EUV. All of the electrons in the system oscillate in these intervals, implying that the $RbIO_2F_2$ compound exhibits an entire reflection due to its metallic behaviour. On the other hand, this coupling produces a highly enhanced sensitivity in the IR detection of the $RbIO_2F_2$surface. Significant optic functions can be estimated using the parts of dielectric such as; absorption coefficient I(ω), refractive index n(ω), energy-loss L(ω) optical and reflectivity index R(ω), illustrated in figure. IV.A.7.

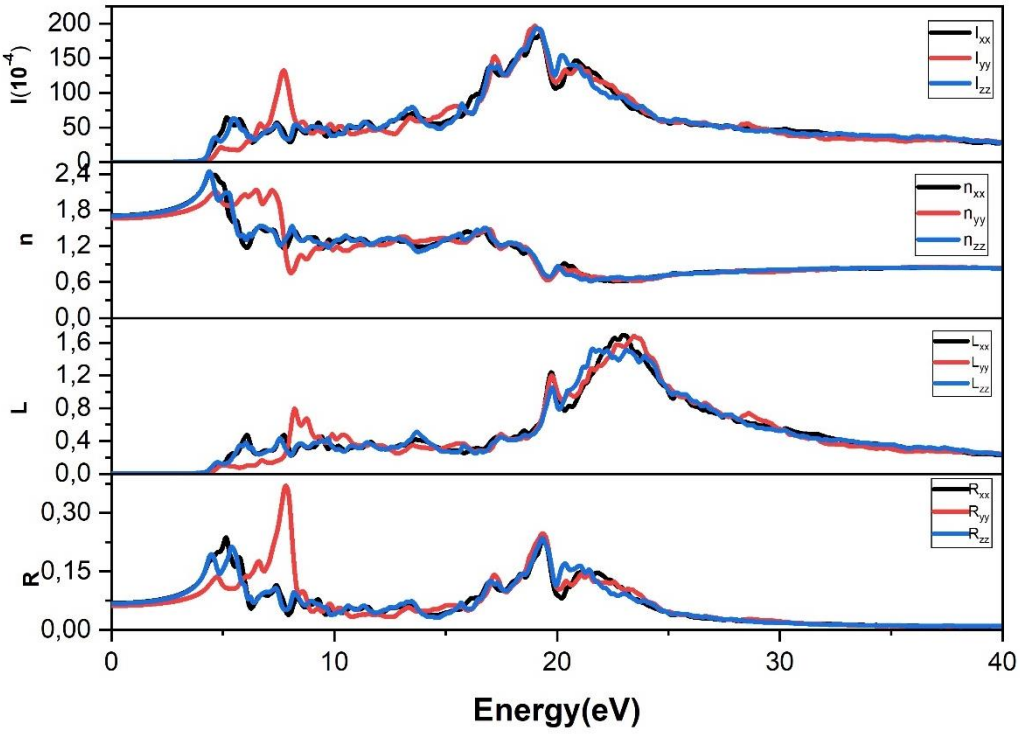

Figure. IV.A. 7. Calculated optical properties for $RbIO_2F_2$: absorption coefficient I(ω) (10^{-4}/cm), reflectivity R(ω), electron energy loss function L(ω) and refractive index n(ω) as function of energy of the incident photon.

Figure.IV.A.7. shows the inter-band absorption spectrum I(ω). The absorption edge starts from 4.26 eV, which exhibits a threshold between direct transition of the lowest CB and the highest VB. From band structure, this direct transition occurs at the Y point with a value of

4.21 eV. This result is in a very good agreement with corresponding results (absorption coefficient) with a percentage error of 1.1%. Consequently, $RbIO_2F_2$ crystal is transparent in the infrared range (IR), visible (Vis) and part of ultraviolet (UV-A) while the maximum of absorption coefficient has the point around 19.4 eV (EUV).

Figure. IV.A.7, also illustrates the behaviour of the refractive index n (ω), which follows the behaviour of real part ε_1 (ω) with energy photon incident through equation in chapter I. The calculated static limit for refractive indices n_{xx}, n_{yy} and n_{zz} are 1.70886, 1.66088 and 1.70295 .

The birefringence index Δn (ω) shown in figure.IV.A.8, according to the dispersion curve, the crystal $RbIO_2F_2$ is optically positive in the limit static on the order of 0.047. If we compare our result of the refractive and birefringence index to those induced by the calculation in ref [24] 0.058, there is a small difference, due to the difference in the two utilized codes. In addition, based on the curve Δn(ω) and n (ω), $RbIO_2F_2$ can be classified as frequency-doubling (SHG) crystal, due to the fact that it satisfies the phase-matching criteria inside its transparent zone, which extends to the mid-IR region.

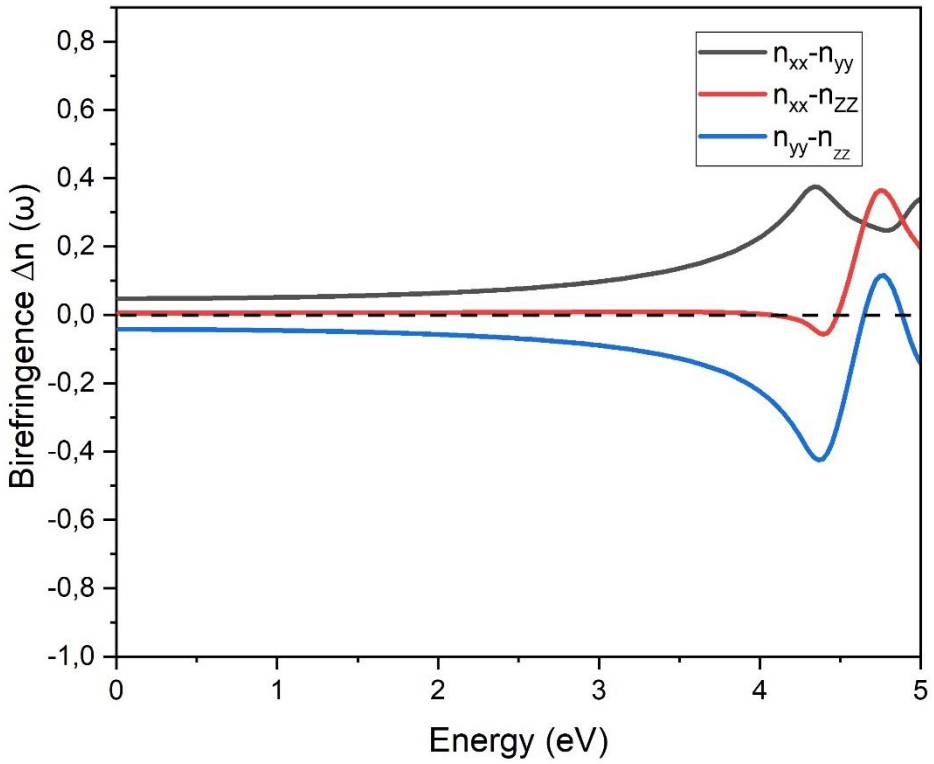

Figure. IV.A. 8. Birefringence of $RbIO_2F_2$.

Figure.IV.A.7, shows the electron energy loss L(ω). As expected from real part of dielectric function, the anisotropic nature of the $RbIO_2F_2$ is manifested in L(ω) through main

peaks, occurring at the energy $\hbar\omega p$ for different directions of light polarizations. L(ω) describes the interaction of rapidly traversing electrons in a solid. At the same time, it expresses two types of excitations; firstly, the collective excitation such as plasmons, excitons… etc. Surface plasmon-polaritons (SPP) can be determined according to real part of the dielectric function [45, 46]. It takes the value of 8.21 eV by (010) direction, and 19.72 eV by all direction of material. Therefore, it can be identified as an optical mode between the interface of a dielectric and a metal. Secondly, the one-electron excitation is due to the inter band transitions [45, 46].The values of ε_1 and ε_2 should tend to zero during this peak excitation. These are consistent with the highest peak in the energy loss function, where ω_p is called screened plasma frequency (volume plasmon-polaritons), positioned at ω_{pxx}=23eV, ω_{pyy} =23.5 eV and ω_{pzz} = 21.5 eV. At this point, the material $RbIO_2F_2$ has behaviour of a free electron gas. Hence, at these frequencies' energy, the reflectivity spectra, in figure.IV.A.7, shows an abrupt reduction in reflectivity.

IV.A.3.4. Mechanical and piezoelectric properties

Mechanical properties of a solid are known by an applying of external stress. The elastic constants C_{ij} are known as the ratio of stress to strain of a material. They have a great role to describe the mechanical properties of the materials such as; the stability, stiffness of the solid and bond strength between adjacent atomic planes. In addition, they are related also with thermodynamic behaviour such as; Debye temperature, specific heat [47-49]. Hence, we calculated the elastic constant for $RbIO_2F_2$ orthorhombic structure with space group $Pca2_1$, Using LDA-PW approximation implemented in ABINIT code.

It is well known that; the orthorhombic system has 9 independent elastic coefficients as follows; C_{11}, C_{12}, C_{13}, C_{22}, C_{23}, C_{33}, C_{44}, C_{55}, and C_{66} are given in table. IV. **A.**5, they must obey the criteria of stability (see chapter II)

Table. IV.A. 5. Calculated elastic constants C_{ij}(in GPa) for $RbIO_2F_2$.

Elastic Constants	**C_{11}**	**C_{22}**	**C_{33}**	**C_{44}**	**C_{55}**	**C_{66}**	**C_{12}**	**C_{13}**	**C_{23}**
$RbIO_2F_2$	**305.51**	**292.89**	**300.96**	**109.66**	**100.16**	**78.2**	**100.93**	**81.99**	**113.6**

After fulfilled the stability conditions for orthorhombic structure, we can confirm that the $RbIO_2F_2$is mechanically stable. The bigger value of C_{11} than C_{22} and C_{33}, as shown in table.

IV.A. 5, indicates that the (100) plane has weak compressibility compared to the other two planes (010) and (001). On the other hand, because C_{22} has a lower value than C_{11} and C_{33}, we may assume that $RbIO_2F_2$'s thermal expansion will occur mostly along the (010) plane. C_{44} is very important parameter to assess the hardness of the materials with indirectly manner because it exhibits the resistance against the monoclinic shear distortion along (100) plane, while the C_{66} parameter exhibits resistance to shear in (110) plane. The large value of C_{44} indicates that $RbIO_2F_2$ has a strong ability to resist the monoclinic shear distortion in the (100) plane. Our findings show that the plane (100) has more mechanical qualities than other planes.

Other parameters such as Debye temperature, anisotropic factors Elastic Modulus, anisotropic factors, and Debye temperature can be computed using elastic constants.

In general, elastic moduli are used mainly to describe the behaviour of materials, using the following approximations; Voigt, and Reuss. Hill proved the intermediate between Reuss and Voigt approximations, representing the lower and upper limits. The calculated Voigt, Reuss, and Hill bulk (B_V, B_R, B_H), shear (G_V, G_R, G_H), Young's moduli (E), B/G ratio and Poisson ratio (ν) are resumed in the table. IV.A. 6

Table.IV.A.6 shows that Young's modulus is greater than bulk B and shear G moduli, indicating that the $RbIO_2F_2$ compound is more resistant to elastic deformation. Our B/G value of 1.71 is slightly smaller than 1.75 (criteria which speared the brittle and ductile manner), so $RbIO_2F_2$ material behaves as least ductile. For the Poisson ratio (ν) [49], we find 0.25 which is smaller than 1/3, corresponding to a brittle behaviour. In this context, the ionic contribution to inter atomic bonding is dominant [50]. In orthorhombic structure, Cauchy pressure in three different planes; (100) = (C_{23}-C_{44}), (010) = (C_{13}-C_{55}) and (001) = (C_{12}-C_{66}) are equalled to 3.94GPa, -18.25GPa and 22.72GPa respectively. The positive and negative values indicate metallic and brittle bonds, respectively; nonetheless, the high Cauchy pressure value, whether positive or negative, indicates the ionic bonds [51] and means that $RbIO_2F_2$ is harder in the (100) plane, as predicted by the C_{ij} values, and that the ionic bond is dominant in the other planes. These results can be confirmed using the above electronic proprieties.

Table. IV.A. 6. Bulk moduli B (GPa), shear moduli G (GPa), Young's moduli E (GPa), Poisson's ratio ν and B/G ratios) of $RbIO_2F_2$.

Modulus	Bv	B_R	B	Gv	G_R	G	E	ν	B /G
$RbIO_2F_2$	165.8	165.8	165.8	97.8	96.1	96.9	243.3	0.25	1.7

IV.A.3.4.1. Debye temperature

The thermodynamic properties of the material are very useful to describe the chemical bonding and thermal properties of materials , [52]. During the laser cladding process, the compound undergoes rapid heating and cooling. The specific heat and melting temperature have a close relationship to the Debye temperature (Θ_D). Usually, the bigger Θ_D reflect the larger micro-hardness. The results are summarized in table. IV.7, which are consistent with the pervious results about intermediate hardness for $RbIO_2F_2$.

Table. IV.A. 7. Transverse (v_t in m/s), Longitudinal (v_l in m/s), mean sound velocity (v_m in m/s) and Debye temperature (Θ_D in K)) of $RbIO_2F_2$.

	ν_l	ν_t	ν_m	Θ_D
$RbIO_2F_2$	679.24	944.06	750.78	110.21

However, we can use our computation of the mechanical properties of $RbIO_2F_2$, as a reference tool, for further analysis or experimental research.

IV.A.3.4.2. Anisotropic factors

Elastic anisotropy can help to measure various properties such as; shear anisotropic (A_G), bulk anisotropic (A_B) and anisotropy of young modulus. It can also give information of atomic planes behaviour among different directions. We have estimated the universal anisotropic index (A^U) and the percent anisotropy (A_B, A_G) in different planes, as summarized in table. IV.A.8.

Table. IV.A. 8.Calculated universal anisotropic index (A^U), anisotropy factors (A_B and A_G) of $RbIO_2F_2$.

Anisotropy	A^U	A_B (%)	A_G (%)
$RbIO_2F_2$.	**0.09**	**0.03**	**0.88**

When the universal anisotropy index A^U=0, the crystal can be considered as isotropic [53] as seen in table. IV.A.8, the universal anisotropy index A^U is characterized $RbIO_2F_2$ by a modest value indicating somewhat anisotropic nature. Clearly demonstrates that A_B value is much smaller than the A_G value, implying that the anisotropic resistance to reversible deformations, created by shear stress [44], is more relevant than the anisotropic resistance to volume change, caused by an applied pressure [49].

We can more intuitively characterize the anisotropy of Young E and Bulk B modulus, by employing their 2D (circular) and 3D (spherical) representations to judge the isotropic and anisotropic properties. We illustrate 2D and 3D projection of the directional dependencies of the Young's and bulk Modulus for the planes XY, XZ, YZ in figures. IV.A.9 and 10, respective.

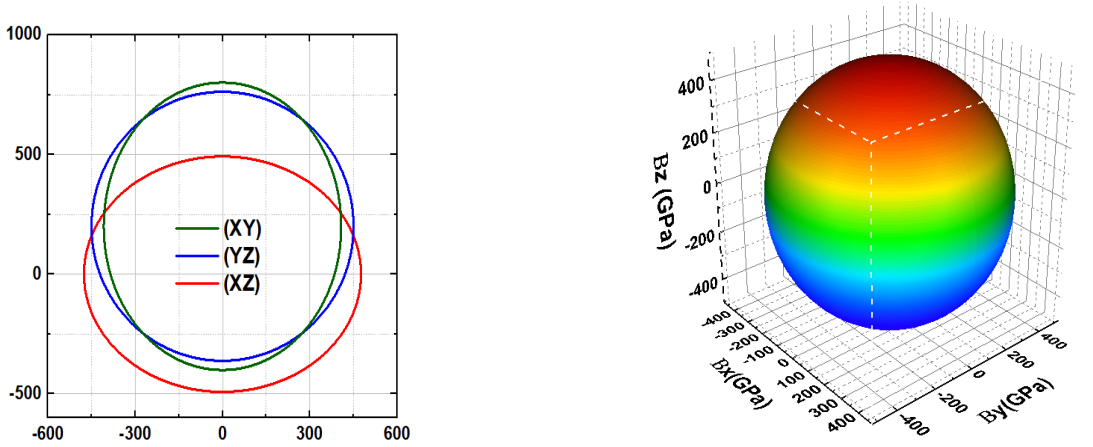

Figure. IV.A. 9. The 3D projection of bulk moduli and your 2D projection of $RbIO_2F_2$

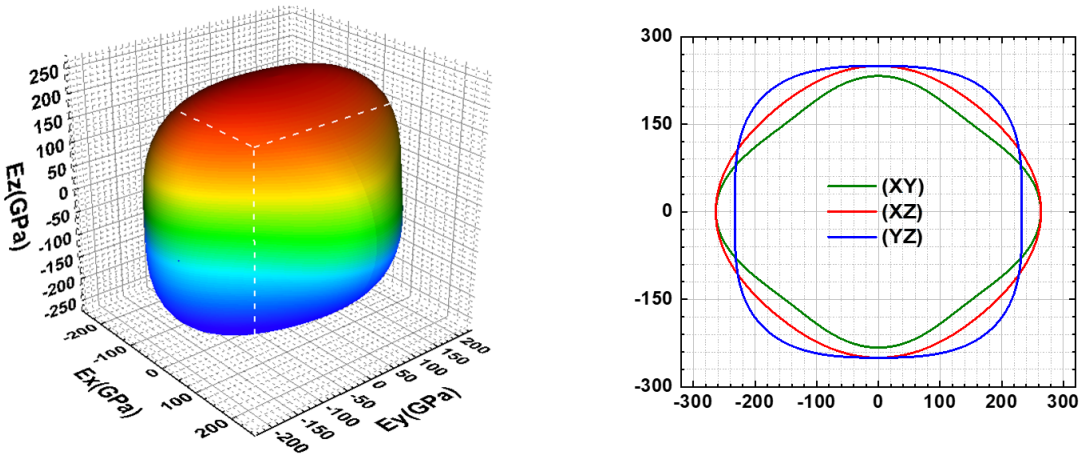

Figure. IV.A. 10. The 3D projection of Young and your 2D projection of $RbIO_2F_2$.

The degree of anisotropy is determined by the deviation of circular or spherical shapes. As a result, the anisotropy of Young's modulus in planes is more obvious than the anisotropy of the bulk modulus, despite the fact that the bulk modulus has a similar anisotropic nature in planes.

IV.A.3.4.3. Piezoelectric property

The piezoelectric stress tensor response, induced by third-rank tensor, which describes the dielectric response to a strain in crystals, is exceptional only for NCS materials and is expressed by:

$$\mathbf{d_{ij}} = \frac{\partial \mathbf{P_i}}{\partial \boldsymbol{\varepsilon}_j} + \frac{\mathbf{e}}{\boldsymbol{\Omega}} \sum_{\mathbf{k}} \frac{\partial \mathbf{P_i}}{\partial \mathbf{u_i^k}} \Big|_{\boldsymbol{\varepsilon}} \frac{\mathbf{du_i^k}}{\mathbf{d}\boldsymbol{\varepsilon}_j}$$

where i = 1; 2; 3, j = 1; 2;: : : ; 6, k is the atom index. Using the Berry-phase approach, the piezoelectric coefficients Pi are calculated directly from the fluctuation in the intensity of the polarization in the I direction caused by the application of strain j, where j is a component of the strain tensor., which is evaluated using modern theory of polarization, e is the electron charge, Ω is the unit cell volume, u_i^k is the i component of the displacement of the k-the atom[54, 55]. Our compound $RbIO_2F_2$ belongs under mm2 class, so it exhibits five nonzero components, namely d_{15}, d_{24}, d_{31}, d_{32}, d_{33}, are resumed in table.A. IV.9. Unfortunately, there are no experimental or theoretical piezoelectric data for $RbIO_2F_2$. For comparison, the well-known piezoelectric material a-quartz has only two independent piezoelectric coefficients, i.e., d_{11} and d_{14}. From table.IV.A.9, we see that; for $RbIO_2F_2$ shows the value of the largest component d_{15} among the other's (7.82 pC/N), which is about three times larger than that of a-quartz d_{11}(-2.3 pC/N).

Table. IV.A. 9. Relaxed ion piezoelectric tensor d_{ij} in PC/N for $RbIO_2F_2$.

d_{15}	d_{24}	d_{31}	d_{32}	d_{33}
7.827	**6.542**	**-1.1356**	**-0.327**	**4.3441**

The large value of d_{15} means that; the polarization along the direction (001) is easily affected by external stress. The large piezoelectric effect in $RbIO_2F_2$ demonstrates its potential applications in sensors fields, surface and bulk acoustic waves.

IV.A.3.5 Nonlinear optical properties

IV.A.3.5.1. Nonlinear optical susceptibilities

Nonlinear optics has important applications thanks to phenomena related to frequency mixing such as second harmonic generation (SHG) in many technical areas such as optoelectronics, laser science, and optical signal processing. By the application of an electric field, a large relative displacement of cationic and anionic sub lattices appears which then induces a shifting of polarization in crystal. The vector polarization *P* for the macroscopic electric field E can be expressed by a Taylor expansion:

$$\mathbf{P_i} = \mathbf{P_i^s} + \sum_{\mathbf{j}} \boldsymbol{\chi}_{\mathbf{ij}}^{(1)} \mathbf{E_j} + \sum_{\mathbf{j,k}} \boldsymbol{\chi}_{\mathbf{ijk}}^{(2)} \mathbf{E_j E_K} + \cdots$$

Where i, j, k denotes Cartesian components. Our compound $RbIO_2F_2$ belongs to the non-centro-symmetric component under mm2 class. We have only considered the second harmonic term, exhibiting the nonlinear optical susceptibility of the second order [56]. We can use the relationship: $d_{ij} = \frac{1}{2}\chi^2_{ijk}$. d_{ij} is known as the non-linear optic (NLO) coefficient or the piezoelectric strain tensor, to represent the third order derivative of the energy of polarization with respect to electric field components , [57]. The Voigt notation represents the NLO tensor (3×6 matrix) by three independent elements nonzero; d_{15}, d_{24} and d_{33} are -0.534 pm/V, -1.125 pm/V and -10.04 pm/V, respectively.

Table. IV.A. 10. Static nonlinear optical coefficients d_{ij} (pm /v) for $RbIO_2F_2$.

	$d_{15}=d_{31}$	$d_{24}=d_{32}$	d_{33}
$RbIO_2F_2$	**0.535**	**1.125**	**10.042**

The real response for each material corresponds to their d_{eff}, which depends on the anisotropy, optical axis, crystal orientation, phase matching types ...etc. For this crystal class (2mm), the d_{eff} is directly related d_{31}, d_{22}, and d_{33} for all different possible phase matching types. The d_{eff} possible values, depending on crystal rotation and phase matching type by the following relations;

$$\mathbf{d_{eff} = d_{15}\sin^2\varphi + d_{24}\cos^2\varphi}$$
$$\mathbf{d_{eff} = d_{31}\sin^2\varphi + d_{32}\cos^2\varphi}$$
$$\mathbf{d_{eff} = d_{15}\sin\theta}$$
$$\mathbf{d_{eff} = d_{31}\sin\theta}$$
$$\mathbf{d_{eff} = d_{32}\sin\theta}$$
$$\mathbf{d_{eff} = d_{24}\sin\theta}$$

The direction of the wave vector is specified by spherical coordinates ($\boldsymbol{\theta}$, $\boldsymbol{\phi}$) referenced to the crystalline axes; $\boldsymbol{\rho}$is the birefringent walkoff angle.

IV.A.3.5.2 Electro-optic tensor

The electro-optic tensor has been calculated, using the Born-Oppenheimer approximation, from the interaction between the electric field E and constitutions of the crystal.

An important phenomenon appears in $RbIO_2F_2$ (class mm2) which is the EO effect with non-zero five independent elements r_{13}, r_{23}, r_{33}, r_{42} and r_{51}.The results of the total and electronic contribution in the EO are resumed in table. IV.A.11. The main contribution comes from the r_{33} which means that; there is a low-frequency mode combining high polarity and high Raman intensity, [58]. The highly distorted structure of $RbIO_2F_2$ is favourable for obtaining a large linear EO effect.

Table. IV.A. 11. linear electro-optic (EO) r_{ij} (Pm / V) for $RbIO_2F_2$.

	r_{51}	r_{42}	r_{13}	r_{23}	r_{33}
Electronic contribution	**0.216**	**0.554**	**0.217**	**0.679**	**4.038**
Total contribution	**-0.211**	**1.109**	**0.242**	**0.283**	**14.346**

IV.A.4. Conclusion

In this work, we used ab-initio method based on DFT and DFPT within GGA-PBE, TB-mBJ and LDA-PW to investigated $RbIO_2F_2$. Both the calculated lattice parameters are in agreement with the experimental results. For the electronic structure of the system, an indirect band gap is found to be (4.17 eV) with a deviation of 0.47% from the experimental value. The optical properties were computed and argued in detail. From the calculated absorption spectra which ensures the high transparency in the infrared, visible and part of ultraviolet (UV-A) ranges, the calculated value of the birefringence $\Delta n(\omega)$ for $RbIO_2F_2$ shows that it is a uniaxial positive crystal and has a small birefringence (0.047). The obtained elastic constants indicate that $RbIO_2F_2$ is mechanically stable. The higher value of Young's modulus than bulk modulus and shear modulus, makes $RbIO_2F_2$a has a greater resistance to elastic deformation. Moreover, B/G ratio show the intermediate hardness of $RbIO_2F_2$. In addition, the anisotropy of the elastic properties is discussed. We have investigated the NLO susceptibilities and EO tensor. The point group mm2 of $RbIO_2F_2$ have three independent elements d_{15}=-0.534 pm/V, d_{24}=1.125 pm/V, and d_{33}= -10.04 pm/V. and the electronic contribution EO tensor has five independent elements r_{13}=0.21 pm/V, r_{23}= 0.67pm/V, r_{33}= 4.03pm/V, r_{42}=0.55pm/V and r_{51}=0.16pm/V. For the piezoelectric stress tensor, there are five independent nonzero elements d_{15}=7.827 pC/N, d_{24}=6.542 pC/N, d_{31}=-1.13 pC/N, d_{32}=-0.32 pC/N, and d_{33}=4.34 pC/N.

Part B

compound $CsIO_2F_2$

IV.B.1. Introduction

Iodates have attracted continuously intensive studies due to their plentiful structures and many important applications in the fields of nonlinear optics, luminescence, photocatalysis, etc, [59-61]. Owing to the lone-pair electron cation (I^{5+}) with stereochemical activity, the iodates tend to crystallize in non-centrosymmetric (NCS) structures and usually show strong second-order polarizability and large optical anisotropy, [12, 62, 63] Moreover, iodates have wide transparent wavelength regions (from UV/Vis to Mid-Infra) and are easy to grow sizable crystals via mild reaction conditions. During the last few decades, a large number of iodates with strong second harmonic generation (SHG) responses and wide transparent ranges have been reported, for example, α-$LiIO_3$,[64] AgI_3O_8,[65] $BaNbO(IO_3)_5$, [66] $BiOIO_3$,[67] etc.

Recently, fluorine-containing systems for designing optical materials,[68, 69]such as iodates, [69]borates,[70]carbonates,[71]phosphates,[72]etc. are very attractive, because the introduction of the F anions into the maternal systems can not only regulate the crystal structure, but also broaden the band gap and generate high laser damage threshold (LDT).

Fluoro-iodine materials provide a good platform for new materials that are promising for optoelectronic and photonic (efficient optical second harmonic (SHG) generation). More recently, there have been a lot of research efforts dedicated to the nonlinear optical (NLO) properties of these Fluoro-iodine materials because of their unique combination of chemical, structural, and optical properties.A large number of NLO materials have been reported in this regardsuchas;$RbIO_2F_2$[24],$CsIO_2F_2$[25],$Bi(IO_3)F_2$[23],$BiFSeO_3$[73],$Bi_3OF_3(IO_3)_4$[27],$ABi_2(IO_3)_2F_5$(A=K, Rb and Cs)[28], Li7(TeO3)3F[74], $ABi_2SeO_3F_5$ (A= K and Rb)[75], SbF_3 [76], $NaSb_3F_{10}$ [77], $K_2SbF_2Cl_3$ [78] and KBi_4F_{13}[79], most of which exhibit large SHG effects and large band gap. Therefore, searching for fluorine-containing compounds could also be a good strategy to explore materials with large band gaps and thus high LDT in the UV region.

The NSC $CsIO_2F_2$ exhibit good nonlinear optical property with large second-harmonic generation (SHG) effects (3 × KH_2PO_4), wideband gaps (4.56 eV), wide transmittance ranges (∼0.27−5.5 μm), and high laser damage thresholds (15 × and 20 × $AgGaS_2$, respectively), which shows that they are potential nonlinear optical materials in near-ultraviolet to mid-infrared, [25]. To investigate its performance in various properties such as lattice dynamics, electronic structure, optical, mechanical, nonlinear optical coefficients, electro-optic tensors, and piezoelectric. properties, we have performed by first-principles calculations DFT.

IV.B.2. Calculation Method

All calculations presented in this part are based on the density functional theory (DFT) [30, 31]combined firstly, with the (FP-LAPW) method, as implemented in the WIEN2 k code [32, 33]. To perform calculations of the structural properties, we used Generalized Gradient Approximation GGA was developed by Perdew-Burker-Ernzerhof (GGA-PBE) [34]. The recently developed modified Becke-Johnson exchange potential (TB-mBJ) is used for the electronic and optical properties, [35]. The valence electron configurations used in the calculations are Cs($5d^{10}6s^26p^3$), I($4d^{10}5s^25p^2$), O($2s^22p^4$) and F($2s^22p^5$). In the present work, the wave function, charge density, and potential are expanded by spherical harmonic functions inside non-overlapping spheres surrounding the atomic sites (muffin-tin spheres) and by a plane wave basis set in the remaining space of the unit cell (interstitial region). The plane-wave cutoff which controls the size of the basis, defined by the product of the smallest atomic sphere radius times the magnitude of the largest reciprocal lattice vector ($R_{MTmin}.K_{max}$), was set to 7.0. The muffin tin radii were set to1.8, 1.75, 1.4, and 1.4 atomic units (a.u) respectively. For a band structure representation, we chose the grid (12 14 12) k-points was generated in the irreducible part of the Brillouin zone (BZ) to compute the total and projected.

And secondly, we implement the calculations using plane-wave energy cutoff of 50 Hartree and 6 6 6 Monkhorst–Pack grid of Brillouin-zone k-points sampling is used to optimize the structure is used to extract the physical properties. The exchange and correlation effects are treated within the local density approximation (LDA). The structures are fully optimized until the residual forces acting on each atom are less than 10^{-7} (hartree/bohr).Density-functional perturbation theory (DFPT)we used to extract the following physical quantities.[80, 81] ; The elastic constant, piezoelectric constant, nonlinear optical coefficient, and electro-optic coefficient, which was we employ ABINIT code in the present study.

IV.B.3. Ground state properties

IV.B.3.1 Structural properties

$CsIO_2F_2$ crystallizes in the NCS structure, which is orthorhombic with the space group $Pca2_1$(No. 29) as presented in the figure. IV.B.1.

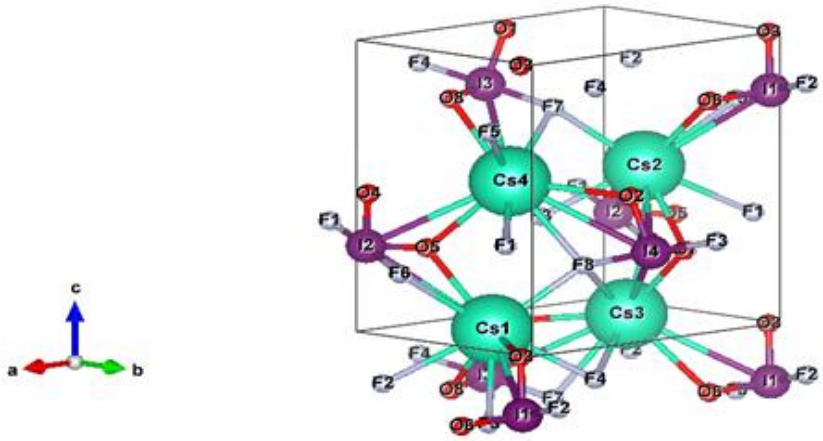

Figure. IV.B. 11. Conventional cell of $CsIO_2F_2$.

After optimizing the structural parameters, the atomic positions are relaxed to reduce the Hellmann-Feynman forces and energy, the relaxed lattice parameters for the a, b, and c crystals are presented in the table.IV.B.1, and are compared with previous experimental data. Our calculated lattice parameters and unit cell volume for $CsIO_2F_2$ are compared with the experimental data, [25]. Our computed lattice parameters for $CsIO_2F_2$ by LDA approximation are underestimated by an error not exscinding 8 %, which is consistent with the general trend of the LDA.for the GGA-PBE approximation is overestimate the all-lattice parameter by 2.5% which is consistent with the general trend of the GGA.

Table. IV.B. 12. Calculated and experimental lattice parameters of $CsIO_2F_2$.

parameters	**Exp (Å) [25]**	**GGA-PBE**	**ΔX /X**	**LDA-PW**	**ΔX /X**
a(Å)	**8.781**	**9.009**	**2.5%**	**8.198**	**6.63%**
b(Å)	**6.3771**	**6.542**	**2.5%**	**6.242**	**2.1%**
c(Å)	**8.868**	**9.098**	**2.5%**	**8.201**	**7.52%**

Table. IV.B.2. Calculated and experimental atomic positions of $CsIO_2F_2$.

Atoms	**Exp. [25]**	**GGA-PBE**	**LDA-PW**
F(1)	**(0.93120 ; 0.75150 ;0.35040)**	**(0.93220 ;0.76150; 0.35340)**	**(0.93522; 0.75101;0.35509)**
F(2)	**(0.94080; 0.67000 ;0.26690)**	**(0.91280; 0.67040; 0.23310)**	**(0.94564; 0.645512; 0.229297)**

I	**(1.00905; 0.95851 ;0.20381)**	**(1.49095; 0.95851; 0.29619)**	**(0.99426;0.98315; 0.29341)**
O(1)	**(0.47270; 0.10450 ;0.01470)**	**(0.48170; 0.14550; 0.02530)**	**(0.47540 ;0.12464 ;0.01150)**
O(2)	**(0.79890 ; 0.11820 ; 0.27420)**	**(0.70110; 0.11820; 0.27420)**	**(0.785251 ;0.12147 ;0.27095)**
Cs	**(0.78520 ; 0.47162 ;0.02371)**	**(0.71480 ; 0.47162 ;0.02371)**	**(0.78568;0.45954;0.01363)**

Table. IV.B. 3. Calculated and experimental bond length of $CsIO_2F_2$.

Bond length (Å)	Exp [25]	GGA-PBE	ΔX /X	LDA-PW	ΔX /X
F (1)-I	**1.981**	**2.032**	**2.5%**	**1.76**	**11.1**
F (2)-I	**2.014**	**2.06661**	**2.5%**	**1.89**	**6.15**
I-O (1)	**1.754**	**1.79936**	**2.5%**	**1.701**	**3.02%**
I-O (2)	**1.767**	**1.81261**	**2.5%**	**1.725**	**2.3%**

Similarly, for the parameter lattice parameter, both LDA and GGA-PBE approach tends to underestimate and overestimate, respectively, the bond length in table. IV.B. 3 are in agreement with data. On another side, the atomic positions in table.IV.B.2 are also shown in good accord with experimental atomic positions.

IV. B.3.2. Electronic structure

The electronic structure is an important quantity dominating the material's properties, and its study is necessary to bridge the relationship between the material structure and properties.

IV.B.3.2.1 Band structure

The band structure of $CsIO_2F_2$ along the high-symmetry directions in the first Brillouin zone (BZ) is TB-mBJ potential which is shown in figure IV**.** B. 2. It is to be noted that the band structure of the orthorhombic structure is determined according to the orthorhombic Brillouin

zone and the electron dispersion curves of the orthorhombic (Pc21a) structure are determined along with ten different symmetry directions in the BZ. The experimental band gap is 4.56 eV, the analysis of our result reflect that the CsIO2F2 is an indirect band gap insulator with valence band maximum at Γ and conduction band minimum at Y point by 4.54 eV value of band gap, which underestimate the value of band gap by 0.4 % it is well known that TB-mBJ produces band gap values in close agreement with experimentally measured values, in our case is confirmed case the trend general of this functional.

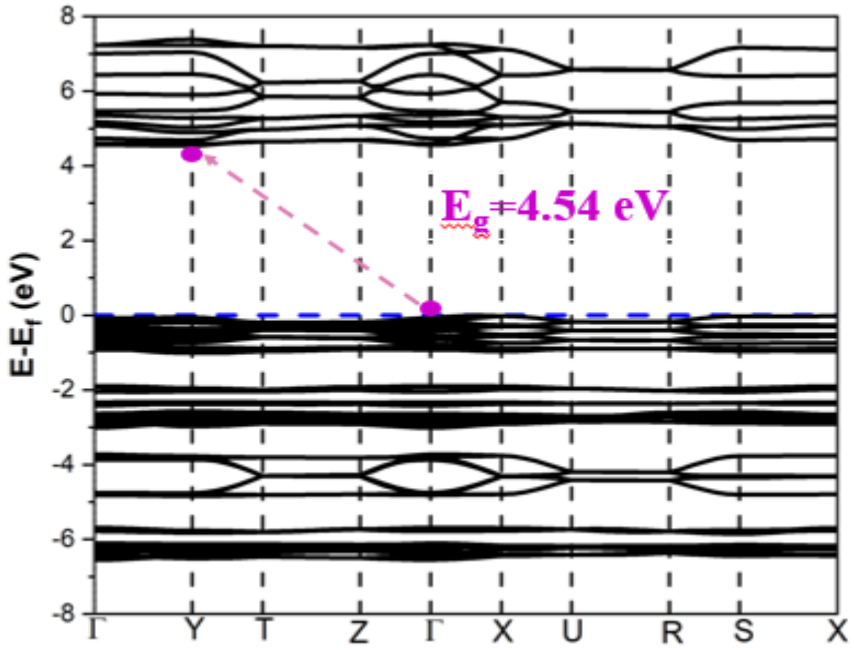

Figure. IV.B. 12. Calculated band structure by using TB-mBJ functional for $CsIO_2F_2$.

IV.B.3.2.2. Density of states

To know the predominant states near valence and conduction bands we have plotted the density of states using TB-mBJ functional as shown in the figure. IV.B.3, As shown in the figure. IV.B.3, the VB edge below the Fermi level at [-1.1;0] eV is mainly composed of O-p states with a slight I- p and F-p states, while the bottom of CBs is occupied by I-p states, which indicates that I-O-F units are the main sources to determine the magnitude of band gaps.

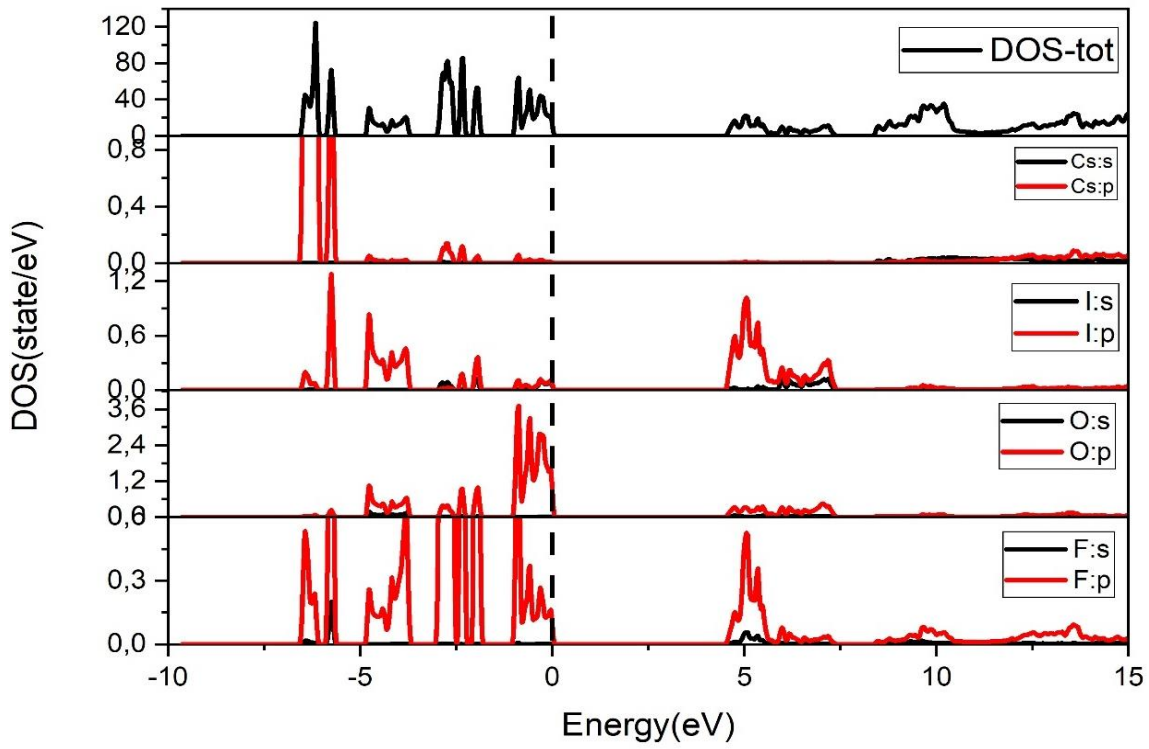

Figure. IV.B. 13. Calculated total and partial DOS for $CsIO_2F_2$.

IV.B.3.2.3. Charge-Density Distribution

Chemical bonding can be well understood from the charge density calculations. We have plotted the charge density difference plot for the $CsIO_2F_2$ host compound as shown in the figure. IV.B.4. From the figure, we can see that the charge present between I, F, and O atoms are mutually shared indicating the covalent nature of the I-O and I-F bond. The quasi-spherical charge distributions between Cs-O indicate the ionic nature of bonding.

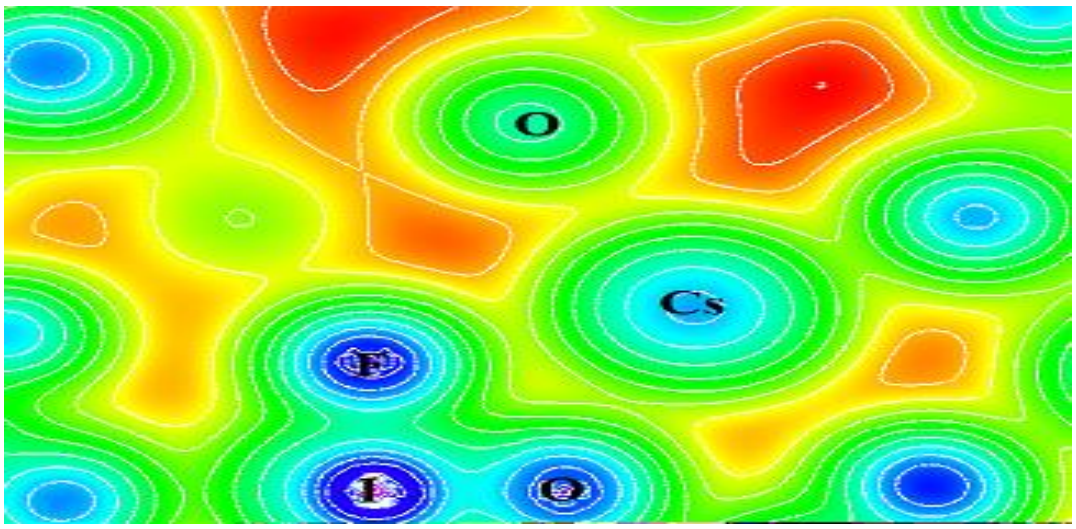

Figure. IV.B. 4. Calculated density of charge in a plane containing Cs, I and O atoms.

IV.3.3. Optical properties

The analysis of the optical properties of the materials leads to a better understanding of the electronic structure and vice versa.

To understand the response of the system to electromagnetic radiation, we have calculated the complex dielectric function ε(ω), absorption coefficient I(ω), refractive index n(ω), electron energy loss function L(ω), reflectivity R(ω) of the host compound. The imaginary part of the complex dielectric function is calculated from the momentum matrix element between the filled and unfilled states. The real part of the dielectric function is calculated from the imaginary part of the dielectric function by using the Kramers-Kronig relation. The calculated dielectric function is shown in the figure. IV.B.5 with real and imaginary parts as a function of photon energy.

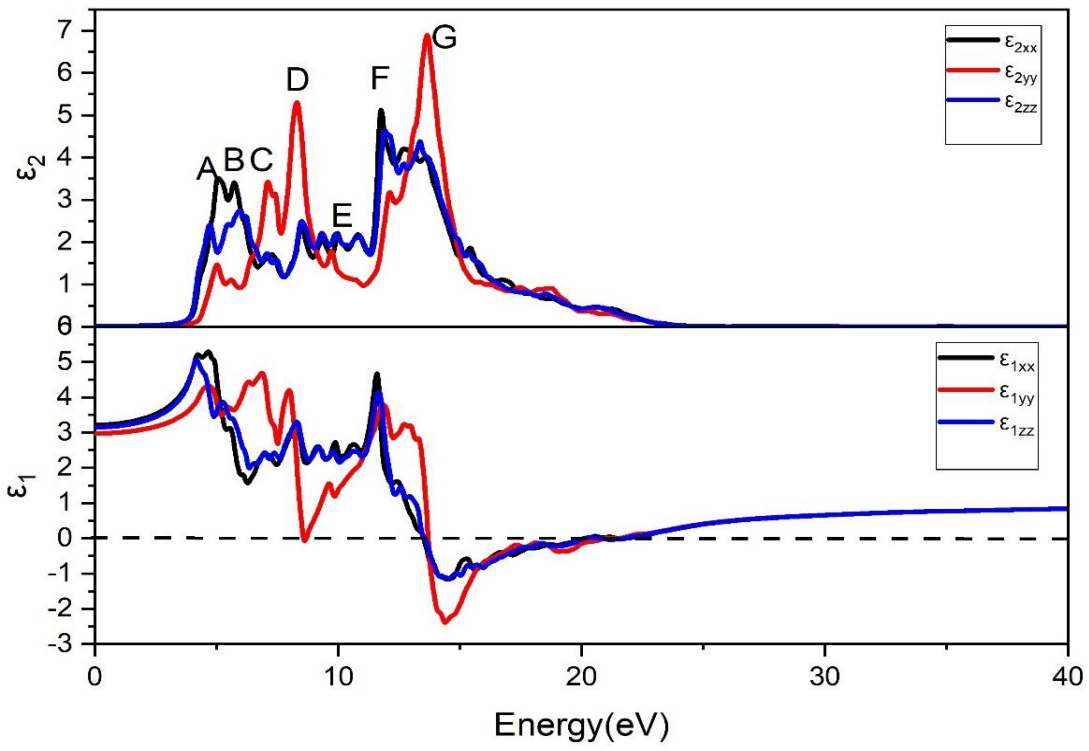

Figure. IV.B. 14. Calculated imaginary $\varepsilon_2(\omega)$ and real $\varepsilon_1(\omega)$ parts of the dielectric function for $CsIO_2F_2$.

The imaginary part of the dielectric function has about 7 peaks (A, B, C, D, E, F, and G) principal, which is due to the transition of electrons from the valence band to the conduction band that is resumed in the table. IV.B.4

Table. IV.B. 4. Peak positions of the $\varepsilon_2(\omega)$ spectrum together with the dominant inter-band transition contributions to every peak for $CsIO_2F_2$.

Dominant inter-band transition contributions			
Peak position	**Energy(eV)**	**Valence band (VBs)**	**Conduction band (CBs)**
A	**[4.96;4.93;4.63]**	**p-F, p-O**	**p-I**
B	**[5.83;5.76;6.09]**	**p-F, p-O**	**p-I**
C	**[7.35;7.11;7.04]**	**p-F, p-O**	**p-I**
D	**[8.46;8.31;8.46]**	**p-Cs, p-F**	**p-I**
E	**[10.07;9.82;10.07]**	**p-Cs, p-F**	**p-I**
F	**[11.74;9.82;11.74]**	**p-I, p-O**	**p-F**
G	**[12.65;13.6;13.42]**	**p-I, p-O**	**p-F**

The real part of the dielectric function shows that $CsIO_2F_2$ is an optically anisotropic compound in the along energy region [0-20] eV unlike along energy region [20-40] eV. The real part of the dielectric function goes to negative values at [13.54-20.33] eV of energy, for this region of energy, will be contributed to enhancing their nonlinear optical property.

The other optical properties such as absorption coefficients I (ω), refractive index n (ω), energy loss function L (ω), and reflectivity R (ω) are plotted in the figure. IV.B.6.

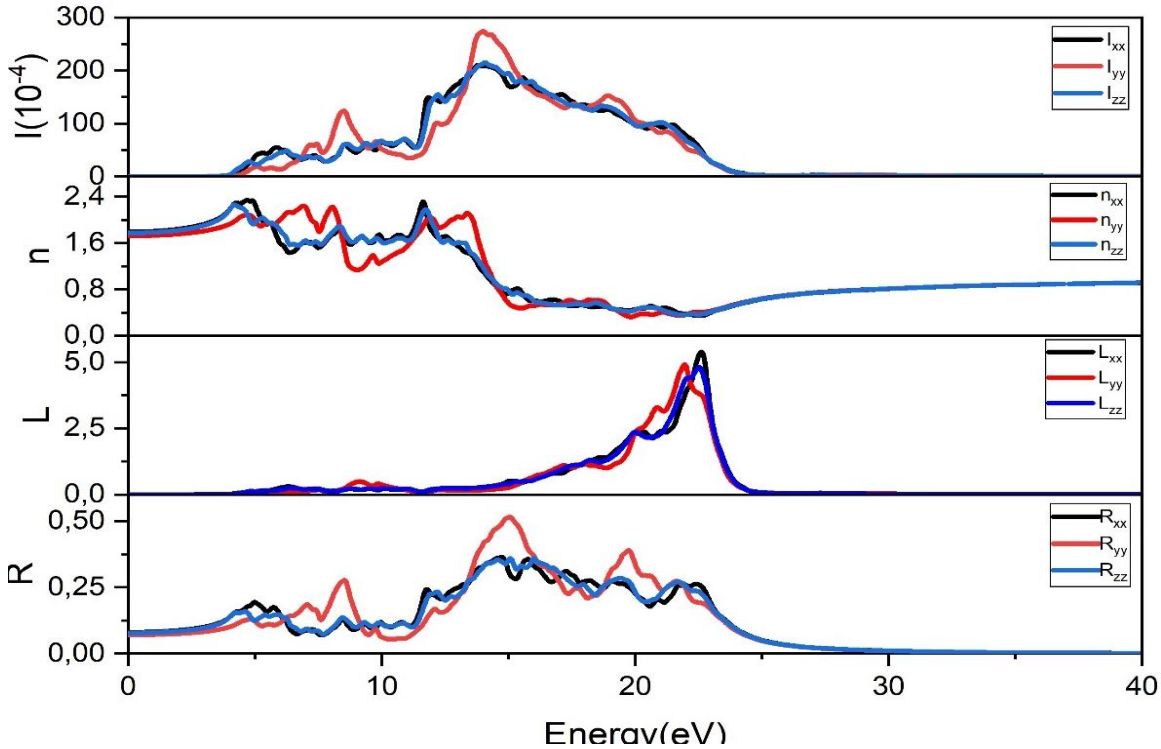

Figure. IV.B. 15. Calculated optical properties: absorption coefficient I(ω) (10^{-4}/Cm), reflectivity R(ω), electron energy loss function L(ω) and refractive index n(ω) as function of energy of the incident photon for $CsIO_2F_2$.

The refractive index n(ω) plots as a function of photon energy, the static refractive index values are found to be 1.79287;1.7245;1.7751 along x; y; z directions respectively. As the birefringence reflects the optical anisotropy of a crystal, and also it is an essential qualification to achieve phase matching, we plotted the birefringence Δn (ω)in the figure. IV.B.7. We present that the Δn (ω) $CsIO_2F_2$ has birefringence positive (n_{xx}-n_{yy}) ~0.06.

We have also calculated the other important optical property i.e., frequency-dependent absorption I (ω). For the present studied $CsIO_2F_2$, there is no absorption below 4.58 eV which shows $CsIO_2F_2$ to be a transparent material below 4.58 eV. Consequently, the $CsIO_2F_2$ crystal is transparent in the infrared range (IR), visible (Vis), and part of ultraviolet (Deep UV (DUV, UV-C)).

Electron energy loss L (ω) function is also calculated from the dielectric. The significant peaks of the function are called the plasma peaks, and they indicate the electronic charge oscillations in the system, and the corresponding frequencies are called plasma frequencies. The plasma peaks are observed around the energy of L_{xx} (ω) =22.48 eV, L_{yy} (ω) =21.88eV, L_{zz}(ω) = 22.48eV. We have noticed that at these values of plasma peak energies, the real part of the

dielectric function crosses the zero value and becomes negative. The reflectivity plot of $CsIO_2F_2$ is correlated with the maximum peak that occurred in our reflectivity spectra and to the crossing zero of refractive index static value, and correspond to edges in R (ω).

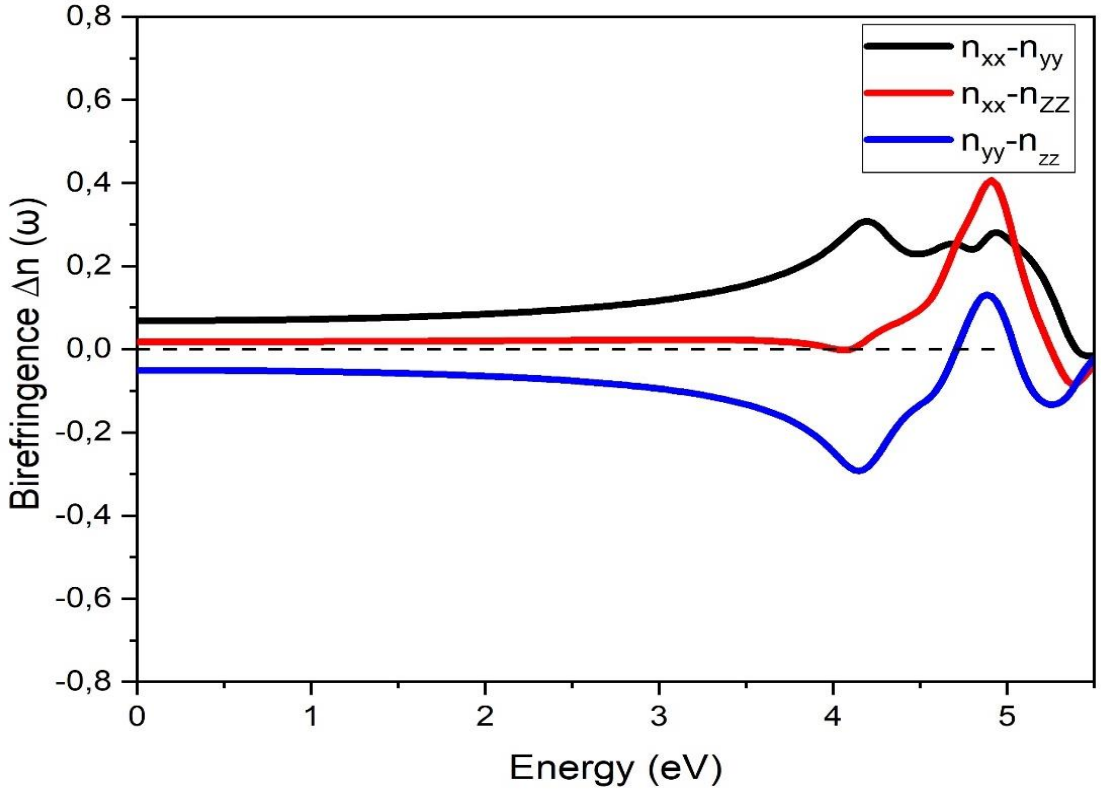

Figure. IV.B. 16. Birefringence of $CsIO_2F_2$.

IV.B.3.4. Mechanical and piezoelectric properties

The elastic property of a material is governed by the atomic arrangements and strength of the bonds between the atoms which make up the material. In other words, the elastic property is determined by the strain (relative change of atom arrangements) and the stress (force per unit area) within a material that has undergone deformation.

The elastic constants C_{ij} are determined by the response of a material to external forces (stresses), the orthorhombic phase is known by nine independent elastic constants (C_{11}, C_{12}, C_{13}, C_{22}, C_{23}, C_{33}, C_{44}, $C_{55,}$ and C_{66}) which are gathered in the table. IV.B.5**.**

Table. IV.B. 5. The calculated elastic constants C_{ij} (in GPa) for $CsIO_2F_2$.

Elastic Constants	C_{11}	C_{22}	C_{33}	C_{44}	C_{55}	C_{66}	C_{12}	C_{13}	C_{23}
$CsIO_2F_2$	260.506	244.3654	244.9712	89.429	83.466	90.407	95.630	82.9159	114.723

According to the table. IV.B.5**.** which reveals that the elastic constants are position and satisfy the stability conditions mentioned in chapter II which declared that the compound $CsIO_2F_2$ is mechanically stable.

From table. IV.B.5, it can be seen that the compression constants C_{11}, C_{22}, and C_{33} are more important than those of the shear C_{44}, C_{55}, and C_{66}, which shows that the compound $CsIO_2F_2$ has a very low shear deformation compared to the compression deformation. The constants C_{22} and C_{33} are almost equal and less important than C_{11} for $CsIO_2F_2$, which reflect the sensitivity of the atomic bond characteristics of the planes (010) and (001) compared to the planes (100) to external conditions.

The other mechanical properties; the bulk modulus B, the shear modulus G, Young's modulus E, and Poisson's ratio ν are collected in table.IV.B.6. They are calculated from the elastic constants C_{ij} in the Voigt-Reuss-Hill approximation (see chapter II)

Table. IV.B. 6. Various elastic modulus in units GPa and B/G ratio and Poisson ratio ν for $CsIO_2F_2$.

Modulus	B_V	B_R	B	G_V	G_R	G	E	ν	B /G
$CsIO_2F_2$	148.49	148.38	148.43	83.099	81.755	82.427	208.66	0.265	1.8

Based on the mechanical properties the behaviors of materials can be introduced according to different criteria such as the Pugh ratio (B/G) and Poisson ratio (ν) our results are represented in the table. IV.B.6, reveals the ductile behavior of $CsIO_2F_2$. The higher the young modulus E value the more rigid the material.

To our knowledge, there are no experimental or theoretical results for comparison purposes, so our results can be considered as a reference for the other works.

IV.B.3.4.1. Debye temperature

In general, the temperature of Deby Θ_D is a very important fundamental parameter to characterize the thermodynamic properties which are related to the elastic constants of one of

the properties is thermal conductivity. One of the methods to determine the Θ_D from the transverse velocity of sound v_t , the longitudinal velocity of sound v_l, and the average velocity of sound v_m which is given in the table. IV.B.7.

Table. IV.B. 7. Longitudinal (v_t in m/s), transverse (v_m in m/s), mean sound velocity (v_m in m/s) and Debye temperature (Θ_D in K) calculation of $CsIO_2F_2$.

	v_t	v_l	v_m	Θ_D
$CsIO_2F_2$	**2146.112**	**4217.862**	**2405.003**	**345.467**

IV.B.3.4.2. Anisotropic factors

Elastic anisotropy provides important information that allows the analysis of variations in the different mechanical properties of a material according to different crystallographic directions.

According to the table. IV.B.8, the universal calculated index A^U is 0.082 which indicate a modest value indicating a somewhat anisotropic nature. In addition, the anisotropy index A_G is significantly higher than that of A_B which shows a very remarkable elastic anisotropy behavior for $CsIO_2F_2$., and has a low resistance to plastic deformation by the shear modulus but a high resistance to elasticity by the bulk modulus.

Table. IV.B. 8. The calculated universal anisotropic index (A^U), bulk anisotropy (A_B and A_G), the shear anisotropic factors (A_1, A_2, A_3) and the bulk anisotropic factors (B_a, B_b, B_c) of $CsIO_2F_2$.

Anisotropy	**A^U**	**A_B (%)**	**A_G (%)**
$CsIO_2F_2$	**0.082**	**0.03**	**0.81**

For better visualization of the anisotropy of Young's modulus E and bulk modulus B, the anisotropy of the two molds in 2D and 3D was traced by the relationships are illustrated in chapiter II

Figure. IV.B.8 and 9 present the projection of the directional dependencies of Young's modulus and the bulk modulus for the planes XY, XZ, YZ. The deviation of the shape of circulars indicates that the degree of anisotropy of the young modulus is more than the bulk modulus. Figure.IV.B. 8 presents projections of 3D surfaces to illustrate elastic anisotropy more directly and reveal interlayer anisotropy of Young's modulus and Bulk modulus.

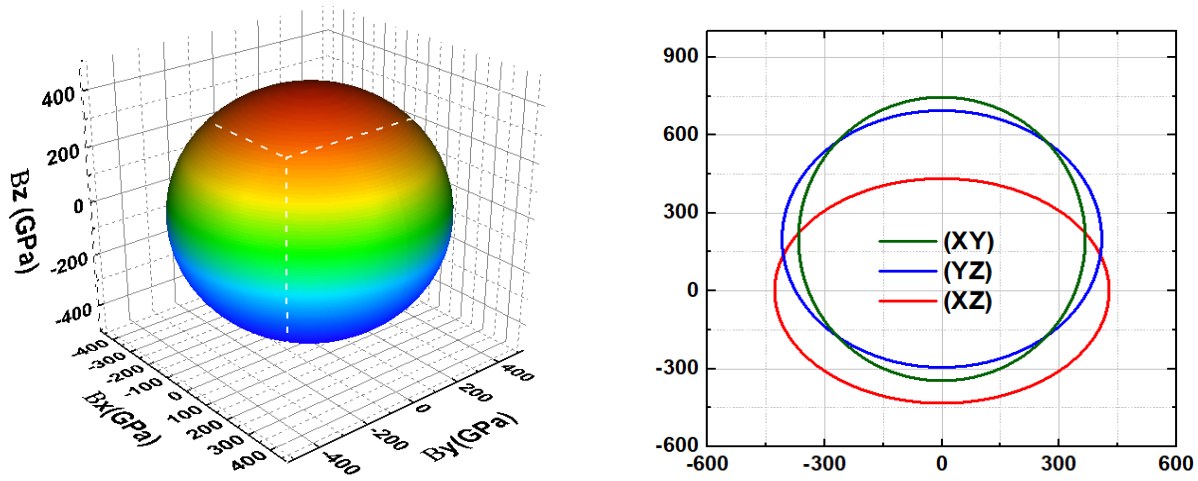

Figure. IV.B. 17. The 3D projection of bulk moduli and your 2D projection of $CsIO_2F_2$.

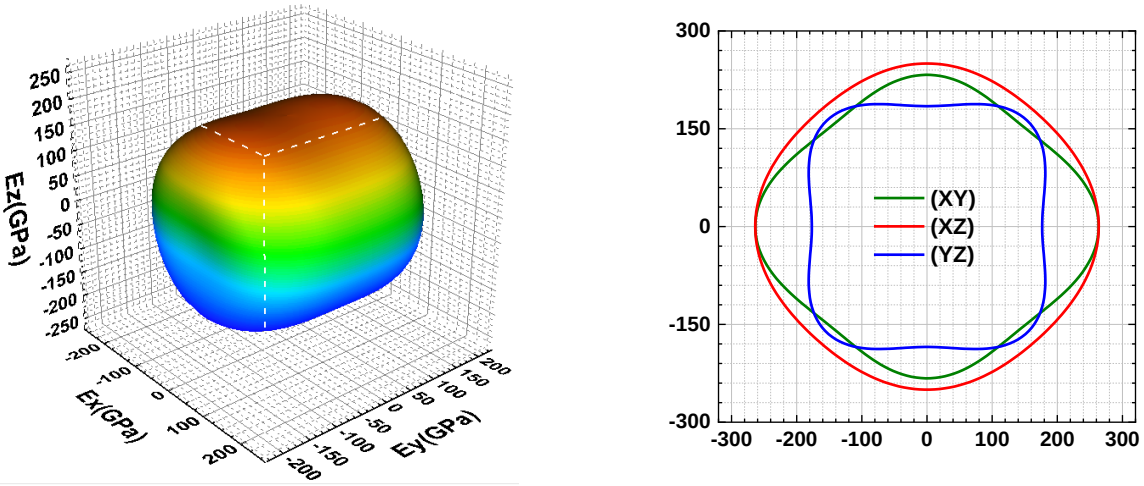

Figure. IV.B. 18. The 3D projection of Young moduli and your 2D projection of $CsIO_2F_2$

IV.B.3.4.3. Piezoelectric property

The piezoelectric constant d_{ij} describes the coupling between dielectric properties and elastic properties, we have calculated the piezoelectric constant of $CsIO_2F_2$ using density-functional perturbation theory, and they are listed in table.IV.B.9. We have five independent piezoelectric constants, in Voigt, notations are presented in table.IV.B.20, which in comparison with quartz (d_{14} = 0.727 pC/N, d_{11} = 2.310 pC/N) suggests that $CsIO_2F_2$ has great important than quartz.

Table. IV.B. 9.Relaxed ion piezoelectric tensor d_{ij} in pC/N for $CsIO_2F_2$.

d_{15}	d_{24}	d_{31}	d_{32}	d_{33}
5.64	**6.46**	**3.73**	**-1.28**	**8.85**

IV.B.3.5 Nonlinear optical properties

IV.B.3.5.1. nonlinear optical susceptibilities

It is well known that nonlinear optical properties are more sensitive to small changes in the band structure than the linear optical properties. This is attributed to the fact that the second harmonic response $\chi_{ijk}^{(2)}$ (ω) involves 2ω resonance in addition to the usual o resonance. Both the 2 ω and o resonances can be further separated into inter-band and intra-band contributions.

Second-order nonlinear optical tensor coefficients $\mathbf{dij} = \frac{1}{2}\boldsymbol{\chi}_{ijk}^{(2)}$ in pm/V and calculated the polarization is calculated using Berry-phase methods, which does not require the random phase approximation and thus includes local field effects properly. The resulting nonlinear optical coefficients are given in table. IV.B.10.

Table. IV.B. 10. Static nonlinear optical coefficients d_{ij} (Pm / V) for $CsIO_2F_2$.

	$d_{15}=d_{31}$	**$d_{24} = d_{32}$**	**d_{33}**
$CsIO_2F_2$	**-0.339**	**-0.811**	**-9.097**

The calculated results show that the three independent elements of the NLO tensor of this compound are $d_{15}=d_{31}$, $d_{24} = d_{32}$, and d_{33} (Voigt notations). If we compared our result for referential available results materials NLO such as KDP (d_{33}=0.39 pm/V) we can present $CsIO_2F_2$ as potential in nonlinear optical magnitude.

IV.B.3.5.2 Electro-optic tensor

The linear electro-optical coefficient (abbreviated as EO) or Pockels coefficient reflects the linear dependence of the refractive index on an applied electric field, and the $CsIO_2F2$ structure has five independent elements. The electronic and total contributions are given in the table. IV.B.11.

The large NLO susceptibilities and EO coefficients reveal that the $CsIO_2F_2$ is a high-performance nonlinear optical crystal.

Table. IV.B. 13. EO tensor in (pm/V) for $CsIO_2F_2$.

	r_{51}	r_{42}	r_{13}	r_{23}	r_{33}
Electron contributions	**0.168**	**0.490**	**0.1673**	**0.592**	**4.55**
Total contributions	**-0.357**	**1.340**	**0.205**	**0.514**	**13.24**

IV.B.4. Conclusion

In the present part, the structural and electronic properties of the $CsIO_2F_2$ is studied within density functional theory (DFT). The Generalized Gradient Approximation GGA developed by Perdew-Burker-Ernzerhof (GGA-PBE) is used to calculate the lattice parameters. The calculated lattice parameters show good behavior according to the experimental data. we adopted Tran and Blaha modified Becke-Johnson (TB-mBJ) potential to investigate the energy band gap; an indirect band gap is found to be (4.54 eV) which underestimate the value of the band gap by 0.4 % than the experimental value, the optical properties such as dielectric function, refractive index, and absorption coefficient, were calculated and explained in detail, from the calculated absorption spectra which ensure the high transparency in the infrared, visible and part of ultraviolet (Deep UV(DUV, UV-C) ranges, the calculated value of the birefringence Δn (ω) for $CsIO_2F_2$ show that it is a uniaxial positive crystal and has birefringence (0.06). All these computations were performed using the FP − LAPW method.

we also used DFPT within LDA-PW approximation to obtain; The elastic constants indicate that $CsIO_2F_2$ is mechanically stable and the higher value of Young's modulus than the bulk modulus and shear modulus, making $CsIO_2F_2$ a has a greater resistance to elastic deformation, Moreover, B/G ratio and v shows the hardness of $CsIO_2F_2$. In addition, the anisotropy of the elastic properties is discussed. We have investigated the NLO susceptibilities and EO tensor. The point group mm2 of RbIO2F2 have three independent elements d_{15}=-0.339pm/V, d_{24}=-0.811 pm/V, and d_{33}= -9.097pm/V,and the electronic contribution EO tensor has five independent elements r_{13}=0.1673 pm/V, r_{23}= 0.490 pm /V, r_{33}= 4.55pm/V, r_{42}=0.490 pm/V and r_{51}=0.16pm/V. For the piezoelectric stress tensor, there are five independent nonzero elements d_{15}=5.64 pC/N, d_{24}=6.46 pC/N, d_{31}=-3.73pC/N, d_{32}=-1.28 pC/N, and d_{33}=8.85 pC/N.

Reference chapter IV

1. Burland, D.M., R.D. Miller, and C.A. Walsh, Second-order nonlinearity in poled-polymer systems. Chemical reviews, 1994. **94**(1): p. 31-75.

2. Weber, M.J., CRC handbook of laser science and Technology supplement 2: optical materials2020: CRC press.

3. Li, Y.-Y., et al., Mixed-anion inorganic compounds: a favorable candidate for infrared nonlinear optical materials. Crystal Growth & Design, 2019. **19**(7): p. 4172-4192.

4. Kang, L., et al., First principles selection and design of mid-IR nonlinear optical halide crystals. Journal of Materials Chemistry C, 2013. **1**(44): p. 7363-7370.

5. Kang, L., et al., Metal thiophosphates with good mid-infrared nonlinear optical performances: a first-principles prediction and analysis. Journal of the American Chemical Society, 2015. **137**(40): p. 13049-13059.

6. Chemla, D., et al., Silver thiogallate, a new material with potential for infrared devices. Optics Communications, 1971. **3**(1): p. 29-31.

7. Boyd, G., H. Kasper, and J. McFee, Linear and nonlinear optical properties of AgGaS 2, CuGaS 2, and CuInS 2, and theory of the wedge technique for the measurement of nonlinear coefficients. IEEE Journal of Quantum Electronics, 1971. **7**(12): p. 563-573.

8. Boyd, G., E. Buehler, and F. Storz, Linear and nonlinear optical properties of ZnGeP2 and CdSe. Applied Physics Letters, 1971. **18**(7): p. 301-304.

9. Halasyamani, P.S. and K.R. Poeppelmeier, Noncentrosymmetric oxides. Chemistry of Materials, 1998. **10**(10): p. 2753-2769.

10. Chen, C.-t. and G.-z. Liu, Recent advances in nonlinear optical and electro-optical materials. Annual Review of Materials Science, 1986. **16**(1): p. 203-243.

11. Chen, X., et al., Hydrothermal synthesis and structural characterization of a novel NLO compound, La (MoO2)(OH)(IO3) 4. Journal of Alloys and Compounds, 2005. **396**(1-2): p. 255-259.

12. Hu, C.-L. and J.-G. Mao, Recent advances on second-order NLO materials based on metal iodates. Coordination Chemistry Reviews, 2015. **288**: p. 1-17.

13. Kong, F., et al., Second-order nonlinear optical materials based on metal iodates, selenites, and tellurites. Structure-Property Relationships in Non-Linear Optical Crystals I, 2012: p. 43-103.

14. Dmitriev, V.G., G.G. Gurzadyan, and D.N. Nikogosyan, Handbook of nonlinear optical crystals. Vol. 64. 2013: Springer.

15. Van Troeye, B., et al., First-principles characterization of the electronic and optical properties of hexagonal LiIO3. Optical Materials, 2014. **36**(9): p. 1494-1501.

16. Atroshchenko, L. and N. Khodeeva, Mechanical strengthening of lithium iodate monocrystals under laser irradiation. Izvestiya Akademii Nauk SSSR, Neorganicheskie Materialy, 1990. **26**(7): p. 1526-1528.

17. Anayan, É.S., et al., Some features of lithium iodate used for intracavity second harmonic generation. Soviet Journal of Quantum Electronics, 1984. **14**(8): p. 1115.

18. Klimova, A.Y., K. Avdienko, and B. Kidyarov, Peculiarities of crystal growth of lithium iodate from acid and neutral solutions and their optical properties. Kristallografiya, 1989. **34**(2): p. 470-473.

19. Hu, C., et al., Advantageous units in antimony sulfides: Exploration and design of infrared nonlinear optical materials. ACS applied materials & interfaces, 2018. **10**(31): p. 26413-26421.

20. Zhang, J., et al., Dielectric, piezoelectric and nonlinear optical properties of polar iodate BiO (IO3) from first-principles studies. Journal of Solid State Chemistry, 2020. **281**: p. 121057.

21. Shi, G., et al., Finding the next deep-ultraviolet nonlinear optical material: NH4B4O6F. Journal of the American Chemical Society, 2017. **139**(31): p. 10645-10648.

22. Zhang, B., et al., Fluorooxoborates: beryllium-free deep-ultraviolet nonlinear optical materials without layered growth. Angewandte Chemie International Edition, 2017. **56**(14): p. 3916-3919.

23. Mao, F.F., et al., Bi (IO3) F2: the first metal iodate fluoride with a very strong second harmonic generation effect. Angewandte Chemie, 2017. **129**(8): p. 2183-2187.

24. Wu, Q., et al., RbIO3 and RbIO2F2: Two promising nonlinear optical materials in mid-IR region and influence of partially replacing oxygen with fluorine for improving laser damage threshold. Chemistry of materials, 2016. **28**(5): p. 1413-1418.

25. Zhang, M., et al., Functional materials design via structural regulation originated from ions introduction: A study case in cesium iodate system. Chemistry of materials, 2018. **30**(3): p. 1136-1145.

26. Abudouwufu, T., et al., Ce (IO3) 2F2· H2O: The First Rare-Earth-Metal Iodate Fluoride with Large Second Harmonic Generation Response. Chemistry–A European Journal, 2019. **25**(5): p. 1221-1226.

27. Zhang, M., et al., Bi3OF3 (IO3) 4: Metal oxyiodate fluoride featuring a carbon-nanotube-like topological structure with large second harmonic generation response. Chemistry of materials, 2017. **29**(3): p. 945-949.

28. Liu, H., et al., ABi2 (IO3) 2F5 (A= K, Rb, and Cs): A Combination of Halide and Oxide Anionic Units To Create a Large Second-Harmonic Generation Response with a Wide Bandgap. Angewandte Chemie, 2017. **129**(32): p. 9620-9624.

29. Miller, R.C., Optical second harmonic generation in piezoelectric crystals. Applied Physics Letters, 1964. **5**(1): p. 17-19.

30. Hohenberg, P. and W. Kohn, Density functional theory (DFT). Phys. Rev, 1964. **136**: p. B864.

31. Kohn, W. and L.J. Sham, Self-consistent equations including exchange and correlation effects. Physical Review, 1965. **140**(4A): p. A1133.

32. Blaha, P., et al., Full-potential, linearized augmented plane wave programs for crystalline systems. Computer physics communications, 1990. **59**(2): p. 399-415.

33. Blaha, P., et al., wien2k. An augmented plane wave+ local orbitals program for calculating crystal properties, 2001. **60**.

34. Perdew, J., K. Burke, and M. Ernzerhof, Perdew, burke, and ernzerhof reply. Physical review letters, 1998. **80**(4): p. 891.

35. Tran, F. and P. Blaha, Accurate band gaps of semiconductors and insulators with a semilocal exchange-correlation potential. Physical review letters, 2009. **102**(22): p. 226401.

36. Hamann, D., et al., Metric tensor formulation of strain in density-functional perturbation theory. Physical Review B, 2005. **71**(3): p. 035117.

37. Troullier, N. and J.L. Martins, Efficient pseudopotentials for plane-wave calculations. Physical Review B, 1991. **43**(3): p. 1993.

38. Ceperley, D.M. and B.J. Alder, Ground state of the electron gas by a stochastic method. Physical Review Letters, 1980. **45**(7): p. 566.

39. Perdew, J.P. and Y. Wang, Pair-distribution function and its coupling-constant average for the spin-polarized electron gas. Physical Review B, 1992. **46**(20): p. 12947.

40. Asada, T. and K. Terakura, Generalized-gradient-approximation study of the magnetic and cohesive properties of bcc, fcc, and hcp Mn. Physical Review B, 1993. **47**(23): p. 15992.

41. Perdew, J.P., et al., Restoring the density-gradient expansion for exchange in solids and surfaces. Physical Review Letters, 2008. **100**(13): p. 136406.

42. Lei, B.-H., et al., Second harmonic generation susceptibilities from symmetry adapted Wannier functions. Physical Review Letters, 2020. **125**(18): p. 187402.

43. Pitarke, J., et al., Theory of surface plasmons and surface-plasmon polaritons. Reports on progress in physics, 2006. **70**(1): p. 1.

44. Guan, S., et al., Electronic, Dielectric and Plasmonic Properties of Two-Dimensional Electride Materials X 2 N (X= Ca, Sr): A First-Principles Study. Scientific reports, 2015. **5**(1): p. 1-14.

45. Bakhshayeshi, A., R.T. Mendi, and M.M. Sarmazdeh, Effect of Hydrostatic Pressure on the Structural, Electronic and Optical Properties of SnS 2 with a Cubic Structure: The DFT Approach. Journal of Electronic Materials, 2018. **47**(2): p. 1472-1480.

46. Güntherodt, G., Optical properties and electronic structure of europium chalcogenides. Physics of condensed matter, 1974. **18**(1): p. 37-78.

47. Lingam, C.B., et al., Structural, electronic, bonding, and elastic properties of NH3BH3: A density functional study. Journal of computational chemistry, 2011. **32**(8): p. 1734-1742.

48. Saidi, F., et al., Structural and mechanical properties of Laves phases YCu2 and YZn2: First principles calculation analyzed with data mining approach. Computational Materials Science, 2014. **89**: p. 176-181.

49. Ravindran, P., et al., Density functional theory for calculation of elastic properties of orthorhombic crystals: Application to TiSi 2. Journal of Applied Physics, 1998. **84**(9): p. 4891-4904.

50. Murugan, A., et al., Structural, electronic, mechanical and magnetic properties of rare earth nitrides REN (RE= Pm, Eu and Yb). Journal of magnetism and magnetic materials, 2015. **385**: p. 441-450.

51. Li, R. and Y. Duan, Structural and anisotropic elastic properties of hexagonal MP (M= Ti, Zr, Hf) monophosphides determined by first-principles calculations. Philosophical Magazine, 2016. **96**(35): p. 3654-3670.

52. Deligoz, E., et al., The first principles study on PtC compound. Materials Chemistry and Physics, 2008. **111**(1): p. 29-33.

53. Ranganathan, S.I. and M. Ostoja-Starzewski, Universal elastic anisotropy index. Physical Review Letters, 2008. **101**(5): p. 055504.

54. Dal Corso, A., et al., Ab initio study of piezoelectricity and spontaneous polarization in ZnO. Physical Review B, 1994. **50**(15): p. 10715.

55. King-Smith, R. and D. Vanderbilt, Theory of polarization of crystalline solids. Physical Review B, 1993. **47**(3): p. 1651.

56. Fox, M., Optical Properties of Solids: Oxford University Press, 2001, Oxford.

57. Nunes, R. and X. Gonze, Berry-phase treatment of the homogeneous electric field perturbation in insulators. Physical review B, 2001. **63**(15): p. 155107.

58. Bera, T.K., et al., Soluble Direct-Band-Gap Semiconductors LiAsS2 and NaAsS2: Large Electronic Structure Effects from Weak As⋯ S Interactions and Strong Nonlinear Optical Response. Angewandte Chemie International Edition, 2008. **47**(41): p. 7828-7832.

59. Becker, P., Borate materials in nonlinear optics. Advanced Materials, 1998. **10**(13): p. 979-992.

60. Kuehne, A.J. and M.C. Gather, Organic lasers: recent developments on materials, device geometries, and fabrication techniques. Chemical Reviews, 2016. **116**(21): p. 12823-12864.

61. Rashkeev, S.N., W.R. Lambrecht, and B. Segall, Efficient ab initio method for the calculation of frequency-dependent second-order optical response in semiconductors. Physical review B, 1998. **57**(7): p. 3905.

62. Wu, C., et al., Recent advances in ultraviolet and deep-ultraviolet second-order nonlinear optical crystals. Coordination Chemistry Reviews, 2018. **375**: p. 459-488.

63. Yu, H., et al., A novel deep UV nonlinear optical crystal Ba 3 B 6 O 11 F 2, with a new fundamental building block, B 6 O 14 group. Journal of Materials Chemistry, 2012. **22**(19): p. 9665-9670.

64. Otaguro, W., E. Wiener-Avnear, and S. Porto, Determination of the second-harmonic-generation coefficient and the linear electro-optic coefficient in LiIO3 through oblique Raman phonon measurements. Applied Physics Letters, 1971. **18**(11): p. 499-501.

65. Xu, X., et al., α-AgI3O8 and β-AgI3O8 with large SHG responses: polymerization of IO3 groups into the I3O8 polyiodate anion. Chemistry of materials, 2014. **26**(10): p. 3219-3230.

66. Sun, C.-F., et al., BaNbO (IO3) 5: a new polar material with a very large SHG response. Journal of the American Chemical Society, 2009. **131**(27): p. 9486-9487.

67. Nguyen, S.D., et al., BiO (IO3): a new polar iodate that exhibits an aurivillius-type (Bi2O2) 2+ layer and a large SHG response. Journal of the American Chemical Society, 2011. **133**(32): p. 12422-12425.

68. Chen, X., et al., Designing an excellent deep-ultraviolet birefringent material for light polarization. Journal of the American Chemical Society, 2018. **140**(47): p. 16311-16319.

69. Chang, T.-Y., et al., M (IO3)(HPO4)(H2O)(M= Sc, Fe, Ga, In): introduction of phosphate anions into metal iodates. Crystal Growth & Design, 2017. **17**(9): p. 4984-4989.

70. Wu, C., et al., Deep-ultraviolet transparent alkali metal–rare earth metal sulfate NaY (SO 4) 2· H 2 O as a nonlinear optical crystal: Synthesis and characterization. CrystEngComm, 2021. **23**(16): p. 2945-2951.

71. Liu, L., et al., Design and synthesis of a series of novel mixed borate and carbonate halides. Chemistry–A European Journal, 2017. **23**(43): p. 10451-10459.

72. Han, G., et al., A fluorooxosilicophosphate with an unprecedented SiO2F4 species. Angewandte Chemie International Edition, 2018. **57**(31): p. 9828-9832.

73. Liang, M.-L., et al., BiFSeO3: an excellent SHG material designed by aliovalent substitution. Journal of the American Chemical Society, 2016. **138**(30): p. 9433-9436.

74. Feng, J.-H., et al., Li7 (TeO3) 3F: a lithium fluoride tellurite with large second harmonic generation responses and a short ultraviolet cutoff edge. Inorganic Chemistry, 2017. **56**(23): p. 14697-14705.

75. Shi, S., et al., A cation size effect on the framework structures in ABi 2 SeO 3 F 5 (A= K and Rb): first examples of alkali metal bismuth selenite fluorides. Dalton Transactions, 2018. **47**(18): p. 6598-6604.

76. Zhang, G., et al., SbF3: A new second-order nonlinear optical material. Optical Materials, 2008. **31**(1): p. 110-113.

77. Zhang, G., et al., NaSb 3 F 10: A new second-order nonlinear optical crystal to be used in the IR region with very high laser damage threshod. Applied Physics Letters, 2009. **95**(26): p. 261104.

78. Huang, Y., et al., A study on K 2 SbF 2 Cl 3 as a new mid-IR nonlinear optical material: new synthesis and excellent properties. Journal of Materials Chemistry C, 2015. **3**(37): p. 9588-9593.

79. Wu, Q., et al., KBi4F13: A New Nonlinear Optical Material with a large damage threshold. Chin. J. Inorg. Chem, 2015. **31**(9): p. 1875-1880.

80. Wu, X., D. Vanderbilt, and D. Hamann, Systematic treatment of displacements, strains, and electric fields in density-functional perturbation theory. Physical review B, 2005. **72**(3): p. 035105.

81. Veithen, M., X. Gonze, and P. Ghosez, Nonlinear optical susceptibilities, Raman efficiencies, and electro-optic tensors from first-principles density functional perturbation theory. Physical review B, 2005. **71**(12): p. 125107.

GENERAL CONCLUSION

General conclusion and perspective

The main objective of this work is to calculate the physical properties of some families of fluoro-iodates and metal chromates especially the quadratic ONL coefficients, distributed over the non-centrosymmetric classes 2mm, $I4^{-}$, and 3m. Additionally, to piezoelectricity properties. For this purpose, the first-principles calculation is performed to predict the crystal structure and properties related to the electron configuration by performing first-principles DFT and DFPT calculations.

The polar chromate Rb Li CrO_4 has the space group (P31c) belongs to the polar point group 3m. It's having an electronic indirect band gap (3.6eV) which depend on a high LDT value. the VB edge below the Fermi level is mainly composed of Cr-d and O-p states with slight Li-s states, while the bottom of CBs is occupied by Cr-d and O-p states, which indicates that Cr-Ounits are the main sources to determine the magnitude of band gaps and the main sources of SHG responses. The large optical gap at 3.61 eV, is reflected in the transparency of $RbLiCrO_4$ along with the Infrared (IR), Visible (Vis), and ultraviolet (UV). Therefore, the small birefringence ($\Delta n=0.047$) can restrict their applications in the transparent region. the computed elastic constant indicates that the compound is mechanically stable according to the elastic stability criteria. Our compound possesses ductile nature. A large SHG coefficient $\boldsymbol{d}_{31} = -1.621\ \boldsymbol{pm}/\boldsymbol{V}$, $\boldsymbol{d}_{22} = 2.272\ \boldsymbol{pm}/\boldsymbol{V}$, and $\boldsymbol{d}_{33} = 4.51\ \boldsymbol{pm}/\boldsymbol{V}$ and high electro-optic coefficients which has a great potential as a candidate material for the (IR), (Vis), and (UV) NLO region. One the other hand, $RbLiCrO_4$ exhibit higher piezoelectric coefficients $\boldsymbol{d}_{15}$, $\boldsymbol{d}_{22}$, $\boldsymbol{d}_{31}$, $\boldsymbol{d}_{33}$ are $22.24\ \boldsymbol{pC}/\boldsymbol{N}, 0.014\ \boldsymbol{pC}/\boldsymbol{N}, -1.68\ \boldsymbol{pC}/\boldsymbol{N}, 3.20\ \boldsymbol{pC}/\boldsymbol{N}$ which in comparison with quartz ($\boldsymbol{d}_{14} = 0.727\ \boldsymbol{pC}/\boldsymbol{N}$, $\boldsymbol{d}_{11} = 2.310\ \boldsymbol{pC}/\boldsymbol{N}$), $RbLiCrO_4$ a promising candidate for piezoelectric applications.

The polar double bismuth-argent chromate $AgBi(CrO_4)_2$ has the space group of Ag $Bi(CrO_4)_2$ ($\boldsymbol{I}\bar{4}$)belongs to the polar point group $\bar{4}$. It's exhibited an electronic indirect bandgap (1.38eV). The electronic properties were investigated, the VB edge below the Fermi level is mainly composed of Cr-d, O-p states, which indicates that Cr-Ounits are the main sources of SHG responses. The optic gap is 1.5 eV which is reflected in the transparency of $AgBi(CrO_4)_2$ along the mid-infrared region. Therefore, the large birefringence of $AgBi(CrO_4)_2$ ($\Delta n=0.18$)

makes this compound a potential candidate in the mid-infrared region. $AgBi(CrO_4)_2$ possesses ductile nature with large SHG coefficients d_{14}= 8.55 pm/V and d_{15}=16.71 pm/V than KDP (0.39 pm/V) and has high electro-optic coefficients which have great potential as a candidate material for the mid-IR NLO region. One the other hand, $AgBi(CrO_4)_2$ exhibit higher piezoelectric coefficients $\boldsymbol{d}_{14}$, $\boldsymbol{d}_{15}$, $\boldsymbol{d}_{31}$, $\boldsymbol{d}_{36}$ are $1.76\ \boldsymbol{pC}/\boldsymbol{N}$, $-4.72\ \boldsymbol{pC}/\boldsymbol{N}$, $-10.47\ \boldsymbol{pC}/\boldsymbol{N}$, $-10.92\ \boldsymbol{pC}/\boldsymbol{N}$ which in comparison with quartz, $AgBi\ (CrO_4)_2$ a promising candidate for piezoelectric applications

The polar fluoro-oxidates $RbIO_2F_2$ has the space group ($Pca2_1$) belongs to the polar point group mm2. the electronic structure of the system has an indirect bandgap by (4.17 eV) with a deviation of 0.47% from the experimental value. the V_B edge below the Fermi level is mainly formed by the p orbital of the O atom and by the contributions of p orbitals of F and I atoms. The C_B is mainly formed by the p orbitals of F and I atoms, respectively denoting that the I-O-F units are the key index for determining the nonlinear properties in the $RbIO2F_2$ compound. From the calculated absorption spectra which ensure the high transparency in the infrared, visible, and part of ultraviolet (UV-A) ranges, the birefringence $\Delta n\ (\omega)$ for $RbIO_2F_2$ shows that it has a small birefringence (0.047). The elastic constants indicate that $RbIO_2F_2$ is mechanically stable and the elastic moduli possesses intermediate hardness. A large SHG coefficient of $RbIO_2F_2$; $\boldsymbol{d}_{15} = -0.534\ \boldsymbol{pm}/\boldsymbol{V}$, $\boldsymbol{d}_{24} = 1.125\ \boldsymbol{pm}/\boldsymbol{V}$, and $\boldsymbol{d}_{33} = -10.04\ \boldsymbol{pm}/\boldsymbol{V}$. and the electronic contribution EO tensor makes a potential candidate for nonlinear applications. piezoelectric coefficients; $\boldsymbol{d}_{15} = 7.827\ \boldsymbol{PC}/\boldsymbol{N}$, $\boldsymbol{d}_{24} = 6.542\ \boldsymbol{PC}/\boldsymbol{N}$, $\boldsymbol{d}_{31} = -1.13\ \boldsymbol{PC}/\boldsymbol{N}$, $\boldsymbol{d}_{32} = -0.32\ \boldsymbol{PC}/\boldsymbol{N}$, and $\boldsymbol{d}_{33} = 4.34\ \boldsymbol{PC}/\boldsymbol{N}$, which in comparison with quartz have $RbIO_2F_2$ a promising candidate for piezoelectric applications.

The polar fluoro-oxidates $CsIO_2F_2$ has the space group ($Pca2_1$) belongs to the polar point group mm2. the electronic structure of the system has an indirect bandgap is found to be (4.54 eV) which underestimate the value of the bandgap by 0.4 % than the experimental value. the VB edge below is mainly composed of O-p states with a slight I- p and F-p states, while the bottom of CBs is occupied by I-p states, which indicates that I-O-F units are the main sources to determine the magnitude of band gaps. from the calculated absorption spectra which ensure the high transparency in the IR, vis, and part of ultraviolet (Deep UV (DUV, UV-C) ranges, the birefringence $\Delta n\ (\omega)$ for $CsIO_2F_2$ shows that it has a birefringence (0.06). The elastic constants indicate that $CsIO_2F_2$ is mechanically stable and possesses ductile nature. A large SHG

coefficient of $CsIO_2F_2$; $d_{15} = -0.339\ pm/V$, $d_{24} = -0.811\ pm/V$, and $d_{33} = -9.097\ pm/V$, and the electronic contribution EO tensor makes a potential candidate for nonlinear applications.

Piezoelectriccoefficients; $d_{15} = 5.64\ pC/N$, $d_{24} = 6.46\ pC/N$, $d_{31} = -3.73\ pC/N$ $d_{32} = -1.28\ pC/N$, and $d_{33} = 8.85\ pC/N$ which in comparison with quartz have $CsIO_2F_2$ a promising candidate for piezoelectric applications.

To further enrich this list, it would be desirable to extend this study by adopting the Strategies for designing NLO compounds to foresee new materials that meet at all levels ONL conditions, by a combination of chemical elements of the periodic table, to have a larger data bank

ملخص- من المعروف جيدًا أن مناهج DFT لديها القدرة على التنبؤ بدقة بخصائص الحالة الأساسية للمواد، وتعد أدوات التحليل المطورة أمرًا حيويًا لفحص آليتها الجوهرية، وفقًا للفئات غير المتناظرة 2mm ،$I\bar{4}$ و3 m. في هذه الدراسة، تم فحص وتحليل الخصائص البصرية الخطية وغير الخطية باستخدام نظرية الكثافة الوظيفية عن طريق الموجة المستوية المعززة الخطية الكاملة المحتملة (FP-LAPW) والاحتمال الزائف للموجة المستوية (PP-PW). تُستخدم طريقة FP-LAPW لدراسة الخصائص الإلكترونية والخصائص البصرية الخطية باستخدام الكثافة الوظيفية المطورة حديثًا لـ Tran و Blaha. علاوة على ذلك، يتم حساب الميزات البصرية مثل الوظائف العازلة للكهرباء، ومعامل الامتصاص، ومعامل الانكسار، والانعكاسية، ووظيفة فقدان طاقة الإلكترون لطاقات الفوتون حتى 40 فولت. تمت دراسة الثابت المرن، البصري غير الخطي (NLO)، التوتر الخطي الكهروضوئي، والتوتر الكهروضغطي في إطار النظرية الحديثة للاستقطاب ونظرية الاضطراب الوظيفي للكثافة (DFPT) بواسطة تقريب PP-PW. استنادًا إلى العلاقات شبه التجريبية، معامل يونغ، ومعامل القص والكتلة، ونسبة بواسون، والعوامل متباينة الخواص، وسرعات الصوت ودرجة حرارة ديباي.

الكلمات المفتاحية :DFT,TB-mBJ,Mechanical properties,nonlinear Optical properties, and Piezoelectricity

Abstract- It is well known that the DFT approaches have the ability to accurately predict the ground-state properties of the materials, and the developed analysis tools are vital to investigating their intrinsic mechanism. According to the non-centrosymmetric classes 2mm, $I4^{-}$, and 3m. In this study, the linear and nonlinear optical properties are investigated and analyzed using the density functional theory by full-potential linearized augmented plane wave (FP-LAPW) and plane wave pseudo-potential (PP-PW). The FP-LAPW method is used to study the electronic properties and linear optical properties with the recently developed density functional of Tran and Blaha. Furthermore, optical features such as dielectric functions, absorption coefficient, refractive index, reflectivity, and electron energy loss function are calculated for photon energies up to 40 eV. The elastic constant, nonlinear optical (NLO), linear electro-optical, and piezoelectric tensor within the framework of the modern theory of polarization and density functional perturbation theory (DFPT) are studied by the PP-PW approximation. Based on the semi-empirical relations, Young's modulus, shear and bulk modulus, Poisson's ratio, anisotropic factors, sound velocities, and Debye temperature.

Keywords: DFT, TB-mBJ, Mechanical properties, nonlinear Optical properties, and Piezoelectricity

Résumé- Il est bien connu que les approches DFT ont la capacité de prédire avec précision les propriétés de l'état fondamental des matériaux, et les outils d'analyse développés sont essentiels pour étudier leur mécanisme intrinsèque.Selon les classes non centrosymétriques 2mm, $I4^{-}$et 3m.Dans cette étude, les propriétés optiques linéaires et non linéaires sont étudiées et analysées en utilisant la théorie de la fonctionnelle de la densité par le plein potentiel linéarisé augmenté onde plane (FP-LAPW) et le pseudo-potentiel onde plane (PP-PW). La méthode FP-LAPW est utilisée pour étudier les propriétés électroniques et les propriétés optiques linéaires avec la fonctionnelle de la densité récemment développée par Tran et Blaha. De plus, les caractéristiques optiques telles que les fonctions diélectriques, le coefficient d'absorption, l'indice de réfraction, la réflectivité, la fonction de perte d'énergie des électrons sont calculées pour des énergies de photons jusqu'à 40 eV. La constante d'élasticité, l'optique non linéaire (NLO), l'électro-optique linéaire, et les tensions piézoélectriques dans le cadre de la théorie moderne de la polarisation et de la théorie de perturbation fonctionnelle de la densité (DFPT) sont étudiées par l'approximation PP-PW. Sur la base des relations semi-empiriques, le module de Young, les modules de cisaillement et compressibilité, le coefficient de Poisson, les facteurs anisotropes, les vitesses du son et la température de Debye.

Mots-clés : DFT, TB-mBJ, propriétés mécaniques, propriétés optiques non linéaires et piézoélectricité